Plasma Physics Reports, Vol. 27, No. 7, 2001, pp. 545–548. Translated from Fizika Plazmy, Vol. 27, No. 7, 2001, pp. 579–583.

TOKAMAKS

Behavior of Hard X-ray Emission in Discharges with Current Disruptions in the DAMAVAND and TVD Tokamaks

E. Farshi*, R. Amrollahy, A. V. Bortnikov***†, N. N. Brevnov***, Yu. V. Gott***, and V. A. Shurygin*****

**Department of Advanced Energy Engineering Science, Kyushu University, Kasuga, Fukuoka, 816-8580 Japan*
***K-N Toosi University of Technology, Tehran, Islamic Republic of Iran*
****Russian Research Centre Kurchatov Institute, pl. Kurchatova 1, Moscow, 123182 Russia*

Received January 10, 2001; in final form, February 9, 2001

Abstract—Results are presented from studies of the behavior of hard X-ray emission in discharges with current disruptions in the DAMAVAND and TVD tokamaks. The current disruptions are caused by either an MHD instability or the instability related to the vertical displacement of the plasma column. Experiments were conducted at a fixed value of the safety factor at the plasma boundary ($q_a \simeq 2.3$). Experimental data show that, during a disruption caused by an MHD instability, hard X-ray emission is suppressed by this instability if the amplitude of the magnetic field fluctuations exceeds a certain level. If the disruption is caused by the instability related to the vertical displacement of the plasma column, then hard X-ray emission is observed at the instant of disruption. The experimental results show that the physical processes resulting in the generation and suppression of runaway electron beams are almost identical in large and small tokamaks. © *2001 MAIK "Nauka/Interperiodica".*

1. INTRODUCTION

Plasma confinement in tokamaks is provided by the plasma current produced by a toroidal eddy electric field. This field leads to the generation of runaway electrons. The current and energy of the runaway electrons depend substantially on the discharge parameters (such as plasma temperature, plasma density, loop voltage, and impurity concentration), the level of the plasma MHD activity, and abrupt changes in the current and in the plasma density. This makes it rather difficult to analyze and interpret the experimental results.

The presence of runaway electron beams in plasma was revealed in early experiments in the TMP, TM-3, T-6, T-10 [1–5], and other tokamaks. The theory of electron acceleration in a plasma is presented, e.g., in [6–9]. Recently, interest in the problems related to electron acceleration has increased in connection with both experiments in large tokamaks and the development of the ITER tokamak reactor project [10]. Fast electrons with energies of tens or hundreds of MeV can carry a significant fraction of plasma energy, which can be locally deposited (during current disruptions or the vertical displacement of the plasma column due to the loss of stability) on the internal components of the tokamak chamber, thus resulting in high heat and electromechanical loads on them. Therefore, the development of methods for suppressing runaway electron beams in a tokamak reactor is an important problem.

Relevant investigations are now being carried out (more or less actively) in almost all of the tokamaks (e.g., TEXTOR, TFTR, JET, and JT-60U [11–18]).

However, in large tokamaks, experiments with disruptive regimes present difficulties because of the negative effect of runaway electron beams on the internal components of the vacuum chamber. In this respect, experiments in small tokamaks are less dangerous and, therefore, are of great interest.

This study is aimed at investigating the behavior of runaway electrons in the DAMAVAND tokamak in discharges with current disruptions caused by an MHD instability [19] and in the TVD tokamak in discharges with disruptions caused by the instability related to the vertical displacement of the plasma column [20].

2. EXPERIMENT

Experiments were conducted in the DAMAVAND (Tehran) and TVD (Kurchatov Institute) tokamaks. The basic parameters of both these tokamaks are the following: $R = 36$ cm, $a = 7$ cm, $B_T \simeq 1$ T, $k = 1.2$, $I_p \leq 40$ kA, $n_e = 3 \times 10^{13}$ cm^{-3}, $T_e = 300$ eV, and $T_i = 150$ eV; the discharge duration is ~15 ms. The elongation factor in the DAMAVAND device ($k = 1.2$) was chosen so as to ensure plasma stability in the vertical direction. In the TVD device, the experiments were conducted at an elongation factor of $1.7 \leq k \leq 2$. To determine the plasma current I_p, the loop voltage V_l, the plasma dis-

† Deceased.

1063-780X/01/2707-0545$21.00 © 2001 MAIK "Nauka/Interperiodica"

Table

	I_p, kA (before disruption)	B_T, T
I	32	1
II	28	0.88
III	24	0.75
IV	21	0.63

placements along the major radius and in the vertical direction (ΔR and Δz, respectively), the time derivative of the poloidal magnetic field $\dot{B}_p$, and the intensity of hard X-ray emission, we used a standard tokamak diagnostic complex. The detector of hard X radiation was positioned at a distance of several meters from the device.

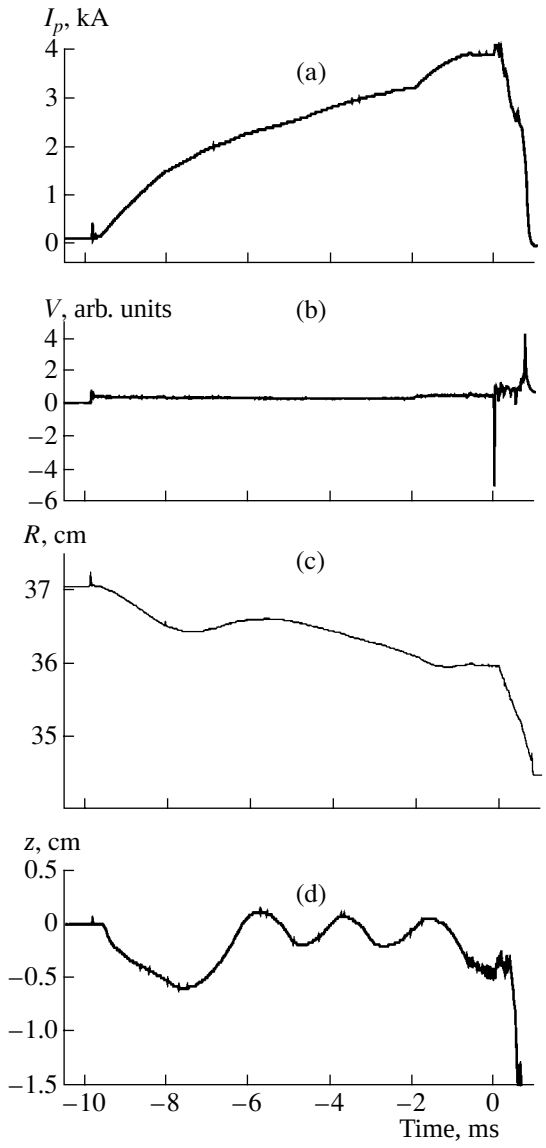

Fig. 1. Typical waveforms of (a) the discharge current, (b) loop voltage, and (c) horizontal and (d) vertical displacements of the plasma column in the DAMAVAND tokamak.

Runaway electrons generated inside the plasma column drift in the radial direction until their orbits meet either the limiter or the wall of the vacuum chamber. Colliding with a solid surface, the electrons produce hard X-ray emission, which provides information on the parameters of runaway electrons in the plasma.

To obtain an MHD-driven disruption of the plasma current, an additional capacitor bank was switched to the inductor. As a result, the discharge current increased by 10–20% and a disruption occurred. Experiments were performed for four values of the plasma current. The current was varied consistently with the toroidal magnetic field so as to keep the safety factor at the plasma boundary nearly constant ($q_a \simeq 2.3$). The relevant data are given in the table.

Typical waveforms of the discharge current, loop voltage, and displacements of the plasma column in the horizontal (R) and vertical (z) directions in the DAMAVAND tokamak are shown in Fig. 1. The time is counted from the instant of disruption. It is seen in the figure that the active feedback system fixes the position of the plasma column rather well up to the instant of disruption.

To study the regimes with current disruptions caused by the vertical displacement of the plasma column in the TVD tokamak, instead of switching on an additional capacitor bank for increasing the current, an active feedback system for the vertical stabilization of the plasma column was switched off at a certain time. In this case, the plasma column began to move in the vertical direction and then a disruption occurred. The corresponding waveforms are shown in Fig. 2. In addition to the time dependences of the discharge current and the vertical and horizontal positions of the plasma column, the figure illustrates the time behavior of the intensity of hard X-ray emission.

3. EXPERIMENTAL RESULTS

3.1. Hard X-ray Emission during an MHD Disruption

Figure 3 shows the typical waveforms of (a) the plasma current, (b) hard X-ray emission intensity, and (c) MHD oscillations with $n = 1$ and $m = 2$. It is seen in the figure that hard X-ray emission disappears when intensive MHD oscillations are excited.

Because of insufficient statistics, we failed to determine how the time interval between the end of hard X-ray emission and the beginning of the current disruption depends on the plasma parameters. In experiments, this interval varied from 0 to 1 ms. It is interesting to note that the time interval between hard X-ray bursts varies only slightly during the discharge. However, two or three bursts before the end of X-ray emission occur with nearly two times shorter time intervals. As the discharge current varies, the time interval between the

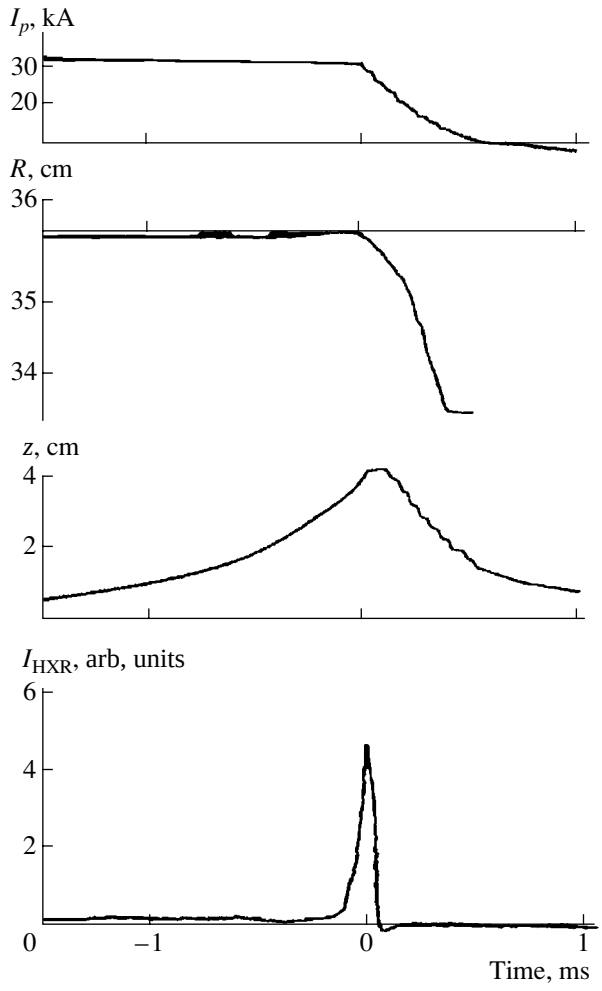

Fig. 2. Typical waveforms of the discharge current I_p, displacements of the plasma column in the horizontal (R) and vertical (Z) directions, and hard X-ray emission intensity I_{HXR} in the TVD tokamak.

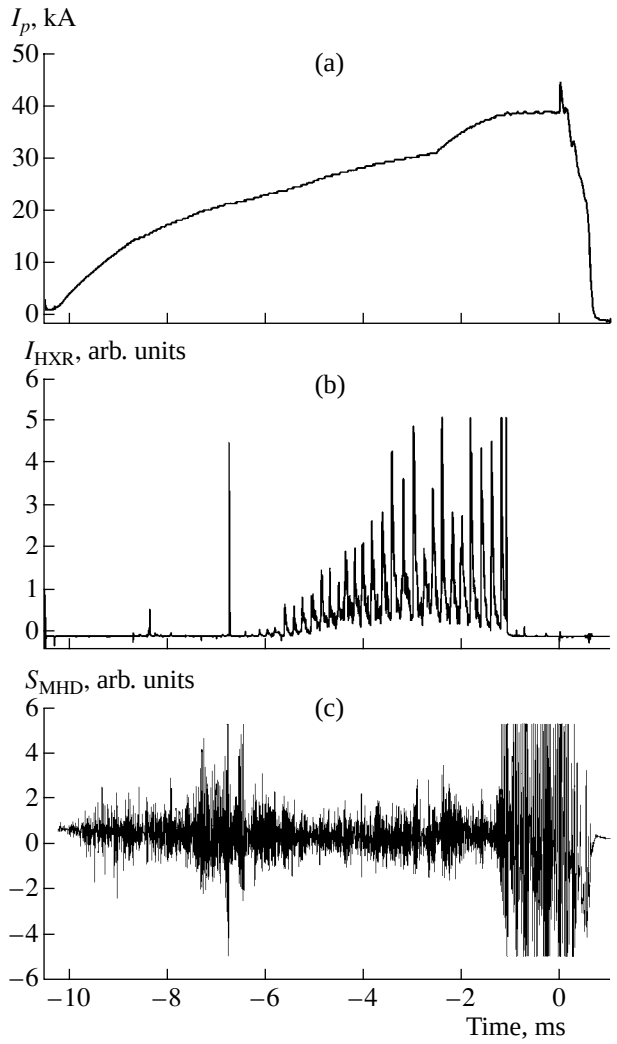

Fig. 3. Typical waveforms of (a) the discharge current, (b) hard X-ray emission intensity, and (c) MHD fluctuations in the discharge with an MHD disruption.

hard X-ray bursts also varies (Fig. 4). It is seen in the figure that, as the current varies by a factor of 1.5, the time interval between the bursts increases by 30%.

3.2. Hard X-ray Emission during a Disruption Caused by the Vertical Instability [20]

Figure 2 shows the typical time behavior of the hard X-ray emission intensity in disruptive discharges in the TVD device. It is seen that, in this case, hard X-ray emission appears immediately at the instant of disruption and decays very rapidly. In this case, we did not observe any significant increase in the amplitude of MHD oscillations.

4. DISCUSSION OF THE RESULTS

Experiments carried out in the regimes with an MHD disruption at $q \simeq$ const show that periodically repeating hard X-ray bursts are observed in the entire range of currents and magnetic fields under study. Presumably, this periodicity is explained by the rotation of the plasma column. It is shown that, if the amplitude of MHD oscillations exceeds a certain level, hard X-ray emission terminates. Such a suppression of hard X-ray emission by MHD oscillations was also observed in other tokamaks (see, e.g., [14]). This evidences that the MHD instability destroys the runaway electron beam, seemingly, due to the formation of magnetic islands. The estimate of the value of $\dot{B}/B_T$ that is necessary for suppressing hard X-ray emission coincides with that obtained, e.g., for the TJ-60U tokamak (≤0.1%) [18]. We may suggest that magnetic islands formed by applying an external poloidal field will also efficiently destroy runaway electron beams.

After a disruption caused by either an MHD instability or the vertical displacement of the plasma col-

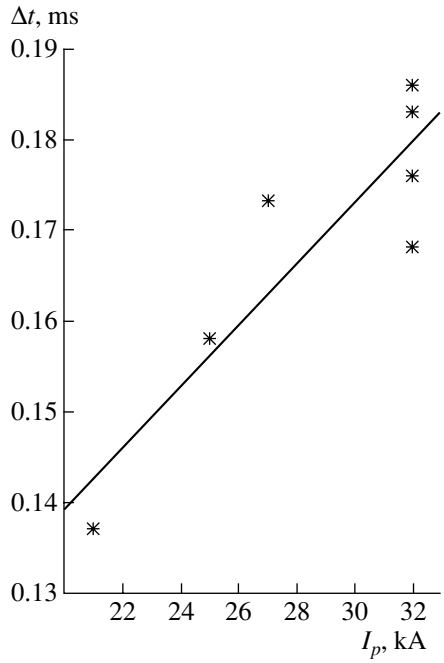

Fig. 4. Time interval between hard X-ray bursts as a function of the discharge current before the disruption.

umn, the current decay rate is $dI/dt \sim 50$ MA/s. In large tokamaks, hard X-ray bursts are usually observed at such current decay rates. In our experiments, hard X-ray emission was observed only after a disruption caused by the vertical instability. This evidences that disruptions in large tokamaks occur primarily due to the loss of vertical stability of the plasma column.

5. CONCLUSIONS

The experimental studies of hard X-ray emission in the DAMAVAND and TVD small tokamaks allow us to draw the following conclusions:

(i) The physical processes resulting in the generation and suppression of runaway electron beams in small tokamaks do not contradict the well-known experimental results obtained for large tokamaks.

(ii) Abrupt changes in the loop voltage and the subsequent decrease in the plasma current (with a current decay rate of several tens of MA/s or higher) favor the generation of runway electrons.

(iii) Runaway electron beams are destroyed in the presence of MHD oscillations when $\dot{B}/B_T \geq 0.1\%$.

(iv) For suppressing runaway electron beams, a tokamak reactor should have a system for controlling the formation of magnetic islands and a facility providing a current decay rate of no higher than 10 MA/s.

ACKNOWLEDGMENTS

We thank the DAMAVAND and TVD teams for their assistance in the experiments.

REFERENCES

1. F. L. Bezbatchenko, I. N. Golovin, P. I. Kozlov, *et al.*, in *Plasma Physics and Problems of Controlled Nuclear Fusion*, Ed. by M. A. Leontovich (Akad. Nauk SSSR, Moscow, 1958), Vol. IV, p. 116.
2. V. S. Strelkov, in *Plasma Physics and Problems of Controlled Nuclear Fusion*, Ed. by M. A. Leontovich (Akad. Nauk SSSR, Moscow, 1958), Vol. IV, p. 156.
3. V. V. Alikaev, K. A. Razumova, and Yu. A. Sokolov, Fiz. Plazmy **1**, 546 (1975) [Sov. J. Plasma Phys. **1**, 303 (1975)].
4. V. S. Vlasenkov, V. M. Leonov, and V. G. Mereshkin, Nucl. Fusion **13**, 509 (1973).
5. A. B. Berlizov, G. A. Bobrovskii, G. E. Notkin, *et al.*, in *Proceedings of the 8th European Conference on Controlled Fusion and Plasma Physics, Prague, 1977*, Vol. 1, p. 29.
6. V. V. Parail and O. P. Pogutse, in *Reviews of Plasma Physics*, Ed. by M. A. Leontovich and B. B. Kadomtsev (Énergoatomizdat, Moscow, 1982; Consultants Bureau, New York, 1986), Vol. 11.
7. H. Knoepfel and D. A. Spong, Nucl. Fusion **19**, 785 (1979).
8. A. J. Russo and R. B. Campbell, Nucl. Fusion **33**, 1305 (1993).
9. S. Tokuda and R. Yoshino, Nucl. Fusion **39**, 1123 (1999).
10. S. Putvinski, H. Berk, D. Borba, *et al.*, Fusion Energy **3**, 1001 (1999).
11. R. J. Spers, K. H. Finken, G. Mank, *et al.*, Nucl. Fusion **33**, 1775 (1993).
12. A. C. Janos, E. D. Fredrickson, K. M. McGuire, *et al.*, Plasma Phys. Controlled Nucl. Fusion Res. **1**, 527 (1993).
13. J. A. Wesson, R. D. Gill, M. Hugon, *et al.*, Nucl. Fusion **29**, 641 (1989).
14. R. D. Gill, Nucl. Fusion **33**, 1613 (1993).
15. R. Yoshino, S. Tokuda, and Y. Kawano, Nucl. Fusion **39**, 151 (1999).
16. Y. Yoshino, R. Kawano, Y. Neyatani, *et al.*, Fusion Energy **1**, 345 (1997).
17. R. Kawano, Y. Yoshino, Y. Neyatani, *et al.*, in *Proceedings of the 24th European Conference on Controlled Fusion and Plasma Physics, Berchtesgaden, 1997* [ECA **21A** (2), 501 (1997)].
18. H. Tamai, R. Yoshino, S. Tokuda, *et al.*, in *Proceedings of the 18th IAEA Fusion Energy Conference, Sorrento, 2000*, paper IAEA-CN-77/EX9/2.
19. R. Amrollahy, I. Farshi, A. V. Bortnikov, *et al.*, Fiz. Plazmy **23**, 609 (1997) [Plasma Phys. Rep. **23**, 561 (1997)].
20. A. V. Bortnikov, N. N. Brevnov, Yu. V. Gott, and V. A. Shurygin, Fiz. Plazmy **21**, 672 (1995) [Plasma Phys. Rep. **21**, 634 (1995)].

Translated by N. F. Larionova

Plasma Physics Reports, Vol. 27, No. 7, 2001, pp. 549–556. Translated from Fizika Plazmy, Vol. 27, No. 7, 2001, pp. 584–591.

PLASMA DYNAMICS

Experimental Verification of the Effect of Different Preionization Systems on the Implosion Dynamics of an Argon Double Gas Puff

A. G. Rousskikh, R. B. Baksht, A. Yu. Labetsky, A. V. Shishlov, and A. V. Fedyunin

Institute of High-Current Electronics, Siberian Division, Russian Academy of Sciences, Akademicheskiĭ pr. 4, Tomsk, 634055 Russia

Received July 25, 2000; in final form, October 31, 2001

Abstract—Experiments are reported on the implosion of argon double gas puffs in the GIT-12 current generator (T_{fr} = 0.25 μs, I_m = 2.3 MA). The gas-puff medium was preionized by different methods. The experimental data provide evidence for a strong effect of the initial conditions for the formation of the current-carrying shell on the implosion process. Emphasis is given to a discussion of the following issues: the enhanced scatter in both the emission power and X-ray yield in the Ar K-lines, the existence of a large number of current filaments, the uncertainty in the process by which the generator current is redistributed among a progressively smaller number of current filaments, and the redistribution of the generator current between the inner and outer gas-puff shells.

1. INTRODUCTION

Although the problem of preionization of gas-puff media has been studied in many papers, it still remains a challenging issue. Specifically, for terawatt-power devices, a fairly simple and efficient preionization method has not yet been developed. In experiments in the GIT-4 inductive storage generator, with a current rise time of about 100 ns [2], a traditional preionization system based on spark illumination in an external magnetic field [1] operated at a fairly high efficiency. However, in the GIT-12 current generator, with a current rise time of about 250 ns at a current amplitude of 1.9–2.2 MA [3], this preionization system gave rise to a significant scatter in both the emitted X-ray power and X-ray yield. This circumstance motivated further investigations in this area. Here, we describe an attempt to elaborate the most promising preionization method and to understand the main effects that occur during the implosion of a gas-puff substance preionized in different ways.

2. DESCRIPTION OF THE EXPERIMENT

Our experiments were carried out in two steps. First, we developed and bench-tested several of the most promising preionization systems. Second, we used these systems in experiments with argon double gas puffs in the GIT-12 device. To simplify matters, we begin with describing the design principles of the developed preionization systems and the results from bench tests. Then, we analyze the results from the related GIT-12 experiments.

2.1. Preionization System Based on a Large Number of Glow Discharges

We considered a glow discharge to be an attractive candidate for preionizing the gas-puff medium. The advantages of a glow discharge–based preionization system are as follows:

(i) The glow discharge does not need to be synchronized with the main current pulse: the discharge may be initiated immediately after the gas fills the interelectrode gap and may be sustained for an infinitely long time.

(ii) Since the glow discharge is a low-current discharge, it causes no significant temperature perturbations and thus does not give rise to additional density gradients in the gas-puff medium.

(iii) The glow discharge is highly uniform, which raises the hope that the main generator current flowing through the gas-puff substance will also be uniform and will result in the formation of a current-carrying shell.

In order for the preionized gas to be as homogeneous as possible, we used wide multiwire arrays, each consisting of 220 wires and rolled onto a cylinder 84 mm in diameter (Fig. 1).

In order to prevent a glow discharge from evolving into an arc discharge, the resistance R_1 = 8 kΩ was connected in series with the capacitance C_1 = 100 μF. This system by itself provides a fairly low degree of gas preionization. However, 1.3 μs before the main current pulse, the GIT-12 device generates a kiloampere current prepulse, which is capable of ensuring a sufficiently high degree of preionization of the gas-puff medium. The only danger is the possible evolution of a volume glow discharge into an arc discharge.

1063-780X/01/2707-0549$21.00

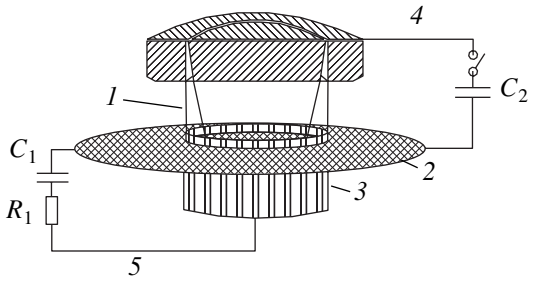

Fig. 1. Schematic of a glow discharge–based system for preionizing gas puffs: (*1*) gas puff shell, (*2*) grid, (*3*) wires for uniform preionization, (*4*) high-current electric circuit, and (*5*) glow-discharge electric circuit.

In order to check that such evolution did not occur, we bench-tested the glow discharge–based preionization system (Fig. 1). The images of glow discharges were recorded on a photographic film of 400/27° ISO. The bench-test discharges aimed at modeling the current prepulse generated by the GIT-12 device in the gas-puff medium were initiated by a trigger, which discharged the capacitor (C_2 = 5 μF, L_2 = 40 nH) charged to 1.3 kV. The current amplitude in the bench-test discharge was 2.5 kA, and the current rise time (to the maximum amplitude) was 1.5 μs.

With the preionization system switched off, the test discharge looked like an expanded diffuse discharge in the central region of the nozzles (Fig. 2a). When the preionization system was switched on, the test pulse excited a uniform discharge (Fig. 2b), which was observed to not evolve into an arc discharge. This circumstance allowed us to hope that, in the main GIT-12 experiments with the glow discharge–based preionization system, the situation would be essentially the same.

2.2. Multiarc Preionization System

In our previous experiments, we found that, during the implosion of gas puffs in megaampere current generators, it is very difficult to avoid the appearance of cathode spots and, accordingly, the possible formation of individual current filaments. In many cases, we observed the onset of a few fairly disordered current filaments in an imploding gas puff. A similar situation may be seen in photographs presented in [4].

A multiarc preionization system is based on the simple but reasonable idea that, instead of trying to avoid the almost inevitable cathode spots, it might be expedient to try to form the desired configuration of cathode spots on the desired sites on the cathode surface, thereby making the implosion process more controllable. The design of the system for producing cathode spots was as follows. A stainless steel grid was equipped with a metal ring with a mean diameter of 84 (or 94) mm (Fig. 3), and 24 (or 48) wires were passed through the ring and grid. The wires were connected in parallel through the same resistances R_1 and were powered by the discharge of a C_1 = 100 μF capacitor charged to a voltage of 1.8 kV. The total current through the wires was 1.5 kA, the oscillation period being about 100 μs. The grid served as a cathode with respect to the nozzles. The electrodes of the arc discharge were held at a negative (relative to the grid) potential.

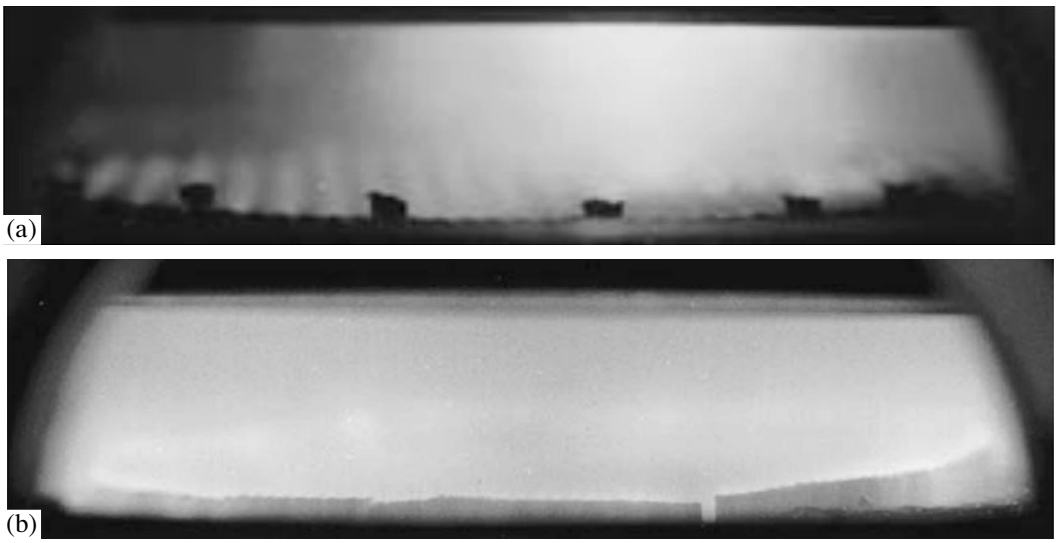

Fig. 2. Time-integrated photographs of the test discharge in a gas puff medium (a) without preionization and (b) with preionization by a system consisting of a large number of glow discharges.

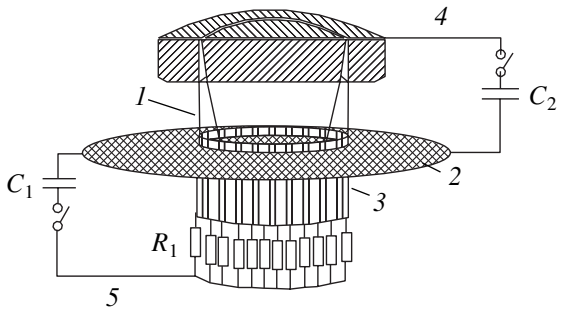

Fig. 3. Preionization system for producing a large number of cathode spots around the perimeter of a gas puff: (*1*) gas puff shell, (*2*) grid, (*3*) 24/48 uninsulated single-conductor wires, (*4*) high-current electric circuit, and (*5*) multiarc-discharge electric circuit.

The test discharge was initiated when the current in the multiarc preionization system reached its maximum. The results from the bench tests of the system are illustrated in Fig. 4. In order to provide a better insight into the behavior of test discharges at higher additional currents in the multiarc system, we increased the test discharge current in several shots by raising the voltage at the capacitor C_2 up to 6 kV (Fig. 3). The data obtained from these shots showed that, even for a test discharge current of about 20 kA, there were many current filaments in the discharge plasma, so that the discharge did not evolve into a single-channel breakdown of a gas-puff medium (Fig. 4b).

2.3. Multiarc Preionization System in an External Magnetic Field

In order to analyze the role of the external magnetic field in the operation of the multiarc preionization system, we carried out a special series of experiments, in which the external magnetic field was initiated by switching on an electromagnet coil that was placed on the side of the nozzles synchronously with the gas puffing. The rise time of the magnetic field to a maximum amplitude of 2.5 kG was about 250 μs. A typical photograph of an arc discharge initiated with the preionization system under investigation is presented in Fig. 5.

It is seen that the external magnetic field strongly affects the discharge plasma distribution. As expected, the plasma channels are observed to stretch out along the magnetic field lines and to behave as if they enter the interior of the external nozzle. In this case, the plasma evolves into a structure whose boundary essentially coincides with the outer boundary of the gas-puff medium. This allows us to hope that the generator current will start flowing through the outer region of the shell, thereby providing a more efficient shell compression. Note, however, that we did not check this multiarc preionization system against the bench-test discharges.

2.4. Double-Sided Spark Preionization System

The double-sided spark preionization system is based on the traditional spark preionization system. The only difference is that the spark discharges emitting UV radiation were initiated both near the anode

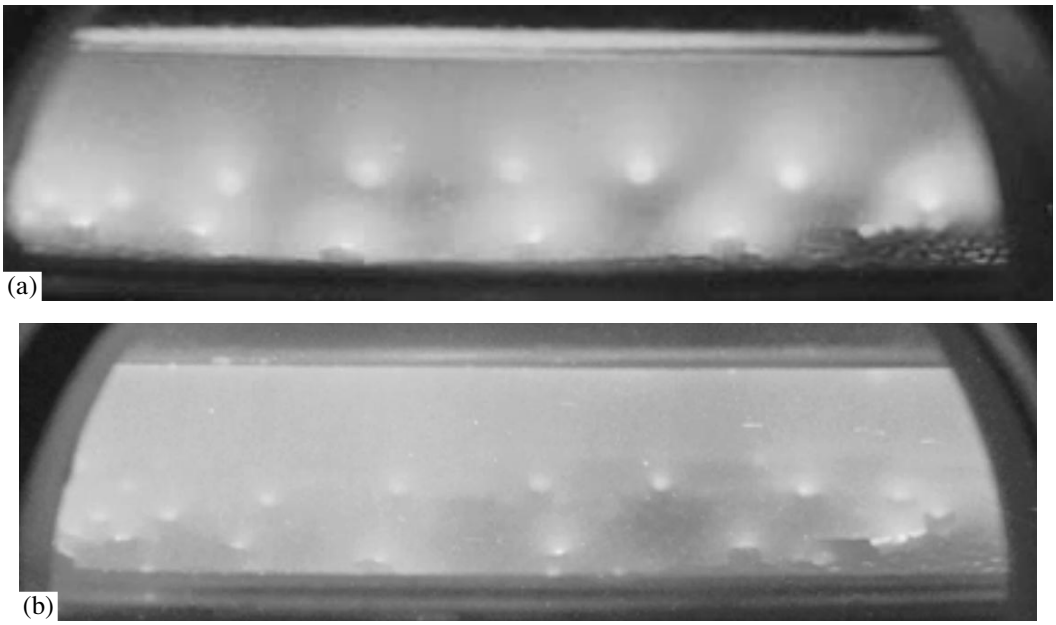

Fig. 4. (a) Time-integrated photographs of arcs (a) without and (b) with a test discharge.

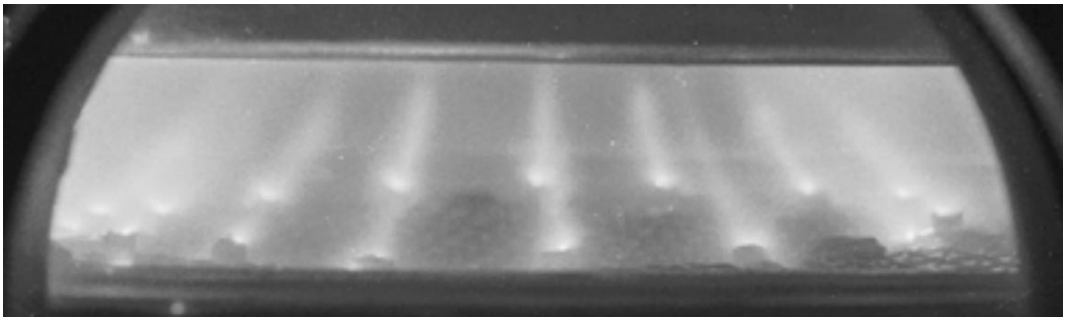

Fig. 5. Time-integrated photograph of arcs with a test discharge in an external magnetic field.

(three sparks at a distance of 2 cm from the nozzle end) and the cathode (five sparks at a distance of 3 cm from the grid). The GIT-12 current generator was switched on 8 μs after UV spark preionization. The relative positions of the GIT-12 generator and the preionization system, as well as the instants at which the generator and the system were switched on, were chosen to satisfy the requirement for the spark-produced plasma not to have enough time to reach the interelectrode gap and thus to substantially perturb the gas-puff medium. The double-sided spark preionization system also was not tested against the bench-test discharges.

3. RESULTS FROM EXPERIMENTS WITH THE GIT-12 GENERATOR

The operation of the above preionization systems was tested experimentally in the GIT-12 generator loaded with an argon double gas puff. The pressure at the entrance to the gas valve [3] was held at fixed levels of 1 atm for the outer shell and 5 atm for the inner shell. The mass ratio of the outer to inner shell was estimated using the following two methods. The first method was based on a zero-dimensional calculation of implosion using the experimentally recorded implosion time and waveforms of the current. The second method was based on the estimation of the amount of puffed gas by analyzing the reading data from the pressure gauges [5]. According to the estimates obtained, the mass ratio of the outer to inner shell was close to unity. Because of the scatter in the action times of the synchronizing trigger, the total gas-puff mass varied from shot to shot over a fairly broad range; however, the mass ratio for the shells was found to be essentially unchanged.

The diagnostic complex included a pinhole camera, an optical streak camera, a polycrystalline diamond detector of X-ray emission in the Ar K-lines, two vacuum X-ray diodes protected by Mylar filters 3 and 1.5 μm thick, and magnetic loops for measuring the derivatives of the current before and after the plasma opening switches. The table summarizes the data from a series of shots.

4. DISCUSSION OF THE RESULTS OBTAINED

The most representative operational characteristic of a preionization system is the form of the dependence of the implosion time T_{imp} of a gas puff on the delay time T_{del} between the instant at which the valve is opened and the instant when the generator is switched on. The time T_{del} determines the mass m of the gas puffed into the interelectrode gap. Since the implosion time obeys the relationship $T_{imp} \sim m^{1/2}$, we have $T_{imp} \sim T_{del}^{1/2}$. The experimentally measured dependence of the implosion time on the delay time (Fig. 6) shows that all preionization systems have a common property: the larger the mass of the puffed gas, the larger the amount of the gas that is lost during the formation of the current-carrying shell. The gas mass losses are maximum for a spark preionization system in an external magnetic field (see Fig. 6, version *1*), in which case we see the appearance of three finite-size plasma filaments (corresponding to the three sparks), which occupy only a fraction of the outer shell of the gas puff. Presumably, it is this fraction that is imploded, while the remaining gas in the outer shell remains immobile. The mass losses were found to be the smallest in a massive gas puff with a multiarc preionization system consisting of 24 arcs on a cylindrical surface 84 mm in diameter.

A multiarc preionization system consisting of 48 arcs on a cylindrical surface 94 mm in diameter in the presence of the external magnetic field was found to be the most appropriate for light gas puffs (see Fig. 6, version *5*). In experiments with this preionization system, the implosion time was observed to be substantially longer. This circumstance provides direct evidence that, under normal operational conditions, the breakdown of a gas puff occurs in the region where the density of the outer shell is the highest. In this case, a substantial amount of the gas experiences no implosion. Increasing the diameter of the cylindrical multiarc array of this preionization system while simultaneously imposing an external magnetic field allowed the outer low-density regions of the gas puff to be involved in the implosion processes. As an example, let us analyze shot nos. 235 and 240, for which the masses of the gas

Summarized data from a series of the GIT-12 shots

Shot no.	Delay time T_{del}, μs	Generator current I_{load}, MA	Implosion time T_{imp}, ns	Emission power P_k in the Ar K-lines, GW	X-ray yield Y_k in the Ar K-lines, J	Comments
225	546	1.899	289	158	653	3 sparks + magnetic field
229	457	2.222	269	130	881	3 sparks + magnetic field
230	447	2.231	260	57	455	3 sparks + magnetic field
265	528	1.915	308	51	271	3 sparks + magnetic field
228	555	1.986	370	11	21	24 arcs (d = 84 mm)
231	427	1.923	211	42	366	24 arcs (d = 84 mm)
232	437	2.048	242	32	310	23 arcs (d = 84 mm)
233	416	1.953	233	56	284	24 arcs (d = 84 mm) + magnetic field
234	426	1.896	228	12	123	24 arcs (d = 84 mm) + magnetic field
235	418	1.824	218	60	478	24 arcs (d = 94 mm)
236	438	1.977	241	39	757	24 arcs (d = 94 mm)
239	399	1.825	249	44	359	48 arcs (d = 94 mm) + magnetic field
240	418	2.150	290	123	545	48 arcs (d = 94 mm) + magnetic field
241	418	2.007	261	33	340	48 arcs (d = 94 mm) + magnetic field
242	514	2.164	337	111	669	220 wires (d = 84 mm)
254	504	2.195	332	29	287	220 wires (d = 84 mm)
255	496	2.262	300	225	852	220 wires (d = 84 mm)
256	500	2.203	320	45	282	220 wires (d = 84 mm)
257	498	2.131	296	61	595	220 wires (d = 84 mm) + 3 sparks
258	480	2.159	296	146	788	3 sparks (anode) + 5 sparks (cathode)
259	496	2.107	316	125	655	3 sparks (anode) + 5 sparks (cathode)
260	530	2.182	323	37	299	3 sparks (anode) + 5 sparks (cathode)

puffed into both inner and outer shells were the same. Shot no. 235 complies with the common dependence of the implosion time on the time delay (Fig. 6), and, in the zero-dimensional approximation, the mass (per unit length) of each of the shells is estimated to be 16 μg/cm. On the other hand, when analyzing shot no. 240 under the assumption that the inner shell is entirely involved in the implosion process, we arrive at the following conclusion: with a preionization system consisting of 48 arcs on a 94-mm-diameter cylindrical surface and with an external magnetic field, the mass of the inner gas-puff shell is 38 μg/cm, which is larger than that for shot no. 235 by a factor of more than two. The streak camera image of the final stage of implosion shows the appearance of only a small number of individual current filaments (Fig. 7a), although the traces on the electrodes indicate that, initially, the current flows through all 48 arcs of the preionization system. This experimental observation provides clear evidence that, during implosion, small-scale current filaments tend to merge into larger-scale filaments. The same effect was described by Branitskiĭ *et al.* [6]. Note that, instead of merging, some of the small-scale filaments were frequently observed to disappear, in which case the current that flowed in these filaments redistributed itself among the remaining filaments.

A comparison between Figs. 8 and 9 shows that, for essentially all of the preionization systems, there is a significant scatter in the data on the emission power and X-ray yield in the Ar K-lines. This indicates that the implosion processes are poorly reproducible even when the preionization conditions are nearly identical.

In other words, since very different results were obtained under the same initial conditions, there is considerable uncertainty as to how the current will flow in imploding gas puffs: it can flow either through the individual channels (whose number changes in the course of implosion) or through the entire finite-thickness cylindrical current-carrying shell. Also, the imploding gas puff may evolve from one of these regimes into another, and vice versa.

Of course, the minimum-inductance principle forces the current to flow through a thin skin layer, in which case, however, it is necessary to take into account the electric conductivity of the gas-puff

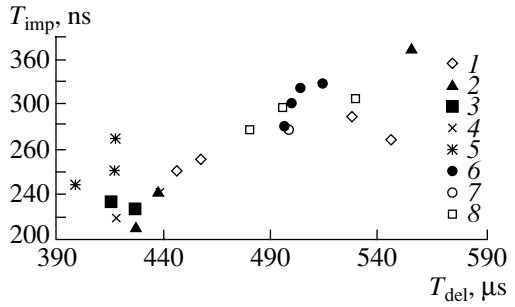

Fig. 6. Dependence of the implosion time T_{imp} of a gas puff on the delay time T_{del} after which the GIT-12 current generator is switched on for different preionization systems: (*1*) spark illumination in an external magnetic field, (*2*) 24 arcs on a cylindrical surface (d = 84 mm), (*3*) 24 arcs on a cylindrical surface (d = 84 mm) in an external magnetic field, (*4*) 24 arcs on a cylindrical surface (d = 94 mm), (*5*) 48 arcs on a cylindrical surface (d = 94 mm) in an external magnetic field, (*6*) 220 glow discharges on a cylindrical surface (d = 84 mm), (*7*) 220 glow discharges combined with sparks, and (*8*) double-sided spark illumination.

medium in the initial stage of implosion. Initially, the current cannot flow through an extremely thin plasma layer, in which the plasma density is still very low and the temperature is insufficiently high. To provide the required conductance, the thickness of the conducting layer should increase, in which case, however, the inductance also increases. The calculations carried out using the methods of [7] show that the inductance of gas puffs with a certain number of current filaments may be the same as that of gas puffs with a finite-thickness cylindrical current-carrying shell. The number of current channels depends on both their radius and the radius of the cylindrical surface on which they appear. Thus, the inductance of an imploding gas puff 80 mm in diameter reaches a minimum after the appearance of 126 filaments, each with a radius of 1 mm. For a cylindrical plasma shell, the same inductance can be obtained with a shell thickness of 10 mm. As the diameter of an imploding gas puff decreases, the number of current filaments decreases, in accordance with the minimum-inductance principle. In the context of the above estimates, it becomes clear why we observed only a small number of filaments (from five to eight) in the final stage of implosion, although we initially initiated 24 (or 48) arcs and were confident that, in the initial stage, they carried the total current. Thus, we can conclude that, in an imploding gas puff, not all of the initial current filaments can be maintained; in order for the inductance of the gas puff to be minimum, the number of filaments should decrease.

The question then arises: why does the current not flow through a cylindrical current-carrying shell? In fact, the situation with a continuous shell of certain thickness is even more preferable from the standpoint of the minimum-inductance principle. However, recall that, in the initial stage of implosion, the thickness of the conducting layer should increase in order to provide the required conductance, in which case the inductance should also increase. As a result, at a certain stage, the formation of filaments may become preferable. In addition, Braginskiĭ and Vikhrev [8] showed that, in the initial stage of breakdown of the gas puff substance, a very important role is played by the step ionization–driven

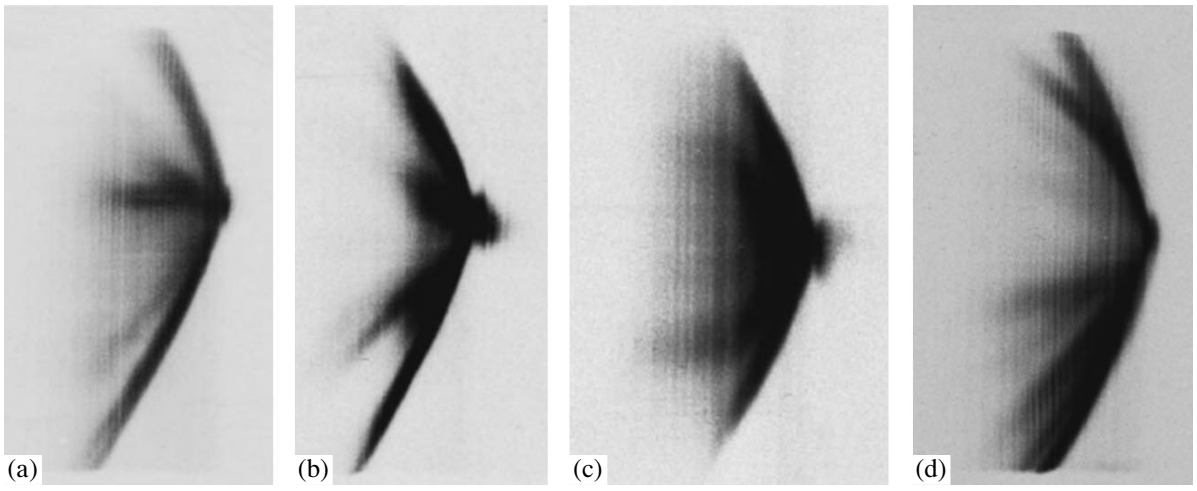

Fig. 7. Streak camera images of the implosion of a double gas puff with different preionization systems based on (a) glow discharges (shot no. 242), (b) 48 wires on a cylindrical surface (d = 94 mm) in an external magnetic field (shot no. 239), (c) 24 wires on a cylindrical surface (d = 84 mm) in an external magnetic field (shot no. 233), and (d) double-sided spark illumination (shot no. 260).

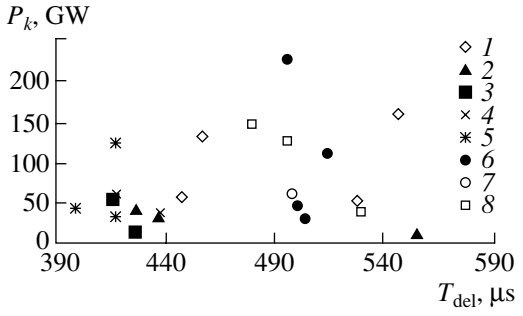

Fig. 8. Power emitted from the gas puff in the Ar K-lines vs. the delay time T_{del} after which the GIT-12 current generator is switched on for the same preionization systems (*1*)–(*8*) as in Fig. 6.

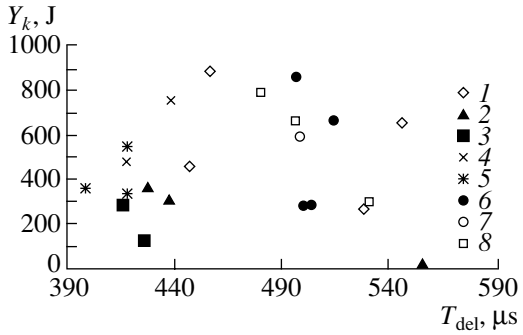

Fig. 9. X-ray yield from the gas puff in the Ar K-lines vs. the delay time T_{del} after which the GIT-12 current generator is switched on for the same preionization systems (*1*)–(*8*) as in Fig. 6.

instabilities and, thereafter, by the thermal instabilities; both of which may give rise to current filaments.

Let us discuss this problem in the context of the developed preionization systems. A glow discharge–based system preionizes the gas-puff medium over the entire volume but to a relatively low level. As was shown above, such conditions are *a priori* favorable for filamentation. In a gas puff with this preionization system, the current is redistributed between the filaments [6], whose number continuously decreases, so that, in the final stage of implosion, the current again flows through a small number of filaments (Fig. 7b). The situation with a multiarc preionization system is essentially the same, although the forced ignition of the cathode spots was expected to ensure a quasiuniform distribution of the current over a large number of filaments. Moreover, recall that the prints on the electrode surfaces indicate that, initially, the generator current flows through all 24 (or 48) wires of the preionization system. However, the streak camera images in Fig. 7a show that the initial current filaments either merge into larger-scale filaments or disappear, thereby inevitably increasing the scatter in the measured data. On the other hand, this was not always the case. Thus, with a multiarc preionization system consisting of 24 arcs on a cylindrical surface 84 mm in diameter, we observed no individual filaments (Fig. 7c), but, in such shots, the emission power and X-ray yield were both measured to be low. Presumably, we dealt with the formation of a fairly thin highly conducting cylindrical current-carrying shell at the periphery of the gas puff, so that such implosion conditions turned out to be preferable from the standpoint of the minimum-inductance principle. The most interesting phenomenon is that, in this situation, the step ionization–driven instabilities and thermal instabilities did not come into play. Nevertheless, we observed that the current redistributed itself between the outer and inner shells, thereby hindering the efficient compression of the gas puff. Varying the gas-puff mass and, accordingly, the particle density, we changed the conditions for current redistribution between the shells. As a result, the implosion processes again became unstable, leading to a significant scatter in the measured data.

The double-sided spark preionization system is the only system that gives rise to insignificant scatter in the measured data. For this reason, the double-sided spark system seems to be the most promising. However, this system requires further testing because the statistical data obtained with it are as yet insufficient. A typical streak camera image of an imploding gas puff with a double-sided spark preionization system is shown in Fig. 7d.

5. CONCLUSIONS

Our experimental investigations allow us to draw the following conclusions:

(i) The implosion process is highly sensitive to the initial conditions for the formation of the current-carrying shell.

(ii) The current generator operates so as to reduce a large number of current filaments by a certain mechanism.

(iii) The significant scatter in the data on the emission power and X-ray yield in the Ar K-lines stems from the uncertainty in the process by which the generator current and gas-puff mass are redistributed among a progressively smaller number of current filaments.

(iv) During the implosions that are not accompanied by the formation of current filaments, the generator current is partially redistributed between the outer and inner gas-puff shells, thereby reducing the emission power and X-ray yield in the Ar K-lines and increasing the scatter in the measured data on these parameters.

(v) The most promising system from the standpoint of the reproducibility of the results at reasonable emission powers and X-ray yields in the Ar K-lines is the double-sided spark preionization system.

REFERENCES

1. G. Rousskikh, R. B. Baksht, A. V. Shishlov, and A. V. Fedyunin, Fiz. Plazmy **25**, 579 (1999) [Plasma Phys. Rep. **25**, 527 (1999)].
2. R. B. Baksht, I. M. Datsko, A. A. Kim, *et al.*, Laser Part. Beams, No. 12, 748 (1994).
3. A. V. Shishlov, R. B. Baksht, A. V. Fedunin, *et al.*, Phys. Plasmas **7**, 1252 (2000).
4. P. Colleman, B. Failor, and J. Lenive, in *Proceedings of the 41st Annual Meeting of the Division of Plasma Physics of the American Physical Society, Seattle, 1999.*
5. A. V. Fedunin, A. Yu. Labetsky, A. G. Rousskikh, *et al.*, Russ. Phys. J. **42**, 1272 (1999).
6. A. V. Branitskiĭ, V. V. Aleksandrov, E. V. Grabovskiĭ, *et al.*, Fiz. Plazmy **25**, 1060 (1999) [Plasma Phys. Rep. **25**, 976 (1999)].
7. P. L. Kalantarov and L. A. Tseĭtlin, *Inductance Calculation* (Énergoatomizdat, Leningrad, 1986).
8. S. I. Braginskiĭ and V. V. Vikhrev, *Formation of a Current-Carrying Shell in a High-Power Pulsed Discharge* (Inst. At. Énerg. im. Kurchatova, Moscow, 1974).

Translated by G. V. Shepekina

Plasma Physics Reports, Vol. 27, No. 7, 2001, pp. 557–562. Translated from Fizika Plazmy, Vol. 27, No. 7, 2001, pp. 592–598.

PLASMA DYNAMICS

Investigation of the Mechanism for Current Switching from the Outer Gas Puff to the Inner Wire Array in a Structured Z-Pinch

R. B. Baksht, A. Yu. Labetsky, A. G. Rousskikh, A. V. Fedyunin, A. V. Shishlov, V. A. Kokshenev, N. E. Kurmaev, and F. I. Fursov

Institute of High-Current Electronics, Siberian Division, Russian Academy of Sciences, Akademicheskiĭ pr. 4, Tomsk, 634055 Russia

Received September 26, 2000

Abstract—Experiments are reported on the implosion of structured loads with outer argon, krypton, and xenon gas puffs and an inner tungsten multiwire array. Experiments were carried out in the GIT-12 generator with a current of 2.6 MA and a current rise time of 270 ns. It is shown that the current successfully switches to the wire array only when the gas puff is sufficiently light. The total implosion time is 300 ns, and the implosion time of a wire array, determined from streak camera images, is 50–70 ns. It is suggested that the switching is efficient only when the active impedance of the gas puff is higher than the transitional resistance of the electrically exploded wires. © *2001 MAIK "Nauka/Interperiodica".*

1. INTRODUCTION

At present, fast Z-pinch-based devices are widely used for generating soft X radiation [1]. The most interesting fast devices are those based on multiwire arrays, which provide more compact compression and higher efficiency of energy transfer from the generator to the load. In this context, it seems worthwhile to carry out experiments aimed at searching for ways to reduce the rise time of the current flowing through a wire array. Preliminary experiments in the 1.4-MA GIT-4 generator, loaded by an outer gas puff and an inner wire array [2], showed that the use of aluminum wire arrays makes it possible to sharply increase the emission power and reduce the pulse duration, because the generator current rapidly switches from the gas puff to the wire array. In this context, note that the authors of [2] did not optimize the switching process or the parameters of the gas puff and did not touch on the questions related to the switching mechanism. At the same time, it is evident that, in order for Z-pinches structured in such a manner to be successfully used in megaampere current generators, it is necessary to gain a clearer insight into the physics of the switching process. Our main objective here is to better understand the implosion of a Z-pinch with an outer gas puff and inner wire array. We chose tungsten as a material for the wire array, because it is the least expensive and, at the same time, a fairly representative metal used in wire arrays. The paper is organized as follows. The experimental setup is described in Section 2. The results from experiments with a structured load are presented in Section 3 and are discussed in Section 4. In the Conclusion, the results are summarized.

2. EXPERIMENTAL SETUP

The experiments were carried out in the GIT-16 device [3] in its 12-module version (GIT-12). GIT-12 is a pulsed current generator with an inductive energy storage and a plasma opening switch (POS). Each of the modules includes a primary energy storage consisting of nine sections connected in parallel according to the Marx generator scheme; a vacuum insulator; and a coaxial line, which connects the module to the central collector. The central collector is connected to the POS and to the load unit. At a charging voltage of 50 kV, the Marx generator stores 2.64 MJ of energy. In order to reduce the effect of the backward half-wave, resistors with a total resistance of 0.042 Ω are built into the elements of the Marx generator. The upstream and downstream inductances are equal to 112 and 55 nH, respectively. The experiments were carried out with a charging voltage at the Marx generator of 50 kV, which ensures a current rise time of 270 ns and a current amplitude of 2.7 MA under short-circuit conditions.

The load unit used in the experiments with an outer gas puff and inner wire array is illustrated schematically in Fig. 1. In the experiments, an electromagnetic gas valve was connected to a ring concentric nozzle [4]. The valve was opened at a speed of about 400 cm/s. The holder of the wire array is mounted on a small insulator. In Fig. 1, we also show the coils that create a magnetic field of 1–3 kG and ensure the initiation of a magnetron discharge preionizing the gas puff.

The mass of the puffed gas is determined by the gas pressure in the valve and the time delay between the instants at which the valve is opened and the generator is switched on. The synchronous operation of the gas

1063-780X/01/2707-0557$21.00 © 2001 MAIK "Nauka/Interperiodica"

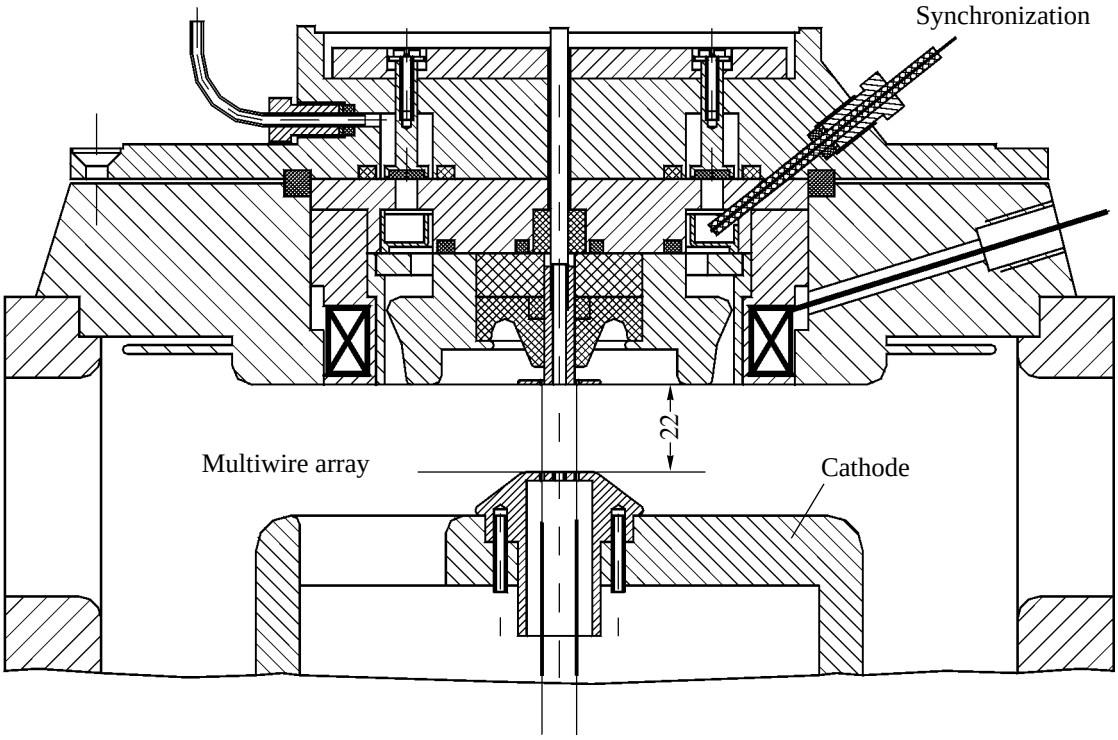

Fig. 1. Load unit of the GIT-12 generator with an outer gas puff and an inner wire array.

valve and the generator was ensured by a synchronizing spark-gap placed in front of the nozzle and charged to a voltage of 4 kV. In the experiments, the typical time delay between the signal from the synchronizing spark-gap and the generator current was 550 μs, and the gas pressure in the valve was up to 5 atm. The gas valve was installed on the anode of the interelectrode gap. The cathode was designed in the form of metal pins that connect the holder of the wire array to the central conductor of the GIT-12 generator. The distance between the cathode and anode was 3.2 cm, the inner radius of the nozzle was 4 cm, and the length of the wire array was 2.2 cm.

The process of liner implosion was investigated using the standard electromagnetic (Rogowski coils and dB/dt detectors) and optical diagnostics. The implosion dynamics was recorded in visible light by a streak camera with a resolution of 125 ns/cm. A pinhole camera with a beryllium filter 10 μm thick was used to record the time-integrated pinch images. The yield and power of soft X radiation were measured by a photoconductive detector (PCD) and vacuum X-ray diodes (XRDs). The PCD was filtered by a 6.35-μm-thick titanium filter, and the XRDs were filtered by a 3-μm-thick Mylar filter.

3. EXPERIMENTAL RESULTS

The objective of our experiments is to find the mass and material of the gas puff at which the current switches to the wire array. The original concept for this switching is as follows. When the gas puff arrives at highly conducting wires arranged on a cylindrical surface, the azimuthal magnetic field is captured by the wires, as was assumed in the model of Davis *et al.* [5]. They also suggested that, the more stable the gas puff, the higher the efficiency with which the azimuthal magnetic field is captured by the cylindrical wire array and, accordingly, the current switches to the wires. For this reason, in the first several shots in the related series of experiments, we stabilized the gas puff by a magnetic field. Moreover, since the previous experiments [6] revealed that heavier gas puffs are more stable, this series of experiments was carried out with comparatively heavy gas puffs, with masses per unit length of 20 to 40 μg/cm. However, we failed to switch the current from a comparatively stable gas puff to the wire array: the streak camera images showed no such switching.

Let us analyze the experimental results in more detail. Most of the experiments in this series were carried out with a tungsten wire array in the form of a 0.9-cm-diameter cylindrical array of eight wires, each 11 μm in diameter. Since these experiments were not aimed at achieving the maximum possible X-ray yield, the number of wires was chosen to simplify the arrangement of the wire array. In order to check the switching efficiency in regimes in which the separation d between the wires is close to the critical separation d_{critical} [7], we also initiated several test shots with a

Table 1. Experimental data on the implosion of a combined load

Pressure, atm	I_{load}, MA	Implosion time, ns	dI/dt, kA/ns (at the time of maximum compression)	XRD signal, V	Presence of implosion in the streak camera image	Shot no.
2.0 (Ar)	1.86	313	0	40	–	132
1.0 (Ar)	1.86	324	4	27	–	142
1.0 (Ar)	1.51	107	0	12	–	130
0.5 (Ar)	1.44	226	1	70	+	134
0.5 (Ar)	1.73	311	6.54	–	+	140
2.0 (Kr)	2.06	369	3.7	118	+	205
2.0 (Kr)	1.85	413	2	74	–	152*
1.5 (Kr)	2.06	296	6.57	175	+	204**
1.5 (Kr)	1.78	361	4.6	87	+	144
1.0 (Kr)	1.72	360	7.9	164	+	147
1.0 (Kr)	1.74	353	6.38	114	+	145
1.0 (Kr)	1.93	323	5	115	+	203
2.5 (Xe)	1.97	351	7.68	84	+	206
4.0 (Xe)	1.96	379	6.6	142	+	207

* With a 30-wire array.
** With a 16-wire array.

larger number of wires. The results from this series of experiments are summarized in Table 1, which, in particular, presents the sort of gas and data on the gas pressure in the valve, the implosion time of a structured load, and the maximum current in the load. The switching efficiency was estimated from the negative value of the derivative dI_{load}/dt of the current in the load at the time of maximum compression of the wire array, the amplitude of the signal from the XRDs, and the streak camera images. From Table 1, we can see that, the lower the gas pressure in the valve, the higher the X-ray emission intensity. The current is always seen to switch to the wire array, regardless of the number of wires.

Figure 2 shows representative waveforms of the derivative of the current and the signal from the XRDs, both obtained for shot no. 142, in which the gas puff was relatively heavy (about 40 μg/cm), the gas pressure in the valve was 1 atm, and the diameter of the wire array was 0.9 cm. In Fig. 2, we also present the streak camera image of this shot. One can see that, immediately after the current starts flowing through the load, large-scale perturbations appear in both the XRD and dI_{load}/dt signals. In [8], it was shown that the signal from the XRDs and the perturbations at the front of the current pulse through the load are both introduced by the electrons that are accelerated during the formation of the current-carrying layer in a gas puff.

We see that, 240 ns after the beginning of the current pulse, the dI_{load}/dt signal reflects a dip accompanied by a short X-ray pulse. The corresponding instant can be identified with the time the gas puff arrives at the Z-pinch axis. At this instant, the streak camera image shows bright wire explosions lasting for 25 ns. Then, the streak camera image shows that only part of the exploding-wire plasma contracts. Accordingly, the amplitude of the second dip in the dI_{load}/dt signal is small and the signal from the XRDs is weak. An analogous situation was observed for all shots with heavy gas puffs: according to the streak camera images, only a small fraction of the exploding-wire plasma was involved in an acceleration process, both the XRD and dI_{load}/dt signals were weak, and no switching occurred.

A radically different situation was observed in the experiments with lighter gas puffs (recall that, the lower the gas pressure in the valve, the lower the gas puff mass) in the absence of a magnetic field (shot nos. 134, 140). First, it is important to note that the related streak camera images provide clear evidence for the implosion of the wire array. The wire array implosion is especially pronounced in experiments with krypton gas puffs (shot nos. 145, 205). The dI_{load}/dt and XRD signals as well as the streak camera image of shot no. 205 are displayed in Fig. 3. With a krypton gas puff, the effects associated with the production of runaway electrons were reduced almost completely. The amplitude of the first dip in the dI_{load}/dt signal is smaller than in the previous case, while the amplitude of the second dip, associated with the implosion of the wire array, is larger. Characteristically, the X-ray pulse becomes far more intense. The time interval between the beginning of the wire explosion and the maximum compression was estimated from the streak camera image and was found to be 65 ±5 ns, which coincides with the time interval between the dips in the dI_{load}/dt signal to within ±5 ns.

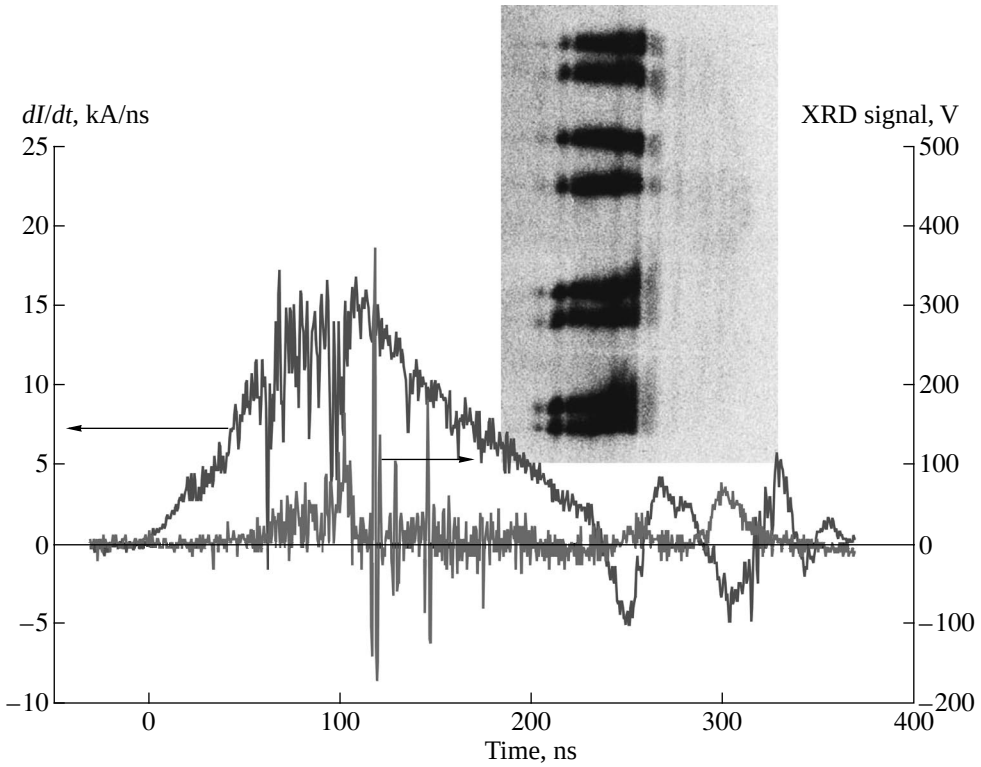

Fig. 2. Waveforms of the derivative *dI*/*dt* and XRD signal in shot no. 142 (a discharge with an outer argon gas puff at a pressure of 1 atm and an inner wire array of eight wires; the array diameter is 9 mm). The inset shows the streak camera image of implosion synchronized with the *dI*/*dt* and XRD signals. The wire explosion is seen to last about 20–30 ns.

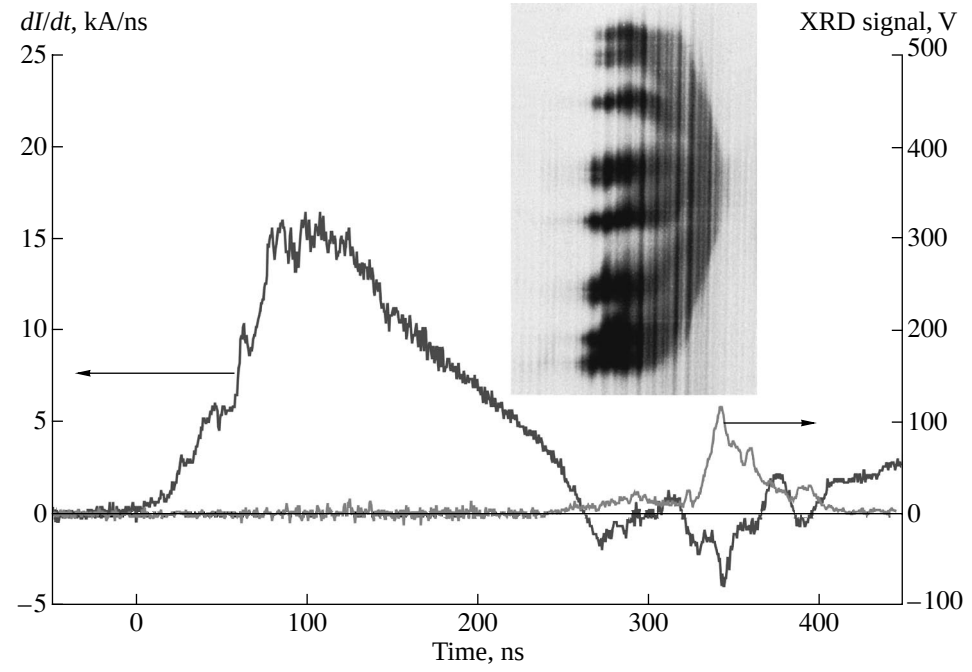

Fig. 3. Waveforms of the derivative *dI*/*dt* and XRD signal in shot no. 205 (a discharge with an outer krypton gas puff at a pressure of 2 atm and an inner wire array of eight wires; the array diameter is 9 mm). The inset shows the streak camera image of implosion synchronized with the *dI*/*dt* and XRD signals. In this shot, the dip in the *dI*/*dt* signal at the time of maximum compression of the wire array (t = 340 ns) is significantly larger in amplitude than the dip in the *dI*/*dt* signal at the time of maximum compression of the gas puff (t = 270 ns).

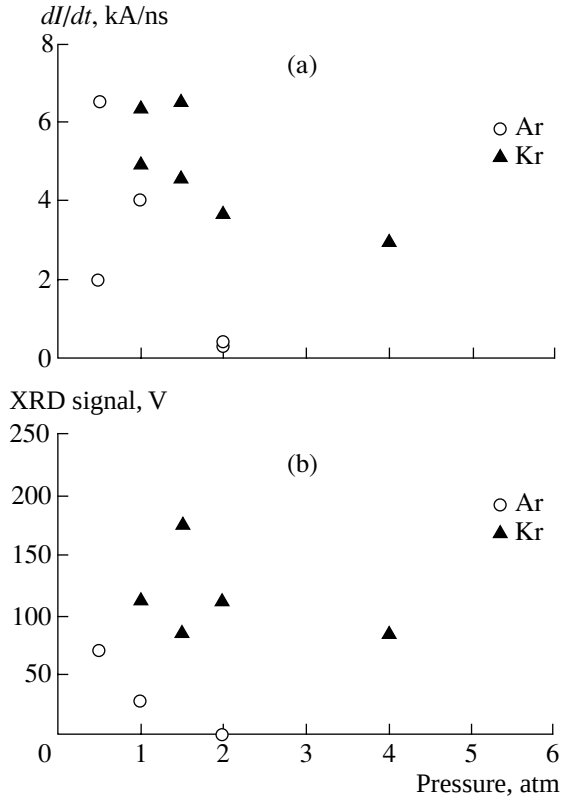

Fig. 4. The amplitudes of (a) the *dI*/*dt* signal and (b) the XRD signal vs. the pressure in the valve.

Now, we present some of the dependences characterizing the efficiency with which the generator current switches to the wire array. Figure 4a shows the derivative dI_{load}/dt as a function of pressure in the valve for argon and krypton gas puffs. In Fig. 4b, we plot the same dependence for the amplitude of the XRD signal. The open circles in Figs. 4a and 4b show that, for argon, the switching efficiency decreases with increasing pressure in the valve and, accordingly, gas mass: at a pressure of 2 atm, the argon gas puff experiences essentially no implosion. For krypton, this effect is less pronounced. In this case, however, the derivative dI_{load}/dt and the emission intensity also tend to decrease with increasing pressure in the valve.

4. DISCUSSION OF THE EXPERIMENTAL RESULTS

An analysis of the above experimental results allowed us to propose the following mechanism by which the generator current switches from the outer gas puff to the inner wire array.

As the gas puff arrives at the wire array, a part of the plasma penetrates through the cylindrical wire array, as was predicted by Davis *et al.* [5]. The streak camera images clearly show wire explosions as the current starts to switch to the wire array.

Bright wire explosions last about 20–30 ns. According to the analysis of [5], it is this time interval during

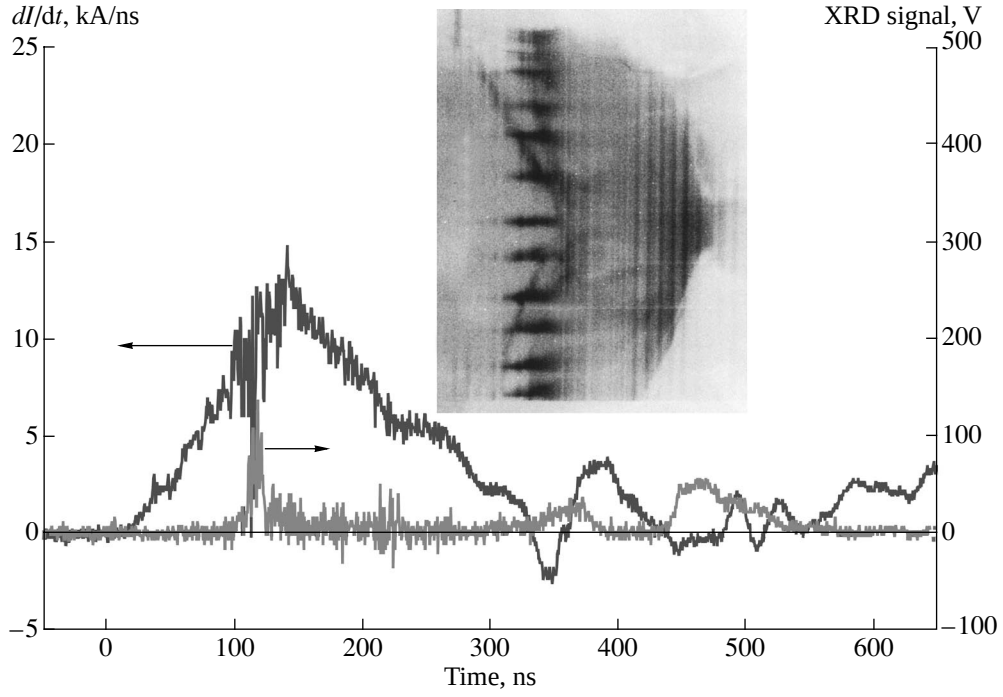

Fig. 5. Waveforms of the *dI*/*dt* and XRD signals in a shot at a high pressure in the valve (a discharge with an outer argon gas puff at a pressure of 2 atm and an inner wire array of 16 wires; the array diameter is 16 mm). The inset shows the streak camera image of implosion synchronized with the *dI*/*dt* and XRD signals. The waveforms clearly reflect the instant at which the gas puff arrives at the axis and the compression of the peripheral layers of the exploding-wire plasma.

Table 2. Active impedance of a gas puff in the absence of a wire array

Gas	Pressure in the valve, atm	R_{load}, Ω
Ar	1	0.05
Ar	0.5	0.17
Ar	0.25	0.224
Kr	5	0.03
Kr	2	0.085
Kr	0.3	0.15
Xe	4.6	0.075
Xe	2.5	0.07

which the azimuthal magnetic field should penetrate through the wire array because of the higher conductivity of the wire array and the mutual inductance of the gas puff and the wire array. However, in our experiments, the scenario of the radial penetration of the azimuthal magnetic field through the wire array differs from that in the idealized model: the magnetic field penetration depends on both the sort of gas and the gas pressure (see Fig. 4 and Table 1). Presumably, this dependence stems from the insufficiently high conductivity of the multiwire array. As is known [9], wires that are exploded at kiloampere currents give rise to both a highly conducting corona at the periphery of the compressed plasma column and a high-resistance core. That is why, in order for the current switching to be efficient, the impedance Z of the plasma shell imploding onto the Z-pinch axis should be higher than the impedance of the high-resistance core. This condition can be written as

$$Z = R_{gas} + dL_{gas}/dt > R_{wa}, \quad (1)$$

where R_{wa} is the total resistance of the wires in the wire array. If condition (1) is not satisfied, then either the current experiences no switching (as is seen in Fig. 2) or it is only the plasma corona of the wires that is contracted (Fig. 5). Under condition (1), the azimuthal magnetic field penetrates through the wire array, which begins to contract 50–70 ns after the arrival of the gas puff (Fig. 3).

When writing condition (1), we assumed that the resistance of the gas puff depends on both the sort of gas and the density of heavy particles in the plasma shell of the imploding gas puff. In order to check the validity of this assumption, we carried out a special series of test experiments without the wire array. We actually observed that the active impedance of the gas puff is one to two orders of magnitude higher than the Spitzer conductivity and depends sensitively on the density of heavy particles in the gas puff. The results of these test experiments were reported in [10]. Here, we only present Table 2, which illustrates the dependence of the active impedance on the gas pressure in the valve and the sort of gas. The data given in Table 2 were obtained for a gas puff 8 cm in diameter and 2 cm in length. The active impedance of the gas puff is seen to differ strongly between different gases and to be as high as several tenths of an ohm at low gas pressures.

5. CONCLUSION

Our experiments show that the generator current can switch from the outer gas puff to the inner wire array only when the active impedance of the gas puff is higher than the transitional resistance of the electrically exploded wires. This circumstance makes it possible to estimate the impedance of the high-resistance core inside the tungsten plasma during electrical explosion. For a wire array composed of $n = 8$ wires, under the condition $R_{gas} \simeq R_{wa}$, the mean transitional resistance of an individual tungsten wire is estimated to be about 1 Ω per centimeter.

ACKNOWLEDGMENTS

This work was supported in part by the Russian Foundation for Basic Research, project no. 98-02-16963.

REFERENCES

1. N. R. Pereira and J. Davis, J. Appl. Phys. **64** (3), R1 (1988).
2. R. B. Baksht, I. M. Datsko, V. I. Oreshkin, *et al.*, Fiz. Plazmy **23**, 135 (1997) [Plasma Phys. Rep. **23**, 119 (1997)].
3. S. P. Bugaev, A. M. Volkov, A. A. Kim, *et al.*, Izv. Vyssh. Uchebn. Zaved., Fiz. **40** (12), 38 (1997).
4. R. B. Baksht, A. V. Fedunin, A. Chuvatin, *et al.*, Instrum. Exp. Tech. **41** (4), 98 (1998).
5. J. Davis, N. A. Golub, and A. L. Velikovich, Appl. Phys. Lett. **70**, 170 (1997).
6. R. B. Baksht, I. M. Datsko, A. A. Kim, *et al.*, Fiz. Plazmy **21**, 959 (1995) [Plasma Phys. Rep. **21**, 907 (1995)].
7. M. K. Matzen, Phys. Plasmas **4**, 1519 (1997).
8. R. B. Baksht, A. Yu. Labetsky, A. G. Russkikh, *et al.*, Phys. Plasmas **4**, 3430 (1997).
9. S. M. Zakharov, G. V. Ivanenkov, A. A. Kolomenskiĭ, *et al.*, Fiz. Plazmy **9**, 469 (1983) [Sov. J. Plasma Phys. **9**, 271 (1983)]; R. B. Baksht, I. M. Datsko, A. F. Korostelev, *et al.*, Fiz. Plazmy **9**, 1224 (1983) [Sov. J. Plasma Phys. **9**, 706 (1983)].
10. R. B. Baksht, A. V. Fedunin, A. Yu. Labetsky, *et al.*, Plasma Phys. Controlled Fusion (in press).

Translated by G. V. Shepekina

Plasma Physics Reports, Vol. 27, No. 7, 2001, pp. 563–569. Translated from Fizika Plazmy, Vol. 27, No. 7, 2001, pp. 599–606.

PLASMA DYNAMICS

Periodic Emission Bursts Accompanying the Interaction of Plasma Flows Propagating Across a Magnetic Field

G. N. Dudkin, B. N. Nechaev, V. N. Padalko, and E. G. Furman

Research Institute of Nuclear Physics, Tomsk Polytechnic University, pr. Lenina 2a, Tomsk, 634050 Russia

Received September 20, 2000; in final form, February 13, 2001

Abstract—It is found experimentally that the interaction of plasma flows propagating in opposite directions across a magnetic field is accompanied by periodic local bursts of intense optical and soft X-ray emission. It is shown that periodic variations in the emission intensity from the interaction region are related to the excitation of steady-state self-oscillations in the plasma. By varying the frequency and amplitude of these oscillations, it is possible to satisfy the resonance conditions at certain characteristic plasma frequencies. © *2001 MAIK "Nauka/Interperiodica".*

1. INTRODUCTION

At present, much attention is being paid to the studies of regular plasma structures and the processes related to their formation [1, 2], because such structures are evidence of strong turbulence and, therefore, a more ordered plasma state. In addition, the generation of regular fields (especially, under resonance conditions) is accompanied by the efficient conversion of the oscillation energy into radiation and the kinetic energy of certain groups of plasma particles [3].

In this paper, we present the results from experimental studies of the interaction of plasma flows propagating in opposite directions across a magnetic field. This interaction leads to the excitation of regular plasma oscillations. The experimental device is described in detail in [4].

2. EXPERIMENT

Figure 1 shows the scheme of the experiment. Two pairs of 30-cm-long and 4-cm-thick electrodes were placed in a ceramic chamber 20 cm in diameter and 150 cm in length. The distance between these pairs of electrodes was 8 cm, and the electrodes in each pair were spaced 2 cm apart. The electric fields in the interelectrode gaps were oppositely directed and were perpendicular to the magnetic field. Two plasma flows drifted from the discharge regions toward each other with the initial velocity $V_d \simeq cE_0/H$ (where c is the speed of light, E_0 is the discharge electric field, and H is the magnetic field) and collided near the axis of symmetry of the chamber. The characteristic size of the plasma flows along the magnetic field was about 10 cm.

The potential differences (along the y-axis) induced at the flow boundaries during the propagation of the

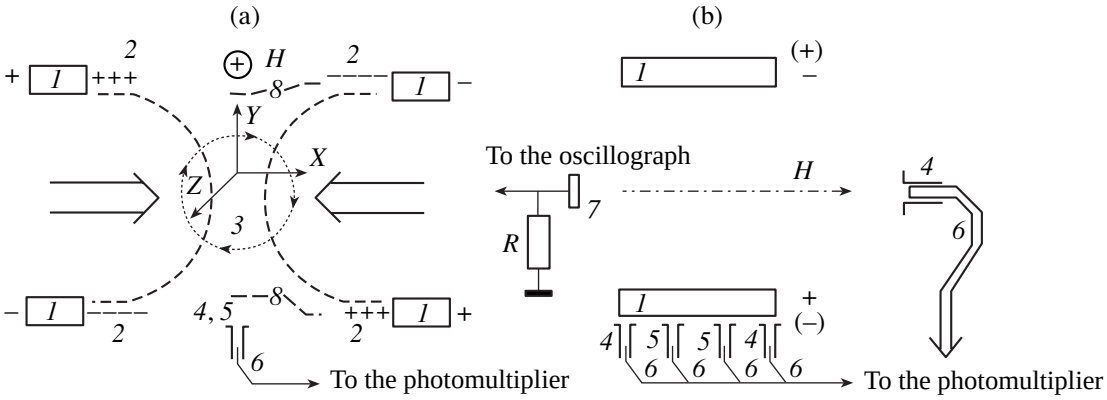

Fig. 1. Scheme of experiment, view (a) along and (b) across the magnetic field: (*1*) electrodes, (*2*) drift channels (large arrows show the directions of plasma flows; the flow boundaries are schematically shown by a dashed line), (*3*) interaction region (arrows show the direction of the charge flow), (*4*) X-ray detectors, (*5*) optical collimators, (*6*) fibers, (*7*) collector, and (*8*) floating probes.

1063-780X/01/2707-0563$21.00 © 2001 MAIK "Nauka/Interperiodica"

flows across the magnetic field were measured by floating probes situated at a distance of 1.5 cm from each pair of electrodes. Probes for measuring the potential difference (along the *y*-axis) in the interaction region of the colliding flows were also located near the axis of symmetry. The size of the region of the efficient flow interaction was determined by shifting these probes across the magnetic field. This region was identified by the probe positions at which the potential difference between the probes along the *y*-axis was minimum.

In the direction perpendicular to the magnetic field, the interaction region was observed by two optical detectors and two X-ray detectors (plastic scintillators) spaced along the magnetic field by 2.2 and 9 cm, respectively. The detectors were located at a distance of 5 cm from the center of the interaction region with a characteristic transverse size of 2–3 cm. The spatial resolution of the optical detectors was 0.8 mm, and that of the X-ray detectors was ~1 cm. A scintillation detector for measuring X-ray radiation in the direction along the magnetic field was located at a distance of 120 cm from the central cross section of the chamber. The scintillators of all the X-ray detectors were protected by 7-μm-thick aluminum foils, which corresponded to a cutoff energy of ~3 keV. On the opposite side of the chamber, at a distance of 75 cm from the central cross section of the chamber, a detector for measuring the current of charged particles along the magnetic field was installed. The time resolution of the optical and X-ray detectors was limited by the 20-ns sampling time of the digital recording system. The record length was 3.2×10^4 counts. The signals from the floating probes and collector were integrated by an integrator with a time constant of ~1 μs.

Experiments were carried out at a plasma density in the flows of 10^{13}–2×10^{14} cm^{-3} and a magnetic field of $H \simeq 10^4$ G. The working gas was nitrogen.

3. EXPERIMENTAL RESULTS

Figure 2 presents the signals from the optical detectors at an initial nitrogen pressure of $\sim 7 \times 10^{-2}$ torr and $E_0 \simeq 300$ V/cm. The corresponding waveforms of the discharge current and voltage (in one discharge gap) are shown in Fig. 3. An analysis of the waveforms in Fig. 2 allows us to make the following inferences:

(i) In the experiment, we observe two regimes. In the first (quasi-steady) regime, which corresponds to the time interval $\Delta t_1 \simeq 100$–320 μs, the mean emission intensity from the interaction region remains almost constant over a wide range of the power deposited in the discharge. The second regime ($\Delta t_2 \simeq 320$–600 μs) is characterized by intense periodic emission bursts, whose amplitude exceeds the mean emission intensity by at least one order of magnitude.

(ii) In the first time interval, plasma emission is modulated with a period of $T_1 \sim 23$ μs. Within this period, the emission has the form of wave packets with a period of $T_2 < 4.5$ μs (Fig. 2b). In the Fourier spectrum (Fig. 4) calculated for this time interval (here and below, the spectra are calculated using the fast Fourier transformation), one can see two pronounced peaks at frequencies of 42.7 and 238 kHz, corresponding to the above modulation periods. For oscillations with period T_2, there is a time delay between the signals from two detectors spaced by 2.2 cm along the magnetic field. The average value of the delay time between two detectors can be estimated from the shift $\Delta t \simeq 200$ ns of the maximum of the cross-correlation function (Fig. 5) calculated for the time interval corresponding to Fig. 2b. Consequently, the phase velocity (along the magnetic field) of these wave perturbations is ~10^7 cm/s.

The modulation of the third level (within T_2) manifests itself in the form of packets with a period of $T_3 \leq 1$ μs. The packets measured by two detectors also correlate with each other. Finally, steady-state emission oscillations with a period of $T_4 \simeq 0.13$ μs are observed within T_3. Oscillations with periods T_3 and T_4 occur throughout almost the entire time interval presented in Fig. 2a. This is illustrated in Fig. 6, which shows the Fourier spectrum for the time interval corresponding to Fig. 2c and including part of a relatively weak burst. The position of this burst is indicated in Fig. 2a by an arrow.

(iii) The quasi-steady emission regime corresponding to the time interval Δt_1 transforms into the regime with intense bursts followed by a period of ~T_1. The emission rise time (from 0.2 to 0.8 of the burst amplitude) in the intense bursts is ≤1 μs.

Figure 7 shows the waveforms from the optical and X-ray detectors for a discharge electric field of $E_0 \simeq 2 \times 10^3$ V/cm. The amplitude of the discharge current in each pair of electrodes is nearly the same as in the previous case (~7 kA), whereas the duration of the discharge current pulse is about 17 times smaller. It follows from Fig. 7 that, in this case, the optical bursts are rare, but the emission modulation is well pronounced. At the same time, intense periodical bursts of X-ray emission (with $T_R \leq 5$ μs) are detected along the magnetic field. The rise time of X-ray pulses is ≤100 ns. X-ray bursts are always accompanied by electron current pulses at the collector (Fig. 8). Periodic bursts are observed within a narrow range of initial gas pressures. A departure of the pressure from the mean level (4.9×10^{-2} torr) by 10% leads to the suppression of X-ray emission. Note that, in the direction perpendicular to the magnetic field, the intensity of X-ray emission is significantly lower.

4. DISCUSSION

In order to interpret the experimental results, we consider the processes of energy conversion of the plasma flows both during their propagation across the

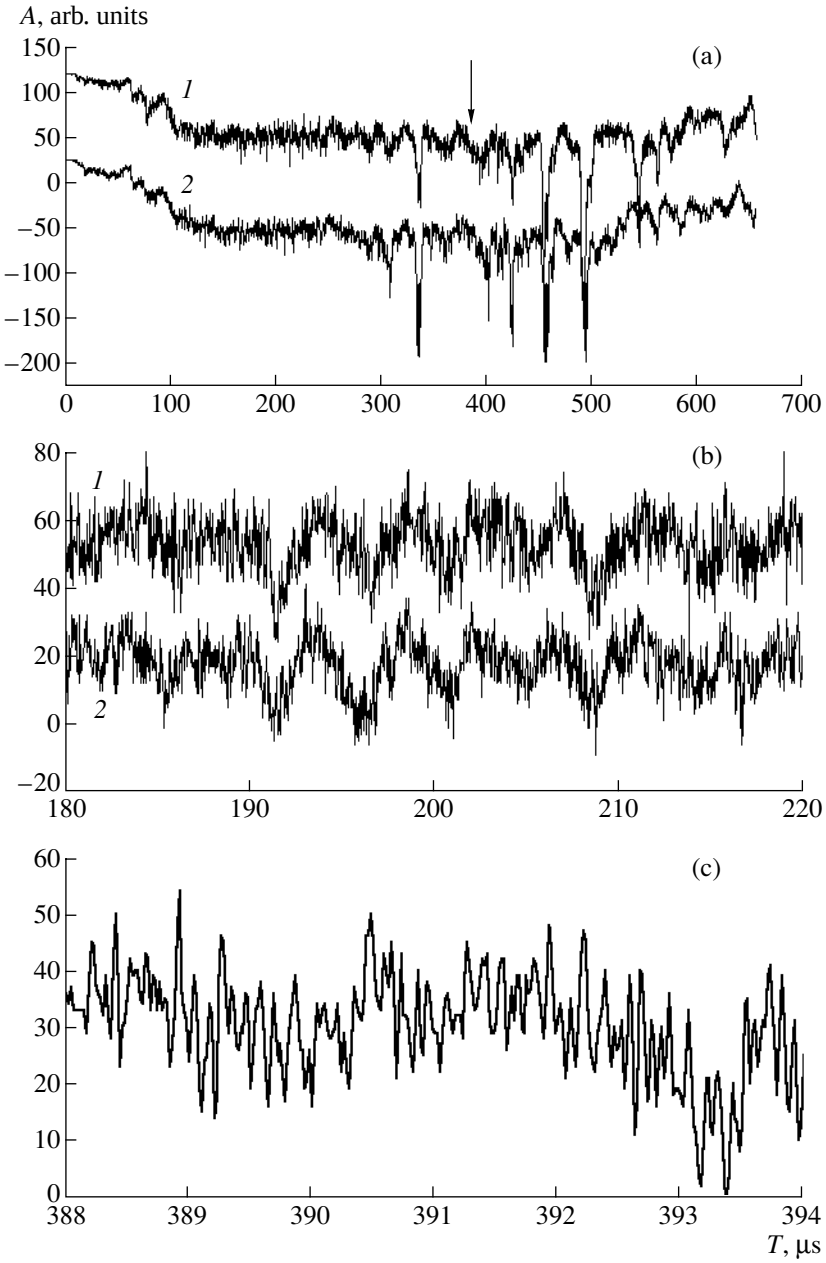

Fig. 2. Signals from optical detectors for $E_0 \simeq 300$ V/cm: (a) waveforms of plasma emission measured by optical detectors *1* and *2*, (b) oscillations of plasma emission with the period T_2, and (c) oscillations of plasma emission at the cyclotron frequency before the burst. Plots (b) and (c) are the fragments of the waveforms shown in plot (a).

magnetic field and in the course of their interaction with each other.

When propagating outside the discharge, the plasma flow, which is bounded in the transverse direction with respect to the magnetic field, is polarized [5]; i.e., a plasma capacitor (drift channel) is formed [6] and the further drift across the magnetic field occurs in the field of this capacitor. The polarization fields of the counter-propagating flows are oppositely directed; consequently, the collision of the plasma flows is accompanied by their depolarization (annihilation of the polarization fields). As a result, the electric field inside the drift channel decreases and the drift flow velocity at which they penetrate each other (in the x direction) tends to zero ($V_d \longrightarrow 0$). At the same time, near the discharge gaps, the potential difference between the floating probes and, accordingly, the drift velocity change only slightly (Fig. 9). Therefore, the directed drift motion of plasma particles in the region where the flows interact (penetrate each other) transforms into

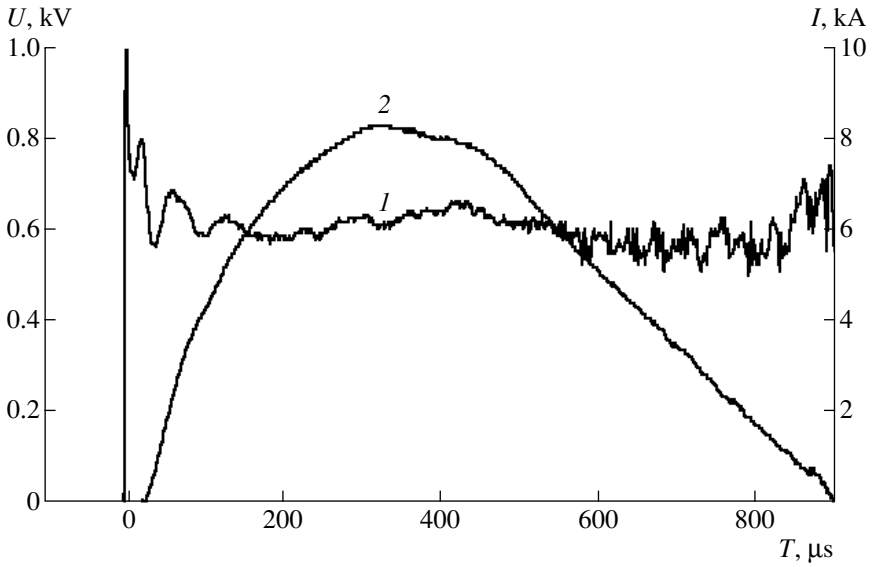

Fig. 3. Waveforms of (*1*) the discharge voltage and (*2*) discharge current in one discharge gap.

rotational motion. The penetration depth (in the *x* direction) is determined by the position of the boundary at which the gas-kinetic pressures inside and outside the interaction region are equal to each other. (We note that the characteristic scale length of the interaction region cannot be smaller than the Larmor radius.) Because of the plasma outflow (along the magnetic field) from the interaction region, the pressure inside this region decreases. The plasma flows follow the shrinking boundary and forms new drift channels, so that a new collision occurs, and so on. Hence, the flow interaction associated with depolarization is periodic in character; i.e., the system is in a self-oscillatory regime.

With allowance for Joule losses (due to the polarization currents), which decrease the flow velocity [6], the period of this oscillation process can be estimated as

$$T \sim \frac{Hl}{cE_0}\left[\exp\left(\frac{2eH^2l}{Mc^2E_0\beta}\right)\right]^{1/2}, \qquad (1)$$

where l is the length of free propagation of the flow (before the collision) and $\beta = \omega_{ce}/\nu_{ei}$ is the degree of

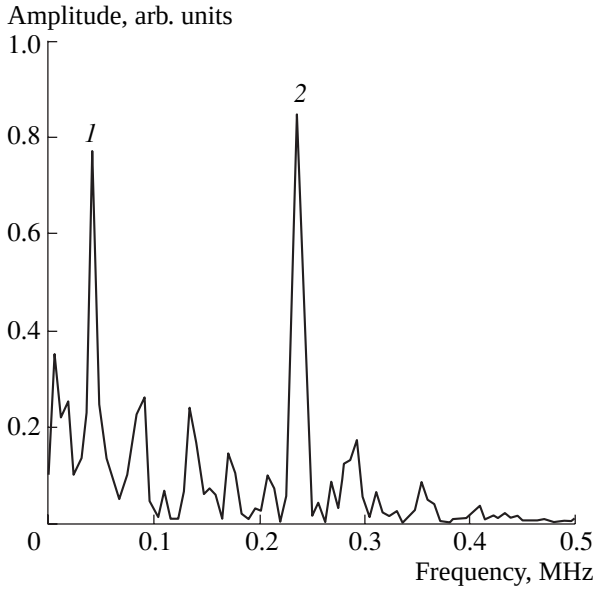

Fig. 4. Fourier spectrum for the time interval 150–320 μs. The peaks correspond to frequencies of (*1*) 42.7 and (*2*) 238 kHz.

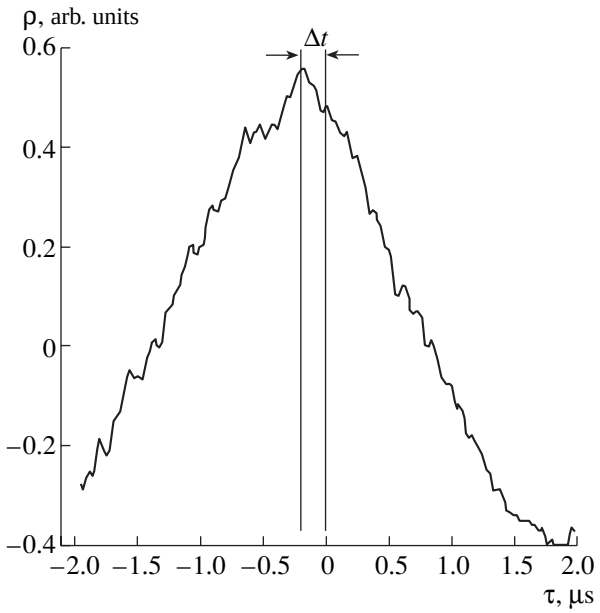

Fig. 5. Correlation function of the signals from optical detectors in the time interval corresponding to Fig. 2b.

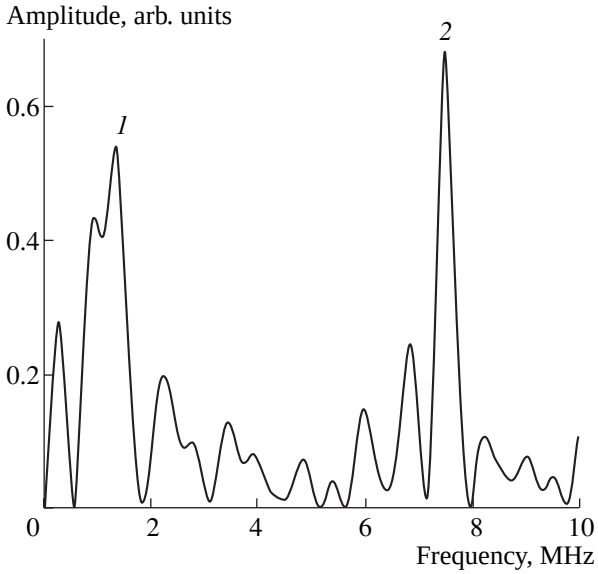

Fig. 6. Fourier spectrum for a time interval near a relatively weak burst in the time interval corresponding to Fig. 2c. The burst is shown by an arrow in Fig. 2a. The peaks correspond to frequencies of (*1*) 1.42 and (*2*) 7.5 MHz.

electron magnetization (where ν_{ei} is the binary collision frequency). In our case, we have $T \simeq T_1$.

During the interaction (depolarization) of the flows under conditions of strong electron magnetization, the electric current between the plasma capacitors is maintained by the ions. Consequently, the inductance of the discharge circuit of the plasma capacitors is determined by the ion Larmor radius R_i ($L \sim R_i$) if the flow size across the magnetic field (along the *y*-axis) is of the same order of magnitude. This parameter also determines the minimum size of the interaction region (along the *x*-axis) in which the drift motion transforms into rotation.

Since the size of the plasma capacitor along the *x*-axis is on the order of *l*, the expressions for the capacitance and inductance of the discharge circuit take the form

$$C \sim \frac{MNc^2 l\Delta z}{H_0^2 \Delta y}, \tag{2}$$

$$L \geq 4\pi^2 \mu_0 R_i^2/\Delta z, \tag{3}$$

where μ_0 is the magnetic permeability and Δy and Δz are the plasma flow dimensions across and along the magnetic field, respectively. The specific energy stored in the plasma capacitor (without allowance for losses) is $\varepsilon \sim MNc^2 E_0^2/H^2$. The energy in the *LC* circuit is expended on both Joule heating and the excitation of plasma waves.

It follows from Figs. 2c and 6 that, inside the wave packets with a period of T_3 (i.e., in relatively weak bursts), the period of the most pronounced oscillations is $\sim 1.3 \times 10^{-7}$ s. The corresponding frequency is close

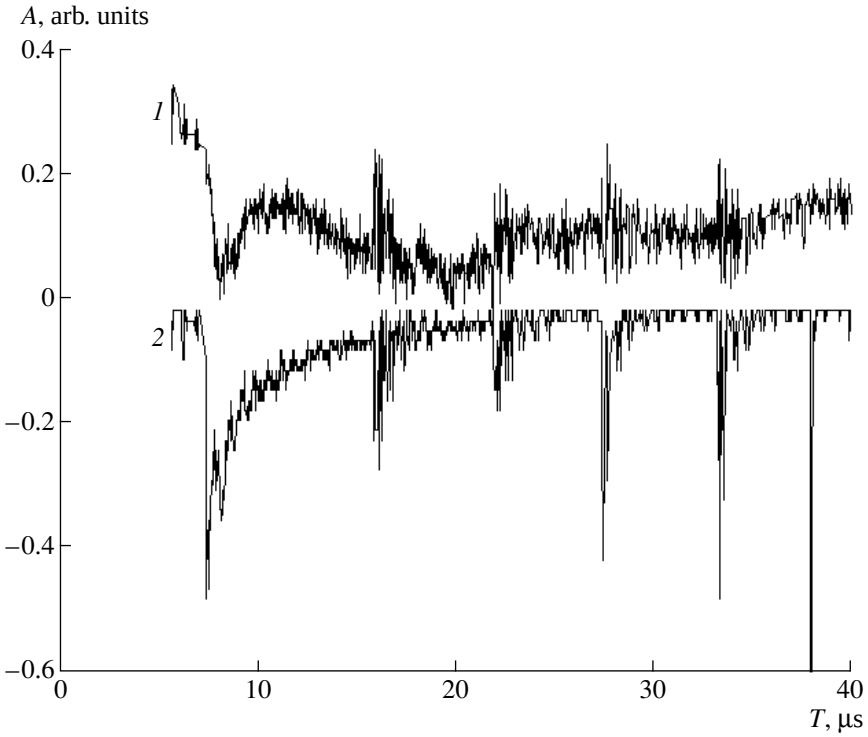

Fig. 7. Waveforms of the signals from (*1*) the optical and (*2*) X-ray detectors for $E_0 \simeq 2$ kV/cm.

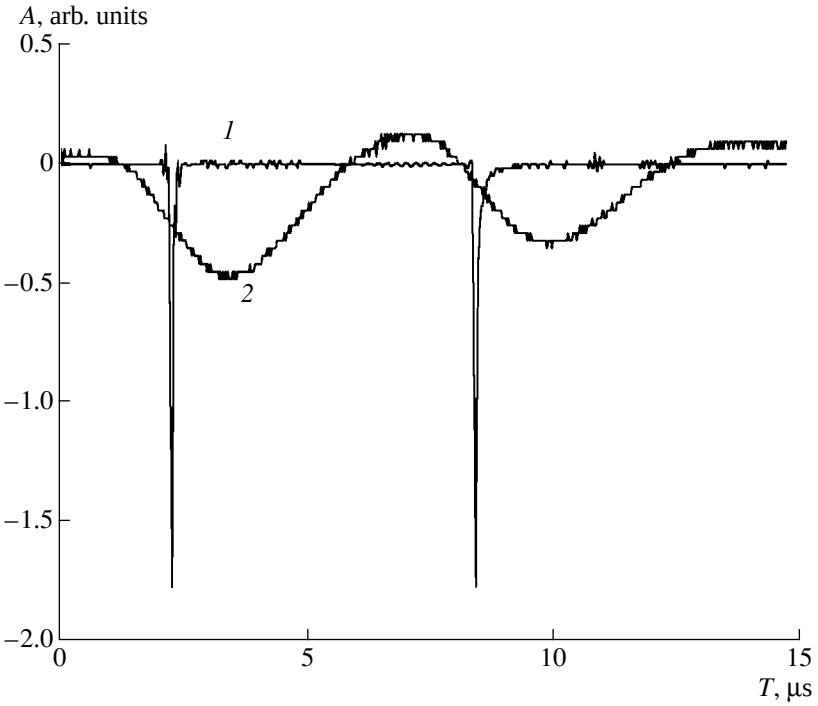

Fig. 8. Waveforms of (*1*) the X-ray emission intensity and (*2*) the electron current at the collector.

to the ion cyclotron frequency at $H = 10^4$ G ($\omega_{ci} \simeq 7 \times 10^6$ s^{-1}). If the characteristic frequency of the *LC* circuit is close to the ion cyclotron frequency, then, under the resonance conditions, the energy stored in the plasma capacitors can be efficiently converted into the energy of ion cyclotron waves. The resonance condition is given by the formula

$$1/(LC)^{1/2} = 2\pi\omega_{ci}. \quad (4)$$

Expressing R_i through the discharge electric field E_0, which determines the drift velocity V_d, and taking into account the capacitances of two flows, we obtain

$$\frac{1}{(2LC)^{1/2}} = \frac{eH^3}{2\pi M^{3/2}c^3E_0}\left(\frac{\Delta y}{2\mu_0 l}\right)^{1/2}N^{-1/2}. \quad (5)$$

Let us estimate the parameters corresponding to the experiment. Taking into account that the distance between the electrodes is 2 cm, from the waveform of the discharge voltage (Fig. 3), we can deduce the value of the electric field $E_0 \simeq 300$ V/cm, which varies only slightly in the interval of interest. Hence, for $\Delta y \simeq 2.5$ cm, $l = 4$ cm, $H = 10^4$ G, we obtain $(2LC)^{-1/2} \simeq 4.2 \times 10^{14} N_{res}^{-1/2} = 2\pi\omega_{ci}$. In this case, the value of the plasma density corresponding to the resonance conditions is $N_{res} \simeq 0.9 \times 10^{14}$ cm^{-3}. This density value is certainly realized under our experimental conditions.

The onset of plasma instabilities against the background of quasi-steady processes under resonance conditions is detected by the optical detectors as intense emission bursts (Fig. 2a). These bursts are related to regular wave packets with the repetition period T_2. The bursts are initiated by the structures characterized by

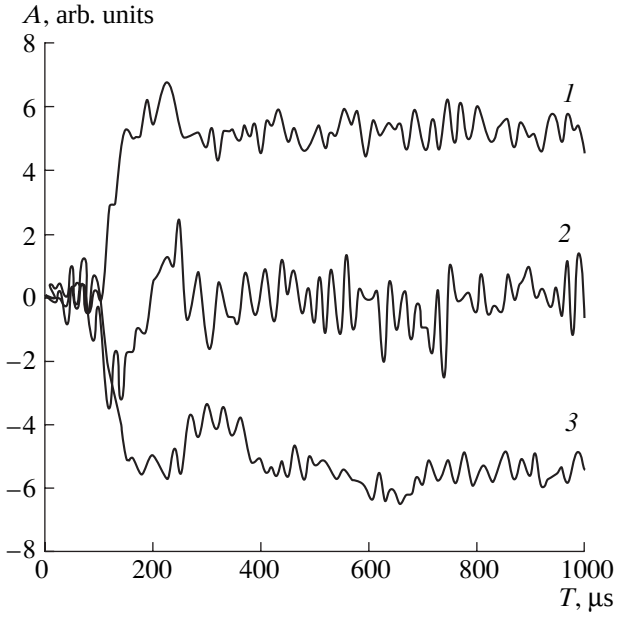

Fig. 9. Waveforms of the signals from the floating probes positioned (*1*, *3*) near the discharge gaps and (*2*) in the region where the plasma flows collide.

the period T_3. The increase in the number of photons emitted per unit time in a fixed solid angle under resonance conditions can occur if both the temperature and the effective collision frequency increase. This is typical of a plasma with strong turbulence, which differs from weak turbulence by the presence of regular plasma perturbations.

Now, we will consider the mechanisms for the generation of X-ray bursts. The presence of an alternating magnetic field in the plasma *LC* circuit leads to electron acceleration. The azimuthal velocity of electrons that produce the diamagnetic current can be estimated as

$$V_\varphi = -\frac{c}{4\pi}\frac{1}{eN}\frac{\partial H_\sim}{\partial R}, \quad (6)$$

where $H_\sim$ is the alternating magnetic field of the oscillatory circuit. Estimates show that the electrons can be accelerated to velocities that correspond to energies of ≤ 3 keV. Consequently, the maximum energy of X-ray bremsstrahlung photons is also limited by this value. However, as was mentioned above, the detectors used could detect only photons with energies above 3 keV. Therefore, in our experiment, the source of X-ray emission cannot be attributed to the electrons accelerated in the alternating magnetic field.

However, under experimental conditions such that the plasma density in the region where the plasma flows collide is $\omega_{ce} \simeq (4\pi Ne^2/m)^{1/2} = \omega_{pe}$, one could expect the excitation of intense electron plasma oscillations and, consequently, electron acceleration (in particular, along the magnetic field [7]). For a magnetic field of $H = 10^4$ G, the plasma density corresponding to the resonance conditions is $N_{res} \simeq 10^5 H^2 \sim 10^{13}$ cm^{-3}, which is typical of the plasma flows in our experiment.

An increase in the energy stored in the plasma capacitor should intensify the process. Indeed, when the discharge field was increased to ~2 kV/cm, a regime characterized by periodic X-ray bursts, which, in turn, were accompanied by the ejection of electrons along the magnetic field (Fig. 8), was realized in a narrow range of initial pressures. The detected X-ray power was no less than 1 W. According to expression (1), the period of X-ray bursts is shorter than that of optical bursts. In this case, the ion cyclotron resonance condition is not satisfied.

5. CONCLUSION

It is shown experimentally that the interaction of plasma flows propagating in opposite directions across the magnetic field can be accompanied by well-reproducible steady-state plasma self-oscillations. The frequency and amplitude of these oscillations can vary over a wide range; in particular, the resonance conditions can be realized. The periodicity of plasma oscillations in certain frequency ranges and their spatiotemporal correlation are evidence of strong turbulence. Strong turbulence leads to an increase in regular field perturbations, which can result in the formation of various coherent structures, such as solitons and nonlinear self-contracting wave packets [3].

Finally, we should mention that we restricted ourselves to burst processes and did not consider the mechanisms for the formation of wave packets (perturbations) characterized by the periods T_2 and T_3. The formation of these packets will be the subject of our further studies.

REFERENCES

1. K. A. Sarksyan, N. N. Skvortsova, N. K. Kharchev, and B. F. Milligen, Fiz. Plazmy **25**, 346 (1999) [Plasma Phys. Rep. **25**, 312 (1999)].
2. S. I. Popel, Author's Abstracts of Doctoral Dissertation (Moscow, 1998).
3. J. Weiland and H. Wilhelmsson, *Coherent Nonlinear Interaction of Waves in Plasmas* (Pergamon, Oxford, 1976; Énergoizdat, Moscow, 1981).
4. G. N. Dudkin, B. A. Nechaev, and V. N. Padalko, Fiz. Plazmy **26**, 142 (2000) [Plasma Phys. Rep. **26**, 129 (2000)].
5. A. G. Belikov and N. A. Khizhnyak, Fiz. Plazmy **21**, 723 (1995) [Plasma Phys. Rep. **21**, 685 (1995)].
6. G. N. Dudkin, B. A. Nechaev, and V. N. Padalko, Fiz. Plazmy **23**, 258 (1997) [Plasma Phys. Rep. **23**, 237 (1997)].
7. A. K. Berezin, E. V. Lifshits, Ya. B. Faĭnberg, *et al.*, Fiz. Plazmy **21**, 226 (1995) [Plasma Phys. Rep. **21**, 214 (1995)].

Translated by N. F. Larionova

Plasma Physics Reports, Vol. 27, No. 7, 2001, pp. 570–575. Translated from Fizika Plazmy, Vol. 27, No. 7, 2001, pp. 607–613.

PLASMA DYNAMICS

Theory of the Near-Wall Conductivity

A. I. Morozov* and V. V. Savel'ev**

**Russian Research Centre Kurchatov Institute, pl. Kurchatova 1, Moscow, 123182 Russia*

***Keldysh Institute of Applied Mathematics, Russian Academy of Sciences, Miusskaya pl. 4, Moscow, 125047 Russia*

Received October 4, 2000

Abstract—A model describing the phenomenon of the electron current in a plane plasma slab bounded by parallel dielectric walls in the presence of a homogeneous magnetic field perpendicular to the walls and an electric field oriented along the walls is presented. The current flows along the electric field because of the electron collisions with diffusely scattering walls. The model takes into account the presence of Debye layers and the non-Maxwellian character of the electron distribution function. Collisions in the plasma volume are ignored. © *2001 MAIK "Nauka/Interperiodica"*.

1. INTRODUCTION

Studies of stationary plasma thrusters (SPTs) have demonstrated that electron transport across the magnetic field is largely governed by electron scattering (more precisely, the termination of the electron drift) at the channel wall [1]. The first step in the development of a theory describing the current flowing across the magnetic field due to collisions with the wall [in the literature, this effect is referred to as the near-wall conductivity (NWC)] was made in [2],[1] where a half-space ($y < 0$) filled with a plasma was considered. The plasma was bounded from above by a plane wall. Both the plasma and the wall were penetrated by a homogeneous magnetic field perpendicular to the wall. In the plasma volume, there was also an electric field parallel to the x-axis (Fig. 1a). Collisions in the plasma volume were ignored. When drifting in the crossed fields (along the z-axis) and moving along the magnetic field lines, the plasma electrons arrive at the wall, are diffusely scattered, and lose their directional drift velocity. In [2], it was assumed that the wall is perfectly smooth on a macroscopic scale, but uneven on a microscopic scale. Here, we will also use this assumption,[2] but consider the processes occurring in a plasma slab (Fig. 1b). In addition, in [2], it was assumed that there is no Debye layer near the wall and the secondary electrons obey a Maxwellian distribution regardless of the distribution function (DF) of the incident electrons. In our paper, we abandon these assumptions. However, in accordance with the properties of real secondary-electron DFs, which are characterized by the weak dependence of the distribution of low-energy ($\mathscr{E}_e \sim 5$ eV) electrons on the incident-particle energy [5], we assume the secondary-electron distribution to be given, but different from Maxwellian. This assumption is also related to the fact that most of the secondary electrons fall in the low-energy range and the electrons that produce most of the current in the SPT have energies of ≤20 eV.

An important feature of the NWC is the oscillating (nonmonotonic) profile of the current density $j_x(y)$. It is this feature that allowed A.I. Bugrova and colleagues to experimentally reveal and study the NWC effect. We note that, if the electron DF can be represented as $f(\mathbf{V}, y = 0) = F_1(V_x)F_2(V_y, V_z)$, the character of the oscillations of $j_x(y)$ in the half-space allows us to determine

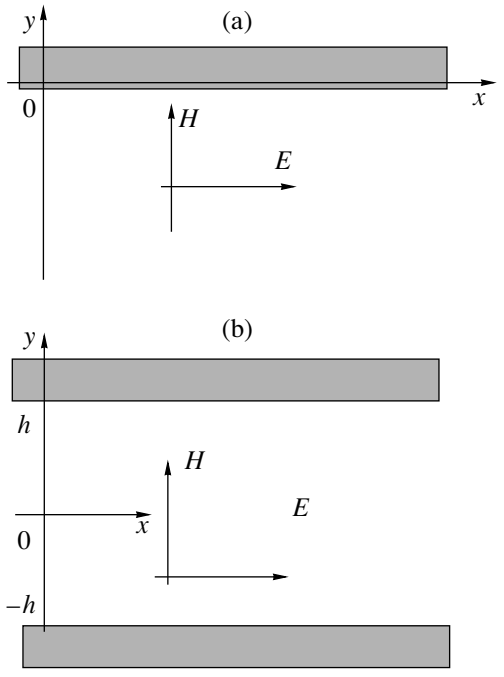

Fig. 1. Geometry of the problem: (a) half-space filled with a plasma and (b) plasma slab.

[1] A review of the present-day concept of NWC can be found in [3].

[2] This assumption is adequate for the initial (~100–500 h) stage of the SPT operation. Later, specific grooves appear on the insulator surface [4]; hence, other models should be applied to this stage.

1063-780X/01/2707-0570$21.00 © 2001 MAIK "Nauka/Interperiodica"

$F_1(V_x)$ (see [6]). In a real situation, because of the presence of a Debye layer near the wall surface, not all of the electrons arrive at the wall [1]. In this paper, we will only consider the dynamics of the secondary electrons emitted from the wall. In [7], an integral equation was derived, which was supposed to correctly describe the NWC in the channel if the secondary-electron emission function is known. However, attempts to solve this equation analytically (even in the simplest case of homogeneous fields) have failed. Hence, in order to determine the NWC characteristics, one should either perform laborious numerical calculations or develop approximate models. At present, the second approach seems to be more preferable, because reliable experimental data on the properties of the Debye layer near the SPT wall are still lacking. The examples of such a model description are given in [8].

2. BASIC FORMULAS FOR $j_x(y)$

Figure 1b shows the geometry of the model in Cartesian coordinates (x, y, and z). The plasma fills the region $|y| \le h$, the electric field is $\mathbf{E} = (E, 0, 0)$, and the magnetic field is $\mathbf{H} = (0, H, 0)$, where E and H are constant values. The electron dynamics in this spatial region is described by the collisionless kinetic equation for the electron DF $f(t, \mathbf{r}, \mathbf{V})$:

$$\frac{\partial f}{\partial t} + \mathbf{V}\frac{\partial f}{\partial \mathbf{r}} + \frac{\mathbf{F}}{m}\frac{\partial f}{\partial \mathbf{V}} = 0, \tag{1}$$

where

$$\mathbf{F} = -e\left(\mathbf{E} + \frac{1}{c}[\mathbf{V}, \mathbf{H}]\right) = -e\left(E - \frac{V_z}{c}H, 0, \frac{V_x}{c}H\right).$$

The distribution function is constant along the characteristics of the linear equation (1), which are determined by the set of equations

$$\frac{dx}{dt} = V_x, \quad \frac{dV_x}{dt} = -\frac{eE}{m} + \omega V_z,$$
$$\frac{dy}{dt} = V_y, \quad \frac{dV_y}{dt} = 0, \quad \omega = \frac{eH}{mc}, \tag{2}$$
$$\frac{dz}{dt} = V_z, \quad \frac{dV_z}{dt} = -\omega V_x.$$

Under the above assumptions, the equations for the characteristics are easily integrated:

$$V_x = V_{x0}\cos\omega t + (V_{z0} - V_E)\sin\omega t,$$
$$x = x_0 + \frac{V_{x0}}{\omega}\sin\omega t + \frac{V_{z0} - U_E}{\omega}(1 - \cos\omega t),$$
$$V_y = V_{y0}, \quad y = y_0 + V_{y0}t,$$
$$V_z = V_{z0}\cos\omega t - V_{x0}\sin\omega t + U_E(1 - \cos\omega t), \tag{3}$$
$$z = z_0 + \frac{V_{z0}}{\omega}\sin\omega t - \frac{V_{x0}}{\omega}(1 - \cos\omega t)$$
$$+ U_E t - \frac{U_E}{\omega}\sin\omega t,$$

where $U_E = cE/H$ is the drift velocity in the crossed electric and magnetic fields.

To determine the DF f throughout the entire region filled with a plasma, it is necessary to specify its values at the boundaries for the *incoming* particles, i.e., to define $f^- = f(y = h, V_y < 0)$ and $f^+ = f(y = -h, V_y > 0)$. Taking into account that the drift velocity U_E in an SPT is usually lower than the thermal velocity of bulk plasma electrons and assuming the wall material to be isotropic, we can also assume that, directly on the wall surface, the secondary-electron DF is isotropic:

$$f^- = F(y = +h, V_{x0}^2 + V_{y0}^2 + V_{z0}^2), \quad V_{y0} < 0,$$
$$f^+ = F(y = -h, V_{x0}^2 + V_{y0}^2 + V_{z0}^2), \quad V_{y0} > 0. \tag{4}$$

We will assume that the thickness of the Debye layer (DL) at the wall surface is negligibly small compared to the electron Larmor radius. Then, after passing across the DL with the potential drop U_D, the DF of the electrons arriving from the upper wall is

$$f_D^- = F\left(y = h, V_{x0}^2 + V_{y0}^2 + V_{z0}^2 - \frac{2eU_D}{m}\right),$$
$$V_{y0} < -\sqrt{\frac{2eU_D}{m}}. \tag{5a}$$

For the electrons arriving from the lower wall, we have

$$f_D^+ = F\left(y = -h, V_{x0}^2 + V_{y0}^2 + V_{z0}^2 - \frac{2eU_D}{m}\right),$$
$$V_{y0} > \sqrt{\frac{2eU_D}{m}}. \tag{5b}$$

Taking into account expressions (3) and the steady-state character of the process, for the electrons arriving from the upper wall, we can write

$$V_{x0} = V_x\cos\left(\omega\frac{h - y}{-V_y}\right) - (V_z - U_E)\sin\left(\omega\frac{h - y}{-V_y}\right),$$
$$V_{y0} = V_y < 0,$$
$$V_{z0} - U_E = V_x\sin\left(\omega\frac{h - y}{-V_y}\right) \tag{6a}$$
$$+ (V_z - U_E)\cos\left(\omega\frac{h - y}{-V_y}\right).$$

Analogously, for the electrons arriving from the lower wall, we have

$$\begin{aligned} V_{x0} &= V_x\cos\left(\omega\frac{h+y}{V_y}\right) - (V_z - U_E)\sin\left(\omega\frac{h+y}{V_y}\right), \\ V_{y0} &= V_y > 0, \\ V_{z0} - U_E &= V_x\sin\left(\omega\frac{h+y}{V_y}\right) \\ &+ (V_z - U_E)\cos\left(\omega\frac{h+y}{V_y}\right). \end{aligned} \tag{6b}$$

Substituting these expressions into formulas (5), we obtain

$$\begin{aligned} f_D^{\pm}(y, \mathbf{V}) &= F\left\{y = \mp h, (V_x + U_E\sin\vartheta^{\pm})^2 + V_y^2\right. \\ &\left. + [V_z - U_E(1 - \cos\vartheta^{\pm})]^2 - \frac{2eU_D}{m}\right\}, \end{aligned} \tag{7}$$

where $\vartheta^{\pm} = \omega\dfrac{y \pm h}{V_y}$. As a result, the secondary-electron DF inside the plasma takes the form

$$f(y, \mathbf{V}) = \begin{cases} f_D^-(y, \mathbf{V}), & V_y < 0 \\ f_D^+(y, \mathbf{V}), & V_y > 0 \end{cases}. \tag{8}$$

Now, we can write the electron current density along the electric field (along the x-axis):

$$j_x(y) = e\int V_x f(y, \mathbf{V}) d\mathbf{V}. \tag{9}$$

To calculate the integral, it is convenient to return to the variables V_{x0}, V_{y0}, and V_{z0}. Then, taking into account that the Jacobian of the transformation is equal to unity, we can write

$$\begin{aligned} j_x(y) &= eU_E\left[\int_{-\infty}^{-V_D} dV_{y0}\sin\left(\frac{y-h}{V_{y0}}\right)\right. \\ &\times \int_{-\infty}^{+\infty}\int_{-\infty}^{+\infty} dV_{x0}dV_{z0}F^-(V_{x0}^2 + V_{y0}^2 + V_{z0}^2 - V_D^2) \\ &+ \int_{V_D}^{\infty} dV_{y0}\sin\left(\frac{y+h}{V_{y0}}\right) \\ &\left.\times \int_{-\infty}^{+\infty}\int_{-\infty}^{+\infty} dV_{x0}dV_{z0}F^+(V_{x0}^2 + V_{y0}^2 + V_{z0}^2 - V_D^2)\right], \end{aligned} \tag{10}$$

where $\left(V_D^2 = \dfrac{2eU_D}{m}\right)$. In Eq. (10), we took into account that the functions $F^{\pm}$ are even with respect to V_{x0} and V_{y0}. Denoting $s = V_{x0}^2 + V_{z0}^2$, we obtain

$$j_x(y) = \pi eU_E[G^-(y-h) + G^+(y+h)], \tag{11a}$$

where

$$\begin{aligned} G^-(y-h) &= \int_{-\infty}^{-V_D} dV_y\sin\left(\omega\frac{y-h}{V_y}\right)\int_0^{\infty} dsF^-(s + V_y^2 - V_D^2), \\ G^+(y+h) &= \int_{V_D}^{\infty} dV_y\sin\left(\omega\frac{y+h}{V_y}\right)\int_0^{\infty} dsF^+(s + V_y^2 - V_D^2). \end{aligned} \tag{11b}$$

These are the general formulas for calculating the electric-current density in a plasma slab in homogeneous electric and magnetic fields. It is clearly seen that the current profile is dependent on the DF of the reflected electrons. Below, we consider the cases when the function F is either Maxwellian or flat-top.

3. MAXWELLIAN DISTRIBUTION FUNCTION

We assume that the surfaces of both the walls have identical properties and the secondary electrons obey the Maxwellian distribution:

$$\begin{aligned} F^- &= F^+ \\ &= n\left(\frac{m}{2\pi kT}\right)^{3/2}\exp\left[-\frac{m}{2kT}(V_{x0}^2 + V_{y0}^2 + V_{z0}^2)\right]. \end{aligned} \tag{12}$$

We introduce the dimensionless variables $\alpha = \dfrac{y}{\rho_T}$ and $\beta_T = \dfrac{V_D}{V_T}$, where $V_T = \sqrt{\dfrac{2kT}{m}}$ and $\rho_T = \dfrac{V_T}{\omega}$, and the function

$$G_M(\alpha, \beta) \equiv \frac{1}{\sqrt{\pi}}\int_{\beta}^{\infty} e^{-\xi^2}\sin\frac{\alpha}{\xi}d\xi. \tag{13}$$

Then, the final expression for the longitudinal current can be written in the following explicit form:

$$\frac{j_x(y)}{enU_E} = G_M\left[\frac{h}{\rho_T}\left(1 + \frac{y}{h}\right), \beta_T\right] + G_M\left[\frac{h}{\rho_T}\left(1 - \frac{y}{h}\right), \beta_T\right]. \tag{14}$$

In particular, for the current density at the wall, we have

$$\frac{j_x(\pm h)}{enU_E} = G_M\left(\frac{2h}{\rho_T}, \beta_T\right).$$

Apparently, the function $G_M(\alpha, \beta)$ refers to the case when the problem is solved in the half-space. In the case when the Debye layer is absent (i.e., $\beta_T = 0$), the function $G_M(\alpha, 0)$ was analyzed qualitatively in [2].

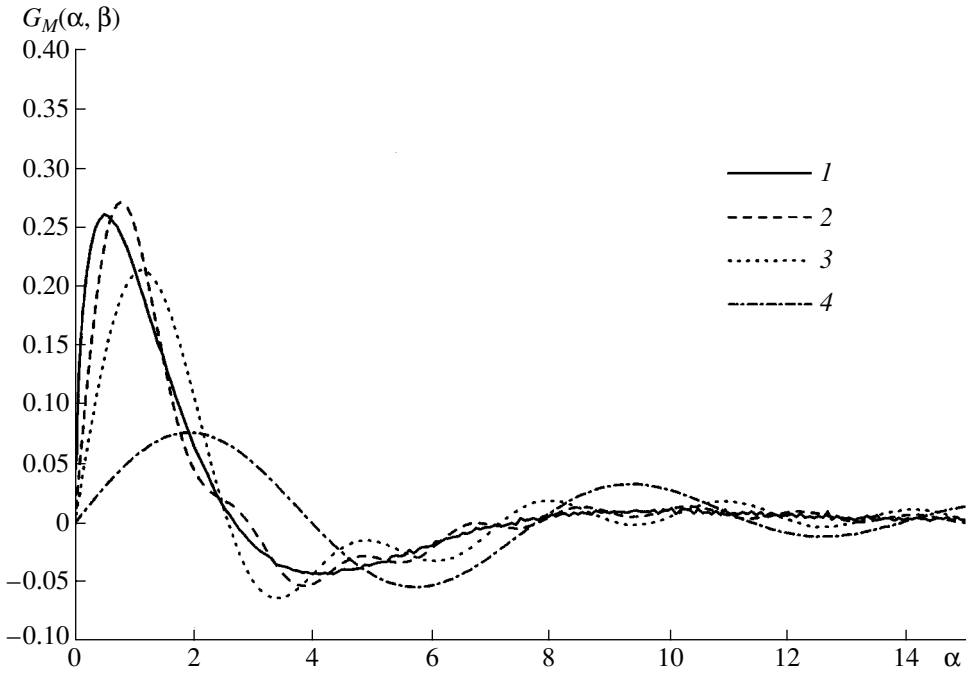

Fig. 2. Plots of the function $G_M(\alpha, \beta)$ for different values of β: (*1*) 0.0, (*2*) 0.3, (*3*) 0.5, and (*4*) 1.0.

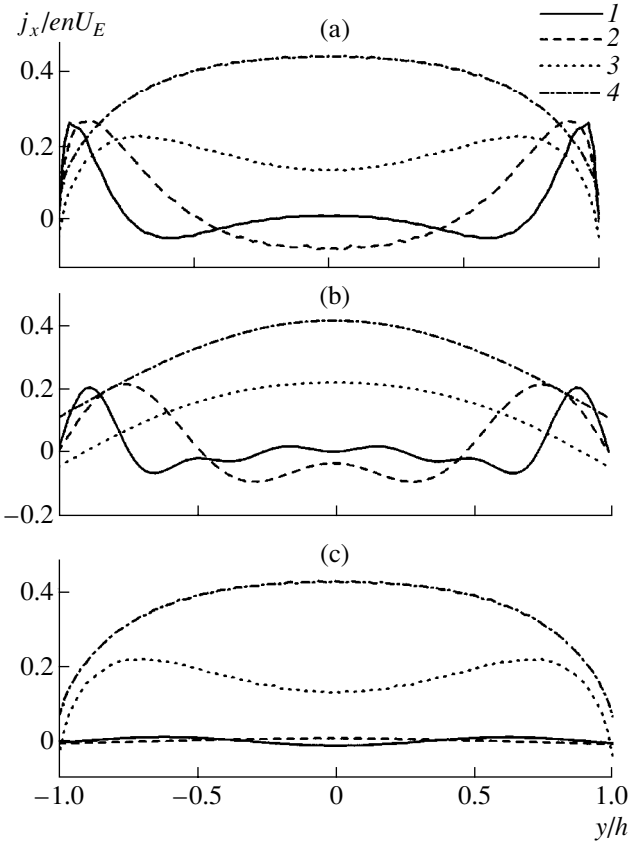

Fig. 3. Profiles of $j_x(y)$ for the Maxwellian DF for β_T = (a) 0, (b) 0.5, and (c) 1.5 and different values of the parameter γ_T = (*1*) 0.1, (*2*) 0.2, (*3*) 0.5, and (*4*) 1.0.

Figure 2 shows $G_M(\alpha, \beta)$ as a function of α for several values of β_T.

Figure 3 shows similar dependences for the plasma slab, i.e., the plots of

$$G_M\left[\frac{h}{\rho_T}\left(1+\frac{y}{h}\right), \beta_T\right] + G_M\left[\frac{h}{\rho_T}\left(1-\frac{y}{h}\right), \beta_T\right]$$

as a function of y in the interval $-h \le y \le h$. Figure 3a shows these dependences for $\beta_T = 0$ and four values of the dimensionless parameter $\gamma_T = \rho_T/h$. The curves in Figs. 3b and 3c are calculated for $\beta_T = 0.5$ and 1.5, respectively.

4. FLAT-TOP DISTRIBUTION FUNCTION

The integrands in expressions (11b) contain the factors of the form $\sin\frac{a}{V_y}$, which significantly complicate the structure of the resulting formulas. Hence, in order to derive explicit analytic expressions for $j_x(y, U_D, F)$, we have to simplify the problem, e.g., using special DFs for which calculations are relatively simple. We consider such an example with the purpose of determining the characteristic analytical properties of $j_x(y, U_D, F)$. We assume that the DFs at the upper and lower walls of the channel differ from each other only in the signs of V_{y0}. Below, for definiteness, we only consider the DF F^+ of the electrons arriving from the lower wall and the flow produced by these electrons. At the lower

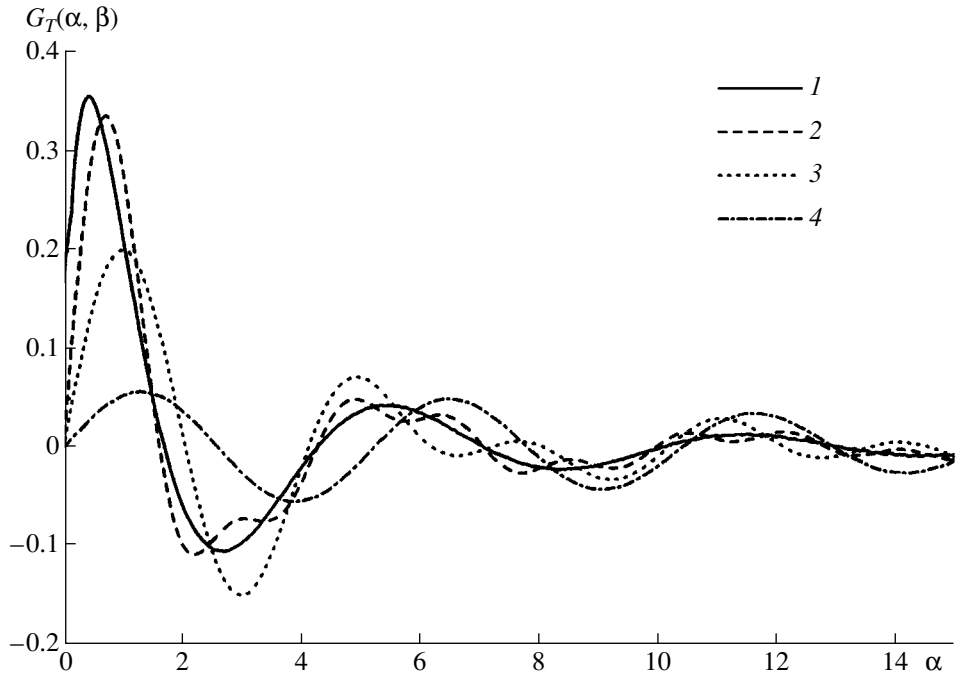

Fig. 4. Plots of the function $G_F(\alpha, \beta)$ for different values of β: (*1*) 0.0, (*2*) 0.3, (*3*) 0.5, and (*4*) 1.0.

wall, the DF is assumed to be rectangular (flat-top) in shape

$$F^+(\mathbf{V}_0^2) = F^+(V_{x0}^2 + V_{y0}^2 + V_{z0}^2) = N\begin{cases} 0, & V_{y0} < 0 \\ 1, & \mathbf{V}_0^2 < V_{0M}^2 \\ 0, & \mathbf{V}_0^2 > V_{0M}^2 \end{cases}. \quad (15)$$

Here, V_{0M} is the parameter of this function (the plateau length) and N is the normalization factor. After passing through the DL, the DF becomes

$$F_D^+(\mathbf{V}_0^2) = N\begin{cases} 0, & V_{y0} < V_D \\ 1, & V_D^2 < \mathbf{V}_0^2 < V_{0M}^2 + V_D^2 \\ 0, & \mathbf{V}_0^2 > V_{0M}^2 + V_D^2 \end{cases}. \quad (16)$$

Substituting this expression into formulas (11), we obtain

$$\int_{V_D}^{\sqrt{V_{0M}^2 + V_D^2}} dV_y \sin\left(\omega\frac{y+h}{V_y}\right)\int_0^\infty ds F_D^+(s + V_y^2 - V_D^2) = N\int_{V_D}^{\sqrt{V_{0M}^2 + V_D^2}} dV_y \sin\left(\omega\frac{y+h}{V_y}\right)(V_{MX}^2 - V_y^2), \quad (17)$$

where $V_{MX}^2 = V_{0M}^2 + V_D^2$.

We normalize the velocities to V_{MX} and introduce the dimensionless variables $\rho_F = \frac{V_{MX}}{\omega}$, $\alpha = \frac{y}{\rho_F}$, and $\beta_F = \frac{V_D}{V_{MX}}$ and the function

$$G_F(\alpha, \beta) = \int_\beta^1 (1 - \xi^2)\sin\frac{\alpha}{\xi} d\xi. \quad (18)$$

The integral in formula (18) is expressed through elementary functions and the integral cosine.[3]

Finally, by analogy to formula (14), we obtain the expression for the longitudinal electric-current density in the plasma slab:

$$\frac{j_x(y)}{j_0} = G_F\left[\frac{h}{\rho_F}\left(1 + \frac{y}{h}\right), \beta_F\right] + G_F\left[\frac{h}{\rho_F}\left(1 - \frac{y}{h}\right), \beta_F\right], \quad (19)$$

where $j_0 = e\pi N U_E V_{MX}^3$.

[3] $G_F(a, b) = \frac{2}{3}\sin a - a\mathrm{Ci}(a) - \frac{a}{6}\cos a + \frac{a^2}{6}\sin(a) - \frac{a^3}{6}\mathrm{Ci}(a) - b\sin\left(\frac{a}{b}\right) + a\mathrm{Ci}\left(\frac{a}{b}\right) + \frac{b^3}{3}\sin\left(\frac{a}{b}\right) + \frac{ab^2}{6}\cos\left(\frac{a}{b}\right) - \frac{a^2 b}{6}\sin\left(\frac{a}{b}\right) + \frac{a^3}{6}\mathrm{Ci}\left(\frac{a}{b}\right)$,

where $\mathrm{Ci}(a) = \gamma + \ln(a) + \int_0^a \frac{\cos(t) - t}{t} dt$.

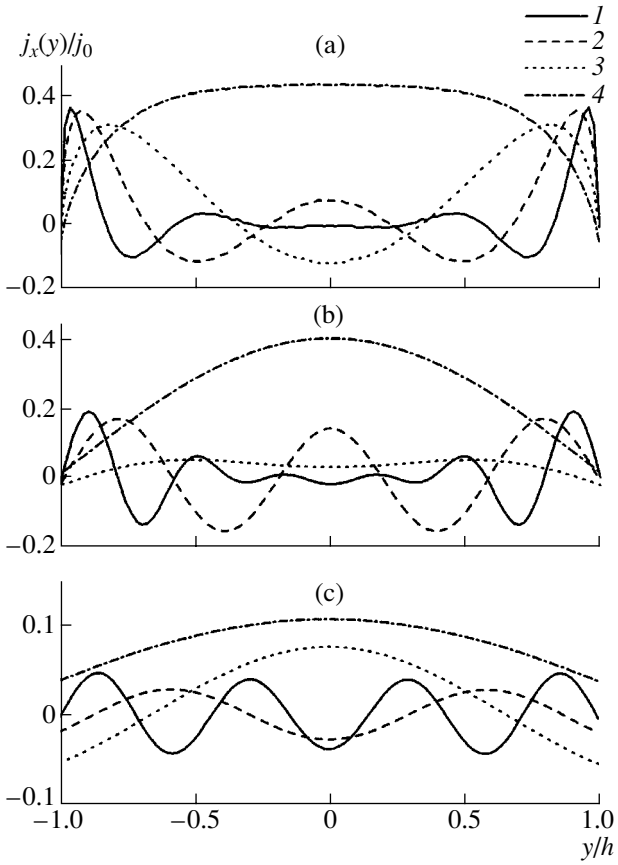

Fig. 5. Profiles of $j_x(y)$ for the flat-top DF for β_F = (a) 0, (b) 0.5, and (c) 0.75 and different values of the parameter γ_F: (*1*) 0.1, (*2*) 0.2, (*3*) 0.5, and (*4*) 1.0.

Hence, even in the considered simplest case of a flat-top distribution, the analytic expression for the current profile is rather cumbersome and depends on two parameters, β_F and $\gamma_F = \dfrac{\rho_F}{h}$.

Figure 4 shows the profiles of $G_F(\alpha, \beta)$, which is proportional to $j_x(y)$ for the half-space. Figure 5 shows the plots of function (19); as in Fig. 3, these plots illustrate the dependence of j_x on y and the variables β_F and γ_F.

As was mentioned above, in both cases, the most interesting feature of the current profiles is that the current density oscillates along the transverse coordinate y. If the Larmor radius is relatively small ($\rho \ll h$), the current is concentrated in the layer with a thickness on the order of ρ; the characteristic current density in the layer is about $\sim enU_E$.

5. CONCLUSION

In our opinion, the model analytic results obtained in this paper provide a general idea of the NWC effect in the channels (in particular, the influence of the Debye layers and the shape of the secondary-electron DF on the current profile). For the most part, these results are only qualitative, and it is difficult to compare them directly with the experimental data for several reasons.

The main reason is the lack of relevant experimental data on the processes in the SPT channels (thus far, the NWC has been studied only in these channels). The wall potential jump U_D in the DL has not yet been studied experimentally, and there is no information on alternative transport mechanisms due to fluctuations and binary collisions. The influence of oscillations in the channel on the transport mechanisms has not been studied; first of all, this concerns the disruption of DLs at high electron temperatures, when the averaged coefficient of secondary electron emission is $\bar{\sigma} > 1$. A more obvious reason is a certain disagreement between our theoretical model and the experimental conditions, because of the axial (rather than planar) geometry of modern SPTs.

Nevertheless, the analytical models presented in this paper provide insights into the NWC effect, and we hope that our study will stimulate further investigations of this interesting and important phenomenon.

ACKNOWLEDGMENTS

We thank A.I. Bugrova and her colleagues for fruitful discussions. This study was supported in part by the SEP firm and the Russian Foundation for Basic Research, project no. 00-01-00395.

REFERENCES

1. A. I. Bugrova and A. I. Morozov, in *Ion Injectors and Plasma Accelerations*, Ed. by A. I. Morozov and N. N. Semashko (Énergoatomizdat, Moscow, 1990), p. 42.
2. A. I. Morozov, Prikl. Mekh. Tekh. Fiz., No. 3, 19 (1968).
3. A. I. Morozov and V. V. Savelyev, in *Reviews of Plasma Physics*, Ed. by B. B. Kadomtsev and V. D. Shafranov (Consultant Bureau, New York, 2000), Vol. 21, p. 203.
4. B. A. Arkhipov, R. Yu. Gnizder, N. A. Maslennikov, and A. I. Morozov, Fiz. Plazmy **18**, 1241 (1992) [Sov. J. Plasma Phys. **18**, 641 (1992)].
5. Yu. A. Volkov and A. I. Morozov, Pis'ma Zh. Tekh. Fiz. **6**, 909 (1980) [Sov. Tech. Phys. Lett. **6**, 393 (1980)].
6. I. M. Bronshteĭn and B. S. Fraĭman, *Secondary Electron Emission* (Nauka, Moscow, 1969).
7. A. I. Morozov and A. P. Shubin, Pis'ma Zh. Tekh. Fiz. **10**, 20 (1984) [Sov. Tech. Phys. Lett. **10**, 12 (1984)].
8. A. I. Morozov, Zh. Tekh. Fiz. **57**, 1512 (1987) [Sov. Phys. Tech. Phys. **32**, 901 (1987)].

Translated by N. F. Larionova

Plasma Physics Reports, Vol. 27, No. 7, 2001, pp. 576–581. Translated from Fizika Plazmy, Vol. 27, No. 7, 2001, pp. 614–619.

PLASMA DYNAMICS

Stratification and Filamentation Mechanism for a Multicharged Plasma of a Z-Pinch

V. I. Afonin

Russian Federal Nuclear Center, All-Russia Research Institute of Technical Physics, Snezhinsk, Chelyabinsk oblast, 456770 Russia

e-mail: afonin@five.ch70.chel.su

Received March 23, 2000; in final form, November 16, 2000

Abstract—The thermal–ionizational instability that gives rise to axial and azimuthal inhomogeneities in the electron temperature and electron density in the form of striations and filaments in a multicharged plasma of a Z-pinch is studied in the linear approximation. The theoretical results on the rate at which the inhomogeneities grow and their characteristic spatial dimension agree with the experimental data. © *2001 MAIK "Nauka/Interperiodica".*

In gas-discharge physics, the thermal–ionizational instability and its role in the stratification and filamentation of gas-discharge plasmas have been investigated fairly well [1]. However, for Z-pinch plasmas (especially for multicharged plasmas), this instability has received less attention. In this context, we can mention papers [2, 3], in which it was suggested that both the thermal instability characteristic of a fully ionized hydrogen plasma heated by an electric current passing through it [2] and the thermal–ionizational instability of a pulsed volume gas discharge [3] may also occur in the initial stage of high-current pulsed discharges of the pinch type, thereby breaking the skin layer into current filaments. A more systematic approach developed in my previous paper [4] in order to investigate the thermal–ionizational instability of multicharged plasmas of Z-pinches revealed that this instability plays an important role in the discharge stratification observed experimentally in the Angara-5-1 facility [5]. However, in [4], no account was taken of the onset and development of azimuthal inhomogeneities in the form of plasma filaments, which were also observed at the surfaces of gas puffs shortly after the electric breakdown and which are explained as arising from the plasma instability when the liner is accelerated nonisothermally. It should be noted that streak-camera images of visible radiation emitted from a liner [5, 6] show that the plasma filaments appear even before the liner develops completely, i.e., before the formation of a strong shock wave behind the front of which the plasma ion temperature is higher than the plasma electron temperature. Also, according to [6], the striations and filaments appear in the current-carrying shell of a gas puff before the stage of efficient plasma compression. This brief analysis shows that it is necessary to turn to another mechanism for the onset of the above plasma inhomogeneities.

This paper is aimed at studying the thermal–ionizational instability that may occur in a multicharged plasma of a Z-pinch and may manifest itself as striations and filaments in the current-carrying shell of a gas puff or in the current-carrying plasma corona produced in the explosion of a metal wire.

By analogy with the theory of the stratification of a gas-discharge plasma [7], we are interested in the conditions for the onset of a thermal–ionizational instability in a homogeneous column of an equilibrium (in the ionization and recombination processes) multicharged plasma of a steady electric discharge sustained by a constant electric field ($\mathbf{E}_0$ = const).

We consider a small perturbation Z_1 in the mean ion charge number such that

$$\begin{aligned} Z(y, t) &= Z_0 + Z_1(y, t) \\ &= Z_0 + \mathrm{Re}[Z_k(t)\exp(-iky)], \end{aligned} \tag{1}$$

where Z_0 is the unperturbed equilibrium ion charge number, k is the wavenumber, and the y-coordinate is directed perpendicular to the electric field $\mathbf{E}_0$ of the plasma current.

It is natural to expect that the related perturbation in the electron density will lead to a redistribution of the current density over the plasma column and a nonuniform plasma heating, thereby giving rise to a perturbation T_1 in the initial electron temperature T_0. Consequently, we can set

$$\begin{aligned} T(y, t) &= T_0 + T_1(y, t) \\ &= T_0 + \mathrm{Re}[T_k(t)\exp(-iky)]. \end{aligned} \tag{2}$$

We assume that Z_0 and T_0 are both constant and consider a plasma with different ion (T_i) and electron (T_0) temperatures, taking into account that the plasma is heated primarily by the current (Joule heating) or by the

1063-780X/01/2707-0576$21.00

energy dissipation associated with the plasma motion (shock waves, strong plasma oscillations driven by instabilities, etc.). Since the energy exchange between the plasma electrons and ions equalizes the electron and ion temperatures, we assume that these temperatures are different (and constant) at least on a time scale shorter than the equalization time.

Our analysis is based on the kinetic equations for plasma particles and the electron energy balance relation. When describing the plasma kinetics, we will take into account only the most important processes such as electron-impact ionization and recombination; moreover, we will distinguish between three-body recombination and photorecombination.

We start by considering the situation in which photorecombination dominates over three-body recombination. In this case, the electron density is known to satisfy the condition [8]

$$n_e < 3 \times 10^{13} T_0^{15/4}/Z. \tag{3}$$

Here and below, the temperature is expressed in eV and the remaining quantities are in CGS units.

The kinetic equations for plasma particles have the form [9]

$$\partial \alpha_z/\partial t = n_e[\alpha_{z-1} C^i_{z-1} - \alpha_z(C^i_z + C^r_z) + \alpha_{z+1} C^r_{z+1}],$$

where α_z is the relative density of the ions with the spectroscopic symbol z. We sum up the kinetic equations multiplied by $z-1$. As a result, in the mean ion charge approximation, $Z = \Sigma \alpha_z (z-1)$, we obtain the equation

$$\partial Z/\partial t = N_A Z(\rho/A)(C^i_Z - C^r_Z), \tag{4}$$

where N_A is Avogadro's number; A is the atomic weight of an element; ρ is the plasma mass density; and C^i_Z and C^r_Z are the ionization and recombination rate constants for an ion with the charge number Z, respectively. The ionization and photorecombination rate constants are described by the expressions [9]

$$C^i_Z = 5.3 \times 10^{-8} (\mathrm{Ry}/T)^{3/2} \xi (x \exp x)^{-1} \times \{\ln[(1+x)/x] - 2/[5(1+x)^2]\}, \tag{5}$$

$$C^r_Z = 5.2 \times 10^{-14} Z x^{3/2} (\mu/2n^2) \times \{\ln[(1+x)/x] - 2/[5(1+x)^2]\}, \tag{6}$$

where $x = U_Z/T$, U_Z is the ionization energy of an ion with the charge number Z, μ is the number of vacancies in the outer electron shell n, and ξ is the number of equivalent electrons in the outer shell of an ion with the principal quantum number n.

Assuming that $x_0 T_1/T_0 < 1$ and $C^i_{Z_0} = C^r_{z_0}$, we linearize Eq. (4) in the small parameters Z_1/Z_0 and T_1/T_0 contained in Eqs. (1) and (2). As a result, we arrive at the following equation for the perturbed ion charge number

$$\partial Z_1/\partial t = \omega_0[(x_0+1)T_1/T_0 - Z_1/Z_0], \tag{7}$$

where $\omega_0 = N_A Z_0 C^i_{Z_0} \rho/A$, $x_0 = U_{Z_0}/T_0$; and $C^i_{Z_0}$ and $C^r_{Z_0}$ are the unperturbed ionization and recombination rate constants, respectively. The linearization procedure puts expressions (5) and (6) for the ionization and recombination rate constants in the form

$$C^i_Z = C^i_{Z_0}[1 + (T_1/T_0)(x_0 + 1/2)],$$

$$C^r_Z = C^r_{Z_0}[1 - T_1/2T_0 + Z_1/Z_0].$$

Another desired equation can be derived from the electron energy balance relation for an immobile inviscid plasma [9]:

$$\frac{3}{2} n_e k_0 \partial T/\partial t = -\nabla \cdot \mathbf{q}_e - Q_{\Delta T} + Q_1 - \mathbf{R} \cdot \mathbf{j}/n_e e - Q, \tag{8}$$

where $\mathbf{q}_e$ is the electron heat flux, $Q_{\Delta T}$ is the specific power of the heat transferred from the electrons to the ions in electron–ion collisions, the term Q_1 accounts for the energy change in the ionization and recombination processes, Q is the specific power of radiative losses in the X-ray continuum, $\mathbf{R} = \mathbf{R}_U + \mathbf{R}_T$ is the frictional force, $\mathbf{j}$ is the current density, e is the electron charge, and $k_0 = 1.6 \times 10^{-12}$ erg/eV. The electron heat flux term incorporates only the heat conduction flux, which is much higher than the heat flux associated with the electron motion, so that we have

$$\mathbf{q}_e = -1.9 \times 10^{20} a_1 k_0 T^{5/2} \nabla T/Z(\Lambda/10),$$

where $a_1(Z)$ is a numerical factor ($a_1 = 3.96$ for $Z \gg 4$) and Λ is the Coulomb logarithm.

Generally, the expression for the term Q_1 describing the energy exchange in electron–ion inelastic collisions is fairly lengthy [9]. Taking into account only the energy change associated with the change in the electron density in ionization–recombination processes, we can write

$$Q_1 = -\frac{3}{2} \Gamma_e k_0 T_0.$$

Here, according to [9], the relevant change in the electron density has the form $\Gamma_e = \Sigma(z-1)\partial(\alpha_z n_e/Z)/\partial t$; in the mean ion charge approximation, this expression can readily be simplified to $\Gamma_e = n_i n_e (C^i_Z - C^r_Z)$, where n_i is the ion density.

The remaining terms in Eq. (8) have the form [9]

$$Q_{\Delta T} = 4.67 \times 10^{-8} (\Lambda/10) Z^3 N_A^2 \rho^2 k_0 (T - T_i)/T^{3/2} A^3,$$

$$\mathbf{R} \cdot \mathbf{j}/n_e e = -\mathbf{j} \cdot \mathbf{E} + k_0 k_2 \mathbf{j} \nabla T/e,$$

$$Q = 1.54 \times 10^{-25} n_e^2 Z T^{1/2},$$

where $k_2(Z)$ is a numerical factor ($k_2 = 1.5$ for $Z \gg 4$), **E** is the total electric field in the plasma, and the term Q incorporates only (for simplicity) the volumetric energy loss due to bremsstrahlung.

Before linearizing Eq. (8), we consider the effect of the perturbed electron temperature on the conditions for the onset of the thermal–ionizational instability. The perturbation in the electron temperature results from the perturbation in the electron plasma density and the associated ambipolar electric field. The total electric field in a plasma is the sum of the ambipolar field and the field of the plasma current. The ambipolar electric field can be deduced from the equation of quasisteady motion of the plasma ions in an electric field [10], $Z_0 e n_i \mathbf{E} - \mathbf{R}_U - \mathbf{R}_T = 0$, provided that the plasma pressure gradient is zero. Here, the Joule force $\mathbf{R}_U$ and the thermal force $\mathbf{R}_T$ have the form $\mathbf{R}_U = e n_e k_1 \mathbf{j}/\sigma$ and $\mathbf{R}_T = -k_2 n_e k_0 \nabla T$, where $k_1(Z)$ is a numerical factor ($k_1 = 0.29$ for $Z \gg 4$), $\sigma = 0.9 \times 10^{13} T^{3/2}/(\Lambda/10)Z$ is the plasma conductivity, and j is the current density. For a current-free plasma ($j = 0$), the equation of ion motion yields $\mathbf{E}_a = -(k_0 k_2/e)\nabla T$. For a current-carrying plasma ($j \neq 0$), we obtain the expression $\mathbf{j} = \sigma(\mathbf{E}_0 + k_0 k_2 \nabla T/e)/k_1$ with the sum of the ambipolar field and the field related to the plasma current on the right-hand side. Hence, we can conclude that $\mathbf{E}_a \perp \mathbf{E}_0$.

We represent the plasma conductivity as $\sigma = \sigma_0 + \sigma_1$, where σ_0 is the unperturbed conductivity and σ_1 is the perturbed conductivity associated with perturbations (1) and (2). The linearized plasma conductivity has the form $\sigma = \sigma_0(1 - Z_1/Z_0 + 3T_1/2T_0)$, so that we arrive at the following linearized expression for the Joule heating power $P = jE$ per unit plasma volume:

$$P = (\sigma_0/k_1)E_0^2(1 + 3T_1/2T_0 - Z_1/Z_0).$$

Here, the first term on the right-hand side describes the heating of the unperturbed plasma and the second and third terms account for the effects of the perturbed electron temperature and electron density. Having derived these expressions, we can easily linearize the last term on the right-hand side of Eq. (8) to obtain $\mathbf{R} \cdot \mathbf{j}/n_e e = -P$. The linearized terms $\mathbf{q}_e$, $Q_{\Delta T}$, Q, and Q_1 have the form

$$\nabla \mathbf{q}_e = -1.9 \times 10^{20} a_1 k_0 T_0^{5/2} \Delta T_1/Z_0(\Lambda/10),$$

$$Q_{\Delta T} = 4.67 \times 10^{-8}(\Lambda/10)Z_0^3 N_A^2 \rho^2 k_0 (T_0 - T_i) \times [1 + 3Z_1/Z_0 - 3T_1/2T_0 + T_1/(T_0 - T_i)]T_0^{3/2} A^3,$$

$$Q = Q_0(1 + T_1/2T_0 + 3Z_1/Z_0),$$

$$Q_1 = -1.5 N_A^2 k_0 Z_0 (\rho/A)^2 T_0 C_{Z_0}^i \times [(x_0 + 1)T_1/T_0 - Z_1/Z_0],$$

so that Eq. (8) becomes

$$\partial T_1/\partial t = \alpha \partial^2 T_1/\partial y^2 - [\beta(x_0 + 1)/T_0 - 3\gamma/T_0 + \gamma/(T_0 - T_i) - \delta/T_0]T_1 - [(\beta - 4\gamma) - 4\delta]Z_1/Z_0. \quad (9)$$

When deriving this equation, we used the following relationship between the unperturbed plasma temperature and plasma density:

$$(\sigma_0/k_1)E_0^2 = 4.67 \times 10^{-8}(\Lambda/10)k_0 N_A^2 \rho^2 Z_0^3 \times (T_0 - T_i)/A^3 T_0^{3/2} + 1.54 \times 10^{-25} N_A^2 \rho^2 Z_0^3 T_0^{1/2}/A^3.$$

For $\Lambda = 10$, the coefficients of Eq. (9) are equal to

$$\alpha = 8.12 \times 10^{-4} A T_0^{5/2}/\rho Z_0^2,$$

$$\beta = 4 \times 10^{23} T_0 (\rho/A) C_{Z_0}^i,$$

$$\gamma = 1.87 \times 10^{16} \rho (Z_0/A)^2 (T_0 - T_i)/T_0^{3/2},$$

$$\delta = 3.85 \times 10^{10} T_0^{1/2} Z_0^2 \rho/A.$$

With allowance for expressions (1) and (2) and Eq. (7), we differentiate Eq. (9) with respect to time in order to obtain the second-order differential equation

$$d^2 T_k/dt^2 + [(\beta x_0 - 3\gamma)/T_0 + \gamma/(T_0 - T_i)]dT_k/dt + (\gamma\omega_0/Z_0)[4x_0/T_0 + 1/(T_0 - T_i)]T_k = 0. \quad (10)$$

Here, we neglect the small terms αk^2, ω_0/Z_0, and δ, which are insignificant under the conditions $T_i/T_0 \ll 1$, $A < 120$, $T_0 < 100$ eV, and $k \ll \min\{c_1, c_2\}$, where $c_1 = 10^9 \xi^{1/2} \rho Z_0^{3/2} x_0/A T_0^{5/2}$ and $c_2 = 10^{10}\rho(1 - T_i/T_0)^{1/2} Z_0^2 x_0^{1/2}/T_0^2 A^{3/2}$. Also, in [11], it was shown that, in the corona approximation, the approximate equality $x_0 \sim 4$–10 holds for $n_e < 10^{21}$ cm^{-3}, provided that the plasma is in a steady ionization equilibrium state, in which case we can use the condition $1/x_0 \ll 1$.

An analysis shows that, for $T_i > T_0$ (i.e., for processes like those that involve, e.g., shock waves and in which the ion temperature is higher than the electron temperature), Eq. (10) describes the damped oscillations. In order for the thermal–ionizational instability to occur, it is necessary (but not sufficient) to satisfy the condition $T_0 > T_i$. We impose the condition $T_0 \gg T_i$, which actually holds in the Joule heating stage of the Z-pinch plasma before the passage of the shock wave, and introduce the notation

$$a = (\beta x_0 - 2\gamma)/T_0, \quad b = 4x_0\gamma\omega_0/T_0 Z_0, \quad (11)$$

in order to rewrite Eq. (10) as

$$d^2 T_k/dt^2 + a dT_k/dt + bT_k = 0. \quad (12)$$

For $a^2 - 4b \neq 0$, this equation has the solution

$$T_k = C_1 \exp(S_1 t) + C_2 \exp(S_2 t), \quad (13)$$

where $S_{1,2} = [(-a \pm (a^2 - 4b)^{1/2}]/2$.

For $4b = a^2$, the solution is

$$T_k = \exp(-at/2)[C_1 t + C_2], \quad (14)$$

where C_1 and C_2 are integration constants.

In the second case, when three-body recombination dominates over photorecombination, the three-body recombination rate can be described by the expression [8]

$$C_Z^r = 8.75 \times 10^{-27} Z^3 n_e / T^{9/2}, \quad (6')$$

so that we have $C_Z^r = C_{Z_0}^r(1 + 4Z_1/Z_0 - 9T_1/2T_0)$, $\partial Z_1/\partial t = \omega_0\{[(x_0 + 1)T_1/T_0 - Z_1/Z_0] + 4T_1/T_0 - 3Z_1/Z_0\}$, and $Q_1 = -1.5 N_A^2 k_0 Z_0 (\rho/A)^2 T_0 C_{Z_0}^i [(x_0 + 5)T_1/T_0 - 4Z_1/Z_0]$. In a similar way, we can obtain Eq. (12) with solution (13) or (14) in which

$$a = (\beta x_0 - 2\gamma)/T_0,$$
$$b = (\omega_0/T_0 Z_0)[4\gamma(x_0 + 4) + 3\beta x_0]. \quad (15)$$

Note that, in this case, we can also use condition $1/x_0 \ll 1$, because, for a thermodynamically equilibrium plasma, we have $x_0 \sim 10$ [9].

As in the case of contraction of a volume gas discharge [1], the azimuthal thermal–ionizational instability can develop under the following two conditions: first, the electrons should be produced in the region where their density is elevated and, second, they should recombine not far from the points where they are produced. Otherwise, the seed perturbation is damped by electron diffusion. For reasons related to this, the characteristic transverse dimension $D \sim \pi/k$ of a filament can be defined as the doubled distance over which an electron diffuses in the ambipolar electric field during a characteristic lifetime equal to the characteristic recombination time $\tau \sim (C_{Z_0}^r n_i)^{-1}$. Since the directed electron velocity with respect to the ions is $\mathbf{V} = \sigma(-\mathbf{E}_0 - k_0 k_2 \nabla T/e)/e^2 n_e k_1$, the mean squared electron displacement $\langle r^2 \rangle$ in the plane perpendicular to the y-axis (for axisymmetric cylindrical geometry) can be found from the Einstein formula [12]: $\langle r^2 \rangle = 4k_0 TB\tau$, where $B = \sigma/e^2 n_e k_1$ is the electron mobility. Hence, we have $D \sim 5.27 \times 10^{-14}(A/\rho Z_0) T_0^{5/4}/(k_1 C_{Z_0}^r)^{1/2}$.

For completeness, we must also analyze the axial perturbations, in which case expressions (1) and (2) should be treated in a coordinate system with the y-axis directed along the liner axis and parallel to the electric field $\mathbf{E}$. One can readily see that this case differs from the situations examined above only in that the seed perturbation in the electron density gives rise to a perturbation in the electric field $\mathbf{E}$, so that we can write $\mathbf{E} = \mathbf{E}_0 + \mathbf{E}_1$, where $\mathbf{E}_0$ and $\mathbf{E}_1$ are the unperturbed field of the plasma current and $\mathbf{E}_1$ is the electric field perturbation. As a result, the third linearized term on the right-hand side of Eq. (8) becomes

$$\mathbf{R} \cdot \mathbf{j}/n_e e = -P + (k_0 k_2/k_1 e)\sigma_0 \mathbf{E}_0 \nabla T_1,$$

where $P = (\sigma/k_1) E_0^2 (1 - 3T_1/2T_0 + Z_1/Z_0)$ is the linearized expression for the Joule heating power per unit plasma volume. The perturbed electric field $E_1 = (Z_1/Z_0 - 3T_1/2T_0)E_0 - (k_0 k_2/e)\partial T_1/\partial y$ is determined from the equation $\mathbf{j} = \sigma(\mathbf{E} + k_0 k_2 \nabla T/e)/k_1$, provided that the current is constant, $j = j_0 = (\sigma_0/k_1)E_0$.

In this way, it is also possible to obtain Eq. (12) with solutions (13) and (14) in which $a = (\beta x_0 - 2\gamma - ik\varepsilon/e)/T_0$ and $\varepsilon = 1.52 \times 10^{-3} T_0^{3/2}/A^{1/2}$. For the case dominated by photorecombination, we have $b = (\omega_0/Z_0 T_0)(4x_0\gamma - ik\varepsilon/e)$, and, when three-body recombination is dominant, we have $b = (\omega_0/T_0 Z_0)[4\gamma(x_0 + 4) + 3\beta x_0 - ik\varepsilon/e]$.

In order to determine the characteristic spatial dimension of the striations, we again consider the stratification mechanism. Inside the striations, we have $j = \sigma E \sim n_e E = \text{const}$, which gives $\delta n_e/n_e = -\delta E/E$, indicating that the electric field is weaker in the regions of elevated electron density, and vice versa. From the solutions for T_1 and Z_1, it is an easy matter to establish that, being the function of n_e, the electron temperature behaves in essentially the same manner. Consequently, in the regions of elevated electron density, the ionization rate becomes lower, while the recombination rate becomes higher. As a result, the electron density fluctuations are either growing or damped, depending on the length D over which the electron temperature relaxes in the electric field E. According to [1], the relaxation length is equal to $D = 0.8L/\delta^{1/2}$, where L is the electron mean free path; $\delta \sim m_e/m_i$ is the energy transferred from an electron to an ion in each collision event; and m_e and m_i are the masses of an electron and ion, respectively. The electron temperature becomes consistent with the field E precisely over the length D. If the half-period of the perturbation is such that $\pi/k < D$, the electron temperature does not have enough time to relax to the level corresponding to the depressed electric field. For $\pi/k \ll D$, the electron temperature is completely insensitive to the field fluctuations. In the opposite case $\pi/k > D$, there is enough time for the electron temperature to follow the evolution of the electric field E, so that the perturbation is damped. That is why it seems reasonable to adopt the length D as a maximum characteristic longitudinal dimension of the striations.

Since $L = v\tau_{ei}$, where $v = 6.7 \times 10^7 T_0^{1/2}$ is the electron thermal velocity and $\tau_{ei} = 3.15 \times 10^8 A\delta T^{3/2}/n_i Z_0^2$ is the electron–ion collision rate [8], we have $D = 4 \times 10^{14} A^{1/2} T_0^2/n_i Z_0^2$.

If the ionization processes result in the production of ions with a completely filled outer electron shell, then we are definitely dealing with a thermal instability

rather than a thermal–ionizational instability. In fact, since the ionization potential of an ion with charge Z_0 is significantly higher than that of an ion with charge $Z_0 - 1$, to pull an electron out of the completely filled outer shell of an ion requires that the plasma electron temperature be sufficiently high. Consequently, in the initial stage of the process, the evolution of the seed perturbation in the electron temperature is described by the linearized equation $dT_k/dt = -aT_k$, whose solution $T_k(t) = T_0\exp(-at)$ describes the thermal instability.

We can assert that an initially homogeneous, equilibrium (in the ionization and recombination processes) multicharged plasma such that $a = (\beta x_0 - 2\gamma)/T_0 < 0$ and $T_i < T_0$ is unstable against both longitudinal and axial perturbations in the electron temperature and/or electron density. During the instability, the plasma evolves into a spatially inhomogeneous state with filaments and striations.

Let us apply the above results to obtain numerical estimates for the experiments carried out by Branitskiĭ *et al.* [5]. Immediately after the electric breakdown of a xenon liner, the authors observed the onset of small-scale ripples 1–2 mm in diameter on the liner surface, which were stretched along the liner axis. Then, the ripples were observed to evolve into dense plasma filaments 1–3 mm in diameter, stretched in the same direction. The initial density of xenon atoms was 2×10^{17} cm^{-3}, and the mean ion charge number outside the plasma filaments was $Z_0 = 3$–5. At the very beginning of filamentation, the electron temperature inside the filaments was estimated to be $T < 50$ eV, the mean ion charge inside the filaments being $Z < 7$.

For specificity, we assume that, outside the plasma filaments, the density of ions with charge number $Z_0 = 3$ is equal to the density of xenon atoms. Since, outside the filaments, the plasma is in equilibrium (in the ionization and recombination processes), we can set $\xi \sim Z_0$ and $T_0 = U_{Z_0}/x_0$ with $U_{Z_0} = 45$ eV and equate the ionization rate (5) to the recombination rate (6); as a result, we easily obtain $x_0 \sim 13$, which gives $T_0 \sim 4$ eV. We thus arrive at the second case, because condition (3) implies that three-body recombination dominates over photorecombination when $T_0 < 18$ eV. Equating the ionization rate (5) to the recombination rate (6'), we readily find $x_0 \sim 6.6$ and $T_0 \sim 7$ eV. In turn, we have $C^i_{Z_0} = C^r_{Z_0} \sim 2 \times 10^{-11}$ cm^3/s, $a \sim -2 \times 10^8$ s^{-1}, and $a^2 - 4b \sim 6.4 \times 10^{15}$ s^{-2}, so that, with allowance for expression (13) and the initial conditions, we can reduce expression (2) for the electron temperature inside a plasma filament to $T(t) \sim T_0[1 + \exp(1.4 \times 10^8 t)]$. Then, we can estimate the characteristic transverse scale length of a filamentary plasma: for $T_0 \sim 7$ eV, $Z_0 = 3$, and $k_1 = 0.4$, it is approximately equal to $D \sim 0.2$ cm, which agrees well with the experimental data of [5].

The growth rate of the axial instability can be estimated in the following way. First, we can readily determine the spatial scale length D of the instability: $D = 0.12$ cm. Next, we direct the x-axis along the liner axis (and parallel to the electric field **E**), set $k \sim \pi/D$, and perform the necessary manipulations, taking into account the fact that the coefficients of Eq. (12) are complex. As a result, in solution (13), we can single out the term that increases most rapidly with time:

$$T_k = T_0\exp(1.42 \times 10^8 t)$$
$$\times \exp[-i(8.25 \times 10^6 t + \pi x/D)].$$

We can see that the axial instability grows faster than the azimuthal instability. For this reason, in the experiments, the axial instability was the first to come into play.

For $Z_0 = 5$ and $T_0 < 25$ eV, three-body recombination dominates over photorecombination. In this case, we can easily find that $C^i_{Z_0} = C^r_{Z_0} \sim 10^{-11}$ cm^3/s for $T_0 = 13$ eV and $x_0 = 6.1$, so that we have $a \sim -0.43 \times 10^8$ s^{-1} and $a_2 - 4b \sim -6.7 \times 10^{15}$ s^{-2}, which give the estimates $T(t) \sim T_0[1 + \exp(0.2 \times 10^8 t)\sin(4 \times 10^7 t)]$ and $D \sim 0.4$ cm for $k_1 = 0.38$. Note that, for $Z_0 = 5$ and $T_0 > 25$ eV, photorecombination cannot dominate over three-body recombination. Actually, from formulas (5) and (6) with $x_0 \sim 4$–8, we can immediately establish that the initial electron temperature should range between 216 and 27 eV, in which case, however, the ionization potential U_{Z_0} of a xenon ion with the charge number $Z_0 = 5$ turns out to be unrealistically high.

Applying the same technique to the axial instability, we arrive at $T_k = T_0\exp(2 \times 10^7 t)\exp[-i(3.7 \times 10^7 t + \pi x/D)]$ and $D = 0.15$ cm.

Hence, we can conclude that, as the plasma outside the filaments is heated, the growth rate of the filamentation instability decreases and its characteristic spatial scale increases; in other words, the plasma filaments become blurred.

The above analysis enables us to describe the dynamics of the electric breakdown of a gas puff [5] as follows. Initially, the electric breakdown of the gas shell gives rise to separate plasma channels in which the plasma temperature and the degree of ionization both increase in the same manner as during the thermal–ionizational instability of a volume pulsed gas discharge: the main effects are the production of ions via gas ionization and three-body recombination of the ionization-produced ions. The resulting intense ultraviolet radiation from the channels is absorbed by the surrounding gas, thereby producing the plasma over the entire volume of a gas puff and initiating the current, which heats the plasma. Ionization-produced multicharged ions give rise to the thermal–ionizational instability, which may be followed by the thermal instability (before the ionization of each next completely filled electron shell of the ions). The instability results in the filamentation and stratification of the plasma. After the

passage of the shock wave, the ion temperature becomes higher than the initial electron temperature, $T_i \geq T_0$, so that the thermal instability is partially suppressed and gives rise to both the Rayleigh–Taylor instability associated with the axial perturbations in the electron temperature [13] and the azimuthal instability associated with the nonisothermal acceleration of the liner [5, 14].

During the electric breakdown of a gas puff, the thermal–ionizational instability and thermal instability do not substantially worsen the final parameters of the compressed plasma or the characteristics of the resulting X-ray pulse [5]. However, in experiments on pinch discharges in a capillary tube (with the purpose of creating X-ray lasers), the situation may be radically different. Under certain conditions, the thermal–ionizational instability in a plasma produced in a capillary tube may give rise to inhomogeneities in the electron temperature and electron density, which, in turn, may strongly affect not only the plasma compression dynamics in a capillary channel but also the global kinetics of the laser working medium. As an example, let us estimate the characteristic spatial scale D of the possible inhomogeneities of a pinch discharge (with a maximum current of 40 kA and a current rise time of 60 ns) in a capillary tube 4 mm in diameter, prefilled with argon with a uniform temperature and an initial uniform density of 1.37×10^{-6} g/cm^3 (the dynamics of this discharge was simulated by Imshennik and Bobrova [15]). For $T_0 = 3$ eV and $Z_0 = 1$, the spatial scale of the possible axial perturbations is estimated as $D \sim 1.6$ cm, which indicates that the discharge in a capillary tube experiences no contraction. The corresponding estimate for the spatial scale of the possible striations is $D = 1.14$ cm. Consequently, for a capillary tube shorter than D, the discharge plasma remains nonstriated; otherwise, the laser working medium should be created over a time interval shorter than the reciprocal of the growth rate of the axial instability.

In conclusion, note that, even with significant simplifying assumptions made when analyzing the thermal–ionizational instability, the above estimates of the parameters of the filaments and striations agree well with the experimental data [5, 6]. This agreement, in particular, provides the basis for neglecting ionization processes that occur via the excitation of autoionization states and, according to [9], may play an important role in a multicharged plasma. For $n_e < 10^{21}$ cm^{-3}, it is also possible to ignore dielectronic recombination, which is weakened because of the collisional quenching of the high-lying excited states [11].

REFERENCES

1. Yu. P. Raizer, *Gas Discharge Physics* (Nauka, Moscow, 1987; Springer-Verlag, Berlin, 1991).
2. B. B. Kadomtsev, in *Reviews of Plasma Physics*, Ed. by M. A. Leontovich (Gosatomizdat, Moscow, 1963; Consultants Bureau, New York, 1966), Vol. 2.
3. E. P. Velikhov, I. V. Novobrantsev, V. D. Pis'mennyĭ, *et al.*, Dokl. Akad. Nauk SSSR **205**, 1328 (1972) [Sov. Phys. Dokl. **17**, 772 (1972)].
4. V. I. Afonin, Fiz. Plazmy **21**, 267 (1995) [Plasma Phys. Rep. **21**, 250 (1995)].
5. A. V. Branitskiĭ, V. D. Vikharev, S. V. Zakharov, *et al.*, Fiz. Plazmy **17**, 531 (1991) [Sov. J. Plasma Phys. **17**, 311 (1991)].
6. A. V. Branitskiĭ, V. V. Aleksandrov, E. V. Grabovskiĭ, *et al.*, Fiz. Plazmy **25**, 1060 (1999) [Plasma Phys. Rep. **25**, 976 (1999)].
7. V. E. Golant, A. P. Zhilinskii, and I. E. Sakharov, *Fundamentals of Plasma Physics* (Atomizdat, Moscow, 1977; Wiley, New York, 1980).
8. Ya. B. Zel'dovich and Yu. P. Raizer, *Physics of Shock Waves and High-Temperature Hydrodynamic Phenomena* (Nauka, Moscow, 1966; Academic, New York, 1966, 1967), Vols. 1, 2.
9. V. I. Derzhiev, A. G. Zhidkov, and S. I. Yakovlenko, *Ion Emission in Nonequilibrium Dense Plasma* (Énergoatomizdat, Moscow, 1989).
10. S. I. Braginskiĭ, in *Reviews of Plasma Physics*, Ed. by M. A. Leontovich (Gosatomizdat, Moscow, 1963; Consultants Bureau, New York, 1963), Vol. 1.
11. A. V. Vinogradov and V. N. Shlyaptsev, Kvantovaya Élektron. (Moscow) **10**, 509 (1983).
12. D. V. Sivukhin, *Thermodynamics and Molecular Physics* (Nauka, Moscow, 1990).
13. V. I. Afonin, V. M. Murugov, S. V. Ponomarev, and A. V. Senik, Fiz. Plazmy **23**, 1008 (1997) [Plasma Phys. Rep. **23**, 930 (1997)].
14. V. D. Vikharev, G. S. Volkov, S. V. Zakharov, *et al.*, Fiz. Plazmy **16**, 379 (1990) [Sov. J. Plasma Phys. **16**, 217 (1990)].
15. V. S. Imshennik and N. A. Bobrova, in *Dynamics of Collisional Plasmas* (Énergoatomizdat, Moscow, 1997), p. 174.

Translated by G. V. Shepekina

Plasma Physics Reports, Vol. 27, No. 7, 2001, pp. 582–590. Translated from Fizika Plazmy, Vol. 27, No. 7, 2001, pp. 620–629.

MAGNETIC CONFINEMENT SYSTEMS

Microwave Processes in the Octupole Galathea

A. I. Morozov*, K. P. Kirdyashev, A. I. Bugrova***, and A. M. Bishaev*****

**Institute of Nuclear Fusion, Russian Research Centre Kurchatov Institute, pl. Kurchatova 1, Moscow, 123182 Russia*

***Institute of Radioengineering and Electronics, Russian Academy of Sciences, pl. Vvedenskogo 1, Fryazino, Moscow oblast, 141120 Russia*

****Moscow State Institute of Radioengineering, Electronics and Automation, pr. Vernadskogo 78, Moscow, 117454 Russia*

Received August 23, 2000; in final form, December 25, 2000

Abstract—Results are presented from experimental studies of electromagnetic emission and plasma oscillations in the plasma-frequency range in the Octupole Galathea confinement system. Experiments are performed in the electric-discharge mode at low magnetic fields (the barrier field is 0.002–0.01 T); the working gas is argon or hydrogen. It is found that the most intense microwave oscillations at frequencies of 1–5 GHz are excited near the plasma axis and in the magnetic-barrier region. The oscillations are excited by the discharge current and decay after the voltage is switched off. The experiments show that microwave oscillations excited in the magnetic-barrier region are responsible for the small value of the energy confinement time in the system.

1. INTRODUCTION

In [1], an electric-discharge plasma confinement system with an octupole magnetic field is described. The toroidal configuration of the magnetic field of the Octupole Galathea device is produced by four current-carrying conductors (myxines) immersed in an argon plasma. The probe measurements of the distributions of the plasma parameters (the electron density and temperature and the electric potential) in the confinement system (without time resolution) showed that, in the plasma, a potential well is formed that confines the ions [2]. The electron temperature T_e in the plasma confinement region is 20–22 eV, the charged-particle density is $n_e \sim 10^{11}$ cm^{-3}, and the potential is $\Phi \approx -50$ V. These plasma parameters refer to the steady-state conditions of magnetic confinement with a barrier field equal to $H_b = 0.005$ T at a voltage of $U_d = 200$ V and discharge current of $I_d = 4.5$ A.

The energy confinement time of this plasma configuration can be estimated as

$$\tau_E = \frac{\int n_e[(3/2)T_e + \bar{E}_i]dV}{I_d U_d}, \qquad (1)$$

where n_e and T_e are the electron density and temperature, I_d and U_d are the discharge current and voltage, and $\bar{E}_i$ is the mean energy of the plasma ions. For the given plasma parameters, we obtain $\tau_E \sim 5$ μs. This is a very short time, nearly two orders of magnitude shorter than the characteristic plasma decay time τ_d [2]. It was shown experimentally that, in the plasma decay phase, the values of τ_d and τ_E are close to each other. In experiments with the octupole confinement system [3], the decay time was ~0.1–1 s. Hence, the difference between the confinement times observed in the presence and absence of the discharge is an established fact. This is also evidenced by simpler observations. Thus, the discharge current (particularly, in a hydrogen plasma) rapidly saturates at a level close to the emission current from a hot cathode, and the plasma potential in the plasma core is close to the anode potential (the depth of the potential well is usually about $(0.1–0.3)U_d$ [1, 2]). This points to a fairly low electrical resistance of the barrier.

When analyzing the processes occurring in the confinement system in the electric-discharge mode, we can use the well-known analogy between the usual binary particle collisions in a plasma and the scattering of electrons by the instability-driven fluctuations of the electric field. Note that the amplitude of the plasma potential fluctuations at frequencies from ≤1 to 100 MHz does not exceed 300 mV [2, 4]; hence, these fluctuations cannot substantially affect the plasma confinement time and the discharge current. In addition, it should be taken into account that the frequencies of these fluctuations are less than the characteristic value of the electron cyclotron frequency and, thus, cannot be responsible for the demagnetization of electrons in the magnetic-barrier region.

On the other hand, the preliminary results of [5] show that microwave oscillations excited in the discharge contribute greatly to the formation of an electron flow through the magnetic barrier from the cathode to anode (the role of anode is played by the metal coating of myxines, the elements of the confinement system, and the vacuum chamber wall). In the electric-discharge mode, electron transport across the magnetic field and the formation of the discharge current may be caused by the scattering of magnetized electrons in the

1063-780X/01/2707-0582$21.00 © 2001 MAIK "Nauka/Interperiodica"

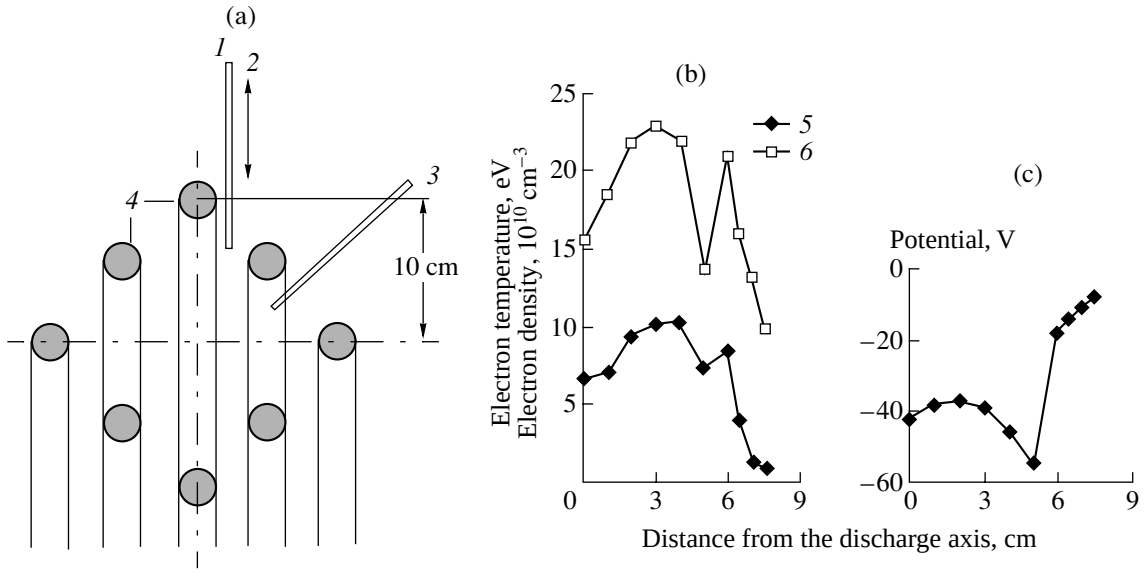

Fig. 1. (a) Scheme of probe measurements and (b, c) the profiles of the plasma parameters in the transverse cross section of the discharge, measured by the Langmuir and microwave probes: (*1*) movable microwave probe, (*2*) Langmuir probe, (*3*) fixed microwave probe, (*4*) myxines, (*5*) electron density, and (*6*) electron temperature.

barrier region by excited microwave oscillations. In this case, microwave oscillations should be responsible for the short energy confinement time of the system.

The goal of this paper is

(i) to reveal the presence of microwave oscillations in the confinement system and determine the frequency range in which these oscillations are most intense,

(ii) to compare the amplitudes of microwave oscillations in the presence and absence of a discharge,

(iii) to study the long-term behavior of the envelope of microwave oscillations,

(iv) to compare the spectral and energy characteristics of microwave oscillations in argon and hydrogen discharges, and

(v) to determine the regions in the plasma where the most intense microwave oscillations are excited.

2. EXPERIMENTAL DEVICE AND DIAGNOSTIC TECHNIQUES

The studies were conducted under the steady-state conditions of the Octupole Galathea operation. The barrier magnetic field confining the plasma varied in the range 0.002–0.01 T. The working gas (argon or hydrogen) was injected into the hot cathode region at a flow rate of 0.6–3 cm^3/s, which corresponded to pressures of $(1.5–4) \times 10^{-4}$ torr. The plasma in the confinement system was produced by an electric discharge. The discharge voltage was 40–200 V, and the discharge current was up to 4.7 A. The design of the discharge device and the main parameters of the electric discharge are described in [1, 2]. The probe measurements show that the electron density in the barrier region varies within the range 3×10^{10}–10^{11} cm^{-3} (Fig. 1) and the plasma is shaped as a torus with rather sharp boundaries, which are determined by the Ohkawa criterion for plasma confinement [3].

2.1. Technique for the Investigation of Microwave Emissions

The investigations were based on the spectral measurements of microwave emissions from the confinement system, along with the measurements of the plasma and device operation parameters. The microwave emission spectrum was measured with tunable detectors operating in the frequency ranges 1.05–2.15, 1.95–4.0, and 3.85–7.15 GHz. The major problem was to reconstruct the microwave spectra from the results of successive measurements in three channels with the use of individual detectors and broadband antennas. The antennas were mounted inside the metal vacuum chamber at a distance of 50–60 cm from the plasma. Under these conditions, we measured the electromagnetic component of the microwave field excited by the plasma device inside the metal vacuum chamber in the above frequency range.

A specific feature of these measurements was that the frequency was scanned at a rate of 5–15 MHz/s in each of the frequency channels in three successive shots of the plasma device. The emission spectra and the dependences of the emission intensity on the operation parameters of the device were measured with a time resolution of 0.1–1 s. At the given frequency-scanning rate, variations in the instrumental gain did not influence the magnitude of signals received.

Information on unsteady microwave processes in the confinement system was obtained by recording the envelope of the received signals at different frequencies with a time resolution of less than 100 μs. This allowed us to compare these data with the data on the cathode filament current and, using the results of two-frequency measurements, to reveal the correlation of the spectral components of microwave emission.

In view of the absolute measurements of microwave emission, we analyzed how the degree of coupling between the microwave antenna and the radiating plasma region, possible reflections of radiation from the metal walls of the vacuum chamber, and the mismatches in the microwave transmission line influenced the magnitude of the signals received. To exclude the influence of these factors, we carried out calibration measurements of microwave emission from a reference source with a known emission intensity [6]. For this purpose, we used a gas-discharge tube whose microwave emission intensity in the frequency range of interest was determined by the parameters of the discharge plasma, specifically, by the electron temperature and density and the effective electron collision frequency. The spectral properties of microwave emission from the gas-discharge plasma were calibrated using the data of previous measurements carried out with a reference blackbody radiation source whose surface configuration was similar to the emission structure of the tube. With the help of a set of gas-discharge tubes, we could obtain the calibration signal from the reference source with the area of the emitting surface close to that of the plasma in the confinement system.

The intensity of microwave emission is characterized by its spectral density S_f normalized to the area of the outer plasma surface. In order to reveal the nonequilibrium regions in the microwave spectra, the results of spectral measurements were compared with the calculated intensity of thermal radiation

$$S_f^* = 2\pi\frac{c^2}{f^2}T_e, \qquad (2)$$

where S_f^* is the spectral density of the unidirectional emission flux caused by plasma thermal fluctuations at the frequency f [7, 8]; T_e is the electron temperature in the radiating plasma layer with the density satisfying the condition for electromagnetic radiation to leave the plasma, $\omega \geq \omega_{Pe}$; and ω_{Pe} is the electron plasma frequency of the radiating layer. The critical plasma densities corresponding to this condition lie in the range 10^{10}–5×10^{11} cm^{-3}. For practical estimates of the thermal emission intensity under our experimental conditions, we used the formula S_f^* [W/(m^2 MHz)] $\approx 1.1 \times 10^{-10} f^2$, where it is assumed that $T_e = 10$ eV and the frequency f is expressed in GHz.

2.2. Diagnostic of Microwave Oscillations inside the Plasma

The microwave fields in the plasma were measured by two-wire microwave probes [6] with an inductive coupling in the measurement circuit. One probe was situated in the magnetic-barrier region, and the other probe could move in the transverse cross section of the plasma torus (Fig. 1). To determine the correlation between the data from local microwave measurements and the parameters of the plasma created in the confinement system, we measured the profiles of the electron density and temperature and electric potential along the path of the microwave probe.

Using microwave probes at the floating potentials, we avoided the dc coupling between the discharge plasma regions with different electric potentials. Microwave probes are usually used for the relative measurements of the magnitude and distribution of the microwave field in a plasma. The difficulties related to absolute measurements are associated with the unknown coupling between the microwave probe and the plasma wave field, the influence of the plasma on the probe parameters, and the nonuniform spectral characteristics of the measurement transmission line. For this reason, particular attention in this study was given to the possibility of determining the energy parameters of microwave fields and their spectral properties from the results of probe measurements.

Note that the main factor influencing the frequency characteristics of the probes used is the inductive coupling in the measurement transmission line. The inductive coupling, the capacitance of the plasma sheath near the probe, and the shunt capacitance at the mismatched ends of the two-wire line form a resonance circuit whose frequency-response properties should be taken into account when carrying out spectral measurements. The magnitude of the signal received in the measurement transmission line depends on the coupling between the probe and the plasma wave field and, consequently, on the oscillation frequency and the plasma parameters. This coupling is capacitive, and the influence of the plasma on the probe parameters is the most pronounced in the frequency range $\omega \approx \omega_{Pe}$, in which the plasma conductivity near the probe is minimum. In this case, the transmission coefficient of the probe signal into the measurement circuit decreases substantially. Estimates show that, in plasma wave measurements, the nonuniformity of the frequency characteristic of the microwave probe can attain 20–25 dB relative to the signals at frequencies different from ω_{Pe}.

The two-wire probe provides the local measurements of microwave fields in the plasma. The spatial resolution of the probe depends on the dimensions of its detecting elements. The characteristic scale length of the electric-field perturbations that can be detected by the probe is determined by the distance between the wires $\Delta l \approx 1$ mm. From the wavenumber spectrum of plasma oscillations $W_{Pe}(k)$, it is possible to extract the

components with $k \le k_{max} \approx (\Delta l)^{-1}$. If the dimensions of the detecting elements of the probe and the wavelength of the electromagnetic wave satisfy the inequality $\Delta l \ll 2\pi c/\omega\sqrt{\varepsilon(\omega)}$, then the probe allows one to detect the longitudinal plasma wave in the channel, the intensity of the electromagnetic component in the detected signal being substantially attenuated.

To exclude the influence of the plasma and the resonance properties of the probe on the intensity of the detected signals at different frequencies, we carried out special probe measurements of the intensity of thermal plasma oscillations in the reference source—a gas-discharge noise generator in which the energy density of microwave oscillations is determined by the electron temperature [6]. The energy density of thermal fluctuations of the electric field in the equilibrium plasma source was estimated by the formula [7, 8]

$$W_0^{Pl} = \frac{T_e}{2}\int_0^\infty \frac{d^3k}{(2\pi)^3}\frac{1}{1+(kr_D)^2}, \quad (3)$$

where r_D is the electron Debye radius. After integrating over wavenumbers in the range $k \le k_{max}$, we obtained that the magnitude of the calibration signal from a microwave probe is proportional to the total energy of thermal fluctuations at $k_{max} = r_D^{-1}$:

$$W_{St}^{Pl} = \frac{T_e}{12\pi^2}\frac{1}{(\Delta l)^3} = \left(\frac{r_D}{\Delta l}\right)^3 W_0^{Pl}. \quad (4)$$

Since the plasma microwave fields were measured by instruments with finite frequency passbands, we considered the value of the spectral energy density of microwave oscillations $W_{St}^{Pl}/\Delta f_{Pl}$ for plasma waves with $k \le (\Delta l)^{-1}$. The width of the plasma fluctuation spectrum Δf_{Pl} was estimated from the effective frequency of electron–neutral collisions. Estimates show that, in the magnetic-barrier region with T_e = 10–20 eV, the energy density of thermal plasma fluctuations in the wavenumber range under consideration is ~10^{-11} J/(m^3 MHz). This value can be used as a threshold level when identifying microwave generation regions in the plasma volume.

3. RESULTS OF EXPERIMENTAL INVESTIGATIONS OF MICROWAVE OSCILLATIONS

3.1. Spectral Density of Electromagnetic Emission

The measurements show that the intensity of microwave plasma emission in the frequency range under study can vary in a wide range, depending on the sort of working gas and the operating conditions, namely, the voltage and the magnetic field. The maximum values of the emission spectral density attains 10^{-5}–10^{-4} W/(m^2 MHz), which is five to six orders of magnitude higher than the thermal level corresponding to an electron temperature of 20 eV. The most intense emission is observed in an argon discharge in the frequency range 1–5 GHz (Fig. 2). As the gas flow rate increases, the maximum of the emission intensity shifts toward higher frequencies, whereas the intensity at frequencies of 5–5.5 GHz drops sharply to the thermal level.

The probe data on the plasma electron density indicate that oscillations in the plasma frequency range are excited in the discharge. The upper boundary of the measured microwave spectrum corresponds to the double plasma frequency calculated for an electron density of (5–7) × 10^{10} cm^{-3} in the barrier region of the discharge. For hydrogen, the maximum emission intensity lies outside the frequency range under study (<1 GHz). In the spectral range 1–2 GHz, the emission intensity turns out to be two to three orders of magnitude lower than that observed in experiments with argon.

One can see that the broadband microwave spectra are irregular and consist of quasi-monochromatic components separated by frequency intervals of 100–150 MHz. This spectral structure is reproduced in the repeated measurements under fixed operating conditions. Characteristically, as the gas flow rate increases, the emission spectrum becomes smoother and the relative contribution of individual quasi-monochromatic components decreases. This circumstance allows us to conclude that the variations in the microwave spectrum intensity are related to the formation of the channels of electron transport through the magnetic barrier.

3.2. Influence of the Operating Conditions on the Microwave Emission Intensity

Based on the results of experiments, we determined the main parameters of the device that govern the microwave emission intensity. At a fixed gas flow rate, these are the discharge voltage and the magnitude of the barrier magnetic field. The data presented in Fig. 3 (the time resolution is 0.1 s) show the dependences of the microwave intensity on the magnetic field and the discharge voltage. The intensity of microwave plasma fluctuations grows most rapidly at magnetic fields of less than 0.006–0.0065 T. The dependences presented reflect the influence of the gas flow rate on the intensity of spectral components of microwave emission from the barrier region. It is seen that the emission is the most intense at low gas flow rates. Note that, as the discharge voltage increases, the emission intensity grows throughout the entire frequency spectrum and, especially, near the spectral maximum.

3.3. Envelope of the Microwave Emission Signal

A distinctive feature of the electric-discharge device described is the use of an ac heated cathode. The filament current is rather high, $I_H \approx 20$ A. The diameter of the cathode wire is 0.5 mm. When the current reaches

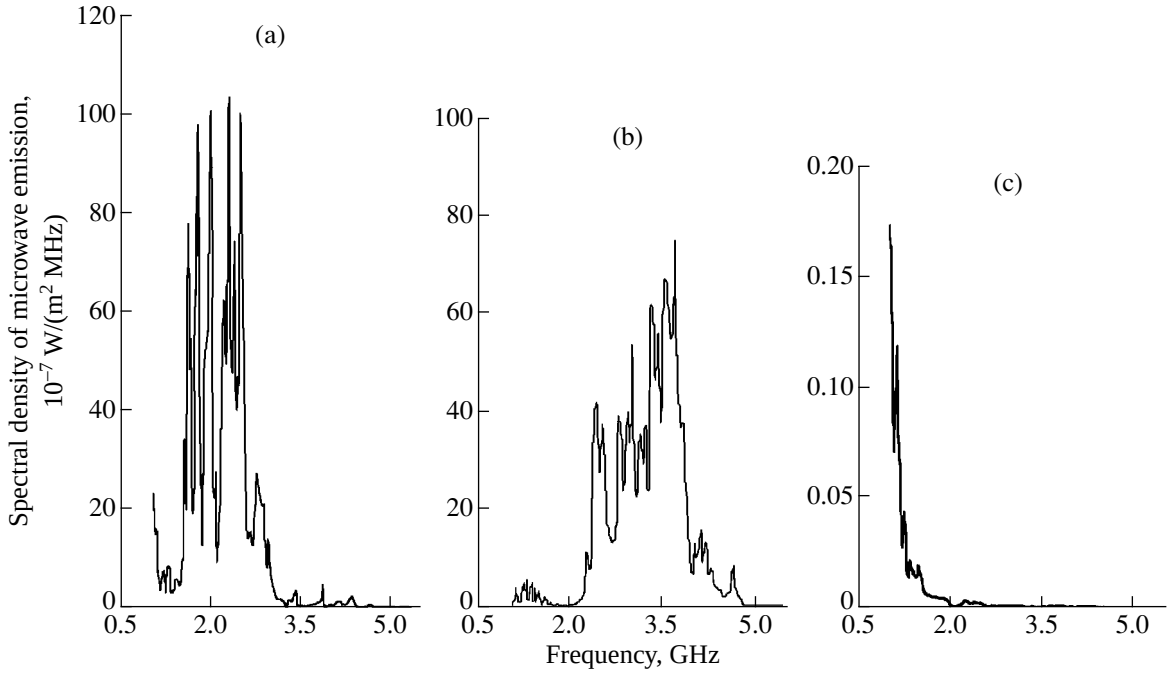

Fig. 2. Spectra of microwave emission from the plasma at a discharge voltage of 200 V, barrier magnetic field of 5×10^{-3} T, and different flow rates of the working gas: (a) the argon flow rate is 0.9 cm^3/s and the discharge current is 3.7 A, (b) the argon flow rate is 3 cm^3/s and the discharge current is 4.3 A, and (c) the hydrogen flow rate is 3 cm^3/s and the discharge current is 3.5 A.

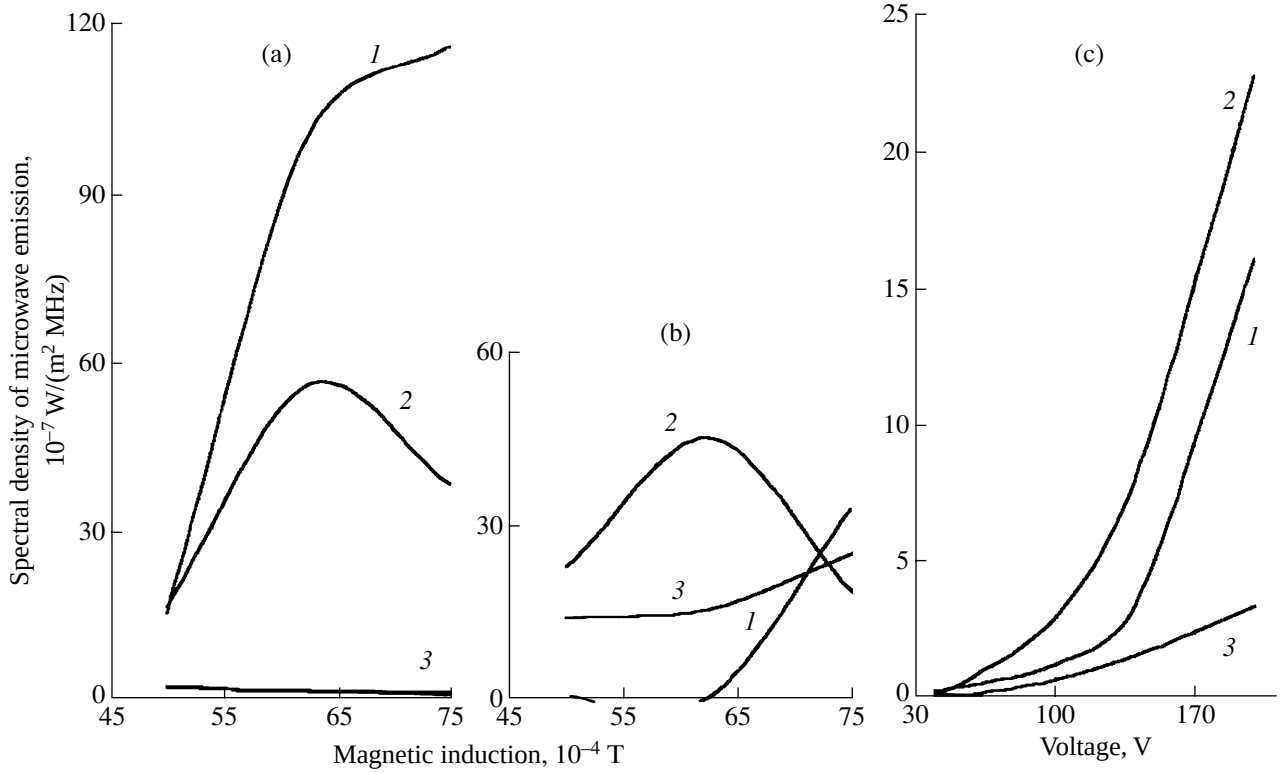

Fig. 3. Spectral intensity of microwave emission at frequencies of (*1*) 1.4, (*2*) 2.7, and (*3*) 4.5 GHz as a function of (a, b) the magnetic field and (c) the discharge voltage: (a) the flow rate is 0.9 cm^3/s and the discharge voltage is 200 V, (b) the flow rate is 3 cm^3/s and the discharge voltage is 200 V, and (c) the flow rate is 0.9 cm^3/s and the barrier magnetic field is 5×10^{-3} T.

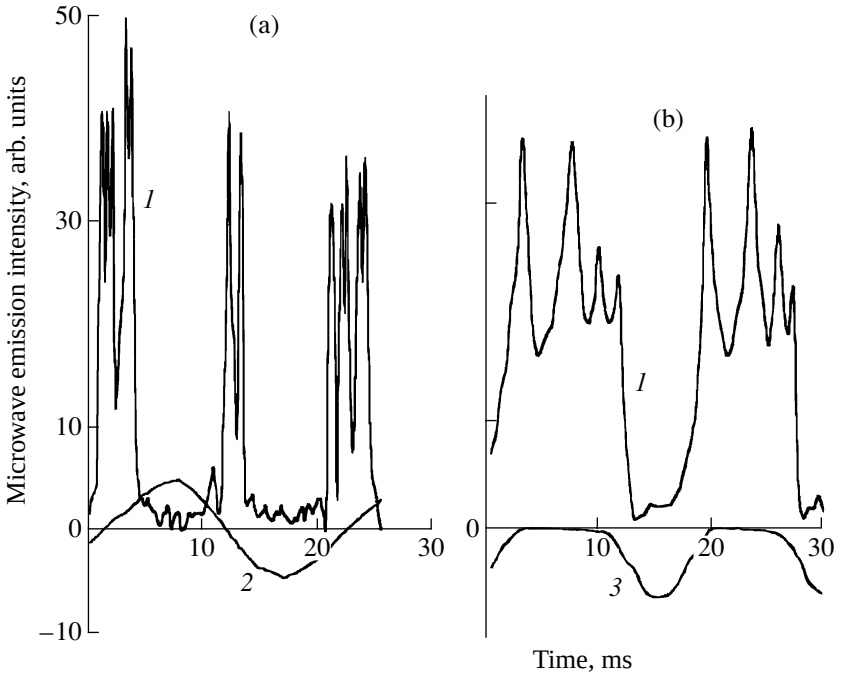

Fig. 4. Comparison of the envelopes of microwave signals with the waveforms of the cathode filament current when (a) the cathode is directly connected to an ac source (f = 1.4 GHz) and (b) the cathode is connected to an ac source through a diode (f = 2.7 GHz): (*1*) envelope of the microwave signal, (*2*) cathode heat current, and (*3*) rectified cathode heat current.

its maximum value (the current amplitude was $I_{H_{\max}} = \sqrt{2}\, I_H$ = 28 A), it produces a magnetic field of ~0.025 T near the cathode. If the electron energy near the cathode is 10 eV, the electron Larmor radius in this magnetic field is ~0.4 mm. Hence, when $I_H(t)$ is sufficiently high, the magnetic field produced by the filament current suppresses the cathode emission. It is reasonable to expect that this circumstance should have a certain effect on the noise envelope during long sweeps. Indeed, this is confirmed in the experiment (Fig. 4). Characteristically, the intense microwave emission takes place in the zero phase of the alternating filament current, whether the cathode is directly connected to the source or through a rectifying diode. As the discharge voltage increases, the intensity of the emission spikes increases; simultaneously, the degree of the frequency correlation decreases and additional spikes appear in time intervals of 10–20 ms.

In the regimes under study, we observed plasma density fluctuations caused by the cathode filament current and detected by the probe floating potential fluctuations at frequencies of ~100 Hz. The amplitude of these fluctuations is $\delta U \sim 0.5$–1 V, which corresponds to the relative electron density fluctuations $\delta n_e/n_e \sim e\delta U/T_e \sim 0.05$–0.1 in the barrier region. This circumstance is an additional factor governing the modulation of a microwave signal at the double frequency of the cathode filament current.

We note that the unsteady character of microwave emission shows up in the time intervals corresponding to the injection of the emitted electrons into the plasma confinement region. The envelope of the microwave signal has the shape of a series of pulses with durations of 200–300 μs and different cross-correlation coefficients at the chosen frequencies (Fig. 5). The absence of correlation between the envelopes at different frequencies is most pronounced for quasi-monochromatic microwave components that are excited when the gas flow rate is low (0.6–0.9 cm^3/s). As the gas flow rate increases to 3 cm^3/s, the duration of the microwave spikes increases and they overlap, so that microwaves are excited throughout the entire period of filament current oscillations. The latter circumstance can probably be attributed to the demagnetization effect of collisions on the electrons in the magnetic field of the cathode filament current.

3.4. Behavior of Microwave Emission after Switching off the Discharge Voltage

The envelope of the microwave emission signal from the detector after switching off the discharge voltage was measured using a differentiating RC circuit. Such a circuit was necessary because of the insufficient time resolution limited by the time constant 100–150 μs of the microwave detector; this time turned out to be close to the plasma decay time in the confinement system. According to the measurements of the probe

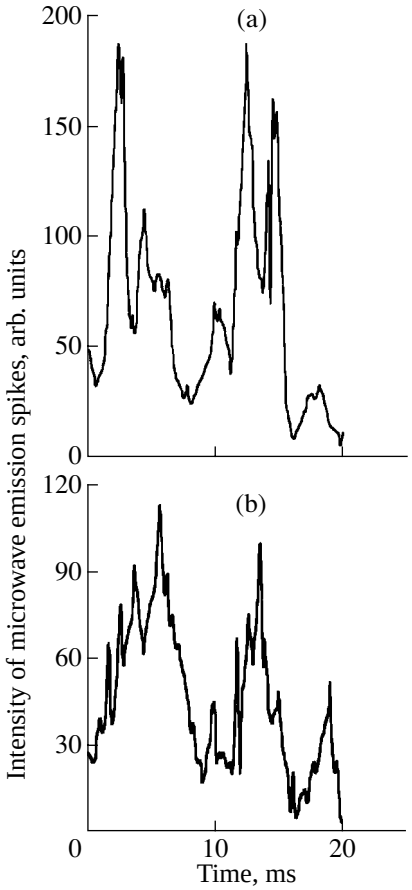

Fig. 5. Waveforms of the envelopes of microwave signals measured simultaneously at frequencies of (a) 1.1 and (b) 3.1 GHz in the argon plasma at a flow rate of 3 cm^3/s, voltage of 200 V, and magnetic field of 5×10^{-3} T.

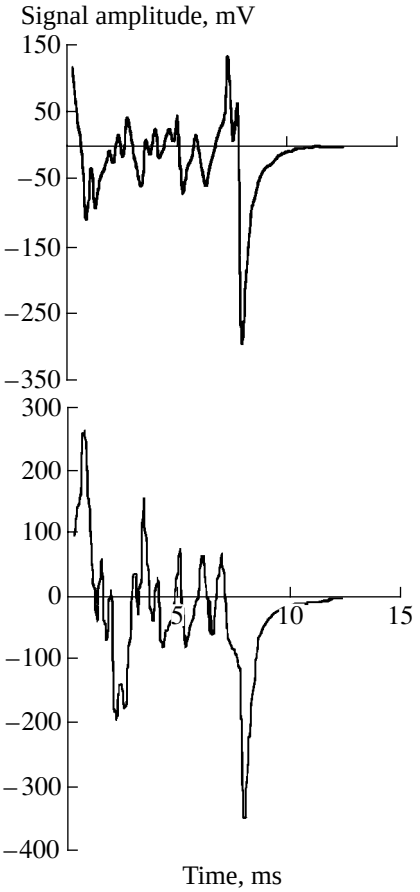

Fig. 6. Waveforms of the signals from the differentiating RC circuit of the microwave detector after the discharge voltage is switched off; the argon flow rate is 3 cm^3/s, the voltage is 200 V, and the magnetic field is 5×10^{-3} T.

ion current [3], this time was 200–300 μs. When measuring the signal through the differentiating RC circuit, we observed that the time derivative of the microwave emission envelope changed its sign after the voltage was switched off. This indicated that the microwave excitation correlated with the current flow through the confinement system. The waveforms in Fig. 6 clearly show the negative phase of the signal from the differentiating circuit after the voltage is switched off and the discharge current terminates. The waveforms are different because the times when the voltage is switched off fall into different (growth or decay) phases in the microwave emission intensity.

3.5. Results of the Experimental Studies of Plasma Fluctuations

The measurements of microwave fields in the plasma give information on the absolute values of the fluctuation energy density and its distribution along the path of the microwave probe. In the barrier plasma region, the energy density of plasma microwave fields in the plasma electron frequency range is higher than 10^{-6} J/(m^3 MHz), which is five orders of magnitude higher than the thermal level. These data correspond to the scale length of plasma electric field perturbations measured by a probe; this scale length is determined by the dimensions of the probe detecting elements (the distance between the probe wires is ~1 mm).

The distribution of the microwave field over the plasma cross section is characterized by maxima of the fluctuation energy density in the axial and barrier regions (Fig. 7). We note that, as the frequency increases, the maximum in the microwave field intensity in the cross section of the torus is displaced to its middle line. The results of the measurements of the envelopes of microwaves signals from two probes positioned at different angular coordinates and minor radii indicate that fluctuations are excited simultaneously throughout the entire region adjacent to the current-carrying coating of an individual myxine. However, at this stage of our study, we have no reason to believe that the microwave excitation is correlated throughout the entire plasma volume. The time behavior of the enve-

lope of the microwave signal is different for different frequencies of the fluctuations measured, and individual spectral components are excited independently.

4. DISCUSSION OF RESULTS

The studies of microwave processes in the Octupole Galathea have answered the questions posed in the Introduction.

(i) Intense microwave emission and, consequently, oscillations in the plasma volume are observed when the device operates in the electric-discharge mode. After the discharge voltage is switched off, fluctuations decrease rapidly (with a characteristic time on the order of the voltage fall time) to a level comparable with the thermal one.

(ii) The emission spectrum has well-defined edges on both the low- and high-frequency sides. The general features of the spectra are the same in argon and hydrogen. As the flow rate $\dot{m}$ of the working gas (the pressure in the chamber) increases, the upper boundary of the spectrum shifts toward higher frequencies as $\sim\sqrt{\dot{m}}$. Taking into consideration the data from experiments [1], according to which the density n_e increases as $\dot{m}$, we obtain the relation between the frequency and the electron density corresponding to the plasma oscillations. The absolute values of the characteristic frequencies also lie in the electron plasma frequency range. Thus, for a working gas (argon) flow rate of 3 cm^3/s, discharge current of 4.3 A, voltage of 200 V, and magnetic field of 0.005 T, the electron density in the barrier region is equal to 5×10^{10}–10^{11} cm^{-3} and the corresponding plasma frequency is $f_{Pe} = (1/2\pi)\sqrt{4\pi e^2 n_e/m_e} \approx$ (2–3) GHz (to within a measurement accuracy of 50% for the data on the electron density presented in Fig. 1).

(iii) Spectral measurements of the intensity of microwave emission from the argon discharge show that the peaks of the microwave spectrum lie in the frequency range 1–3 GHz. The highest spectral peaks are in the high-frequency range corresponding to the double plasma frequency. This makes it reasonable to assume that the observed microwave radiation is generated in a nonlinear process resulting in the merging of two plasma waves in the plasma barrier region. We note that a small peak in the low-frequency spectral range (Fig. 2b) corresponds to the frequency approximately equal to ω_{Pe}; this emission peak probably corresponds to the transformation of Langmuir waves at plasma inhomogeneities.

(iv) Probe measurements of microwave oscillations in the plasma showed that the noise level is the highest in the magnetic barrier and the axial region adjacent to the cathode. Oscillations near the cathode are very similar to those in a beam–plasma discharge. Thus, in the Octupole device, specific features of such a discharge are observed in this region. The generation of oscillations in the magnetic barrier seems to be natural because the discharge currents observed in the experiment cannot be explained by classical conductivity. At the same time, there are reasons for the excitation of oscillations. For $\bar{H} \approx (1/2)H_b \sim 0.005$ T, a voltage drop across the barrier of ~60 V, and a barrier thickness of 3 cm, the electron drift velocity in the barrier can be estimated as $v_D = 4\times10^7$ cm/s. This value does not exceed the thermal electron velocity $v_{Te} \sim 2\times10^8$ cm/s (at $T_e \approx 10$ eV) in the confinement system. Under these conditions, the electron distribution over transverse (with respect to the magnetic field) velocities is nonequilibrium and a group of electrons with the transverse

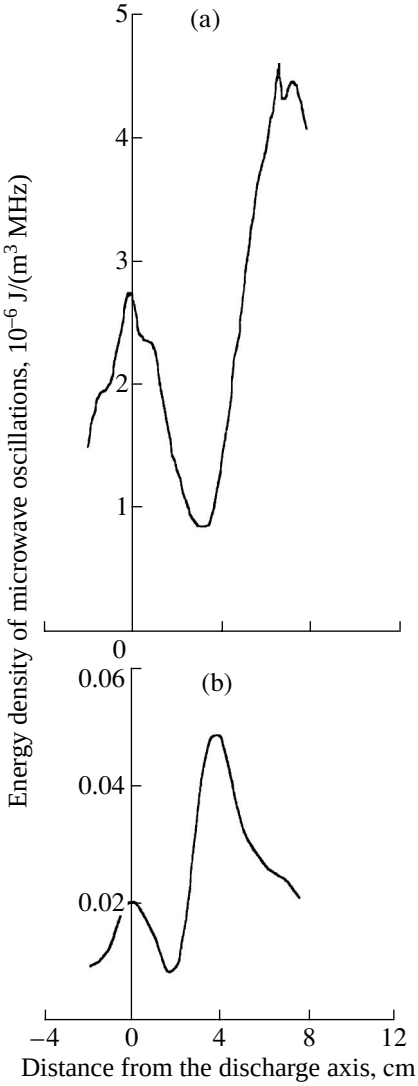

Fig. 7. Distribution of the energy density of microwave oscillations over the transverse plasma cross section for frequencies of (a) 3 and (b) 4 GHz at an argon flow rate of 3 cm^3/s, a voltage of 200 V, and a magnetic field of 5×10^{-3} T.

velocities $v_{e\perp} > v_{Te}$ is formed in the magnetic barrier region. This velocity is determined by the potential drop across the magnetic barrier; for typical values of the electric potential in Fig. 1c, this velocity is above 5×10^8 cm/s, which substantially exceeds the velocity of the electrons produced in the plasma volume due to gas ionization. The frequencies and wavenumbers of the plasma oscillations excited in the barrier region satisfy the condition [9] $\omega \approx \omega_{Pe} > \omega_{Be}$ and $k_\perp \rho_{Be} > 1$, where ω_{Be} is the electron Larmor frequency and $\rho_{Be} = v_{e\perp}/\omega_{Be}$. The role of electron gyration reduces to the generation of oscillations with $\omega \approx n\omega_{Be}$ (where n is the number of the harmonic of the electron Larmor frequency ω_{Be}) and $k_\perp v_{e\perp} \approx \omega_{Pe}$. In this case, the wavelength of longitudinal microwave oscillations providing the penetration of electrons through the magnetic barrier does not exceed the Larmor radius in order of magnitude. Evidently, for $\omega_{Pe} \gg \omega_{Be}$, a continuous spectrum of microwave oscillations can be formed in the frequency range $\sim\omega_{Pe}$; in fact, such a spectrum was observed in spectral measurements of the microwave oscillation intensity (Fig. 2). We note that similar effects were observed during the onset of high-frequency instabilities in a plasma with an accelerating layer [10, 11]. At present, the interpretation of our experimental results is hindered because a microwave oscillation theory incorporating a number of important factors governing the onset of instability (such as the nonuniform distribution of the plasma parameters, the ionization of the working gas, and the saturation of the amplitude of the excited oscillations in the barrier region) is still lacking. Such a theory is necessary for evaluating the turbulent plasma conductivity caused by anomalous transverse electron mobility. Special studies are also required to perform a comprehensive analysis of oscillations in the magnetic barrier.

(v) The microwave power in the plasma volume defined as

$$P_{\mathrm{MW}} = \int (E_{\mathrm{pl}}^2/8\pi)\, v_{Te}\sqrt{\varepsilon(\omega)}\, dS, \qquad (5)$$

can be evaluated from the probe measurements of the electric field strength E_{pl} taking into account the group velocity of the plasma wave $v_{Te}\sqrt{\varepsilon(\omega)}$ in the frequency range $\omega \approx \omega_{Pe}$, in which $|\varepsilon(\omega)| \approx \nu_{\mathrm{eff}}/\omega_{Pe}$, where ν_{eff} is the effective electron collision frequency and integration is performed over the magnetic barrier surface. One should keep in mind that a two-wire probe with an interwire distance of Δl = 1–1.5 mm, which substantially exceeds r_{D}, measures the average magnitude of the microwave field in the plasma. Nevertheless, if we take the mean-square value of the electric field measured directly by the probe, then, for an argon discharge at a current of 4.3 A, voltage of 200 V, magnetic field of 0.005 T, and gas flow rate of 3 cm^3/s, the power is estimated as $P_{\mathrm{MW}} \approx$ 100–500 W, which is a very high value, comparable with the discharge power.

ACKNOWLEDGMENTS

We thank V.A. Nevrovskiĭ, V.L. Zarembo, and A.A. Pushkin for fruitful discussions and assistance in experiments. This study was supported by the Ministry of Atomic Energy of the Russian Federation.

REFERENCES

1. A. I. Morozov, A. I. Bugrova, A. M. Bishaev, and V. A. Nevrovskiĭ, Pis'ma Zh. Tekh. Fiz. **25** (17), 57 (1999) [Tech. Phys. Lett. **25**, 700 (1999)].
2. A. I. Morozov, V. A. Nevrovskiĭ, V. K. Kharchevnikov, *et al.*, in *Proceedings of the XXVI Zvenigorod Conference on Plasma Physics and Controlled Nuclear Fusion, Zvenigorod, 1999*, Abstracts of Papers, p. 38.
3. T. Ohkava and M. Yoshikava, Phys. Rev. Lett. **17**, 685 (1996).
4. A. I. Morozov, A. I. Bugrova, A. M. Bishaev, *et al.*, in *Proceedings of the XXVI Zvenigorod Conference on Plasma Physics and Controlled Nuclear Fusion, Zvenigorod, 1999*, Abstracts of Papers, p. 37.
5. A. M. Bishaev, A. I. Bugrova, K. P. Kirdyashev, *et al.*, in *Proceedings of the XXVII Zvenigorod Conference on Plasma Physics and Controlled Nuclear Fusion, Zvenigorod, 2000*, Abstracts of Papers, p. 62.
6. K. P. Kirdyashev, in *High-Frequency Wave Processes in Plasmadynamic Systems* (Énergoatomizdat, Moscow, 1982), p. 142.
7. *Radiation Processes in Plasmas*, Ed. by G. Bekefi (Wiley, New York, 1966; Mir, Moscow, 1971).
8. A. G. Sitenko, *Electromagnetic Fluctuations in Plasma* (Kharkovskiĭ Univ., Kharkov, 1965; Academic, New York, 1967).
9. A. V. Timofeev and V. I. Pistunovich, in *Reviews of Plasma Physics*, Ed. by M. A. Leontovich (Atomizdat, Moscow, 1967; Consultants Bureau, New York, 1970), Vol. 5.
10. A. A. Kalmykov, in *Physics and Applications of Plasma Accelerations*, Ed. by A. I. Morozov (Nauka i Tekhnika, Minsk, 1974), p. 48.
11. V. I. Aref'ev and K. P. Kirdyashev, Zh. Tekh. Fiz. **45**, 527 (1975) [Sov. Phys. Tech. Phys. **20**, 330 (1975)].

Translated by N. F. Larionova

Plasma Physics Reports, Vol. 27, No. 7, 2001, pp. 591–597. Translated from Fizika Plazmy, Vol. 27, No. 7, 2001, pp. 630–636.

PLASMA OSCILLATIONS AND WAVES

Reduced MHD Equations with Allowance for Slow Magnetosonic Waves

V. P. Zhukov

Institute of Computational Technologies, Siberian Division, Russian Academy of Sciences, pr. akademika Lavrent'eva 6, Novosibirsk, 630090 Russia

e-mail: mife@net.ict.nsc.su

Received February 28, 2000; in final form, October 24, 2000

Abstract—The so-called reduced magnetohydrodynamics, which deals with the motion of incompressible fluids and is usually applied to describe plasma flows in a strong toroidal magnetic field, has a number of drawbacks and, in some cases, fails to produce correct results. The equations proposed here are simpler than the original MHD equations and are free of these drawbacks. These equations, like reduced MHD equations, make it possible to remove from consideration fast magnetosonic waves and to introduce the vector potential for the poloidal magnetic field. However, our equations differ from the reduced MHD equations in that they completely incorporate slow magnetosonic waves, the specific features of the toroidal geometry, and the effects of the toroidal velocity. © *2001 MAIK "Nauka/Interperiodica".*

1. INTRODUCTION

Many problems in plasma physics deal with configurations in which the magnetic field component in a certain direction (the toroidal component) is much larger than the component in the transverse direction (the poloidal component), whereas the longitudinal gradients of all the quantities are much lower than the transverse gradients. Such plasma configurations are characteristic of, e.g., tokamaks, and the plasma flows in them are successfully described by a simplified (reduced) set of MHD equations (i.e., RMHD equations), which are derived by the method of expansion in the large parameter R—the toroidal-to-poloidal magnetic field ratio [1]. The expansion is carried out in such a way that RMHD equations describe the plasma as an incompressible medium. As a result, fast magnetosonic (FMS) waves associated with the compression of the toroidal magnetic field are excluded from consideration and the configurations in question become simpler to analyze both analytically and numerically. However, the RMHD equations have some disadvantages. For example, under the assumption that the plasma is incompressible, they eliminate from consideration not only FMS waves but also slow magnetosonic (SMS) waves. For the tokamak plasma configurations under discussion, the speed of SMS waves is lower than the speed of FMS waves by a factor of R^2. Consequently, the time interval over which the RMHD model can be applied is bounded both from below and from above: $1 \ll t \leq R$. Thus, the problem of the onset of a tearing mode and its subsequent relaxation in a tokamak plasma was considered in [2] by using unreduced two-dimensional MHD equations. The calculations carried out in [2] show that, during magnetic reconnection, the plasma can be assumed with high accuracy to be incompressible. In contrast, in the relaxation stage, the dimensionless amplitude of the density oscillations in the absence of heat conduction is comparable to unity, whereas, in the presence of heat conduction, the oscillation amplitude is much smaller. In a real tokamak plasma, the longitudinal thermal conductivity is high enough for the plasma density to oscillate only slightly in both reconnection and relaxation stages. However, these results show that special care is needed in using RMHD equations. Note that, regardless of the value of the thermal conductivity, the magnetic reconnection stage is fairly well described by the RMHD model. Presumably, this circumstance is attributed to a combination of two factors: first, the duration of the reconnection stage is much shorter than that of the relaxation stage, and, second, in the reconnection stage, the poloidal magnetic field decreases substantially in the region in which the plasma motion is most intense. Consequently, the toroidal-to-poloidal magnetic field ratio R increases with time, so that the applicability condition $t \leq R$ for the RMHD model is increasingly well satisfied, although the time t increases. In the relaxation stage, the poloidal magnetic field gradually increases in time due to the diffusion of the magnetic flux from the peripheral region.

Another drawback of RMHD equations is that they do not incorporate the effects of the toroidal plasma flow velocity. Thus, the problem of ergodic divertors, which is important from a practical standpoint, deals with the following situation [3]. Let a magnetic field perturbation running along the toroidal axis of the torus be specified in the form $f(\varphi)\cos(m\varphi + n(z - V_p t)/R)$ at the tokamak wall. Here, $m = 12$, $n = 4$, z is the toroidal coordinate, φ is the poloidal angle, R is the aspect ratio

1063-780X/01/2707-0591$21.00

of a tokamak (the major radius divided by the minor radius), V_p is the phase velocity, and the rectangular function $f(\varphi)$ is assumed to be nonzero within a finite interval along the φ-direction. Since the plasma thermal conductivity is high, even perturbations with a low phase velocity V_p cannot penetrate into a plasma for a large distance because of the skin effect. However, the plasma velocity may reach the phase velocity and thus cancel the effect of V_p, in which case the toroidal plasma velocity $V_z \sim V_p$ can be low enough for all of the applicability conditions for the RMHD model to be satisfied. However, an important small parameter in this problem is the ratio $(V_z - V_p)/\nu$ (where $\nu \ll 1$ is the magnetic viscosity) rather than V_z. Incorporating the toroidal plasma velocity into the RMHD equations requires additional effort.

Furthermore, the RMHD model is difficult to generalize to the case of nonplanar geometry.

In a number of papers (see, e.g., [4–8]), efforts were made to refine the RMHD model by taking into account corrections associated with the toroidal geometry, toroidal plasma velocity, etc. However, the refinements turned out to be insufficiently systematic. Thus, in [4–8], the toroidicity-induced corrections were taken into account by expanding the equilibrium solution and metric tensor in powers of R^{-1}. In [5–8], the toroidal plasma velocity was accounted for as follows. In contrast to [1] and the present paper, in which the plasma pressure is assumed to be $p \sim R^{-2}$, the authors of [5–8] treated the case of higher pressures, $p \sim R^{-1}$. In this case, the reduced equations can only be derived by calculating the plasma pressure, which, in turn, requires calculation of the toroidal plasma velocity. In deriving the remaining equations, the toroidal velocity is neglected. Thus, in [4–8], the plasma was assumed to be incompressible, so that SMS waves were ignored. With this approach, the MHD equations and the RMHD equations have different steady solutions.

Here, we derive RMHD equations that are free of these drawbacks. For some problems, the applicability range of the proposed RMHD equations is extended to time scales characteristic of SMS waves, $t \le R^2$, and, therefore, is wider than that for the conventional RMHD model.

The equations proposed are very similar in structure to the ideal MHD equations obtained by Pastukhov [9], who used a method that differs radically from those adopted here and in [1, 4–8, 10–12]. The equations derived by Pastukhov [9] contain terms whose order is higher than that required by the expansion method utilized here. Nevertheless, this circumstance yields no additional errors in integrating the equations of [9] over time intervals that are as long as $t \gg R^2$. However, the generalization of Pastukhov's results to systems with dissipation is a complicated task.

The structure of the paper is as follows. First, we consider a simple example in order to illustrate the role of SMS waves. Then, we derive equations that incorporate both SMS waves and the toroidal plasma velocity. The equations proposed here, like RMHD equations, make it possible to introduce the vector potential for the poloidal magnetic field and to exclude from consideration FMS waves, thereby becoming easier to investigate analytically and to integrate numerically. In addition, they completely take into account corrections introduced by the toroidal geometry. As a result, the MHD equations and the proposed equations have the same steady solutions. The results obtained are summarized in the Conclusion.

Note that, in this study, the effects associated with the electron dynamics are neglected, which reduces the applicability range of the proposed equations. The derivation of MHD equations with allowance for the electron dynamics in an arbitrarily strong magnetic field is a separate task [8, 10–12].

2. THE ROLE OF SMS WAVES

As was noted above, the RMHD equations apply to an incompressible plasma and are thus incapable of incorporating SMS waves. That is why the applicability range of the RMHD model is, strictly speaking, limited to time scales $t \le R$. Let us discuss this point in more detail. For simplicity, we restrict ourselves to a two-dimensional ($\partial/\partial z = 0$) problem and start with the one-fluid MHD equations written in a standard dimensionless form [2, 4–9, 13]. We also represent the toroidal magnetic field as $H_z = 1 + h_z$.

We consider a very slow plasma motion such that the poloidal velocity $\mathbf{V}$ and the partial time derivative $\partial/\partial t$ are both on the order of R^{-2}. As in the RMHD model, we assume that the poloidal magnetic field is $\mathbf{H} \sim R^{-1}$ and the term h_z and pressure p are both on the order of R^{-2}. In order to apply the above expansion method, we must also require that the toroidal plasma velocity be $V_z \sim R^{-1}$. Recall that the RMHD equations are valid under the conditions $V_z \sim R^{-2}$ and $\mathbf{V}, \partial/\partial t \sim R^{-1}$.

As a result, we arrive at the equations

$$\begin{gathered}
\partial A/\partial t + (\mathbf{V}\cdot\nabla)A = 0, \\
\nabla\cdot\mathbf{V} = (\mathbf{H}\cdot\nabla)V_z, \\
\nabla(p + h_z) + \Delta A \nabla A = 0, \\
\rho(\partial V_z/\partial t + (\mathbf{V}\cdot\nabla)V_z) = (\mathbf{H}\cdot\nabla)h_x, \\
\partial p/\partial t + (\mathbf{V}\cdot\nabla)p = -\gamma p\,\nabla\cdot\mathbf{V} + (\gamma-1)\chi\Delta T, \\
\partial\rho/\partial t + (\mathbf{V}\cdot\nabla)\rho = -\rho\nabla\cdot\mathbf{V}.
\end{gathered} \tag{1}$$

Here, γ is the adiabatic index, χ is the thermal conductivity, ρ is the plasma density, and A is the vector

potential of the magnetic field. Accordingly, we have $(\mathbf{H}\cdot\nabla)A = 0$. From Eqs. (1), we can readily obtain

$$dp/dt = -\gamma p(\mathbf{H}\cdot\nabla)V_z + (\gamma-1)\chi\Delta T,$$
$$\rho dV_z/dt = -(\mathbf{H}\cdot\nabla)p,$$

where $d/dt = \partial/\partial t + (\mathbf{V}\cdot\nabla)$. Analyzing these two equations, we can easily draw the following conclusions. (i) The perturbations propagate at the velocity $(\gamma pH^2/\rho)^{1/2}$, which corresponds to the speed of SMS waves in the limit of a strong toroidal magnetic field [14]. (ii) If, at the start time, the spatial variations δp of the plasma pressure are on the order of p, then, for $\chi = 0$, the toroidal plasma velocity V_z is on the order of $O(R^{-1}) \gg V \sim O(R^{-2})$ and, by virtue of the adiabaticity of the plasma motion, the plasma density variations are on the order of $\delta p/p \sim 1$. Note that, at the start time, the plasma density can be uniform and the plasma itself can move exclusively in the poloidal direction, $V_z = 0$.

In the problem treated in [2], the plasma density and toroidal plasma velocity were found to behave in essentially the same manner.

3. "SLOW" MHD MODEL

Now, we derive RMHD equations that incorporate SMS waves. We introduce a coordinate system in which the length element is equal to $dl^2 = dr^2 + r^2d\varphi^2 + g^2(r, \varphi)dz^2$. In toroidal geometry, we have $g = 1 + (r/R)\cos\varphi$. To be specific, we consider a plasma bounded by the surface $r = 1$.

Henceforth, unless otherwise stated, we will denote the poloidal plasma velocity and poloidal magnetic field by $\mathbf{V}$ and $\mathbf{H}$, respectively. We represent the toroidal magnetic field H_z in the form $H_z = \langle H_z\rangle g^{-1}/\langle g^{-1}\rangle + h_z$, where $\langle f(z,t)\rangle = \pi^{-1}\int_0^1 rdr\int_0^{2\pi} d\varphi f(r, \varphi, z, t)$ is the value of a function f averaged over the cross section z = const.

For the quantities under consideration, we impose the following order of smallness:

$$O(1): \nabla, \rho,$$
$$O(R^{-1}): \partial/\partial z, \partial/\partial t, \mathbf{H}, \mathbf{V}, V_z, \quad (2)$$
$$O(R^{-2}): h_z, p.$$

The equations to be derived are also valid when V_z is on the order of R^{-1} but $\partial/\partial t$ and $\mathbf{V}$ are both proportional to R^{-2}.

For simplicity, we assume that the plasma viscosity ν and magnetic viscosity η are both constant. For the expansion method to be correct, we must require that ν, η, and ∇g be smaller than or on the order of R^{-1}.

The accuracies of calculating the quantities under consideration are as follows:

$$O(R^{-2}): \mathbf{H}, \mathbf{V}, p,$$
$$O(R^{-1}): \langle H_z\rangle, V_z, \rho. \quad (3)$$

We consider the equations for the magnetic field. When these equations are written in their most general form, we can neglect only the term $\partial h_z/\partial t$, in which case, with accuracies (3), we obtain

$$\frac{1}{r}\frac{\partial E_r}{\partial\varphi} - \frac{1}{r}\frac{\partial(rE_\varphi)}{\partial r} = \frac{g^{-1}}{\langle g^{-1}\rangle}\frac{\partial\langle H_z\rangle}{\partial t}, \quad (4)$$

$$\frac{\partial H_r}{\partial t} = \frac{1}{g}\frac{\partial E_\varphi}{\partial z} - \frac{1}{gr}\frac{\partial(gE_z)}{\partial\varphi}, \quad (5)$$

$$\frac{\partial H_\varphi}{\partial t} = \frac{1}{g}\frac{\partial(gE_z)}{\partial r} - \frac{1}{g}\frac{\partial E_r}{\partial z}, \quad (6)$$

where $\mathbf{E} = -\mathbf{V}\times\mathbf{H} + \nu\nabla\times\mathbf{H}$ is the electric field.

To the desired accuracy, the averaged toroidal magnetic field $\langle H_z\rangle$ can be found from the solvability condition for Eq. (4):

$$\frac{\partial\langle H_z\rangle}{\partial t} = -\frac{1}{\pi}\int_0^{2\pi} E_\varphi d\varphi. \quad (7)$$

Although the derivative $\partial\langle H_z\rangle/\partial t$ may be very small, it is of fundamental importance to take it into account in order for the equations to be solvable. In addition, even for small $\partial\langle H_z\rangle/\partial t$, the averaged toroidal magnetic field $\langle H_z\rangle$ can change substantially on sufficiently long time scales.

Equations (4)–(6) imply that the vector potential for the components H_r and H_φ can be introduced under the condition $\partial^2\langle H_z\rangle/\partial t\partial z = 0$, which is satisfied for a wide range of problems. However, even if this condition fails to hold, the fact that $\langle H_z\rangle$ is independent of r and φ makes the equations for the magnetic field far easier to solve numerically. Actually, the function G, which enters the expressions

$$H_r = (gr)^{-1}\partial(gA)/\partial\varphi - \frac{\partial G}{\partial r}\frac{\partial\langle H_z\rangle}{\partial z},$$

$$H_\varphi = -g^{-1}\partial(gA)/\partial r - \frac{1}{r}\frac{\partial G}{\partial\varphi}\frac{\partial\langle H_z\rangle}{\partial z},$$

and depends only on r and φ, satisfies the simple equation

$$\frac{1}{r}\frac{\partial}{\partial r}\left(rg\frac{\partial G}{\partial r}\right) + \frac{1}{r^2}\frac{\partial}{\partial\varphi}\left(g\frac{\partial G}{\partial\varphi}\right) = \frac{g^{-1}}{\langle g^{-1}\rangle}.$$

Equations (4)–(7) supplemented with unreduced equations for the plasma velocity, plasma pressure, and magnetic field (see below) constitute a closed set of

equations and make it possible to exclude FMS waves from consideration, to take into account the toroidal plasma velocity V_z, and to incorporate all of the properties associated with the toroidal geometry. This set of equations possesses the energy conservation law in terms of the specific energy density

$$(\langle H_z\rangle g^{-1}/\langle g^{-1}\rangle)^2/2 + \rho(\mathbf{V}^2 + V_z^2)/2 + \mathbf{H}^2/2 + p/(\gamma - 1).$$

Let us make an important remark concerning the values of transport coefficients and the condition $\mathbf{\nabla} \sim 1$. In some problems (e.g., magnetic reconnection problems), small transport coefficients can give rise to regions (current sheets) in which the gradients of the quantities are large ($\mathbf{\nabla} \gg 1$) and, accordingly, the order of smallness (2) is violated. The situation with $\mathbf{\nabla} \gg 1$ renders the justification of the solutions obtained especially difficult, because, in this case, the terms with large gradients and small coefficients may be large. Note that the same difficulty arises in deriving RMHD equations.

However, Eqs. (4)–(7) also apply to the case with large gradients. In fact, when deriving Eqs. (4)–(7), we neglected only the term $\partial h_z/\partial t$. Let us analyze whether this term can be omitted in the equations describing a plasma with a current sheet of thickness $l \ll 1$. By virtue of the force balance relation and the conditions $V \le R^{-1}$ and $\partial/\partial t \le R^{-1}$, the quantity h_z is on the order of R^{-2}. These conditions may fail to hold for singular current sheets with $\nu = 0$ and thus should be controlled when deriving the solution. For resistive current sheets, the conditions of interest are satisfied. Accordingly, for $l \le 1$, the derivative $\partial h_z/\partial t \sim R^{-3}$ is much smaller than $\mathbf{\nabla} \cdot (\mathbf{V} \times \mathbf{H}) \sim R^{-1}/l$.

Since, for resistive current sheets, we have $l \sim \nu^{1/2}$, the term $\nu\Delta h_z \sim R^{-2}$ may also be larger than $\partial h_z/\partial t$. In addition, although the plasma flow velocity along the poloidal magnetic field in a current sheet can be as high as $V \sim H \sim R^{-1}$, we always have $\partial/\partial t \sim \nu^{1/2} \ll R^{-1}$, in which case we are even more justified in neglecting the term $\partial h_z/\partial t$. Note that the equations for the poloidal magnetic field cannot be simplified in a similar way, because all the terms in these equations are of the same order. Note also that, in the problems related to tokamak plasmas, the role of the poloidal magnetic field H is often played by the field $\mathbf{H}_* = \mathbf{H} - qH_\varphi\mathbf{e}_\varphi$, where q is a certain number. Since this field is much lower (in absolute value) than H, the effective value of R in these problems is larger.

Hence, we can conclude that there are problems in which the applicability range of the proposed equations is wider than $\mathbf{\nabla} \sim R^{-1}$.

The actual restrictions on the plasma conductivity are associated with the fact that the higher the conductivity, the smaller the thickness l of the current sheet. As a result, the ratio of the ion dispersion scale length to l can be large, so that it becomes necessary to take into account the electron dynamics (i.e., to pass over to the two-fluid MHD model). Consequently, in problems associated with magnetic reconnection in typical tokamak plasmas, the applicability of one-fluid RMHD equations is restricted to the peripheral regions of the plasma column, because the edge plasma temperature and, accordingly, the edge plasma conductivity are lower and the current sheets are thicker than those in the plasma interior. In problems in which the gradients are on the order of unity, the RMHD model under discussion also applies to the central region of the tokamak plasma. A discussion of the reduced two-fluid MHD models [8, 10–12] goes beyond the scope of this paper.

For $\partial^2\langle H_z\rangle/\partial t\partial z = 0$, the above set of MHD equations supplemented with Eq. (4) for H_z in principle satisfies all of the requirements mentioned in the introduction. For $\partial\langle H_z\rangle/\partial t = 0$, this set can be further simplified.

First, in the expressions for E_r and E_φ, the terms $\nu\mathbf{\nabla} \times \mathbf{H}$ can be neglected under the condition $l \gg \nu R^{-1}$, which follows from the estimates $\mathbf{V} \times \mathbf{H} \sim R^{-1}$ and $\nu\mathbf{\nabla} \times \mathbf{H} \sim \nu R^{-2}/l$ for the corresponding vector components. In the presence of resistive current sheets, we have $l \le \nu^{1/2}$, so that this condition is satisfied by an ample margin.

With the above analysis in mind, we can introduce the function Φ such that

$$H_zV_r - H_rV_z = \frac{1}{r}\frac{\partial\Phi}{\partial\varphi}, \quad H_zV_\varphi - H_\varphi V_z = -\frac{\partial\Phi}{\partial r}, \quad (8)$$

in which case Eqs. (4)–(6) can be rewritten as

$$\frac{\partial}{\partial r}(r(H_zV_r - H_rV_z)) + \frac{\partial}{\partial\varphi}(H_zV_\varphi - H_\varphi V_z) = 0, \quad (9)$$

$$\frac{\partial A}{\partial t} + V_r\frac{1}{g}\frac{\partial(gA)}{\partial r} + V_\varphi\frac{1}{gr}\frac{\partial(gA)}{\partial\varphi} = \frac{1}{g}\frac{\partial\Phi}{\partial z} + \nu\Delta_* A, \quad (10)$$

$$\Delta_* A = \left(\frac{1}{r}\frac{\partial}{\partial r}\left(\frac{r}{g}\frac{\partial(gA)}{\partial r}\right) + \frac{1}{r^2}\frac{\partial}{\partial\varphi}\left(\frac{1}{g}\frac{\partial(gA)}{\partial\varphi}\right)\right), \quad (11)$$

and Eq. (10) becomes

$$\partial A/\partial t = H_z^{-1}(\mathbf{H} \cdot \mathbf{\nabla}\Phi) + \nu\Delta_* A. \quad (12)$$

Here, the three-dimensional operator $(\mathbf{H}\mathbf{\nabla})$ has the form

$$\mathbf{H} \cdot \mathbf{\nabla} = H_r\frac{\partial}{\partial r} + H_\varphi\frac{1}{r}\frac{\partial}{\partial\varphi} + H_z\frac{1}{g}\frac{\partial}{\partial z}.$$

Note that there is no need to simplify the equations for the plasma velocity components. However, in order to ensure the accuracy (3), it is sufficient to calculate p and H_z to within an error $O(R^{-2})$ for each term in the

equation for the poloidal plasma velocity, except for the terms

$$\nabla p^{(3)} + H_z g^{-1} \nabla (g H_z^{(3)}) - \nabla (\eta/3) \nabla \cdot \mathbf{V}$$

for which the plasma pressure $p^{(3)}$ and toroidal magnetic field $H_z^{(3)}$ should be calculated to a higher (third-order) accuracy, $O(R^{-3})$, as is indicated by the superscript $^{(3)}$. As a result, these terms can be rewritten as

$$\nabla p + H_z g^{-1} \nabla (g \tilde{H}_z) + O(R^{-4}),$$

where $\tilde{H}_z = H_z + (H_z^{(3)} - H_z) + (p^{(3)} - p) - \eta/3 \nabla \cdot \mathbf{V} + O(R^{-4})$. Since Eq. (9) and the condition $\nabla g \le O(R^{-1})$ imply that $\nabla \cdot \mathbf{V} \sim R^{-2}$, we have $\tilde{H}_z = H_z + O(R^{-3})$. For all of the remaining expressions and equations, it is sufficient to calculate the quantities H_z and p to second-order accuracy. Consequently, we can replace H_z with $\tilde{H}_z$ everywhere. The quantity $\tilde{H}_z$ can be found by simultaneously solving Eq. (9) and the equations for the plasma velocity components under the normalizing condition $\langle \tilde{H}_z \rangle = \langle H_z \rangle = \text{const}$. Below, for brevity, we will omit the tilde from $\tilde{H}_z$.

We neglect the derivatives with respect to z in viscous terms in the equations for the plasma velocity. As a result, the equations become

$$\rho\left(\frac{\partial V_z}{\partial t} + (\mathbf{V} \cdot \nabla) V_z + \frac{V_r V_z}{g} \frac{\partial g}{\partial r} + \frac{V_\varphi V_z}{g r} \frac{\partial g}{\partial \varphi}\right) = -\frac{1}{g} \frac{\partial (p + H_r^2/2 + H_\varphi^2/2)}{\partial z} + H_r \frac{1}{g} \frac{\partial (g H_z)}{\partial r} + H_\varphi \frac{1}{r g} \frac{\partial (g H_z)}{\partial \varphi} + \eta \Delta_* V_z, \quad (13)$$

$$\rho\left(\frac{\partial V_r}{\partial t} + (\mathbf{V} \cdot \nabla) V_r - \frac{V_\varphi^2}{r}\right) = F_r, \quad (14)$$

$$\rho\left(\frac{\partial V_\varphi}{\partial t} + (\mathbf{V} \cdot \nabla) V_\varphi + \frac{V_r V_\varphi}{r}\right) = F_\varphi. \quad (15)$$

Here,

$$\mathbf{V} \cdot \nabla = V_r \frac{\partial}{\partial r} + V_\varphi \frac{1}{r} \frac{\partial}{\partial \varphi} + V_z \frac{1}{g} \frac{\partial}{\partial z}$$

and the vector $\mathbf{F} = (F_r, F_\varphi)$ has the form

$$\mathbf{F} = \rho V_z^2 g^{-1} \nabla g + \eta \Delta_\perp \mathbf{V} - \nabla p - (\Delta_* A) g^{-1} \nabla (g A) + H_z g^{-1} \partial \mathbf{H}/\partial z - H_z g^{-1} \nabla (g H_z), \quad (16)$$

where

$$(\Delta_\perp \mathbf{V})_r = \frac{\partial}{\partial r}\left(\frac{1}{r g} \frac{\partial (r g V_r)}{\partial r}\right) + \frac{1}{r g} \frac{\partial}{\partial \varphi}\left(\frac{g}{r} \frac{\partial V_r}{\partial \varphi}\right) - \frac{1}{r g} \frac{\partial}{\partial \varphi}\left(\frac{g}{r} \frac{\partial (r V_\varphi)}{\partial r}\right) + \frac{\partial}{\partial r}\left(\frac{1}{r g} \frac{\partial (g V_\varphi)}{\partial \varphi}\right),$$

$$(\Delta_\perp \mathbf{V})_\varphi = \frac{1}{g} \frac{\partial}{\partial r}\left(\frac{g}{r} \frac{\partial (r V_\varphi)}{\partial r}\right) + \frac{1}{r^2} \frac{\partial}{\partial \varphi}\left(\frac{1}{g} \frac{\partial (g V_\varphi)}{\partial \varphi}\right) + \frac{1}{r^2} \frac{\partial}{\partial \varphi}\left(\frac{1}{g} \frac{\partial (r g V_r)}{\partial r}\right) - \frac{1}{g} \frac{\partial}{\partial r}\left(\frac{g}{r} \frac{\partial V_r}{\partial \varphi}\right).$$

By virtue of Eq. (9), we can assume that the plasma heating due to the work done by viscous forces in displacing the plasma as a solid dominates over the plasma heating due to compression. Under this assumption, we can omit the term $(\eta/3)(\mathrm{div}\,\mathbf{V})^2$ in the equation for the plasma pressure. Since the variation of the toroidal magnetic field H_z is smaller than the poloidal magnetic field by a factor of R, we can also neglect plasma heating by the poloidal current. These simplifications are allowed by the orders of smallness (2) and (3). As a result, we arrive at the following equation for the plasma pressure p:

$$\frac{1}{\gamma - 1}(\partial p/\partial t + \nabla \cdot (\mathbf{V} p)) = -p \nabla \cdot \mathbf{V} + \nu (\Delta_* A)^2 + \eta Q,$$

$$Q = \left(\frac{1}{g} \frac{\partial (g V_z)}{\partial r}\right)^2 + \left(\frac{1}{g r} \frac{\partial (g V_z)}{\partial \varphi}\right)^2 + \left(\frac{1}{r} \frac{\partial (r V_\varphi)}{\partial r} - \frac{1}{r} \frac{\partial V_r}{\partial \varphi}\right)^2 + \left(\frac{1}{g r} \frac{\partial (r g V_r)}{\partial r} + \frac{1}{g r} \frac{\partial (g V_\varphi)}{\partial \varphi}\right)^2. \quad (17)$$

The equation for the plasma density has the form

$$\partial \rho/\partial t + \nabla \cdot (\mathbf{V} \rho) = 0. \quad (18)$$

In Eqs. (17) and (18), the div operator is the conventional three-dimensional operator

$$\nabla \cdot \mathbf{V} = \frac{1}{r g}\left(\frac{\partial (r g V_r)}{\partial r} + \frac{\partial (g V_\varphi)}{\partial \varphi}\right) + \frac{1}{g} \frac{\partial V_z}{\partial z}.$$

The set of equations (8)–(18), which may be referred to as "slow" MHD (SMHD) equations, possesses the energy conservation law in terms of the specific energy density

$$\rho(\mathbf{V}^2 + V_z^2)/2 + \mathbf{H}^2/2 + p/(\gamma - 1).$$

Note that the SMHD equations differ from the complete set of MHD equations in that, first, they do not contain the terms $\partial h_z/\partial t$, νj_r, and νj_φ or the related heating terms and, second, the equations of motion do not include the term $\nabla(\eta/3)\nabla \cdot \mathbf{V}$. However, by virtue of Eq. (9), the last term enters the expression for $\tilde{H}_z$, thereby making no contribution to the plasma flow velocity. Also, in the SMHD model, the terms with $\partial/\partial z$

in the expression for the viscous force are discarded. In contrast to the RMHD model, the method used here to derive SMHD equations from the complete set of MHD equations assumes no expansion of the purely geometrical terms in the large parameter R, thereby making it possible to completely incorporate the features of a realistic toroidal geometry. In addition, the basic MHD equations and the proposed SMHD equations possess the same steady-state solutions.

SMHD equations possess the properties of both RMHD equations and Eqs. (1) for SMS waves. Linear analysis shows that the SMHD model correctly incorporates all types of waves except for the highest frequency waves, i.e., those whose dimensionless frequencies are on the order of unity. The applicability range of both SMHD and RMHD equations is restricted to time scales no longer than $t \le R$. However, for problems with the parameter ordering $V_z \sim R^{-1}$ and $\mathbf{V}$, $\partial/\partial t \sim R^{-2}$, the SMHD equations are applicable on longer time scales: $t \le R^2$. Among such problems, we can mention, e.g., the problem of the relaxation to a new quasi-equilibrium magnetic configuration after the magnetic reconnection stage during the development of tearing modes in tokamaks [2]. Since SMS waves are more completely described by SMHD equations than RMHD equations, we may hope that, on long time scales, the SMHD model will be better suited than the RMHD model for solving problems with the parameter ordering $\mathbf{V}$, $\partial/\partial t \sim R^{-1}$.

A drawback of the SMHD model is that, in the dissipationless limit, the helicity $S = \mathbf{H} \cdot \mathbf{V} + H_z V_z$ is not conserved. In addition, if Eq. (9) is treated as an external constraint on the possible plasma flow velocity, then the equation $\partial H_z/\partial t = (\nabla \times [\mathbf{V} \times \mathbf{H}])_z$ fails to hold, thereby indicating the presence of a magnetic charge.

These drawbacks can be overcome by replacing the quantity H_z in all of the SMHD equations with a time-independent quantity H_{z0}, which differs from H_z by an amount on the order of $O(R^{-2})$. The only exception is the term $\nabla(gH_z)$ in Eq. (13) for the poloidal velocity and the term $\mathbf{H} \cdot \nabla(gH_z)$ in Eq. (16) for the toroidal velocity. The replacement of H_z by H_{z0} is consistent with the above method of expansion. The equations resulting from this replacement will be referred to as SMHD1 equations.

One can readily see that, in the SMHD1 model, the energy and (in the dissipationless limit) the helicity $S = \mathbf{H} \cdot \mathbf{V} + H_{z0} V_z$ are both conserved.

We can introduce an analogue of the z-component of the vorticity, $\Omega = (\nabla \times (g\rho H_{z0}^{-1} \mathbf{V}))_z$. In the dissipationless limit, the H_z-independent equations for S and Ω and the remaining equations, which are also independent of H_z, make it possible to determine all of the desired quantities without recourse to the basic equations for the plasma flow velocity.

Since the SMHD1 equations for the helicity and vorticity are independent of H_z, we can treat the vector $\mathbf{B} = (H_r, H_\varphi, H_{z0})$ as a new magnetic field, which satisfies the equation $\partial \mathbf{B}/\partial t = \nabla \times [\mathbf{V} \times \mathbf{B}]$.

If the quantity H_{z0} is chosen to be the initial distribution of H_z, then the steady solutions of the basic MHD equations are steady solutions to the SMHD1 equations. However, with this choice, the SMHD1 model contains a special parameter—the initial distribution of H_z. This situation seems unnatural. If the quantity H_{z0} is chosen to be $\langle H_z \rangle g^{-1}/\langle g^{-1} \rangle$, the SMHD1 model does not include any special parameter, but the steady solutions of the SMHD1 equations coincide with the steady solutions to the basic MHD equations only when $H_z(t = 0) = \langle H_z \rangle g^{-1}/\langle g^{-1} \rangle$.

Although the SMHD1 equations are very similar in structure to the equations obtained by Pastukhov [9], they are not identical. Note that it is a nontrivial task to generalize the results obtained in [9] to systems with dissipation.

Generally, the SMHD model is applicable to perturbations propagating with the phase velocity V_p in the frequency range bounded from above by frequencies on the order of R^{-1}; i.e., we have $V_p < O(R^{-1})$. For practical applications, this condition is, in principle, satisfied quite well.

However, the phase velocity V_p of the waves that run in the z-direction satisfies a less restrictive condition. An important point here is that, for running waves, we can pass over to the variable $Z = z - V_p t$ in the basic MHD equations, in which we must also make the replacement $\partial/\partial t = \partial/\partial t - V_p \partial/\partial Z$. When the vector potential for the poloidal magnetic field can be introduced (it is this case that is of primary interest to us), we have $\partial \langle H_z \rangle/\partial Z \sim R^{-3}$ and the above method of expansion of the basic MHD equations (written in terms of the Z variable) in the large parameter R yields SMHD equations, in which we must also replace z with Z and $\partial/\partial t$ with $\partial/\partial t - V_p \partial/\partial Z$. The SMHD equations derived in this way turn out to be valid for $V_p \sim 1$, at least until the toroidal velocity V_z becomes of order unity. However, for $V_z \sim 1$, essentially all of the SMHD equations and expressions can be obtained to within terms of the first order in the expansion in the large parameter R. The only exception is the centrifugal force $\rho V_z^2 g^{-1} \nabla g$, which turns out to be on the order of R^{-1}. Such a strong centrifugal force either gives rise to intense poloidal plasma flows or changes the equilibrium conditions (in which all the forces become on the order of R^{-1}). In this case, it is impossible to construct SMHD equations. However, if the geometry of the problem is such that $\nabla g \sim R^{-2}$, then the SMHD model is always valid for $V_p \sim 1$.

Recall that, the toroidal plasma velocity V_z can only be incorporated into the RMHD equations to the next

(third) order in the expansion in R. Hence, it is very difficult to apply the RMHD model to describe the waves running in the z-direction, because, in this case, the RMHD equations are very involved.

For perturbations propagating with the velocity V_p in the φ direction, the SMHD and RMHD equations are both applicable in the range $V_p < O(R^{-1})$. However, under certain conditions, plasma flows with the velocity $V_p \sim 1$ may be quasi-one-dimensional and thus can be described by the SMHD and RMHD models. A discussion of this question, which is related to the characteristic features of a particular problem, goes beyond the scope of our paper.

4. CONCLUSION

Hence, the proposed SMHD equations (8)–(18) are a generalization of the RMHD equations. The SMHD model, like the RMHD model, possesses the energy conservation law and makes it possible to remove from consideration FMS waves and to introduce the vector potential for the poloidal magnetic field. On the other hand, the SMHD model offers the following advantages over the RMHD model. The SMHD equations incorporate SMS waves and thus are sometimes applicable on time scales up to $t \leq R^2$. They also take into account the effects of the toroidal plasma velocity and all of the specific features of the toroidal geometry. In addition, the basic MHD equations and the SMHD equations have the same steady solutions. Owing to these properties, the proposed equations are convenient to analyze, especially numerically.

A drawback of the SMHD equations is that, in the dissipationless limit, they do not pass over to the equations derived by Pastukhov [9], which are valid on time scales $t \gg R^2$ and have some other advantages. In this context, it should again be emphasized that the generalization of the results obtained in [9] to systems with dissipation is a nontrivial task.

REFERENCES

1. B. B. Kadomtsev and O. P. Pogutse, Zh. Éksp. Teor. Fiz. **65**, 575 (1973) [Sov. Phys. JETP **38**, 283 (1974)].
2. V. P. Zhukov and G. Fuchs, Fiz. Plazmy **24**, 996 (1998) [Plasma Phys. Rep. **24**, 929 (1998)].
3. *Dynamic Ergodic Divertor (DED) for TEXTOR-94*, Ed. by K. H. Finkel (IPP Euroatom-KFA, Juelich, 1996).
4. H. R. Strauss, Phys. Fluids **19**, 134 (1976).
5. H. R. Strauss, Nucl. Fusion **23**, 649 (1983).
6. H. R. Strauss, Phys. Fluids **20**, 1354 (1977).
7. R. Izzo, D. A. Monticello, W. Park, *et al.*, Phys. Fluids **26**, 2240 (1983).
8. R. D. Hazeltine, M. Kotshenrenther, and P. J. Morrison, Phys. Fluids **28**, 2466 (1985).
9. V. P. Pastukhov, Fiz. Plazmy **26**, 566 (2000) [Plasma Phys. Rep. **26**, 529 (2000)].
10. Xiogang Wang and A. Bhattacharjee, Phys. Plasmas **2**, 171 (1995).
11. R. D. Hazeltine, C. T. Hsu, and P. J. Morrison, Phys. Fluids **30**, 3204 (1987).
12. L. Zakharov and B. Rogers, Phys. Fluids B **4**, 3285 (1992).
13. K. V. Brushlinskiĭ, A. M. Zaborov, and S. I. Syrovatskiĭ, Fiz. Plazmy **6**, 297 (1980) [Sov. J. Plasma Phys. **6**, 165 (1980)].
14. L. D. Landau and E. M. Lifshitz, *Electrodynamics of Continuous Media* (Nauka, Moscow, 1982; Pergamon, New York, 1984).

Translated by I. A. Kalabalyk

Plasma Physics Reports, Vol. 27, No. 7, 2001, pp. 598–607. Translated from Fizika Plazmy, Vol. 27, No. 7, 2001, pp. 637–646.

PLASMA INSTABILITY

Suppression of the Current Instability by Decay Processes

B. Atamanyuk* and A. S. Volokitin**

**Institute of Fundamental Technological Research, Polish Academy of Science, Warsaw 00-049, Poland*

***Institute of Terrestrial Magnetism, the Ionosphere, and Radio Wave Propagation, Russian Academy of Sciences, Troitsk, Moscow oblast, 142092 Russia*

Received October 5, 2000; in final form, January 12, 2001

Abstract—A study is made of the instability of lower hybrid waves in an isothermal magnetized current-carrying plasma. It is assumed that the dynamic suppression of the current instability is associated with the excitation of a quasi-monochromatic wave near the instability threshold and its subsequent decay into two strongly damped lower hybrid waves. It is shown that the decay process results in the onset of either a quasi-periodic or stochastic nonlinear stabilization regime involving a small number of modes. The anomalous resistance is estimated. © *2001 MAIK "Nauka/Interperiodica".*

1. INTRODUCTION

The physical processes in laboratory plasmas often occur under weakly nonequilibrium conditions near the instability threshold. This is equally true for natural plasmas near the Earth and in space. There are two mechanisms for suppressing instability: the quasilinear relaxation of a plasma to an equilibrium state and the nonlinear conversion of the energy of unstable modes to the energy of damped modes. Slightly above the threshold, the number of damped modes remains finite, indicating the onset of either periodic nonlinear oscillations or plasma turbulence involving a small number of modes. The specific features of these stabilization regimes with a small number of modes require a separate analysis. Although this problem has been studied in many papers (see, e.g., [1–5]), some aspects are still unclear. Among them are the conditions and parameters for the onset of stochastic and periodic stabilization regimes.

Here, we consider the nonlinear suppression of the current instability by a three-wave decay process in an isothermal magnetized plasma. We assume that, slightly above the threshold, only one lower hybrid wave can be excited, which then decays into two other lower hybrid waves. We also assume that, near the threshold, the two decay waves are not amplified by an electric current and thus are strongly damped. As a result, the dynamic suppression of the instability stems from both the energy conversion from an unstable lower hybrid wave into the damped modes and the associated plasma heating. Our example not only illustrates the general situation but is also of practical interest for the study of natural processes in the ionospheric plasma.

2. CURRENT INSTABILITY OF LOWER HYBRID WAVES

We consider the instability of lower hybrid waves in a magnetized current-carrying plasma. It is well known [6] that, in a plasma in which the electron temperature does not differ greatly from the ion temperature, $T_e < (3–4)T_i$, and the drift velocity v_d of the electrons is lower than their thermal velocity v_{Te}, $v_d < 0.8v_{Te}$, the ion acoustic waves are strongly damped and there exist only electrostatic ($c^2k^2 \gg \omega_p^2$) lower hybrid waves described by the dispersion relation

$$\omega_k^2 \simeq \frac{\omega_e^2\omega_p^2}{\omega_p^2 + \omega_e^2}\left(\frac{m_e}{m_i} + \frac{k_z^2}{k^2}\right), \tag{1}$$

where ω_p is the electron plasma frequency, ω_e is the electron cyclotron frequency, and k and k_z are the wave vector and its longitudinal (magnetic field–aligned) component.

We consider the energy exchange between waves and electrons

$$\frac{\partial}{\partial t}W_k = \langle \mathbf{j}_e\mathbf{E}\rangle + \langle \mathbf{j}_i\mathbf{E}\rangle = (\gamma_e + \gamma_i)W_k, \tag{2}$$

where $W_k = |E_k|^2/4\pi(\omega_p^2/\omega_e^2)\{1 + \omega_e^2/\omega_p^2\}$ is the energy density of a lower hybrid wave and $|E_k|^2/4\pi$ is the energy density of an alternating electric field. The mean work done by the electric field on the electrons is equal to

$$\langle \mathbf{j}_e\mathbf{E}\rangle = +i\varphi_k^*\int(-en)(k_z v_z + k_x v_x)\delta f(k, \theta, \omega) + \text{c.c.}, \tag{3}$$

1063-780X/01/2707-0598$21.00 © 2001 MAIK "Nauka/Interperiodica"

where the electron distribution function perturbed by the wave field has the form

$$\delta f(k, \theta, \omega) = \frac{e\varphi_k}{m_e}\sum_{-\infty}^{\infty}\sum_{-\infty}^{\infty} J_{n'}J_n \frac{e^{i(n-n')\theta}}{n\omega_e + k_z v_z - \omega} \times\left[k_z\frac{\partial f}{\partial v_z} + n\omega_e\frac{\partial f}{v_\perp \partial v_\perp}\right]. \quad (4)$$

Representing the unperturbed electron distribution function as

$$f = f_\parallel(v_z) f_\perp(v_\perp), \quad f_\perp(v_\perp) = \frac{1}{2\pi v_e^2} e^{-\frac{v_\perp^2}{2v_e^2}}, \quad \frac{\partial f_\perp(v_\perp)}{v_\perp \partial v_\perp} = -\frac{f_\perp(v_\perp)}{v_e^2} \quad (5)$$

we take the integrals over the transverse velocity in expression (3),

$$\int \pi dv_\perp^2 J_n^2\left(\frac{kv_\perp}{\omega_e}\right) f_\perp(v_\perp) = e^{-\left(\frac{kv_e}{\omega_e}\right)^2} I_n\left(\left(\frac{kv_e}{\omega_e}\right)^2\right) = A_n\left(\left(\frac{kv_e}{\omega_e}\right)^2\right), \quad (6)$$

and, after some manipulations, obtain

$$\langle \mathbf{j}_e\mathbf{E}\rangle = \pi\frac{\omega\omega_p^2|E_k|^2}{4\pi k^2} \times\sum_{-\infty}^{\infty} A_n\left[\frac{\partial f_\parallel(v_z)}{\partial v_z} + \frac{n\omega_e}{k_z v_e^2} f_\parallel(v_z)\right]\Bigg|_{v_z = \frac{\omega - n\omega_e}{k_z}}. \quad (7)$$

Then, we can readily find the growth rate of the current instability:

$$\gamma_e = \langle \mathbf{j}_e\mathbf{E}\rangle/W_k = \pi\frac{\omega\omega_e^2\omega_p^2}{(\omega_p^2 + \omega_e^2)k^2} \times\sum_{-\infty}^{\infty} A_n\left[\frac{\partial f_\parallel(v_z)}{\partial v_z} + \frac{n\omega_e}{k_z v_e^2} f_\parallel(v_z)\right]\Bigg|_{v_z = \frac{\omega - n\omega_e}{k_z}}. \quad (8)$$

This formula can also be derived by substituting the corresponding expression for the dielectric function of a magnetized plasma into the relationship $\gamma_k = -\mathrm{Im}\varepsilon/\frac{\partial \mathrm{Re}\,\varepsilon}{\partial\omega}$.

Taking into account the fact that, for $\omega \gg \omega_i = eB/m_i c$, the ions are unmagnetized and performing the necessary manipulations, we arrive at the following expression for the wave damping rate in the interaction with the ions, which are assumed to obey the Maxwellian distribution function

$$f = \left(\frac{2}{\pi}\right)^{3/2}\frac{1}{v_{Ti}^3}\exp\left(-\frac{v^2}{2v_{Ti}^2}\right):$$

$$\gamma_i = \frac{\omega_e^2\omega_{pi}^2}{\omega_p^2 + \omega_e^2}\int\frac{(\mathbf{kv})}{k^2}\frac{\mathbf{k}\frac{\partial}{\partial\mathbf{v}}f}{(\omega_k - \mathbf{kv})} = -\frac{1}{2}\sqrt{\frac{\pi}{2}}\frac{\omega_k^2}{k^3 v_{Ti}^3}\exp\left(-\frac{1}{2}\left(\frac{\omega_k}{kv_{Ti}}\right)^2\right)\frac{\omega_{pi}^2\omega_e^2}{\omega_e^2 + \omega_p^2}. \quad (9)$$

The electric current in a plasma is usually described by a Maxwellian distribution function with a shifted argument:

$$f_e = \sqrt{\frac{2}{\pi}}\frac{1}{v_{Te}}\exp\left(-\frac{(v_z - v_d)^2}{2v_{Te}^2}\right), \quad \frac{\partial f_e}{\partial v_z} = -\frac{v_z - v_d}{v_{Te}^2} f_e.$$

Taking into account only the Cherenkov resonance of the wave with the electrons and neglecting cyclotron resonances yields

$$\gamma_e = \langle \mathbf{j}_e\mathbf{E}\rangle/W_k = en\left\langle\int v_z\delta f_e E_z\right\rangle/W_k = \frac{\pi\omega_k\omega_e^2}{k^2(1 + \omega_e^2/\omega_p^2)}\frac{\partial f_e}{\partial v_z}\Bigg|_{v_z = \omega_k/k_z} \simeq \pi\frac{\omega_k^3}{k_z^2}\frac{\partial f_e}{\partial v_z}\Bigg|_{v_z = \omega_k/k_z}. \quad (10)$$

The condition $\gamma \equiv \gamma_e + \gamma_i = 0$ implies that the instability can develop only when the electron drift velocity is above a certain threshold:

$$\frac{v_d}{v_{Te}} \geq \frac{1}{k\rho_e} + \frac{4v_{Te}^2}{v_{Ti}^2}\frac{\omega_k}{kv_{Ti}} \times\exp\frac{1}{2}\left(\left(\frac{1}{k\rho_e} - \frac{v_d}{v_{Te}}\right)^2 - \left(\frac{\omega_k}{kv_{Ti}}\right)^2\right); \quad (11)$$

where $\rho_e^2 = v_{Te}^2/\omega_e^2$. In many cases, this condition is too restrictive. We note that, in a current-carrying plasma, the electron distribution can differ from the shifted Maxwellian distribution; specifically, it may have a tail of electrons accelerated in the direction opposite to the external electric field [7]. In this case, cyclotron resonances may become important and a fan instability may develop. In order to analyze the fan instability, we specify the electron tail as a half-Max-

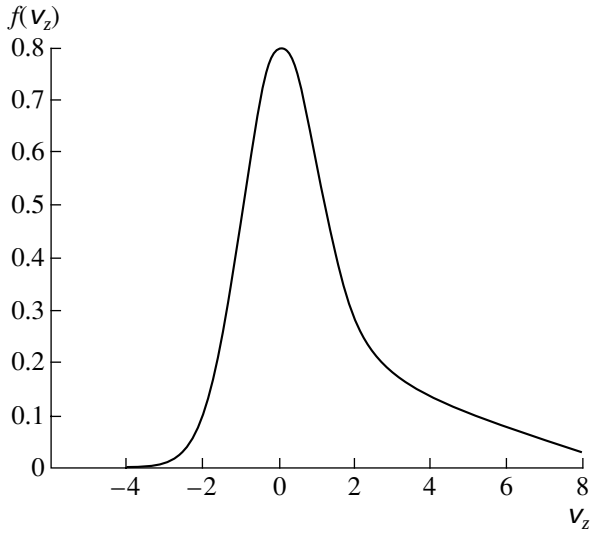

Fig. 1. Electron distribution function over longitudinal velocities in a current-carrying plasma.

wellian function with a high temperature such that $v_h > v_{Te}$ (see Fig. 1):

$$f_e(v_z) = \sqrt{\frac{2}{\pi}}\frac{1}{v_{Te}} \times \begin{cases} \exp\left(-\dfrac{v_z^2}{2v_{Te}^2}\right), & v_z < 0 \\ \left(1 - \dfrac{n_h}{n_0}\dfrac{v_{Te}}{v_h}\right)\exp\left(-\dfrac{v_z^2}{2v_{Te}^2}\right) + \dfrac{n_h}{n_0}\dfrac{v_{Te}}{v_h}\exp\left(-\dfrac{v_z^2}{2v_h^2}\right), & v_z \geq 0 \end{cases} \quad (12)$$

The current velocity corresponding to this function is equal to

$$\frac{v_d}{v_{Te}} = \int \frac{v_z}{v_{Te}} dv_z f_e(v_z) = \sqrt{\frac{2}{\pi}}\frac{n_h}{n_0}\left(\frac{v_h^2 - v_{Te}^2}{v_{Te}v_h}\right) \simeq \sqrt{\frac{2}{\pi}}\frac{n_h v_h}{n_0 v_{Te}}. \quad (13)$$

If the tail electrons are sufficiently energetic,

$$f_\parallel\left(\frac{\omega - \omega_e}{k_z}\right) - f_\parallel\left(\frac{\omega + \omega_e}{k_z}\right) > \frac{k_z v_e}{A_1 \omega_e}\left[4\sqrt{\frac{2}{\pi}}\frac{v_e \omega_k}{(v_{Ti})^3}\exp\left(-\frac{1}{2}\left(\frac{\omega_k}{k v_{Ti}}\right)^2\right) - A_0 v_e \frac{\partial f_\parallel(v_z)}{\partial v_z}\bigg|_{v_z = \frac{\omega}{k_z}}\right] \quad (14)$$

the contribution to the growth rate from the anomalous Doppler resonance exceeds the contribution from both the normal Doppler resonance and Cherenkov resonance with the electrons and ions.

The exact threshold for the instability and its growth rate can be determined only numerically with allowance for high cyclotron resonances. As an example, Fig. 2 illustrates the results of computations carried out for $v_h = 3v_{Te}$, $n_h/n_0 = 0.25$, and $v_d = 0.6v_{Te}$. We can see that an instability with the growth rate $\gamma/\omega \sim 0.05$ develops in a narrow range of the wave vectors $k_\perp l_D \simeq 0.4$–0.6 for $k_z/k_\perp \simeq 0.2$–0.3 (here, the Debye length l_D is defined as $l_D = v_{Te}/\omega_p$).

Our simulations show that, as the thermal velocity of the tail electrons increases, the wave vectors of the waves that are the first to start growing become longer. When the two factors—the asymmetric tail in the electron distribution function and the mean shift corresponding to the electron drift velocity—are combined together, the instability threshold is lower and the instability itself is more dangerous than when only one of these factors comes into play.

3. PLASMON DECAY IN A STRONG MAGNETIC FIELD

The general nonlinear interaction between the waves in a magnetized plasma was considered by Sturman [8] in the hydrodynamic approximation. In particular, he calculated the elements of the matrix describing the three-wave interaction. Here, we restrict ourselves to the conditions $\omega_e \gg \omega_p$, $c^2k^2 \ll \omega_e^2$, and $(k_z/k)^2 > m_e/m_i$, under which the nonlinear interaction between lower hybrid waves is easier to describe. The dispersion relation

$$\omega = \frac{\omega_e \omega_p}{\sqrt{\omega_p^2 + \omega_e^2}}\frac{k_z}{k} \simeq \omega_p \frac{k_z}{k} \quad (15)$$

implies that, in the case at hand, the resonance conditions $\omega_0 = \omega_1 + \omega_2$ and $\mathbf{k}_0 = \mathbf{k}_1 + \mathbf{k}_2$ for the three-wave decay process are satisfied. In particular, the three-wave decay is possible when the absolute values of the wave vectors of the three waves are nearly the same and the three transverse wave vectors form an equilateral triangle.

Let us derive equations describing the three-wave interaction. We take into consideration the fact that, since the plasma electrons are magnetized, their motion in the electrostatic wave field $\mathbf{E} = -\nabla\varphi$ is one-dimen-

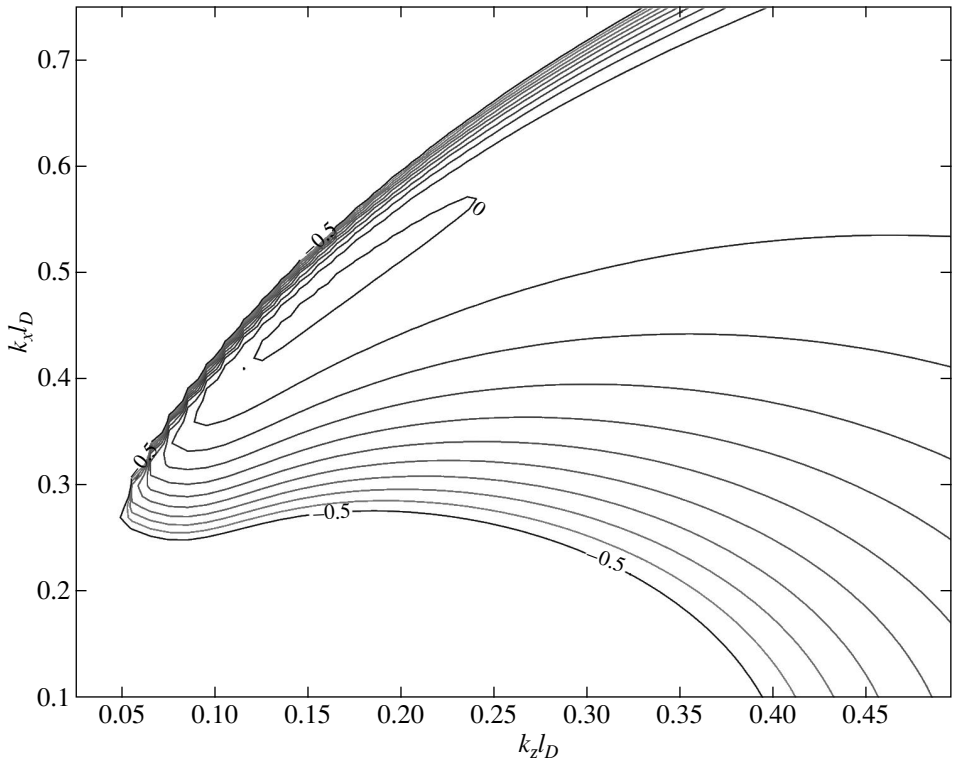

Fig. 2. Growth rate of the instability of lower hybrid waves vs. wave vector in a plasma with an electric current.

sional. From the equation of electron motion and Poisson's equation,

$$\frac{\partial v_z}{\partial t} = \frac{\partial}{\partial z}\left(\frac{e\varphi}{m_e} - \frac{v_z^2}{2}\right), \quad \nabla^2\varphi = 4\pi e\delta n, \qquad \frac{\partial}{\partial t}\frac{\delta n}{n} + \frac{\partial v_z}{\partial z} = -\frac{\partial}{\partial z}\frac{\delta n}{n}v_z \tag{16}$$

we find

$$\frac{\partial^2}{\partial t^2}\nabla^2\varphi + \omega_p^2\frac{\partial^2}{\partial z^2}\varphi = 4\pi en\left(\frac{\partial^2}{\partial z^2}\frac{v_z^2}{2} - \frac{\partial}{\partial z}\frac{\partial}{\partial t}\frac{\delta n}{n}v_z\right). \tag{17}$$

We substitute the linear electron velocity and linear perturbed electron density,

$$v_{zk} = -\sum_k \frac{k_z}{\omega_k}\frac{e\varphi_k}{m_e}e^{i\mathbf{kr}}, \quad \delta n = -\sum_k \frac{k^2}{4\pi e}\varphi_k e^{i\mathbf{kr}}$$

into the right-hand side of Eq. (17) and represent the wave fields in terms of their spatial Fourier harmonics. As a result, we arrive at the following equations for the slowly varying Fourier amplitudes of the electric potential:

$$2i\frac{\partial}{\partial t}\varphi_{k_0} = -\frac{e}{2m_e}\frac{k_z^2}{k^2}\sum_{k_0 = k_1 + k_2}\varphi_{k_1}\varphi_{k_2}e^{i(\omega_{k_0} - \omega_{k_1} - \omega_{k_2})t} \times\left(\frac{\omega_p^2 k_{1z}k_{2z}}{\omega_{k_2}\omega_k\omega_{k_1}} + \frac{k_{2z}k_1^2}{k_z\omega_{k_2}} + \frac{k_{1z}k_2^2}{k_z\omega_{k_1}}\right)$$
$$= -\frac{e}{m}\sum_{k_0 = k_1 + k_2}\varphi_{k_1}\varphi_{k_2}e^{i(\omega_{k_0} - \omega_{k_1} - \omega_{k_2})t}\frac{k_z}{k_0} \times\left\{\frac{\omega_1 + \omega_2}{\omega_2}\frac{k_1^2 k_{2z}}{k_{1z} + k_{2z}} + \frac{\omega_1 + \omega_2}{\omega_1}\frac{k_2^2 k_{1z}}{k_{1z} + k_{2z}} + \frac{\omega_p^2}{\omega_1\omega_2}k_{1z}k_{2z}\right\}. \tag{18}$$

We can, as usual, introduce the normal wave amplitudes, $C_k = |k|\varphi_k/\sqrt{4\pi\omega_k}$, in order to rewrite Eqs. (18) in the form

$$i\frac{\partial}{\partial t}C_{k_0} = \sum_{k_0 = k_1 + k_2}V_{k_0k_1k_2}C_{k_1}C_{k_2}e^{i(\omega_{k_0} - \omega_{k_1} - \omega_{k_2})t}, \tag{19}$$

where the matrix element $V_{k_0k_1k_2}$ describing the three-wave interaction satisfies the necessary symmetry

property $V_{k_0k_1k_2} = V_{k_0k_2k_1}$ [9] and is equal to

$$V_{k_0k_1k_2} = -\frac{\sqrt{4\pi}e}{4m_e}\frac{k_z^2}{k_0|k_1||k_2|}\frac{\sqrt{\omega_{k_1}\omega_{k_2}}}{\sqrt{\omega k_0}}$$

$$\times\left(\frac{\omega_p^2 k_{1z}k_{2z}}{\omega_{k_2}\omega_{k_0}\omega_{k_1}} + \frac{k_{2z}k_1^2}{k_z\omega_{k_2}} + \frac{k_{1z}k_2^2}{k_z\omega_{k_1}}\right) \tag{20}$$

$$= -\frac{(k_0 + k_1 + k_2)}{4\sqrt{m_e n}}\frac{\sqrt{\omega_{k_0}\omega_{k_1}\omega_{k_2}}}{\omega_p}.$$

The growth rate of the decay instability can be found in the usual way [9]:

$$\gamma_d = \left|V_{k_0k_1k_2}\right| = \frac{|k_1| + |k_2| + |k_0|}{4\sqrt{mn}}\left(\frac{\omega_1\omega_2\omega_0}{\omega_p^2}\frac{|E_0|^2}{4\pi\omega_0}\right)^{1/2}$$

$$= \frac{v_{Te}(k_0 + k_1 + k_2)}{4}\left(\frac{\omega_1\omega_2}{\omega_p^2}\frac{|E_0|^2}{4\pi nT_e}\right)^{1/2} \tag{21}$$

$$\leq \frac{3}{8}k_0 v_{Te}\left(\frac{|E_0|^2}{4\pi nT_e}\right)^{1/2},$$

The instability growth rate is seen to reach a maximum at $k_1 \approx k_2 \approx k_0$ and $k_{1z} \approx k_{2z} \approx k_{0z}/2$.

4. STEADY STATES

Near the threshold of linear instability (in our case, the current instability of lower hybrid waves), an unstable lower hybrid wave can decay into two damped waves before other possible stabilization mechanisms come into play. There can be different nonlinear stabilization regimes. First, we consider the regime described by a steady solution to the equations for the three-wave decay process. In accordance with the above analysis, these equations should be supplemented with the linear terms that are proportional to $\gamma_{0,1,2}$ and account for both the current instability of the wave with $k = k_0$ and the damping of the decay waves ($\gamma_0 > 0$, $\gamma_{1,2} < 0$). It is also convenient to introduce the detuning $\delta = \delta_1 + \delta_2 - \delta_0 = \omega_1 + \omega_2 - \omega_0$ and the wave phases and amplitudes:

$$C_i = \sqrt{s_i}\exp(-i\alpha_i + i\delta_i t),$$
$$V_{012} = V, \quad \psi = \alpha_1 + \alpha_2 - \alpha_0. \tag{22}$$

Then, the equations for the three-wave decay process become

$$\left(\frac{d}{dt} - 2\gamma_0\right)s_0 = 2V\sqrt{s_0s_1s_2}\sin\psi,$$

$$\left(\frac{d}{dt} - 2\gamma_1\right)s_1 = -2V\sqrt{s_0s_1s_2}\sin\psi,$$
$$\left(\frac{d}{dt} - 2\gamma_2\right)s_2 = -2V\sqrt{s_0s_1s_2}\sin\psi, \tag{23}$$

$$\frac{d\psi}{dt} - \delta = V\sqrt{s_0s_1s_2}\cos\psi\left[\frac{1}{s_0} - \frac{1}{s_1} - \frac{1}{s_2}\right].$$

For a zero detuning ($\delta = 0$), Eqs. (23) have the familiar first integral

$$\frac{d\ln(\cos^2\psi)}{dt} + \sum\frac{1}{s_i}\left(\frac{d}{dt}\right)s_i$$
$$= \frac{d}{dt}\ln(s_0s_1s_2\cos^2\psi) = 2\sum\gamma_i \tag{24}$$

or

$$s_0s_1s_2\cos^2\psi = \text{const}\cdot\exp(2\sum\gamma_i t), \tag{25}$$

which obviously implies that Eqs. (23) with $\delta = 0$ have no steady solutions. For $\delta \neq 0$, Eqs. (23) admit steady solutions satisfying the relationships

$$-V\sqrt{s_0s_1s_2}\sin\psi = \gamma_0 s_0 = -\gamma_1 s_1 = -\gamma_2 s_2, \tag{26}$$

which imply that the steady state exists only under the conditions $V\sin\psi < 0$ and $\gamma_0\gamma_{1,2} < 0$. Then, we find

$$\delta\tan\psi = -V\sqrt{s_0s_1s_2}\sin\psi\left[\frac{1}{s_0} - \frac{1}{s_1} - \frac{1}{s_2}\right]$$
$$= (\gamma_0 + \gamma_1 + \gamma_2). \tag{27}$$

For $V > 0$, we must choose a solution to the equation $\tan\psi = (\gamma_0 + \gamma_1 + \gamma_2/\delta)$ such that it satisfies the relationship

$$\sin\psi = \frac{-|\gamma_0 + \gamma_1 + \gamma_2|}{\sqrt{\delta^2 + (\gamma_0 + \gamma_1 + \gamma_2)^2}}. \tag{28}$$

As a result, we obtain

$$V^2 s_0 = \gamma_1\gamma_2\frac{\delta^2 + (\gamma_0 + \gamma_1 + \gamma_2)^2}{(\gamma_0 + \gamma_1 + \gamma_2)^2},$$
$$s_{1,2} = -\frac{\gamma_0}{\gamma_{1,2}}s_0. \tag{29}$$

Figure 3 shows the amplitude of an unstable wave in a steady state as a function of the damping rates of the decay waves.

Let us analyze the stability of the steady-state nonlinear regime. We linearize Eqs. (23) in small perturba-

tions of the wave amplitudes about the steady state to obtain

$$\frac{d\delta s_0}{dt} = 2\gamma_0\delta s_0 + V\sqrt{s_0s_1s_2}\sin\psi\left(\frac{\delta s_0}{s_0}+\frac{\delta s_1}{s_1}+\frac{\delta s_2}{s_2}\right) + 2V\sqrt{s_0s_1s_2}\cos\psi\delta\psi, \quad (30)$$

$$\frac{d\delta s_1}{dt} = 2\gamma_1\delta s_1 - V\sqrt{s_0s_1s_2}\sin\psi\left(\frac{\delta s_0}{s_0}+\frac{\delta s_1}{s_1}+\frac{\delta s_2}{s_2}\right) - 2V\sqrt{s_0s_1s_2}\cos\psi\delta\psi, \quad (31)$$

$$\frac{d\delta s_2}{dt} = 2\gamma_2\delta s_2 - V\sqrt{s_0s_1s_2}\sin\psi\left(\frac{\delta s_0}{s_0}+\frac{\delta s_1}{s_1}+\frac{\delta s_2}{s_2}\right) - 2V\sqrt{s_0s_1s_2}\cos\psi\delta\psi, \quad (32)$$

$$\left(\frac{d}{dt}+V\sqrt{s_0s_1s_2}\sin\psi\left[\frac{1}{s_0}-\frac{1}{s_1}-\frac{1}{s_2}\right]\right)\delta\psi = \frac{V}{2}\sqrt{s_0s_1s_2}\cos\psi\left(\left(\frac{1}{s_0}+\frac{1}{s_1}-\frac{1}{s_2}\right)\frac{\delta s_1}{s_1} + \left(\frac{1}{s_0}-\frac{1}{s_1}+\frac{1}{s_2}\right)\frac{\delta s_2}{s_2} - \left(\frac{1}{s_0}+\frac{1}{s_2}+\frac{1}{s_1}\right)\frac{\delta s_0}{s_0}\right). \quad (33)$$

The coefficients $V\sqrt{s_0s_1s_2}\sin\psi$ and $V\sqrt{s_0s_1s_2}\cos\psi$ can be found from relationships (26) and Eq. (27):

$$V\sqrt{s_0s_1s_2}\sin\psi = -\gamma_0 s_0, \qquad V\sqrt{s_0s_1s_2}\cos\psi = \frac{-\delta\gamma_0 s_0}{(\gamma_0+\gamma_1+\gamma_2)}. \quad (34)$$

Introducing the notation $d/dt = \Gamma$, we arrive at the equations

$$(\Gamma-\gamma_0)\delta s_0 = \gamma_1\delta s_1 + \gamma_2\delta s_2 - 2\frac{\delta\gamma_0 s_0}{(\gamma_0+\gamma_1+\gamma_2)}\delta\psi,$$

$$(\Gamma-\gamma_1)\delta s_1 = \gamma_0\delta s_0 + \gamma_2\delta s_2 + 2\frac{\delta\gamma_0 s_0}{(\gamma_0+\gamma_1+\gamma_2)}\delta\psi,$$

$$(\Gamma-\gamma_2)\delta s_2 = \gamma_0\delta s_0 + \gamma_1\delta s_1 + 2\frac{\delta\gamma_0 s_0}{(\gamma_0+\gamma_1+\gamma_2)}\delta\psi,$$

$$2(\Gamma-\gamma_0-\gamma_1-\gamma_2)\delta\psi = \frac{-\delta}{(\gamma_0+\gamma_1+\gamma_2)}\left((\gamma_0-\gamma_1+\gamma_2)\frac{\delta s_1}{s_1} + (\gamma_0+\gamma_1-\gamma_2)\frac{\delta s_2}{s_2} - (\gamma_0-\gamma_1-\gamma_2)\frac{\delta s_0}{s_0}\right),$$

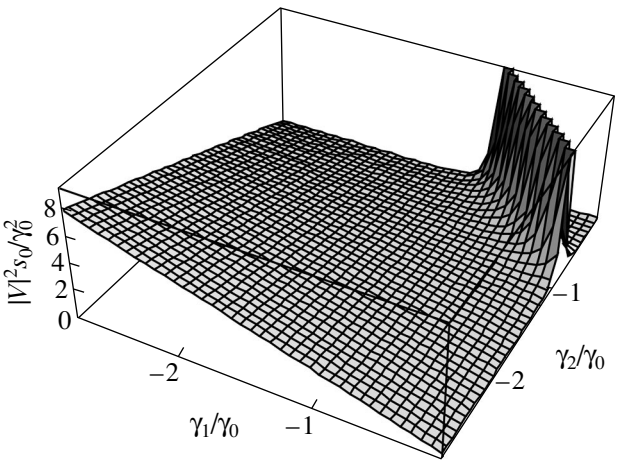

Fig. 3. Normalized amplitude of the unstable lower hybrid wave in steady state vs. damping rates of the decay waves for $\delta/\gamma_0 = 0.25$.

$$\delta s_0 = \frac{\gamma_1}{(\Gamma-\gamma_0)}\delta s_1 + \frac{\gamma_2}{(\Gamma-\gamma_0)}\delta s_2 - \frac{2\delta\gamma_0 s_0}{(\Gamma-\gamma_0)(\gamma_0+\gamma_1+\gamma_2)}\delta\psi,$$

$$(\Gamma-\gamma_1)\delta s_1 = \frac{\gamma_0\gamma_1\delta s_1}{(\Gamma-\gamma_0)} + \frac{\gamma_0\gamma_2\delta s_2}{(\Gamma-\gamma_0)} - \frac{2\delta\gamma_0\gamma_0 s_0\delta\psi}{(\Gamma-\gamma_0)(\gamma_0+\gamma_1+\gamma_2)} + \gamma_2\delta s_2 + 2\frac{\delta\gamma_0 s_0\delta\psi}{(\gamma_0+\gamma_1+\gamma_2)},$$

$$(\Gamma-\gamma_2)\delta s_2 = \gamma_0\delta s_0 + \gamma_1\delta s_1 + 2\frac{\delta\gamma_0 s_0}{(\gamma_0+\gamma_1+\gamma_2)}\delta\psi,$$

which give

$$\Gamma(\delta s_1-\delta s_2) = -2\gamma_2\delta s_2 + 2\gamma_1\delta s_1,$$

$$\Gamma(\delta s_0+\delta s_1) = 2\gamma_1\delta s_1 + 2\gamma_0\delta s_0,$$

$$\Gamma(\delta s_0+\delta s_2) = 2\gamma_2\delta s_2 + 2\gamma_0\delta s_0.$$

Performing the necessary manipulations, we finally obtain the following fourth-order equation for the growth rate Γ of the instability in the steady-state nonlinear regime:

$$\left(\frac{\Gamma}{\gamma_0 - A\gamma_0(\gamma_0-\gamma_1-\gamma_2)}-1\right)\times\left(\frac{\Gamma-\gamma_1-\gamma_2}{\gamma_0(\gamma_1+\gamma_2)-(\gamma_1-\gamma_2)^2}-A\right) = \frac{\gamma_1+\gamma_2}{\gamma_0(\gamma_1+\gamma_2)-(\gamma_1-\gamma_2)^2}-A, \quad (35)$$

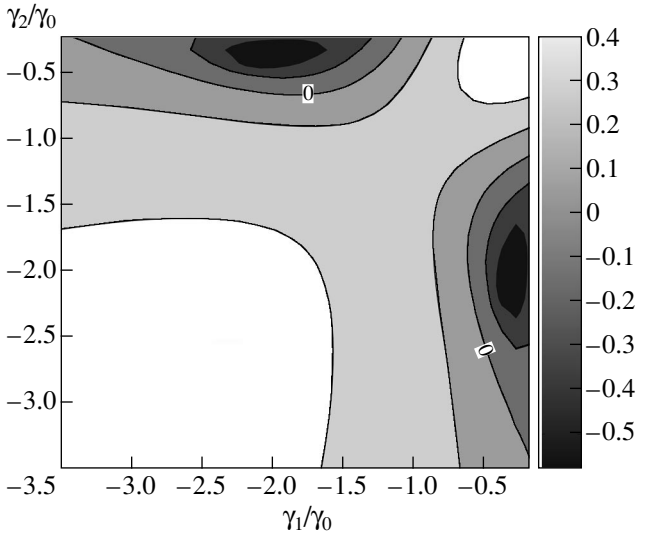

Fig. 4. Relief of the function $\Gamma(\gamma_1, \gamma_2)/\gamma_0$ for $\delta/\gamma_0 = 1.25$ (the contour $\Gamma = 0$ is indicated).

where

$$A = \frac{\delta^2}{(\Gamma - \gamma_1 - \gamma_2 - \gamma_0)(\gamma_0 + \gamma_1 + \gamma_2)^2}. \qquad (36)$$

For $\gamma_1 = \gamma_2$, Eq. (35) was investigated by Gol'tsova *et al.* [1]. For $\gamma_1 \neq \gamma_2$, the parametric dependence of Γ can be calculated numerically. Figure 4 displays contours of $\Gamma(\gamma_1, \gamma_2)$ for $\delta/\gamma_0 = 1.25$. We can see that, for $\delta \neq 0$, the steady states are stable if the decay waves are damped at moderate rates: γ_1 and γ_2 should satisfy the conditions $1 \leq |\gamma_1/\gamma_0|, |\gamma_2/\gamma_0| \leq 3$–4.

5. DYNAMIC STABILIZATION REGIMES

The above analysis shows that it is only in rare cases that the current instability is suppressed in the regime in which the steady-state amplitudes of the three interacting waves are constant (in particular, for this regime to arise, the frequency detuning between the waves should be sufficiently large). Generally, the instability is suppressed in various regimes in which the amplitudes of the interacting waves vary strongly in time [1, 10]. If the damping rates of the parametrically excited waves are insufficiently high, the dynamic suppression of the instability in the three-wave interaction does not occur and the amplitudes of the three interacting waves start growing exponentially [10]. When the dissipation is sufficiently high, the energy is exchanged between the three interacting waves either in a periodic regime (possibly, with many different periods) or in a stochastic regime (when fairly short time intervals, during which the amplitudes of the three strongly interacting waves increase substantially, alternate in a random fashion with longer time intervals, during which the original unstable wave stores energy and its amplitude grows exponentially). Which of the regimes occurs depends, in a fairly complicated manner, on the relationship between the instability growth rate and the wave damping rates. In these oscillatory regimes, the mean wave energy and the energy fluxes differ strongly from those in the steady-state regime.

The nonlinear dynamics of the three-wave interaction was studied in a number of papers (see, e.g., [1–5]), which revealed the possible existence of a strange attractor, on which the stabilization regime is stochastic. The most efficient method of studying the dynamics of the interacting waves is that of solving the basic equations numerically for different parameters of the system. It is convenient to express the time in units of the instability growth rate, $\tau = \gamma_{k_0} t$, and to introduce the dimensionless wave amplitudes $\tilde{C}_k = C_k/C_*$ such that $|V_{k_0 k_1 k_2} C_*| = \gamma_0$, in which case the dynamics of the three coupled waves is governed by only two parameters: $\tilde{\gamma}_{1,2} = \gamma_{k_{1,2}}/\gamma_k$. Figure 5 shows the behavior of the wave amplitudes, calculated by numerically solving the equations for the three-wave interaction for the parameter values corresponding to a periodic regime. In order to better illustrate the above analysis of the instability of the steady states and to shorten the time over which an asymptotic regime is achieved, the initial wave amplitudes were chosen to correspond to the slightly perturbed steady states described by Eq. (27) and condition (26).

In agreement with the above analysis of the instability of the steady states, the wave dynamics becomes stochastic when the decay waves are damped at higher rates. The stochastic behavior of the wave amplitudes is illustrated in Fig. 6.

In Fig. 7a, the Fourier spectrum of the wave amplitude obeys a power law, which indicates that the wave dynamics is stochastic (the Fourier spectra for periodic regimes contain pronounced peaks, corresponding to periodic energy exchange between the interacting waves). In Fig. 7b, the phase trajectory of the system of interacting waves in the three-dimensional space of the wave amplitudes is seen to be complicated and disordered, which is also typical of the stochastic regime.

From the standpoint of applications, the most important problem is that of determining the mean energy levels of the interacting waves and the energy influx into the plasma. Figure 8 shows the time-averaged squared amplitudes of the unstable wave and damped waves, $N_i = \langle |C_{k_i}|^2 \rangle$, calculated by solving the equations of the three-wave interaction for given values of γ_0 and γ_2. Note that the ratio $\gamma_1/\gamma_0 = -2.5$ corresponds to the quasi-periodic stabilization regime and the ratio $\gamma_1/\gamma_0 = -5.5$ refers to the stochastic regime.

The above analysis of the system of interacting waves allows us to draw several physical conclusions. First, we can determine the mean energy influx from

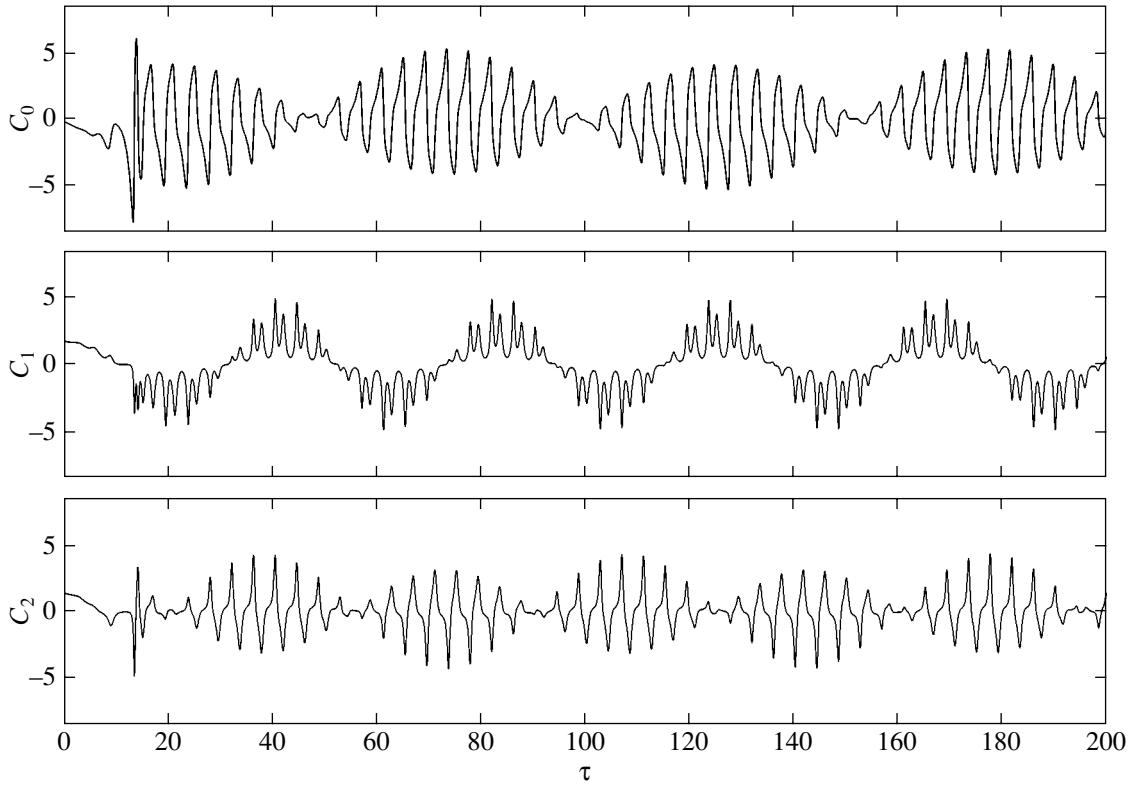

Fig. 5. A representative quasiperiodic regime for $\gamma_1/\gamma_0 = -1.8$, $\gamma_2/\gamma_0 = -2.8$, and $\delta/\gamma_0 = 0.3$.

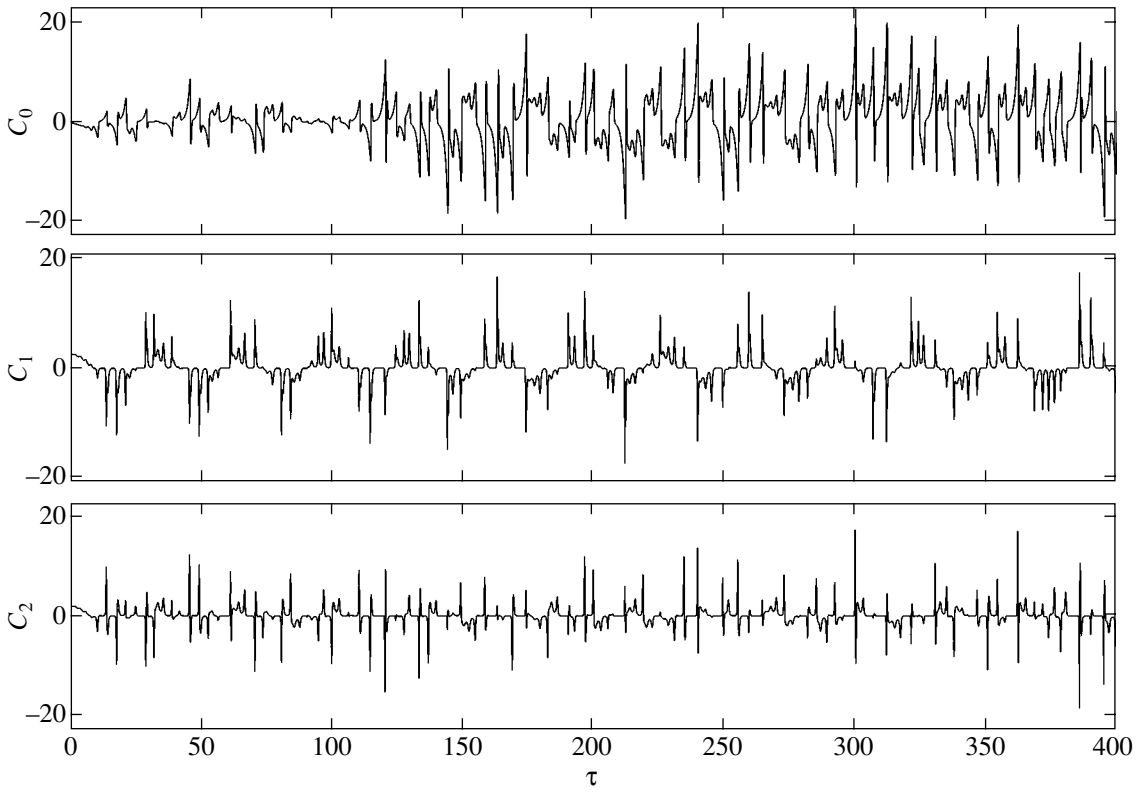

Fig. 6. A representative stochastic regime for $\gamma_1/\gamma_0 = -3.8$, $\gamma_2/\gamma_0 = -6.5$, and $\delta/\gamma_0 = 0.3$.

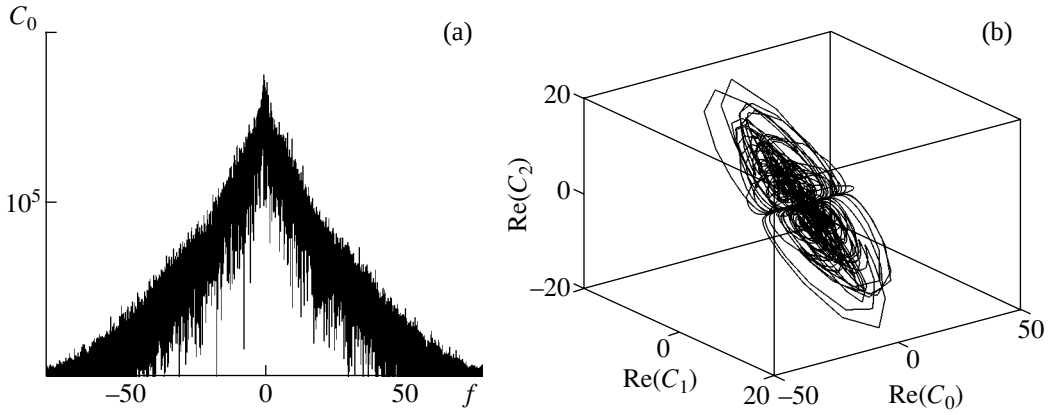

Fig. 7. (a) Fourier spectrum of the time-dependent amplitude C_1 for $\gamma_1/\gamma_0 = -3.8$, $\gamma_2/\gamma_0 = -6.5$, and $\delta/\gamma_0 = 0.3$. (b) Phase trajectory of the system of interacting waves in the three-dimensional space of the wave amplitudes.

the external source into the plasma in terms of the electron drift velocity:

$$Q = \left(\frac{\gamma_{k_0}}{V_{k_0k_1k_2}}\right)^2 (\gamma_{k_1}\omega_{k_1}N_{k_1} + \gamma_{k_2}\omega_{k_2}N_{k_2})$$
$$\approx 16\frac{\gamma_{k_0}^2\omega_p^2}{(k+k_1+k_2)^2 v_{Te}^2\omega_k}\left(\frac{\gamma_{k_1}}{\omega_{k_2}}N_{k_1} + \frac{\gamma_{k_2}}{\omega_{k_1}}N_{k_2}\right)nT_e, \quad (37)$$

where $N_{k_1} = \langle|\tilde{C}_{k_1}|^2\rangle$. Then, we find the effective plasma conductivity from the formula

$$j_e = \sigma_{\text{eff}}E_0 = \frac{\omega_p^2}{4\pi\nu_{\text{eff}}}E_0 \quad (38)$$

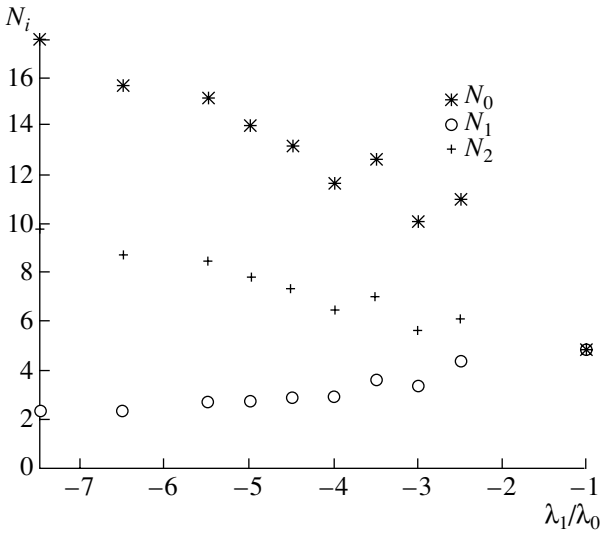

Fig. 8. Time-averaged squared wave amplitudes vs. γ_1 for $\gamma_2/\gamma_0 = -1.8$ and $\delta/\gamma_0 = 0.3$.

and use the energy balance relation in order to estimate the electric field energy expended on performing work against the decelerating force exerted by the waves on the electrons that are scattered in the three-wave interaction:

$$j_eE_0 = \frac{\nu_{\text{eff}}}{\omega_p^2}j_e^2 = Q$$
$$\approx \frac{16\gamma_{k_0}^2\omega_p^2}{(k+k_1+k_2)^2 v_{Te}^2\omega_k}\left(\frac{\gamma_{k_1}}{\omega_{k_2}}N_{k_1} + \frac{\gamma_{k_2}}{\omega_{k_1}}N_{k_2}\right)nT_e. \quad (39)$$

As a result, we arrive at the following expression for the effective scattering rate ν_{eff}, which determines the anomalous resistance of a collisionless plasma near the instability threshold:

$$\frac{\nu_{\text{eff}}}{\omega_{k_0}} = \frac{\omega_p^2}{(k+k_1+k_2)^2 v_{Te}^2}\left(\frac{\gamma_{k_0}}{\omega_{k_0}}\right)^2\left(\frac{n_0 v_{Te}}{n_h v_h}\right)^2$$
$$\times 32\pi^2\left(\frac{\gamma_{k_1}}{\omega_{k_2}}N_{k_1} + \frac{\gamma_{k_2}}{\omega_{k_1}}N_{k_2}\right) \quad (40)$$
$$\approx \frac{3\pi^2\alpha}{k_0^2 l_D^2}\left(\frac{\gamma_{k_0}}{\omega_{k_0}}\right)^2\left(\frac{n_0 v_{Te}}{n_h v_h}\right)^2\left(\frac{\gamma_{k_1}\gamma_{k_2}}{\omega_{k_1}\omega_{k_2}}\right)^{1/2}.$$

When deriving expression (40), we took into account the relationship $j_e^2 \simeq j_{th}^2 = (en_0v_{Te})^2(n_hv_h/n_0v_{Te})^2$, which holds with sufficient accuracy near the instability threshold. We also introduced the coefficient α, which depends on the mean amplitudes of the damped waves:

$$\alpha = \left(\sqrt{\frac{\omega_{k_1}\gamma_{k_1}}{\omega_{k_2}\gamma_{k_2}}}N_{k_1} + \sqrt{\frac{\omega_{k_2}\gamma_{k_2}}{\omega_{k_1}\gamma_{k_1}}}N_{k_2}\right). \quad (41)$$

The results of our simulations show that the coefficient α is weakly sensitive to the parameters of the interacting waves and is approximately equal to 10–20. Since formula (40) contains a large numerical factor and the threshold flux of superthermal electrons satisfies the inequality $n_h v_h \ll n_0 v_{Te}$, the effective scattering rate ν_{eff} can be fairly high ($\nu_{\text{eff}} \geq 10^{-2}\omega_{k_0} \gg \gamma_{k_0}$) even when the instability threshold is exceeded only slightly, $\gamma_{k_0}/\omega_{k_0} \sim 10^{-3}$ and $(\gamma_{k_1}\gamma_{k_2}/\omega_{k_1}\omega_{k_2})^{1/2} \sim 10^{-2}$.

6. CONCLUSION

Our analysis of the instability of the longitudinal electric current carried by hot electrons obeying an anisotropic distribution in a plasma with moderately different ion and electron temperatures shows that lower hybrid waves excited near the instability threshold are in cyclotron resonance with the current-carrying superthermal electrons. Just above the threshold, only one lower hybrid wave can be excited. After the amplitude of the wave exceeds the threshold for the decay instability, the wave itself comes into resonance with other (damped) lower hybrid waves. As a result, the current instability is suppressed in the nonlinear regime, which may be either quasi-periodic or stochastic, depending on the relationship between the instability growth rate and the damping rates of the interacting waves. The stochastic regime of the three-wave interaction is characterized by an irregular sequence of fairly short time intervals during which the intensities of the interacting waves become fairly high and longer time intervals during which the wave intensities are very low. This feature distinguishes the stochastic regime under consideration from analogous stochastic regimes in other (conservative) systems with a small number of waves (see, e.g., [11]). Nevertheless, our simulations revealed no marked difference between the time-averaged wave intensities in the stochastic and quasi-periodic regimes with short-duration events of wave activity.

We have estimated the effective rate at which the plasma electrons are scattered by waves. The effective scattering rate has been used to estimate the anomalous resistance of the plasma during suppression of the current instability as a result of energy exchange between waves and electrons in the three-wave interaction. We have revealed no significant difference between the values of anomalous resistance in the stochastic and quasi-periodic regimes.

The above-described mechanism for suppression of the current instability in a magnetized plasma competes with the suppression mechanism due to the quasilinear relaxation of the unstable electron distribution [7]. However, when the spectrum of the excited waves is sparse (as in the case of stabilization near the instability threshold), the use of the quasilinear approximation to describe the dynamics of the electron distribution does not seem to be justified and requires a separate analysis.

ACKNOWLEDGMENTS

This study was supported in part by the KBN (Poland), grant no. 2PO3-001-16.

REFERENCES

1. Yu. K. Gol'tsova, M. I. Rabinovich, and V. P. Reutov, Fiz. Plazmy **1**, 594 (1975) [Sov. J. Plasma Phys. **1**, 329 (1975)].
2. V. I. Dubrovin, V. R. Kogan, and M. I. Rabinovich, Fiz. Plazmy **4**, 1174 (1978) [Sov. J. Plasma Phys. **4**, 658 (1978)].
3. J.-M. Wersiger, J. Finn, and E. Ott, Phys. Fluids **23**, 1142 (1980).
4. D. W. Hughes and M. Proctor, Physica D (Amsterdam) **46**, 163 (1990).
5. C. Meunier, M. Bussak, and G. Laval, Physica D (Amsterdam) **4**, 236 (1982).
6. A. B. Mikhailovskii, *Theory of Plasma Instabilities* (Atomizdat, Moscow, 1975; Consultants Bureau, New York, 1974).
7. Y. Omelchenko, V. Shapiro, V. Shevchenko, *et al.*, J. Geophys. Res. A **99**, 5965 (1994).
8. B. I. Sturman, Zh. Éksp. Teor. Fiz. **71**, 613 (1976) [Sov. Phys. JETP **44**, 322 (1976)].
9. A. A. Galeev and P. Z. Sagdeev, in *Reviews of Plasma Physics*, Ed. by M. A. Leontovich (Atomizdat, Moscow, 1973; Consultants Bureau, New York, 1979), Vol. 7.
10. B. A. Al'terkop, A. S. Volokitin, and V. P. Tarakanov, Zh. Éksp. Teor. Fiz. **71**, 548 (1976) [Sov. Phys. JETP **44**, 287 (1976)].
11. B. A. Buts, O. V. Manuĭlenko, K. N. Stepanov, and A. P. Tolstoluzhskiĭ, Fiz. Plazmy **20**, 794 (1994) [Plasma Phys. Rep. **20**, 714 (1994)].

Translated by I. A. Kalabalyk

Plasma Physics Reports, Vol. 27, No. 7, 2001, pp. 608–613. Translated from Fizika Plazmy, Vol. 27, No. 7, 2001, pp. 647–652.

PLASMA INSTABILITY

Role of the Ridley–Watkins–Hilsum Mechanism in the Stabilization of Surface Plasma Waves

Yu. O. Averkov and V. M. Yakovenko

Institute of Radiophysics and Electronics, National Academy of Sciences of Ukraine, ul. akademika Proskury 12, Kharkov, 61085 Ukraine

Received February 15, 2001

Abstract—The stabilization of unstable harmonic oscillations of the surface charge density and electromagnetic field that are excited by a low-density electron beam propagating parallel to the plane boundary of a half-space occupied by gallium arsenide (GaAs) is studied in the hydrodynamic approximation. It is shown that, for gallium arsenide semiconductors (and, generally, for other so-called $A^{III}B^{V}$ compound semiconductors), these oscillations are stabilized primarily by the Ridley–Watkins–Hilsum mechanism. The equilibrium field amplitudes and equilibrium surface charge densities of both the semiconductor and the beam are obtained for a slightly overcritical level, i.e., for electrons with energies slightly greater than the energy gap between the lower and higher valleys. *© 2001 MAIK "Nauka/Interperiodica".*

1. INTRODUCTION

Beam–plasma instabilities, which were discovered as long ago as 1949 by Akhiezer and Faĭnberg [1, 2] and, independently, by Bohm and Gross [3], continue to be the subject of much theoretical and experimental research, because they find practical applications in such areas as turbulent heating of fusion plasmas, the acceleration of charged particles, and the amplification of high-frequency oscillations. In recent years, increasing attention has been focused on the problems of the interaction of electron beams with solid-state plasmas. As compared to gaseous plasma, solid-state plasma exhibits a number of new properties associated with the peculiar features of charge carriers (their band spectra, the mechanisms for their scattering, etc.). In turn, these properties open new possibilities for creating semiconductor devices and improving semiconductor technology.

It is well known (see, e.g., [4, 5]) that, in semiconductors, the states of charge carriers may become unstable after applying a constant or alternating electromagnetic field and also when the semiconductor is affected by a beam of charged particles. Beletskiĭ *et al.* [4] showed that, in principle, there exist several dominant mechanisms for suppressing these instabilities. For example, the role of the suppression mechanism can be played by an external electric field, in which the drift velocity and relaxation rate of the charge carriers change because they both become dependent on the squared field amplitude. Also, the suppression mechanism can be associated with the nonlinearities in the current–voltage characteristic of a semiconductor (by analogy with the solution describing a solitary pulse [6]), the energy transfer from oscillations to the higher damped field harmonics, and three-wave processes. Although the papers cited dealt with internal plasma waves, the instabilities related to the excitation of surface plasma waves should definitely be suppressed by the same physical mechanisms. In the previous studies on the stabilization of surface plasma waves excited by an electron beam, the instability was assumed to be suppressed mainly by the trapping of beam electrons by the plasma wave; moreover, the plasma was treated in a linear approximation [7–9]. In [10], this approach was shown to be valid only for the single-particle Cherenkov effect (or Thomson emission mechanism). In the case of the collective Cherenkov effect (or Raman emission mechanism), in which the nonlinear nature of the motion of the beam and plasma electrons should be taken into account, the stabilization mechanism is associated with the nonlinear frequency shift and violation of the resonance conditions. In [11], it was shown that unstable oscillations of both the surface wave field and surface charge density can be stabilized by an additional potential field that arises from the nonlinear interaction of a beam of charged particles with the wave field and thus influences the beam dynamics.

Here, we investigate the role of the nonlinear properties of a gallium arsenide (GaAs) semiconductor in stabilizing a harmonic electromagnetic surface wave excited by an electron beam propagating parallel to the dielectric–semiconductor contact. We show that an increase in the amplitude of the electric field of a surface wave increases the electron relaxation rate, which depends on the squared field amplitude. As a result, the instability saturates. The stabilization mechanism is associated with the following distinguishing features of the band structure of the $A^{III}B^{V}$ semiconductors (in particular, GaAs). In an unperturbed state, the electrons in the semiconductor are in the conduction band with a minimum energy at the center of the Brillouin zone (in the $\langle 000 \rangle$ direction). When the amplitude of an external

1063-780X/01/2707-0608$21.00

electric field applied to the GaAs semiconductor exceeds a certain critical value, the electrons pass from the ⟨000⟩ band to the neighboring bands with minimum energies in the ⟨100⟩ directions (the so-called Ridley–Watkins–Hilsum mechanism [12]). The stronger the external field, the higher the rates are of the electron energy and momentum relaxation (by optical phonons) in such excitations. This effect is responsible for the stabilization of the surface field oscillations and the oscillations of the surface electron densities in both the beam and the semiconductor.

2. EQUATION FOR THE SLOWLY VARYING FIELD AMPLITUDE

We consider a dielectric–semiconductor system such that the half-space $y < 0$ is occupied by a uniform GaAs semiconductor and the half-space $y > 0$ is occupied by a uniform dielectric. We assume that there is no external magnetic field. Let an electron beam propagate at a velocity $\mathbf{v}_0$ in a dielectric along the x-axis, and let a harmonic plasma wave with a frequency ω and wave vector $\mathbf{q}$ run in the same direction along the dielectric–semiconductor contact. For such a system, we have $\mathbf{q} \parallel \mathbf{v}_0 \parallel \mathbf{e}_x$.

In contrast to a gas-discharge plasma, in the system under consideration, the electron momentum relaxation rate ν may be considerably higher than the frequency ω of the surface plasma wave, $\nu \gg \omega$. This circumstance allows the beam instabilities in such systems to be described in the hydrodynamic approximation. Formally, a hydrodynamic description of the electrons in a semiconductor is justified when the electron–electron collision frequency is much higher than the rates at which the electron energy and momentum relax in the electron–lattice interaction. It is well known [12] that, for a particular semiconductor, the hydrodynamic approach can be used if the electron density N exceeds a certain critical density N_{cr}. The value of N_{cr}, which differs between different semiconductors, may be fairly high; for example, for GaAs, we have $N_{cr} \propto 10^{17}$ cm^{-3}. Although we are interested here in the case $N \ll N_{cr}$, which is most frequently encountered in experiments, we can apply the hydrodynamic approach, because, even in this case, it provides a fairly reasonable qualitative description of the electrons in the system and gives correct order-of-magnitude estimates [12].

We start with the following set of hydrodynamic equations supplemented with Maxwell's equations for the potential field:

$$\begin{gathered}\frac{\partial N}{\partial t} + \nabla \cdot (\mathbf{v}N) = 0,\\ \left[\frac{\partial}{\partial t} + (\mathbf{v}_0 \cdot \nabla)\right]\mathbf{v} = \frac{e}{m}\mathbf{E} - \nu\mathbf{v},\\ \nabla \cdot \mathbf{D} = 4\pi eN,\\ \nabla \times \mathbf{E} = \nabla \times \mathbf{B} = 0.\end{gathered} \tag{1}$$

Here, N is the volume electron density, $\mathbf{v}$ is the alternating component of the electron velocity, e and m are the charge and mass of an electron, and the electron momentum relaxation rate ν is $\nu = \nu_b \ll \omega$ for the beam electrons and $\nu = \nu_s \gg \omega$ for the electrons in the semiconductor. This set of equations applies to both the beam and the semiconductor, which will be distinguished below by the subscripts 1 and 2, respectively.

At the dielectric–semiconductor contact $y = 0$, the tangential component of the electric field of a surface plasma wave is continuous:

$$E_{x1}(0) = E_{x2}(0). \tag{2}$$

The boundary condition for the normal component of the electric induction vector can be obtained by integrating the third equation in set (1) across a transitional layer between two media [4]:

$$\lim_{\alpha \to 0}\int_{-\alpha}^{\alpha} \nabla \cdot \mathbf{D}\,dy = 4\pi e \lim_{\alpha \to 0}\int_{-\alpha}^{\alpha} N\,dy. \tag{3}$$

For inhomogeneous media, formula (3) gives

$$\varepsilon_1 E_{y1}(0) - \varepsilon_2 E_{y2}(0) = 4\pi e(n_1 - n_2), \tag{4}$$

where ε_1 and ε_2 are the permittivities of the dielectric and semiconductor lattice and n_1 and n_2 are the surface densities of the beam electrons and the electrons in the semiconductor, respectively. Below, we will assume that $E_j \propto \exp(\kappa_{1,2}y)\exp[i(qx - \omega t)]$, where $j = x, y$; $\kappa_1 = -\kappa$; and $\kappa_2 = \kappa$. The relationship between $E_{y1}(0)$ and $E_{y2}(0)$ can be found from the conditions that the electron densities in the deep interiors of the media are in equilibrium ($\nabla \cdot \mathbf{D} = 0$) and the wave field is potential ($\nabla \times \mathbf{E} = 0$):

$$E_{y1}(0) = -E_{y2}(0), \quad \kappa = q. \tag{5}$$

Substituting relationship (5) into formula (4) yields

$$E_{y1}(0) = E_y(0) = \frac{4\pi e}{\varepsilon_1 + \varepsilon_2}(n_1 - n_2). \tag{6}$$

Integrating the continuity equation across a transitional layer between two media and using the second equation in set (1), we arrive at the following set of equations:

$$\begin{gathered}\left(\frac{\partial}{\partial t} + v_0\frac{\partial}{\partial x}\right)^2 n_1 + \nu_b\left(\frac{\partial}{\partial t} + v_0\frac{\partial}{\partial x}\right)n_1 + \frac{eN_{10}}{m_0}E_y(0) = 0,\\ \frac{\partial^2 n_2}{\partial t^2} + \nu_s\frac{\partial n_2}{\partial t} - \frac{eN_{20}}{m^*}E_y(0) = 0,\end{gathered} \tag{7}$$

where N_{10} is the equilibrium volume density of the beam electrons and N_{20} and m^* are, respectively, the equilibrium volume density and effective mass of the

electrons in a semiconductor. It is convenient to rewrite Eqs. (7) in the form

$$\left(\frac{\partial}{\partial t}+v_0\frac{\partial}{\partial x}\right)^2 n_1+\nu_b\left(\frac{\partial}{\partial t}+v_0\frac{\partial}{\partial x}\right)n_1+\Omega_b^2(n_1-n_2)=0,$$
$$\frac{\partial^2 n_2}{\partial t^2}+\nu_s\frac{\partial n_2}{\partial t}-\Omega_s^2(n_1-n_2)=0, \quad (8)$$

where

$$\Omega_b^2=\frac{4\pi e N_{10}}{m_0(\varepsilon_1+\varepsilon_2)}, \quad \Omega_s^2=\frac{4\pi e N_{20}}{m^*(\varepsilon_1+\varepsilon_2)}.$$

We adopt the following parameter ordering:

$$\nu_s \gg \Omega_s \propto \omega \gg \Omega_b \gg \nu_b. \quad (9)$$

Equations (8) can be solved by the method of successive approximations. To do this, we obtain a solution to the first equation (the equation for the beam) in set (8) under the assumption that $\nu_b = n_2 = 0$:

$$n_1^{(0)}=a\cos(qx-\omega t), \quad (10)$$

where a = const and $\omega = qv_0 \pm \Omega_b$. We insert solution (10) into the second equation (the equation for the electrons in the semiconductor) in set (8) in order to arrive at the following solution describing undamped (for $\nu_s \gg \Omega_s$) oscillations:

$$n_2^{(0)}=-\frac{\Omega_s^2}{\nu_s^2\omega^2+(\omega^2-\Omega_s^2)^2}\times\left[(\omega^2-\Omega_s^2)n_1^{(0)}+\nu_s\frac{\partial n_1^{(0)}}{\partial t}\right]. \quad (11)$$

We substitute solution (11) into the equation for the beam in set (8) and omit the zero subscript to obtain

$$\left(\frac{\partial}{\partial t}+v_0\frac{\partial}{\partial x}\right)^2 n_1+\Omega_b^2 n_1 = -\left[\nu_b+\frac{\Omega_s^2\Omega_b^2\nu_s}{\nu_s^2\omega^2+(\omega^2-\Omega_s^2)^2}\right]\frac{\partial n_1}{\partial t} - \left[\nu_b v_0\frac{\partial n_1}{\partial x}+\frac{\Omega_s^2\Omega_b^2(\omega^2-\Omega_s^2)}{\nu_s^2\omega^2+(\omega^2-\Omega_s^2)^2}n_1\right]. \quad (12)$$

Let us estimate the quantities in angular brackets on the right-hand side of Eq. (12). For a GaAs semiconductor and for $N_{10} \propto 10^{10}$ cm^{-3} and $N_{20} \propto 10^{14}$ cm^{-3}, we have $\Omega_b \approx 10^9$ s^{-1} and $\Omega_s \approx 5.8\times 10^{11}$ s^{-1}. The relaxation rate ν_b can be estimated from the formula [13]

$$\nu_b \approx \frac{\sqrt{2}\pi N_{10}e^4\lambda}{\varepsilon_1^2 m_0^{1/2}}T_b^{-3/2}, \quad (13)$$

where $\lambda = \ln(N_{10}^{-1}(T_b/e^2)^3)$ is the Coulomb logarithm and T_b is the temperature of the beam electrons (in energy units). For example, for $T_b/k_B = 300$ K (where k_B is Boltzmann's constant), we have $\nu_b \approx 10^8$ s^{-1}. The formula for ν_s will be analyzed in detail in the next section. At this point, note only that, for $T/k_B = 300$ K, this relaxation rate is about $\nu_s \approx 7\times 10^{12}$ s^{-1}.

Choosing the quantity

$$\delta=\frac{\nu_b}{\omega}\propto 10^{-4}, \quad (14)$$

as a small parameter, we obtain the estimates

$$\frac{1}{\omega}\frac{\Omega_s^2\Omega_b^2\nu_s}{\nu_s^2\omega^2+(\omega^2-\Omega_s^2)^2}\propto 10^{-6}\propto\delta^{3/2}, \quad \frac{1}{\omega}\frac{\Omega_s^2\Omega_b^2(\omega^2-\Omega_s^2)}{\nu_s^2\omega^2+(\omega^2-\Omega_s^2)^2}\propto 10^{-8}\propto\delta^2. \quad (15)$$

Now, we discard the terms on the order of $O(\delta^2)$ on the right-hand side of Eq. (12) and introduce the dimensionless time $\tau = \omega t$. As a result, we obtain the equation

$$\left(\frac{\partial}{\partial\tau}+\frac{v_0}{\omega}\frac{\partial}{\partial x}\right)^2 n_1+\frac{\Omega_b^2}{\omega^2}n_1 = -\delta\left[\left(1+\frac{\Omega_s^2\Omega_b^2}{\nu_s\nu_b\omega^2}\right)\frac{\partial n_1}{\partial\tau}+\frac{v_0}{\omega}\frac{\partial n_1}{\partial x}\right]+O(\delta^2). \quad (16)$$

We solve this equation by the van der Pol method [14]. In this way, we represent the desired solution as

$$n_1=a(\tau)\cos(qx-\omega t+\varphi(\tau)), \quad (17)$$

where $a(\tau)$ and $\varphi(\tau)$ are slowly varying functions of time. Then, we substitute expression (17) into Eq. (16) and collect the coefficients of the same powers of δ and the same harmonics to arrive at the following set of equations for the slowly varying (in time) amplitude and phase of the oscillations:

$$\frac{da}{d\tau}=-\delta\frac{a}{2}\left(1+\frac{\Omega_s^2\Omega_b^2}{\nu_s(a)\nu_b\omega(\omega-qv_0)}\right)+O(\delta^2) = -\frac{a}{2}\left(\delta+\frac{\Omega_s^2\Omega_b^2}{\nu_s(a)\omega^2(\omega-qv_0)}\right)+O(\delta^2), \quad \frac{d\varphi}{d\tau}=O(\delta^2), \quad (18)$$

where the relaxation rate $\nu_s(a)$ is a function of the field amplitude. Note that, for $\omega = qv_0 + \Omega_b$, the right-hand side of the equation for the field amplitude in set (18) is negative, so that the wave is damped. For $\omega = qv_0 - \Omega_b$,

the right-hand side of this equation is nonnegative when

$$0 \le 1 - \frac{\nu_s(a)\nu_b\omega}{\Omega_s^2\Omega_b}. \quad (19)$$

Below, we will be interested only in the wave with the frequency $\omega = qv_0 - \Omega_b$, for which Eqs. (18) reduce to

$$\frac{da}{d\tau} = -\delta\frac{a}{2}\left(1 - \frac{\Omega_s^2\Omega_b}{\nu_s(a)\nu_b\omega}\right) + O(\delta^2), \qquad \frac{d\varphi}{d\tau} = O(\delta^2). \quad (20)$$

3. NONLINEAR STABILIZATION

The nonlinear stabilization mechanism under discussion is associated with the dependence of the relaxation rate of the electrons in a semiconductor on the amplitude of the electric field of the surface wave. According to Eq. (20), the relaxation rate ν should increase as the electric field becomes stronger, i.e., as the field amplitude a increases. This dependence $\nu_s(a)$, which is actually observed for $A^{III}B^{V}$ semiconductors when the electric field amplitude exceeds a certain critical value, can be explained in terms of the Ridley–Watkins–Hilsum mechanism. In this context, gallium arsenide is the best-studied semiconductor among $A^{III}B^{V}$ compounds. That is why it was chosen to be the subject of our analysis. Note that, for GaAs, the frequency $\nu_s(a)$ is governed completely by the Ridley–Watkins–Hilsum mechanism and is the highest among the relaxation rates in the problem under consideration.

The physical essence of the Ridley–Watkins–Hilsum mechanism can be outlined as follows. In GaAs in a thermodynamic equilibrium state, the majority of electrons occur in the valley with a minimum energy at the center of the Brillouin zone (the $\langle 000\rangle$ valley), in which the effective electron mass is equal to $m^*_{\langle 000\rangle} = 0.067m_0$. The next several higher valleys with minimum energies in the $\langle 100\rangle$ directions are separated from the $\langle 000\rangle$ valley by the energy gap $\Delta = 0.36$ eV, the effective electron mass in the higher valleys being $m^*_{\langle 100\rangle} = 1.2m_0$. Since the density of states is proportional to $m^{*3/2}$, the density of states for the valleys in the $\langle 100\rangle$ directions is higher than that for the $\langle 000\rangle$ valley by a factor of approximately 75. Therefore, it is far more probable for electrons whose energies θ exceed Δ to occur in the $\langle 100\rangle$ valleys than in the $\langle 000\rangle$ valley. The electron transitions between the valleys are accompanied by the emission or absorption of optical phonons with energies $\hbar\bar{\omega} \approx 0.8\hbar\omega_l$, where $\hbar\omega_l$ is the energy of an optical phonon running in the longitudinal direction. Consequently, the initial condition for the field amplitude a in Eq. (20) should correspond to the value $a(0) = a_{cr}$ at which $\theta = \Delta + \hbar\bar{\omega}$.

At the boundary between two media, the electron energy θ can be expressed in terms of the squared amplitude of the wave field by using Eqs. (6), (10), and (11) and the heat balance equations [13]:

$$\theta = T + \left(\frac{4\pi e}{\varepsilon_1 + \varepsilon_2}\right)^2 \frac{a^2}{2m^*\eta\nu_s^2}[1 + O(\Omega_s/\nu_s)], \quad (21)$$

where the parameter η describing inelastic scattering of electrons is equal to

$$\eta = \frac{(\hbar\omega_l)^2}{\theta T}. \quad (22)$$

With allowance for expression (21), we obtain the following initial condition for a in Eq. (20):

$$a(0) = a_{cr} = \frac{\varepsilon_1 + \varepsilon_2}{4\pi e^2}\nu_{s0}\sqrt{2m^*_{\langle 000\rangle}\eta(\Delta + \hbar\bar{\omega} - T)}. \quad (23)$$

Here, the relaxation rate of the electrons in valley-to-valley transitions with energies $\theta = \Delta + \hbar\bar{\omega}$ is chosen as ν_{s0}. For $\theta > \Delta + \hbar\bar{\omega}$, the rate ν_s at which the momentum of the electrons scattered in valley-to-valley transitions relaxes has the form [12]

$$\nu_s = \nu'(\xi_\Delta)^{-1/2}[(\xi + \xi_{ph} - \xi_\Delta)^{1/2} + \exp(\xi_T)(\xi - \xi_{ph} - \xi_\Delta)^{1/2}], \quad (24)$$

where

$$\nu' = \frac{d^2(m^*_{\langle 100\rangle})^{3/2}\Delta^{1/2}}{\sqrt{2}\pi\hbar^3\rho\bar{\omega}}(\exp(\xi_T) - 1)^{-1},$$

$$\xi = \frac{\theta}{\hbar\omega_l}, \quad \xi_{ph} = \frac{\hbar\bar{\omega}}{\hbar\omega_l}, \quad \xi_\Delta = \frac{\Delta}{\hbar\omega_l}, \quad \xi_T = \frac{\hbar\bar{\omega}}{T};$$

d is the deformation potential, and ρ is the density of the semiconductor. For a slightly overcritical level ($\theta - \Delta - \hbar\bar{\omega} \ll \hbar\bar{\omega}$), the first term in square brackets in formula (24) is much larger than the second term, so that the expression for ν_s can be written as

$$\nu_s = \nu_{s0}\left(1 + \frac{\xi - \xi_{ph} - \xi_\Delta}{4\xi_{ph}}\right), \quad (25)$$

where $\nu_{s0} = \nu'(\xi_\Delta)^{-1/2}\sqrt{2\xi_{ph}}$. In this case, the condition for the electron energy to be slightly overcritical becomes

$$\frac{\xi - \xi_{ph} - \xi_\Delta}{4\xi_{ph}} \ll 1. \quad (26)$$

With allowance for expressions (21) and (25) and the initial condition (23), Eq. (20) for the field amplitude

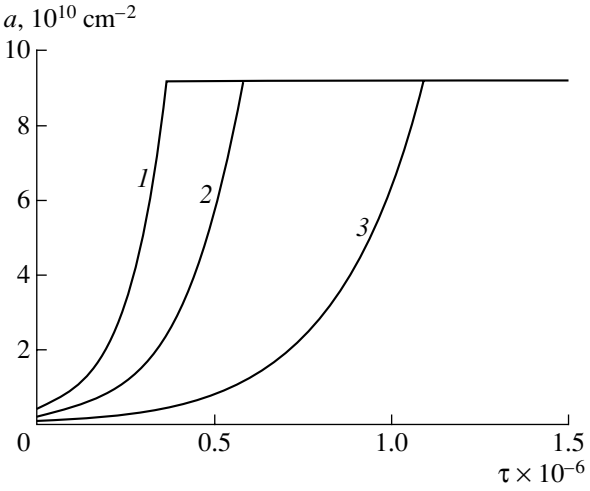

Time evolution $a(\tau)$ of the surface density of the beam electrons for (*1*) $N_{20} = 10^{14}$ cm^{-3} ($N_{10} \approx 10^{10}$ cm^{-3}), (*2*) $N_{20} = 5 \times 10^{13}$ cm^{-3} ($N_{10} \approx 5 \times 10^{9}$ cm^{-3}), and (*3*) $N_{20} = 2 \times 10^{13}$ cm^{-3} ($N_{10} \approx 2 \times 10^{9}$ cm^{-3}).

has the solution

$$a = \frac{a_\infty}{\sqrt{1 + C \cdot \exp(-\gamma_{nl} t)}}, \tag{27}$$

where

$$a_\infty = a_{cr}\sqrt{1 + C},$$
$$C = \frac{4\hbar\bar{\omega}}{\Delta + \hbar\bar{\omega} - T}\left(1 - \frac{\nu_{s0}\nu_b\omega}{\Omega_s^2\Omega_b}\right) \ll 1, \tag{28}$$

$$\gamma_{nl} = \frac{\Omega_s^2\Omega_b}{\omega\nu_{s0}}\left(1 - \frac{\nu_{s0}\nu_b\omega}{\Omega_s^2\Omega_b} + \frac{\Delta + \hbar\bar{\omega} - T}{4\hbar\bar{\omega}}\right) \ll \Omega_s, \tag{29}$$

and condition (26) has the form

$$0 \le \left(1 - \frac{\nu_{s0}\nu_b\omega}{\Omega_s^2\Omega_b}\right) \ll 1. \tag{30}$$

Using the above numerical estimates for the quantities in condition (30), we readily obtain

$$a_\infty \approx a_{cr} \approx 9 \times 10^{10}\ \text{cm}^{-2}, \quad C \approx 0.01,$$
$$\gamma_{nl} \approx 7 \times 10^{-4}\Omega_s, \quad \left(1 - \frac{\nu_{s0}\nu_b\omega}{\Omega_s^2\Omega_b}\right) \approx 0.04. \tag{31}$$

Note that the beam electrons with the temperature $T_b/k_B = 300$ K (corresponding to the velocity $v_0 = 0.1c$, where c is the speed of light in a vacuum), at which the relaxation rate ν_b satisfies condition (30), are monoenergetic [15]:

$$v_{Tb} = \sqrt{\frac{T_b}{m_0}} \propto 10^6\ \text{cm/s}$$
$$\ll v_0\left(\frac{N_{10}}{N_{20}}\right)^{1/3}\sqrt{1 - \frac{v_0^2}{c^2}} \propto 10^8\ \text{cm/s}. \tag{32}$$

Solution (27) implies that, to within small corrections, the equilibrium amplitude a_∞ is equal to the critical amplitude a_{cr}; i.e., we have $a_\infty \approx a_{cr}$. The figure shows time evolutions of the function $a(\tau)$ (where $\tau = \omega t$ with $\omega \propto \Omega_s$) for different volume densities of the electrons in a semiconductor and for $T/k_B = T_b/k_B = 300$ K. Note that, by τ, we mean the total rise time of the instability (from its onset up to the time of complete stabilization). We can see that a plateau in the time evolutions $a(\tau)$ forms immediately after the field amplitude reaches a critical level. As the initial value $a(0)$, we adopted the amplitude corresponding to the energy W_{th} of the thermal noise fluctuations in the system before the onset of the instability:

$$W_{th} \approx \frac{N_{20}T}{N_D}, \quad N_D \approx N_{20}(T/N_{20}e^2)^{3/2} \gg 1; \tag{33}$$

where N_D the number of electrons within the Debye sphere. We can also see that, the lower the density N_{20} (or, equivalently, the larger the number N_D), the longer the time required is for the field amplitude to reach a critical level and the smaller the initial field amplitude $a(0)$ is (or, equivalently, the lower the initial thermal noise level is).

Let us analyze the problem of the stability of an equilibrium state with the field amplitude $a = a_\infty$. In accordance with the corresponding Lyapunov stability criterion [14], we set $a = a_\infty + \psi$, where ψ is a small deviation of the field amplitude from its equilibrium value (i.e., $\psi/a_\infty \ll 1$). We insert this expression for a into Eq. (20) and expand the right-hand side of the resulting equation in powers of ψ to obtain

$$\frac{\partial\psi}{\partial t} = -2\gamma_{nl}\psi + O[(\psi/a_\infty)^2]. \tag{34}$$

We can see that the solution to Eq. (34) is an exponentially decreasing function $\psi = \psi_0\exp(-2\gamma_{nl}t)$, which indicates that the equilibrium state with $a = a_\infty$ is stable.

The final expressions for the quantities $n_1(x, t)$, $n_2(x, t)$, $E_y(0)$, and $E_{y1,2}(x, y, t)$ in the equilibrium state have the form

$$n_1(x, t) = a_\infty\cos(qx - \omega t), \tag{35}$$

$$n_2(x, t) = -\frac{\Omega_s^2}{\nu_{s0}\omega}a_\infty\sin(qx - \omega t) + O\left(\frac{\Omega_s^2}{\nu_{s0}^2}\right), \tag{36}$$

$$E_y(0) = \frac{4\pi e}{\varepsilon_1 + \varepsilon_2}\left[a_\infty \cos(qx - \omega t) + O\left(\frac{\Omega_s}{\nu_{s0}}\right)\right], \quad (37)$$

$$\begin{aligned} E_{y1}(x, y, t) &= E_y(0)\exp(-qy), \\ E_{y2}(x, y, t) &= -E_y(0)\exp(qy). \end{aligned} \quad (38)$$

4. CONCLUSION

The stabilization of unstable oscillations of both the surface electron density and the electric field of an electromagnetic surface wave that are excited by an electron beam propagating parallel to the plane boundary of GaAs has been studied in the hydrodynamic approximation under the assumption that the beam density is much lower than the electron density in a semiconductor and that the field of an electromagnetic surface wave is potential and harmonic. We have shown that, for GaAs (as well as for other $A^{III}B^{V}$ compound semiconductors), the stabilization mechanism is associated with the transitions of electrons between the neighboring valleys, provided that the electric field is above a certain critical level (the Ridley–Watkins–Hilsum mechanism). For a slightly overcritical level, we have derived expressions for the amplitude of the electric field of the surface wave and for the surface densities of both the beam electrons and the electrons in a semiconductor. We have established that, in this case, the equilibrium values of the electric field amplitude and electron density coincide with their critical values to within small corrections. We have also shown that, in the equilibrium state, the oscillations are Lyapunov-stable and the condition for the beam electron energy to be slightly above the critical level is satisfied only for monoenergetic beams.

ACKNOWLEDGMENTS

We are grateful to V.I. Karas' for a discussion of the results and useful remarks.

REFERENCES

1. A. I. Akhiezer and Ya. B. Faĭnberg, Dokl. Akad. Nauk SSSR **69**, 555 (1949).
2. A. I. Akhiezer and Ya. B. Faĭnberg, Zh. Éksp. Teor. Fiz. **21**, 1262 (1951).
3. D. Bohm and E. P. Gross, Phys. Rev. **75**, 1864 (1949).
4. N. N. Beletskiĭ, A. A. Bulgakov, S. I. Khankina, and V. M. Yakovenko, in *Plasma Instabilities and Nonlinear Phenomena in Semiconductors* (Naukova Dumka, Kiev, 1984), p. 192.
5. N. N. Beletskiĭ, V. M. Svetlichnyĭ, D. D. Khalameĭda, and V. M. Yakovenko, in *Electromagnetic Microwave Phenomena in Heterogeneous Semiconductor Structures* (Naukova Dumka, Kiev, 1991), p. 216.
6. V. B. Krasovitskiĭ, in *Nonlinear Regular Oscillations in Nonequilibrium Plasma and Gaseous Media*, Vol. 1: *Instabilities of a Relativistic Electron Beam in Plasma* (Folio, Kharkov, 2000), p. 268.
7. B. A. Al'terkop, S. E. Rosinskiĭ, and V. P. Tarakanov, Fiz. Plazmy **5**, 291 (1979) [Sov. J. Plasma Phys. **5**, 164 (1979)].
8. V. K. Grishin, S. T. Ivanov, and M. F. Kanevskiĭ, Fiz. Tekh. Poluprovodn. (Leningrad) **17**, 1417 (1983) [Sov. Phys. Semicond. **17**, 900 (1983)].
9. M. V. Kuzelev, O. V. Lazutchenko, and A. A. Rukhadze, Izv. Vyssh. Uchebn. Zaved., Radiofiz. **62**, 958 (1999).
10. Yu. V. Bobylev, M. V. Kuzelev, and A. A. Rukhadze, Zh. Éksp. Teor. Fiz. **118**, 105 (2000) [JETP **91**, 93 (2000)].
11. V. M. Yakovenko and I. V. Yakovenko, Dopov. Akad. Nauk Ukr., No. 1, 70 (2000).
12. E. M. Conwell, *High-Field Transport in Semiconductors* (Academic, New York, 1967; Mir, Moscow, 1970).
13. F. G. Bass and Yu. G. Gurevich, in *Hot Electrons and High-Power Electromagnetic Waves in Semiconductor and Gas-Discharge Plasmas* (Nauka, Moscow, 1975), p. 400.
14. A. A. Andronov, A. A. Vitt, and S. É. Khaikin, *Theory of Oscillators* (Fizmatgiz, Moscow, 1959; Pergamon, Oxford, 1966).
15. Ya. B. Faĭnberg and V. D. Shapiro, in *Interaction of Charged Beams with Plasmas* (Naukova Dumka, Kiev, 1965), p. 92.

Translated by I. A. Kalabalyk

Plasma Physics Reports, Vol. 27, No. 7, 2001, pp. 614–618. Translated from Fizika Plazmy, Vol. 27, No. 7, 2001, pp. 653–657.

BEAMS IN PLASMA

Beam–Plasma Interaction in a Hybrid Plasma Waveguide in the Pulsed Mode of Microwave Generation

A. N. Antonov, E. A. Kornilov, O. F. Kovpik, K. V. Matyash, and V. G. Svichenskiĭ

Kharkov Institute of Physics and Technology, National Science Center, Akademicheskaya ul. 1, Kharkov, 61108 Ukraine

Received November 23, 2000

Abstract—Results are presented from experimental studies of the energy spectra of an electron beam in a model beam–plasma oscillator based on a hybrid plasma waveguide in the pulsed mode of microwave generation with a pulse duration of 1 μs or shorter. The beam energy spent on sustaining the beam–plasma discharge in a slow-wave structure is measured. A correlation between the type of excited waves and the generation of a group of accelerated beam electrons with energies exceeding the injection energy is revealed. It is shown that the pulsed mode of microwave generation is related to the time variations in the plasma density profile in the waveguide and the trapping of beam electrons by the excited microwave field. *© 2001 MAIK "Nauka/Interperiodica".*

1. INTRODUCTION

In [1–6], we studied the excitation of direct waves by an electron beam in a hybrid plasma waveguide—a chain of inductively coupled resonators with a plasma-filled transit channel. In this paper, we present the results of experimental studies of the beam–plasma interaction in such a structure under conditions such that the continuous mode of microwave generation changes to the pulsed mode with a short pulse duration. Up to now, this stage of the plasma–beam interaction has been poorly understood. The results obtained may be useful for developing a complete self-consistent theory of the oscillation excitation by an electron beam in a hybrid plasma waveguide [4, 6] and are important for developing high-power microwave beam–plasma oscillators and amplifiers.

2. EXPERIMENTAL SETUP AND DIAGNOSTIC TECHNIQUES

We carried out experiments with a pulsed electron beam with an energy of 5–40 keV, a current of 1–10 A, and a pulse duration of 2 ms. The experimental setup and diagnostic techniques are described in [1, 2, 5]. A plasma with a density of ~10^{17} m^{-3} in the channel of inductively coupled resonators with a magnetic field of ~0.3 T was produced via the ionization of a gas in the slow-wave structure by both the beam electrons and the plasma electrons accelerated in the excited microwave field (the plasma–beam discharge) [7].

We studied the correlation between the amplitude of excited oscillations at frequencies of 2.4–4.4 GHz, the energy distribution function (EDF) of the beam electrons, the energy released in the oscillator elements, and the temporal behavior of the plasma density at the entrance and exit of the waveguide.

3. ENERGY SPECTRA OF THE BEAM ELECTRONS UPON CHANGES IN THE TYPE OF EXCITED WAVES

Investigations using the above techniques show that the interaction of an electron beam with the field of a plasma-filled slow-wave structure depends strongly on the nonlinear properties of the latter [2, 3] and, first of all, on the nonlinear wave dispersion caused by the change in the plasma density. This is clearly seen in the dynamics of microwave generation.

As the beam current or gas pressure in the slow-wave structure increases, the power of microwave oscillations excited in the waveguide grows and, when it exceeds a certain level, low-frequency ion-acoustic and slow magnetosonic waves are excited in the plasma column. The wave excitation is caused by the action of the microwave pressure on the plasma and occurs when the microwave power exceeds the threshold level, which is determined by the waveguide field topography. The low-frequency oscillations and the additional gas ionization in the beam-excited microwave fields, in turn, produce a nonuniform time-varying profile of the plasma density along the waveguide. As is well known, the plasma density in the slow-wave structure governs the type of the eigenmodes, the mode composition, and the phase velocity of the excited microwaves [8, 9]. If the beam excites direct waves, then, at certain instants when the descending plasma density profile is formed along the waveguide, the phase velocity of the waveguide eigenmodes decreases in the beam propagation direction. Since the beam-electron energy decreases during microwave generation, this makes it possible to maintain the resonance between the phase velocity of the excited microwave and the beam-electron velocity. Under these conditions, the conversion efficiency of the beam energy into microwave energy

1063-780X/01/2707-0614$21.00 © 2001 MAIK "Nauka/Interperiodica"

can attain 80–90%. This is confirmed by the measurements of the electron EDF and the beam energy loss at the exit from the waveguide.

The time-averaged EDF of the beam electrons is characterized by the presence of two peaks. One of them lies in the range below 10 keV, and the second corresponds to the energy that is several kiloelectronvolts lower than the energy with which the electrons are injected into the slow-wave structure. As the generated microwave power increases, the peaks of the beam-electron EDF shift toward lower energies and the second peak becomes smoother. Simultaneously, we observe the generation of fast electrons whose energy is higher than the electron energy at the entrance to the waveguide.

If the microwave power exceeds the threshold value, then the continuous increase in the modulation depth of the plasma density to 100% and the time evolution of the density profile along the waveguide are accompanied by a decrease in the duration of microwave pulses at the waveguide exit from several tens to 1 μs and shorter. In this case, the generation of microwave pulses becomes chaotic.

The increase in the plasma density in the waveguide is accompanied by an increase in the phase velocities of the waveguide eigenmodes. Conversely, when the plasma is expelled from the waveguide under the action of the microwave pressure, the phase velocities of the eigenmodes decrease and approach the phase velocities of the eigenmodes of a slow-wave structure free of plasma [8, 9]. This circumstance, as well as the decrease in the energy of the beam electrons, should lead to the suppression of microwave generation and the alternate excitation of direct and backward waves. As a result, microwave oscillations should be observed alternately at the entrance and exit of the waveguide. Such alternate excitation of microwave oscillations was observed experimentally in the pulsed mode of microwave generation. Figure 1 shows a simplified diagram that illustrates how the resonance between the electron-beam velocity and the wave phase velocity is displaced along the dispersion curve as the plasma density in the plasma waveguide increases and the beam energy is converted into microwave energy.

Experiments show that, in the pulsed mode of microwave excitation, a group of electrons with energies twice as high as the energy of the injected beam appears in the electron EDF. Since the direct-wave excitation is always accompanied by a decrease in the beam-electron energy, the generation of this group of electrons may be associated with backward-wave excitation due to the nonlinear dispersion of the waveguide modes caused by the microwave pressure. To verify this assumption, the beam injection energy and the plasma density were chosen such that, according to theoretical calculations of the waveguide dispersion relations, the microwave generation should begin with the excitation of the backward wave. In this experiment, we carried

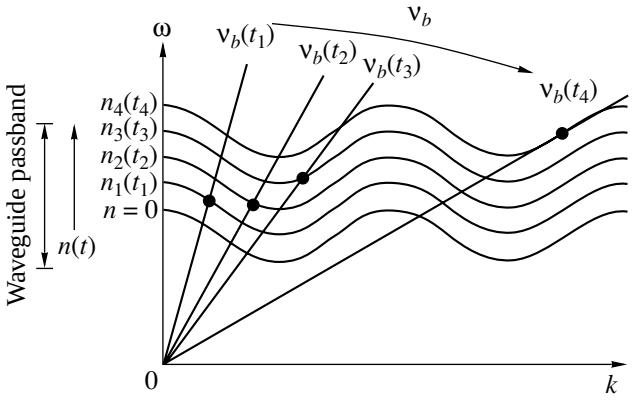

Fig. 1. Dispersion curves of the longitudinal waves of a hybrid waveguide for a gradually increasing plasma density $n(t)$. The points show the resonant values of ω and k for microwave oscillations excited by the electron beam whose energy decreases with time $v_b(t_1) > v_b(t_4)$.

out simultaneous measurements of the current of accelerated electrons and the microwave power at the entrance and exit of the waveguide. The results of these measurements are presented in Fig. 2. It is seen from the figure that electrons with an energy of 46.8 keV (the beam injection energy being 28 keV) are observed when the microwave power at the entrance to the waveguide is maximum and the plasma density at the exit from the waveguide is several times higher than that at the entrance. Although the peak power of direct waves at the exit from the waveguide is higher than the microwave power at the entrance by a factor of 2–3, the number of accelerated electrons with energies higher than the injection energy is nearly ten times less in the same time intervals.

Taking into account the observed correlation between the generation of accelerated electrons and the amplitude of the generated microwaves, as well as the previous results [1, 2], we can conclude that, in spite of the fact that the plasma density varies along the waveguide, the resonant conditions for the beam velocity and the wave phase velocity (self-resonance) are always satisfied due to the plasma–beam interaction in the slow-wave structure filled with a plasma that is sustained by a beam–plasma discharge. This occurs because the beam electrons lose their energy. One of the reasons why the system passes over to the pulsed mode of microwave generation is that both the type of the waveguide eigenmodes and the beam-energy conversion efficiency vary with time.

Figure 3 shows the EDF of the beam electrons at the exit from the waveguide for a beam injection energy of 30 keV and current of 4 A. In this case, chaotic microwave spikes with a mean power of 50 kW are generated. A specific feature of the electron EDF in this case is that the EDF has three peaks. (In contrast, in the case of the self-resonance between the beam and hybrid waves [5], when the beam velocity and the plasma den-

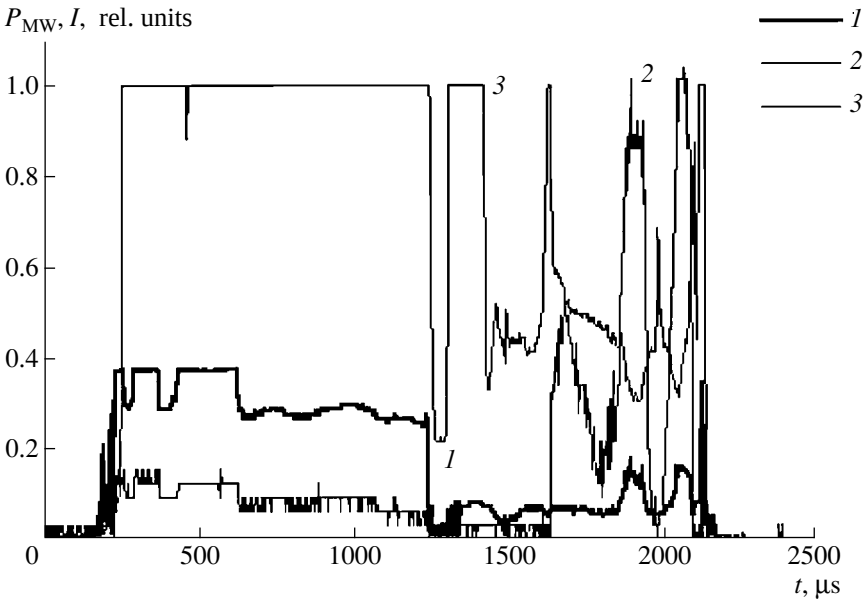

Fig. 2. Waveforms of the microwave power P_{MW} at (*1*) the entrance and (*2*) exit of the waveguide and (*3*) the current I of electrons with an energy of 46.8 keV. Unity corresponds to a microwave power of 63 kW. The parameters of the injected beam are $E_b = 28$ keV and $I_b = 4$ A; the gas pressure in the slow-wave structure is $p = 10^{-5}$ torr.

sity vary self-consistently, there are only two peaks in the electron EDF.) The peaks in the electron EDF are found to appear simultaneously with the microwave power at the entrance to the waveguide.

An analysis of the EFD in Fig. 3 shows that, after the interaction with the plasma in the hybrid waveguide, the number of beam electrons with energies higher than the injection energy is 39%. The total number of electrons with energies in the range 5–46 keV is lower than the number of injected electrons. Presumably, after the interaction, a fraction of the beam electrons have energies lower than 5 keV. In this energy range, it is difficult to detect these electrons against the background of plasma electrons. A fraction of the electrons have energies above 46 keV; it is difficult to determine the number of electrons in this energy range because of large measurement errors.

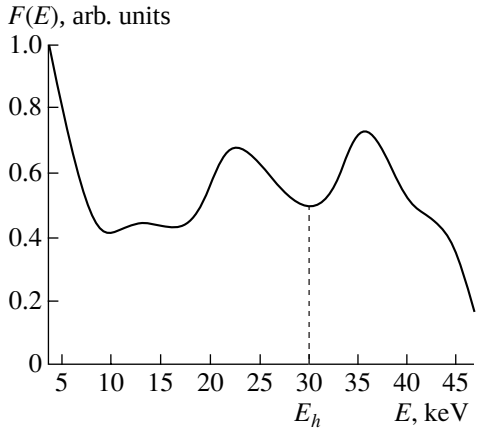

Fig. 3. Electron distribution function at the exit from the waveguide in the pulsed mode of microwave generation (chaotic generation of pulses with a duration of 0.5–1 μs). The energy of the injected electrons is $E_b = 30$ keV ($I_b = 4$ A); the pressure in the slow-wave structure is $p = 8 \times 10^{-5}$ torr.

The pulsed mode of microwave generation is characterized by an increase in the energy spent by the beam on gas ionization and the formation of flows of accelerated particles at the axis of the structure. The presence of accelerated particle flows is evidenced by variations in the magnitude and sign of the current at the collector. Most likely, the electrons with energies under 5–6 keV are plasma electrons. A fairly large fraction of the beam energy (up to 20–30%) is spent on sustaining the plasma, radiative losses, and the generation of accelerated particles. When calculating the energy deposited at the collector, the beam was assumed to consist of electrons with energies of 5–30 keV and the EDF shown in Fig. 3. It is these electrons that take part in the processes occurring in the waveguide, whereas the accelerated electrons do not participate in microwave generation and only extract the energy from the wave.

4. DISCUSSION OF RESULTS

Our experiments, as well as the previous studies [1–5], show that the plasma nonlinearity caused by the pressure of the excited microwaves and additional gas ionization by the beam plays a decisive role in the beam–plasma interaction (particularly, in the development of

the beam–plasma instability) in plasma-filled slow-wave structures (plasma waveguides). The onset of pulsed microwave generation is related to time variations in the longitudinal plasma density profile and the type of excited waves.

When direct waves are excited and the plasma density decreases in the beam propagation direction, the nonlinear properties of the plasma play a dominant role. When both the plasma density and the phase velocity of the waveguide eigenmodes increase in the beam propagation direction, the effects related to the nonlinearity of the beam electron motion come into play. The beam electrons that are in phase with waves are trapped and accelerated. These electrons extract the energy from the wave, so that the microwave power at the waveguide exit decreases. As the plasma density in the waveguide varies with time, the conditions for the efficient excitation of the direct waves by the electron beam are restored [2, 5]. The experimentally observed beam electron EDF with two peaks equidistant from the electron injection energy indicates that the trapped electrons remain in phase with the wave for no longer than one bounce period [10].

It should be noted that the pulsed microwave generation may also be influenced by other processes such as radial plasma loss and additional ionization of the gas emerging from the structure wall due to bombardment by the beam electrons scattered by the microwaves generated [5]. The effects observed can also be produced by the deep modulation of the plasma density at distances shorter than the size of the slow-wave structure if the plasma density in the transit channel becomes such that the frequency passband lies beyond the matching range of the output facility of the hybrid waveguide and the beam excites waves with zero group velocity. In this case, conditions can be created for the formation of short-lived plasma cavities (resonators), in which the electrons are accelerated.

Studies of the structure of the excited microwave pulses show that the amplitude modulation depth can be about 100% during the entire pulse, the modulation period being 10–30 ns [2]. We cannot ignore the effect of parametric decay instabilities on the duration of the microwave pulse, as well as the change of the mechanism for microwave generation due to the beam scattering by microwave fields.

Computer simulations of the interaction of an electron beam with a preformed magnetized plasma in a cylindrical waveguide in which the additional gas ionization by the beam is absent show that the effects related to the plasma nonlinearity are accompanied by energy transfer of the excited oscillations to the short-wavelength region of the spectrum [11]. The energy transfer is caused by the stimulated scattering of Langmuir waves by slow plasma electrons. During this process, the electron beam can excite higher order spatial harmonics [11, 12]. The amplitude of the excited oscillations saturates because the electrons are trapped by the beam and plasma waves and the short-wavelength oscillations are strongly damped via Landau damping by the plasma electrons [13]. When the noise or pulsed perturbations are excited in the beam–plasma system, the electrons are distributed chaotically, with a velocity spread on the order of the initial beam velocity. The highest plasma electron energy approaches the lower boundary of the beam EDF (see Figs. 11b, 11c, 13c in [11]). One can expect that the time-averaged EDF of the electrons leaving the beam–plasma system is similar to that shown in Fig. 3. Under certain conditions, one can observe the pulsed microwave generation and the periodical generation of accelerated beam electrons (with energies twice as large as the injection energy) and accelerated plasma electrons. For the hybrid plasma waveguide used in our experiments, this situation can take place when the plasma density in the transit channel is higher than 10^{17} m^{-3} (i.e., at high values of the beam current and plasma density in the structure). According to [11], the maximum conversion efficiency of the electron beam energy into microwave oscillations does not exceed 20–30%.

Our experiments show that the conversion efficiency of the electron beam energy into the total microwave energy at the entrance and exit of the waveguide in the pulsed mode of microwave generation can be higher than 50%. We note that, for the given type of hybrid waveguide, there is an optimal beam current at which microwave generation is most efficient. When the beam current exceeds a certain level, the microwave power at the exit from the waveguide decreases, while the energy deposition in the plasma increases. This effect may be attributed to the nonlinear processes considered in [11].

The following result of our study is of most practical importance. In order to obtain all the advantages of the hybrid plasma waveguide when designing high-power microwave amplifiers and oscillators with stable parameters, it is necessary that the plasma in slow-wave structures be produced by an independent auxiliary source and have a sharp radial boundary and that the degree of ionization of a gas with a high atomic weight be high [14]. It is also necessary to maintain the optimal plasma density profile along the waveguide. Furthermore, it is necessary to search for a new design of the hybrid plasma waveguide with a slow-wave structure such that low-frequency oscillations are excited at a higher level of microwave power. From the point of view of designing high-power beam–plasma microwave devices, it is of interest to consider ring plasma waveguides [15] and plasma-filled coaxial lines with disks at the electrodes [16].

In the future, it will be of interest to carry out experiments on pulsed microwave generation by an electron beam in a slow-wave structure whose transit channel is filled with a plasma produced by an auxiliary source with no additional ionization and to compare the results with those obtained in our study.

ACKNOWLEDGMENTS

We thank Ya.B. Faĭnberg, Yu.P. Bliokh, and V.A. Buts for fruitful discussions and M.G. Sokolov and B.P. Sevast'yanov for technical assistance. This study was supported in part by the Ukrainian Science and Technology Center, grant no. 256.

REFERENCES

1. A. N. Antonov, V. A. Balakirev, Yu. P. Bliokh, *et al.*, in *Proceedings of the 12th International Conference on High-Power Particle Beams (BEAMS'98), Haifa, 1998*, p. 286.
2. A. N. Antonov, Yu. P. Bliokh, E. A. Kornilov, *et al.*, Fiz. Plazmy **26**, 1097 (2000) [Plasma Phys. Rep. **26**, 1027 (2000)].
3. Yu. P. Bliokh, M. G. Lyubarsky, I. N. Onishchenko, *et al.*, in *Lectures on Microwave Electronics and Radiophysics, IX SGU Winter School, 1992*, p. 66.
4. Yu. P. Bliokh, Ya. B. Fainberg, M. G. Lyubarsky, and V. O. Podobinsky, Proc. SPIE **3158**, 182 (1997).
5. A. N. Antonov, Yu. P. Bliokh, E. A. Kornilov, *et al.*, Fiz. Plazmy **27**, 268 (2001) [Plasma Phys. Rep. **27**, 251 (2001)].
6. Yu. P. Bliokh, in *Proceedings of the International Conference "UHF-99," St. Petersburg, 1999*, p. 44.
7. I. F. Kharchenko, Ya. B. Faĭnberg, E. A. Kornilov, *et al.*, in *Proceedings of the International Conference on Plasma Physics, Salzburg, 1961*, Paper CN-10/20.
8. Ya. B. Faĭnberg, Yu. P. Bliokh, E. A. Kornilov, *et al.*, Dokl. Akad. Nauk Ukr. SSR, Fiz.-Mat. Tekh. Nauki, No. 1, 55 (1990).
9. Ya. B. Faĭnberg, Yu. P. Bliokh, M. G. Lyubarskiĭ, *et al.*, Fiz. Plazmy **20**, 757 (1994) [Plasma Phys. Rep. **20**, 681 (1994)].
10. V. A. Buts, O. V. Manuĭlenko, and A. P. Tolstoluzhskiĭ, Ukr. Fiz. Zh. **39**, 429 (1994).
11. M. V. Kuzelev, O. V. Lazutchenko, and A. A. Rukhadze, Izv. Vyssh. Uchebn. Zaved., Radiofiz. **62**, 958 (1999).
12. R. Ando, V. A. Balakirev, K. Kamada, *et al.*, Fiz. Plazmy **23**, 1042 (1997) [Plasma Phys. Rep. **23**, 964 (1997)].
13. E. M. Lifshitz and L. P. Pitaevskii, *Physical Kinetics* (Nauka, Moscow, 1979; Pergamon, Oxford, 1981).
14. E. A. Kornilov, O. F. Kovpik, S. M. Krivoruchko, and Ya. B. Faĭnberg, Fiz. Plazmy **24**, 1039 (1998) [Plasma Phys. Rep. **24**, 971 (1998)].
15. V. A. Balakirev, V. I. Karas', E. A. Kornilov, and Ya. B. Faĭnberg, Fiz. Plazmy **24**, 895 (1998) [Plasma Phys. Rep. **24**, 832 (1998)].
16. E. A. Kornilov, P. I. Markov, and G. V. Sotnikov, in *Proceedings of the International Conference "UHF-99," St. Petersburg, 1999*, p. 341.

Translated by N. F. Larionova

Plasma Physics Reports, Vol. 27, No. 7, 2001, pp. 619–624. Translated from Fizika Plazmy, Vol. 27, No. 7, 2001, pp. 658–663.

PLASMA DIAGNOSTICS

Optical Diagnostics of Lead and $PbGa_2S_4$ Layered Crystal Laser Plasmas

A. K. Shuaibov, A. I. Dashchenko, and I. V. Shevera

Uzhhorod National University, Pidgirna str. 46, Uzhhorod, 88000 Ukraine

Received June 5, 2000; in final form, November 13, 2000

Abstract—Laser plasmas produced at the surfaces of lead and a $PbGa_2S_4$ layered crystal irradiated by a neodymium laser with $\lambda = 1.06$ μm, pulse duration $\tau = 20$ ns, and intensity $W = (1–2) \times 10^9$ W/cm^2 are studied using optical diagnostics. It is shown that, in a lead plasma, the most intense (characteristic) lines are the PbI 405.7-nm, PbI 368.3-nm, PbI 364-nm, and PbII 220.4-nm lines. In a layered crystal plasma, the emission spectrum is an aggregation of the most intense PbI and GaI lines, whereas sulfur lines are absent. The bottlenecks of the recombination of the ionic and atomic components of the lead and $PbGa_2S_4$ crystal plasmas are determined. The average propagation velocity of the lead laser plume is 18–20 km/s. A comparative analysis of the emission dynamics of PbI and GaI lines in the laser plasmas of these metals and in the plasma of a $PbGa_2S_4$ crystal is carried out. The results obtained are important for the optical diagnostics of the plasmas of lead- and gallium-containing crystals and for the optimization of laser deposition of the thin films of these substances. © *2001 MAIK "Nauka/Interperiodica".*

1. INTRODUCTION

Optical diagnostics of the emission of lead, cadmium, and zinc gallate laser plasmas (along with mass-spectrometry and probe measurements) are of great importance for the optimization of laser deposition of thin composite films. The sputtering of such compounds occurs at a moderate neodymium laser intensity of 10^8–10^9 W/cm^2, and the laser plasma produced contains a fairly wide set of ion species. Thus, in a monocrystal $CdGa_2S_4$ laser plasma, S^+, Ga^+, and $CdGa_2S_4^+$ ions were recorded [1]. The emission spectra of crystal laser plasmas are rather complicated [2]; hence, it is important to study the optical characteristics of laser plasmas for individual crystal constituents at a moderate laser intensity. Thus far, such measurements for Pb, Cd, Zn, and Ga targets at moderate laser intensities have not been conducted by means of modern photoelectric recording systems. Optical diagnostics of the $PbGa_2S_4$ layered crystal laser plasma also have not been used.

In this paper, we present the results of optical diagnostics of the emission of lead and $PbGa_2S_4$ layered crystal laser plasmas obtained by irradiating a target in vacuum by a YAG:Nd^{3+} laser.

2. EXPERIMENTAL SETUP

Laser plasmas were produced by a repetitive neodymium laser with a pulse duration of 20 ns, repetition rate of 12 Hz, and focal-spot intensity of (1–2) × 10^9 W/cm^2. A plate of very-high-purity lead and a crystal were placed in a vacuum chamber ($P = 3$–12 Pa) and could be moved in the plane perpendicular to the laser beam at a speed of 0.5–2.0 mm/min. The laser plasma emission in the 210- to 600-nm spectral range was studied with the help of an MDR-2 monochromator, a FEU-106 photomultiplier, and a KSP-4 recorder. The recording system was calibrated with hydrogen and band lamps, which allowed us to measure the relative intensities of the emission lines J/k_λ, where k_λ is the relative spectral sensitivity of the monochromator–photomultiplier system. The relative intensities were measured with an accuracy of no less than 5%. The time evolution of the emission from the core of the laser plasma was recorded with a time resolution of 1–3 ns using an ÉLU-14FS photomultiplier and a 6LOR-04 high-speed oscillograph. The longer emission pulses from the laser plume were recorded with a time resolution of 30 ns using a pulsed FOTON photomultiplier and S1-99 oscillograph. The emission spectra were interpreted using the data from tables [3, 4] and papers [5, 6].

3. OPTICAL CHARACTERISTICS OF THE PLASMA

The time-averaged emission spectrum of a lead laser plasma is shown in Fig. 1. The spectrum was recorded from the laser plume axis at a distance of $r = 7$ mm from the target surface. The spectrum consists of a weak continuum and PbI and PbII line emission. There is no emission of PbIII or ions with higher charge numbers. The relative intensities of PbI and PbII emission lines and the distribution of the effective radiation fluxes related to the PbI and PbII transitions ($\Delta J/k_\lambda$) are presented in Table 1. The quantity $\Delta J/k_\lambda$ is the ratio (in percent) of J/k_λ for a given line to the total line emission

1063-780X/01/2707-0619$21.00 © 2001 MAIK "Nauka/Interperiodica"

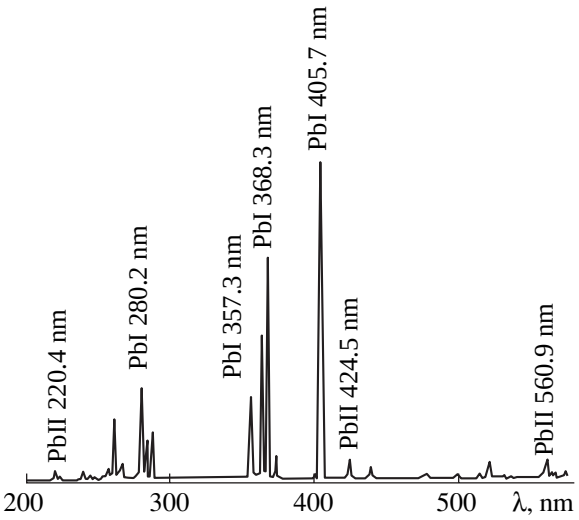

Fig. 1. Emission spectrum from the lead laser plasma recorded at a distance of r = 7 mm from the lead surface.

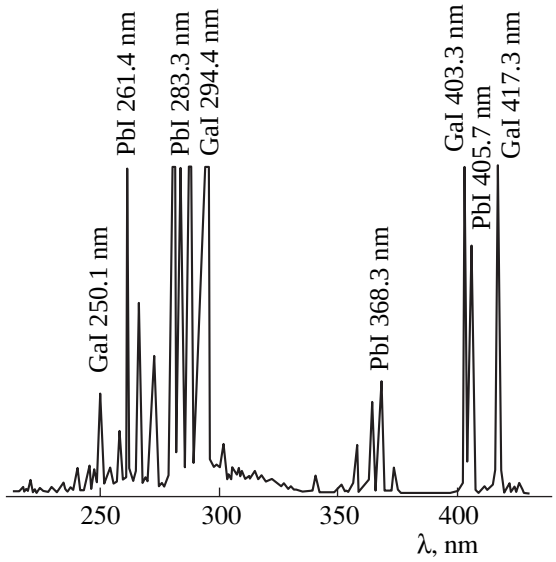

Fig. 2. Emission spectrum from the core of the $PbGa_2S_4$ layered crystal laser plasma recorded at a distance of r = 1 mm from the crystal surface.

intensity within the 210- to 600-nm spectral range. The most intense lines are the PbI 405.7-nm, PbI 368.3-nm, and PbI 364.0-nm lines, which carry half of the total line emission intensity. Among the ion lines, the PbII 220.4-nm line is the most intense. It is seen from Table 1 that the low-lying energy states of PbI with energies E_{up} of 4.34–4.37 eV and PbII with E_{up} = 14.79 eV are the most populated. The metastable states $6p^2\ ^3P_1$ and $6p^2\ ^3P_2$ with E_{up} = 0.97 and 1.32 eV and lifetimes of 0.14 and 2.6 s [7], respectively, are the lower levels for the most intense PbI emission lines. Presumably, the relatively low intensity of the resonant PbI 283.3-nm line is related to substantial self-absorption in the laser plasma.

The main mechanism for the production of excited particles in metal laser plasmas is the recombination of ions with low-energy electrons (provided that the plasma is formed in a vacuum without the influence of the outer atmosphere) [8, 9]. In our experiments, the recombination bottleneck (the highest lying upper levels related to the recorded emission lines) is the $^2F^0_{5/2}$ and $5f^2F^0_{7/2}$ PbII levels with E_{up} = 18.89 eV; for lead atoms, this is the $6p(^2P_{1/2})7d\ ^3D_2$ PbI level (E_{up} = 6.50 eV).

The emission spectrum from the core of the laser plasma of a $PbGa_2S_4$ layered crystal is shown in Fig. 2. The identified lines, relative line intensities, and quantities $\Delta J/k_\lambda$ for this multicomponent plasma are presented in Table 2. The last column presents the $\Delta J/k_\lambda$ values for a gallium laser plasma. The most intense spectral lines are the PbI and GaI lines from the low-lying electronic states with E_{up} = 3.07 and 4.31 eV for GaI and E_{up} = 4.37, 5.71, and 5.74 eV for PbI. In the crystal plasma, the recombination bottleneck is located at E_{up} = 6.50–6.51 eV and is related to the PbI line emission. There were practically no sulfur lines in the spectrum. At the given laser power, no laser plume was formed at the surface of the very high purity sulfur, and the glowing point on the target surface radiated mainly in continuum.

For most of the emission lines of a $PbGa_2S_4$ layered crystal plasma, the effective radiation fluxes are much less than in lead or gallium plasmas (see Tables 1, 2). In the crystal plasma, the most intense and clearly resolved spectral lines are the PbI 405.7-nm, PbI 283.3-nm, PbI 280.2-nm, PbI 261.4(3)-nm, GaI 403.3-nm, GaI 294.4-nm, and GaI 272.0-nm lines. These lines can be used to determine the electron density and temperature, the densities of lead and gallium atoms in the ground and metastable states, and other plasma parameters using various optical techniques, such as absorption, emission, and stimulated luminescence. The $PbGa_2S_4$ laser plasma contains complex ions; therefore, in addition to dielectronic recombination ($Pb^+ + 2e \longrightarrow Pb^* + e$), dissociative recombination ($PbGa_2S_4^+ + e \longrightarrow Pb^*(Ga^*) +$ products) can significantly contribute to the population of the excited atomic states. The rate constants of these processes increase with increasing ion complexity and can attain $(1–2) \times 10^{-6}$ cm^3/s [10].

To study the mechanisms for the production of excited particles in the lead and $PbGa_2S_4$ crystal laser plasmas in more detail, we investigated the dynamics of the line emission from different spatial regions of the laser plasma.

Table 1. Intensity distribution in the emission spectrum of the lead laser plasma (r = 7 mm)

Atom (ion) λ, nm	Transition	E_{up}, eV	J/k_λ, rel. units	$\Delta J/k_\lambda$, %
PbII 560.9	$7s^2S_{1/2}$–$7p^2P^0_{3/2}$	17.00	0.20	<5
PbI 520.1	$6p^21S_0$–$6p(^2P_{1/2})8s^3P^0_1$	6.04	0.10	<5
PbI 500.5	$6p^21S_0$–$6p(^2P_{3/2})7s^1P^0_1$	6.13	0.05	(<1)
PbII 478.8	–	–	0.05	(<1)
PbII 438.7	$^2D_{3/2}$–$^2F^0_{5/2}$	18.89	0.05	(<1)
PbII 424.5	$6d^2D_{5/2}$–$5f^2F^0_{7/2}$	18.89	0.10	<5
PbI 405.7	$6p^23P_2$–$6p(^2P_{1/2})7s^3P^0_1$	4.37	1.00	25
PbI 374.0	$6p^21D_2$–$6p(^2P_{3/2})7s^3P^0_2$	5.97	0.10	<5
PbI 368.3	$6p^23P_1$–$6p(^2P_{1/2})7s^3P^0_0$	4.34	0.70	15
PbI 364.0	$6p^23P_1$–$6p(^2P_{1/2})7s^3P^0_1$	4.37	0.50	10
PbI 357.3	$6p^21D_2$–$6p(^2P_{3/2})7s^1P^0_1$	6.13	0.25	5
PbI 287.3	$6p^23P_2$–$6p(^2P_{1/2})6d^3F^0_2$	5.63	0.20	<5
PbI 283.3	$6p^23P_0$–$6p(^2P_{1/2})7s^3P^0_1$	4.37	0.15	<5
PbI 280.2	$6p^23P_2$–$6p(^2P_{1/2})6d^3F^0_3$	7.74	0.35	8
PbI 266.3	$6p^23P_2$–$6p(^2P_{3/2})7s^3P^0_2$	5.97	0.05	<5
PbI 261.4(3)	$6p^23P_1$–$6p(^2P_{1/2})6d^3D^0_{2,1}$	5.71	0.25	5
PbI 257.7	$6p^23P_2$–$6p(^2P_{3/2})7s^1P^0_1$	6.13	0.05	<5
PbI 239.4	$6p^23P^0_2$–$6p(^3P_{1/2})7d^3F_3$	6.50	0.05	<5
PbI 224.7	$6p^23P^0_1$–$6p(^2P_{1/2})7d^3D_2$	6.48	0.05	<5
PbII 220.4	$6p^2P_{3/2}$–$7s^2S_{1/2}$	14.79	0.20	5

Typical waveforms of the intensities of the PbI and PbII line emission from the plasma core are shown in Fig. 3. In all of the waveforms, the time is counted from the leading edge of the neodymium laser pulse. The continuum emission lasts for 20–30 ns (which is close to the duration of the laser pulse) and has a specific shape with two maxima. Most of the waveforms of the PbI and PbII line intensities also have two maxima. As in an aluminum laser plasma and the plasmas of some other metals [8], the duration hierarchy of the emissions related to PbI and PbII transitions corresponds to the recombination mechanism for populating the upper excited states. Two maxima in the waveforms of the PbI and PbII line intensities may be related to the two phases of the target surface evaporation [9]. In most cases, the two maxima in the waveforms of the ion line intensities reveal themselves (with a delay for recombination) in the waveforms of the PbI line intensity. The recombination times (τ_r) of PbIII and PbII ions in the plasma core were determined by the formula

$$\ln[J(t)/J(0)] = -t/\tau_r,$$

where J is the emission intensity at the trailing edge of the emission pulse and t is time. The recombination time of PbIII ions was determined from the waveform

Table 2. Intensity distribution in the emission spectrum of the core of the $PbGa_2S_4$ layered crystal laser plasma (r = 1 mm)

Atom (ion) λ, nm	Upper state	E_{up}, eV	J/k_λ, rel. units	$\Delta J/k_\lambda$, % [$PbGa_2S_4$]	$\Delta J/k_\lambda$, % [Ga]
GaII 426.2	–	17.02	0.05	<1	<1
GaI 417.3	$5^2S_{1/2}$	3.07	0.10	1.3	30
PbI 405.7	$6p(^2P_{1/2})7s^3P_1^0$	4.37	0.50	6.0	–
GaI 403.3	$5^2S_{1/2}$	3.07	0.70	8.0	15
PbI 374.0	$6p(^2P_{3/2})7s^3P_2^0$	5.97	0.05	<1	–
PbI 368.3	$6p(^2P_{1/2})7s^3P_0^0$	4.34	0.25	3.5	–
PbI 364.0	$6p(^2P_{1/2})7s^3P_1^0$	4.37	0.20	2.5	–
PbI 357.3	$6p(^2P_{3/2})7s^1P_1^0$	6.13	0.10	1.3	–
PbII 301.6	–	12.75	0.15	2.0	–
GaI 294.4	$4^2D_{5/2,\,3/2}$	4.31	1.00	12.0	30
GaI 287.4	$4^2D_{3/2}$	4.31	0.85	10.0	15
PbI +287.3	$6p(^2P_{1/2})6d^3F_2^0$	5.63	–	–	–
PbI 283.3	$6p(^2P_{1/2})7s^3P_1^0$	4.37	0.65	8	–
PbI 280.2	$6p(^2P_{1/2})6d^3F_3^0$	5.74	0.75	9	–
GaI 272.0	$6^2S_{1/2}$	4.66	0.40	5	<5
GaI 266.5	$4s4p^{24}P_{3/2}$	4.75	0.50	6	<5
PbI +266.3	$6p(^2P_{3/2})7s^3P_2^0$	5.97	–	–	–
PbI 261.4(3)	$6p(^2P_{1/2})6d^3D_{2,\,1}^0$	5.71	0.95	11	–
PbI 257.7	$6p(^2P_{3/2})7s^1P_1^0$	6.13	0.20	2.5	–
GaI 250.1	$5^2D_{5/2,\,3/2}$	5.06	0.35	4.0	5
PbI 247.6	–	5.98	0.10	1.3	–
GaI 245.0	$5^2D_{3/2}$	5.06	0.10	1.3	<5
PbI 239.4	$6p(^3P_{1/2})7d^3F_3$	6.50	0.15	2.0	–
PbI 223.7	–	6.51	0.10	1.3	–
PbII 220.4	$7s^2S_{1/2}$	14.79	0.20	2.5	–

of the PbII 438.7-nm line intensity, and that of PbII ions was determined from the waveforms of the PbI 405.7-nm and PbI 280.2-nm line intensities. The values of τ_r were determined from the slope of the $\ln[J(t)/J(0)]$ curve and were found to be 20 ns for the PbII 438.7-nm line, 50 ns for the PbI 280.2-nm line, and 170 ns for the PbI 405.7-nm line.

As the distance between the observation point and the target surface increased to $r = 7$ mm, the full widths of the PbI and PbII line emission pulses increased to 2–3 μs (Fig. 4). Since the intensities of the PbII lines were very low, their waveforms were recorded with a fairly high input resistance of the S1-99 oscillograph ($r_{in} = 6.3$ kΩ), whereas the waveforms of the PbI line emission were recorded with $r_{in} = 0.43$ kΩ. This resulted in a substantial increase in the recorded duration of the PbII line emission compared with that of PbI emission. The average propagation velocity v of the laser plume, which was estimated from the waveforms of the PbI 405.7-nm line emission, was $v = 18$–20 km/s. The PbI 280.2-nm line emission was delayed by $t_d = 200$ ns with respect to the PbI 405.7-nm and PbI 364.0-nm lines, which are related to transitions from the lower lying energy levels. The lower level for both the PbI 405.7-nm and PbI 280.2-nm lines is the metastable $6p^2\ ^3P_2$ state; hence, the delay in the 280.2-nm line emission is related to different mechanisms for populating their upper levels (in particular, the common upper level for the PbI 405.7-nm and PbI 364.0-nm lines is populated via cascade transitions, whereas the cascade mechanism does not contribute to the population of the upper level for the PbI 280.2-nm line). The same time delay was observed for the PbI 261.3(4)-nm lines, whose upper levels were not populated via cascade transitions.

Figure 5 presents the time evolution of the emission intensity from the core of a $PbGa_2S_4$ layered crystal laser plasma. In this multicomponent plasma, the waveforms of PbI and GaI line emission, which consist of a short primary pulse followed by the main long pulse (with a full width of $t = 150$–200 ns), are much shorter than those in pure metal (Pb or Ga) plasmas. The GaI 403.3-nm resonant line emission has the shortest duration. The intensity of GaI line emission from the lowest $5^2S_{1/2}$ level ($E_{up} = 3.07$ eV) is maximum at 20–30 ns, whereas the main maximum of the waveforms of PbI and GaI line emission from the higher lying levels is delayed by 50–80 ns. Presumably, this dynamics of the PbI and GaI line emission in a $PbGa_2S_4$ laser plasma is related to a significant contribution from the dissociative recombination of complex ions ($PbGa_2S_3^+$, $PbGa_2S_4^+$, etc.) with electrons. These reactions are characterized by the selective population of low-lying energy levels of the decay products of the complex ions. The rate constants of dissociative recombination and dielectronic recombination depend on the electron temperature as $k_1 \sim (T_e)^{-1/2}$ and $k_2 \sim (T_e)^{-9/4}$ [10, 11],

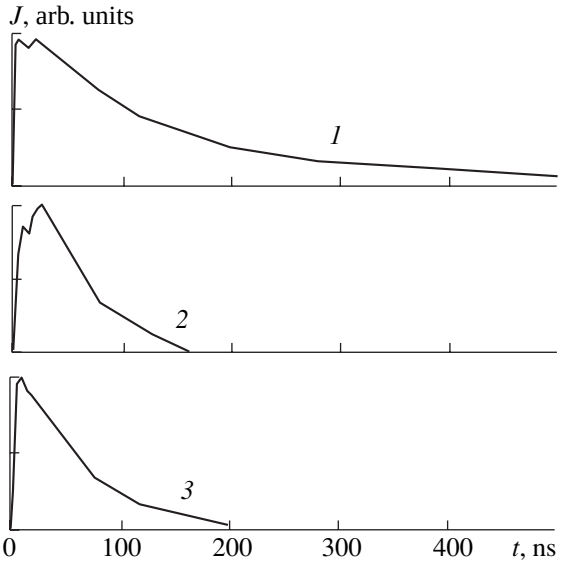

Fig. 3. Waveforms of the line emission intensity from the core of the lead laser plasma: (*1*) PbI 405.7-nm, (*2*) PbII 438.7-nm, and (*3*) PbI 280.2-nm lines.

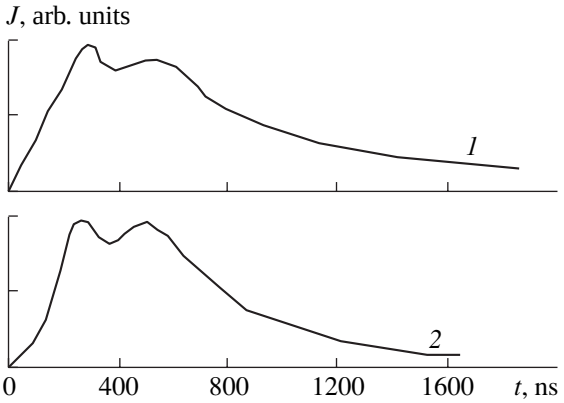

Fig. 4. Waveforms of the line emission intensity from the lead laser plume: (*1*) PbI 405.7-nm and (*2*) PbII 438.8-nm lines.

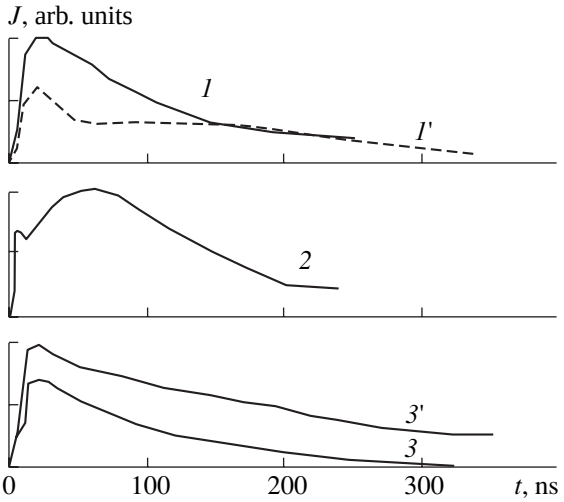

Fig. 5. Waveforms of the line emission intensity from the core of the (*1–3*) $PbGa_2S_4$ layered crystal plasma and (*1'*, *3'*) gallium laser plasma: (*1*, *1'*) GaI 417.3-nm, (*2*) PbI 405.7-nm, and (*3*, *3'*) GaI 403.3-nm lines.

respectively, which also intensifies dissociative recombination at elevated T_e (in the core of the laser plasma).

4. CONCLUSION

We have shown that, when lead or $PbGa_2S_4$ crystal targets are irradiated by a neodymium laser with an intensity of $(1–2) \times 10^9$ W/cm^2, the optical characteristics of the lead plasma are determined by the PbI 405.7-nm, PbI 368.3-nm, and PbI 364-nm lines with an upper level energy of 4.34–4.37 eV and the PbII 220.4-nm ion line. The recombination bottleneck is the $^2F_{5/2}$ and $5f\,^2F^0_{7/2}$ states of PbII (E_{up} = 18.89 eV); for the atomic component, the bottleneck is the $6p(^2P_{1/2})7d^3D_2$ state (E_{up} = 6.50 eV). In the $PbGa_2S_4$ crystal laser plasma, the most intense spectral lines are PbI and GaI lines, whereas SII and SI lines are absent. The average propagation velocity of the lead laser plume is 18–20 km/s. The dynamics of the PbI and GaI line emission in laser plasmas of these metals and in the $PbGa_2S_4$ crystal plasma are quite different, which may be related to the contribution from the dissociative recombination of complex ions ($PbGa_2S_4^+$, $Ga_2S_4^+$, etc.) to the population of PbI and GaI excited states in the $PbGa_2S_4$ mulicomponent plasma. The most intense PbI and GaI lines in the $PbGa_2S_4$ crystal laser plasma, which is used to deposit thin films of the given compound, are of interest from the standpoint of measuring the parameters of this plasma (n_e, T_e, metastable atom density, etc.).

REFERENCES

1. I. É. Kacher, I. I. Opachko, and M. Yu. Rigan, Ukr. Fiz. Zh. **34**, 1728 (1989).
2. B. K. Kotlyarchuk, D. I. Popovich, and V. Ya. Pentko, Zh. Tekh. Fiz. **57**, 1824 (1987) [Sov. Phys. Tech. Phys. **32**, 1091 (1987)].
3. A. N. Zaĭdel', V. K. Prokof'ev, S. M. Raĭskiĭ, *et al.*, *Tables of Spectral Lines* (Nauka, Moscow, 1969; Plemun, New York, 1970).
4. A. P. Striganov and G. A. Odintsova, *Handbook of Spectral Lines of Atoms and Ions* (Énergoatomizdat, Moscow, 1982).
5. L. L. Shimon, É. I. Nepiĭpov, V. L. Goldovskiĭ, and N. V. Golovchak, Ukr. Fiz. Zh. **20**, 232 (1975).
6. I. S. Aleksakhin, A. A. Borovik, V. P. Starodub, and I. I. Shafran'osh, Opt. Spektrosk. **46**, 1125 (1979) [Opt. Spectrosc. **46**, 636 (1979)].
7. A. A. Radtsig and B. M. Smirnov, *Reference Data on Atoms, Molecules, and Ions* (Énergoatomizdat, Moscow, 1986; Springer-Verlag, Berlin, 1985).
8. V. I. Derzhiev, A. G. Zhidkov, and S. I. Yakovlenko, *Ion Radiation in Nonequilibrium Laser Plasma* (Énergoatomizdat, Moscow, 1986).
9. L. T. Sukhov, *Laser Spectrum Analysis (Physical Principles)* (Nauka, Novosibirsk, 1990).
10. A. V. Eletskiĭ and B. M. Smirnov, Usp. Fiz. Nauk. **136**, 25 (1982) [Sov. Phys. Usp. **25**, 13 (1982)].
11. *Gas Lasers*, Ed. by E. W. McDaniel and W. Nigan (Academic, New York, 1982; Mir, Moscow, 1986).

Translated by N. N. Ustinovskiĭ

Plasma Physics Reports, Vol. 27, No. 7, 2001, pp. 625–633. Translated from Fizika Plazmy, Vol. 27, No. 7, 2001, pp. 664–672.

LOW-TEMPERATURE PLASMA

Ionization of Sputtered Metal Atoms in a Microwave ECR Plasma Source

N. P. Poluektov, V. N. Kharchenko, and I. G. Usatov

Moscow State University of Forestry, Pervaya Institutskaya ul. 1, Mytishchi, Moscow oblast, 141005 Russia

Received November 29, 2000; in final form, February 2, 2001

Abstract—The ionization of sputtered aluminum atoms in the plasma of a microwave ECR discharge intended for metal coating of submicron-size structures in microelectronics is studied. The spatial distributions of xenon plasma parameters and their variations under the action of metal atoms are investigated using probe and optical emission spectroscopy techniques. © *2001 MAIK "Nauka/Interperiodica".*

1. INTRODUCTION

Present-day ULSI technology requires the metallization of submicron-size vias and trenches with an aspect (depth-to-width) ratio of 2–5. The use of magnetron sputtering for this purpose encounters serious difficulties. The flow of sputtered metal is almost completely atomic. The angular distribution of sputtered atoms is approximately described by a cosine function. When filling high-aspect-ratio submicron structures, this nearly isotropic distribution of metal atoms results in the formation of an overhang at the entrance to the structure and a void inside it. In order for the filling to be conformal, it is necessary that the majority of incident particles be accelerated perpendicular to the substrate surface. The broad angular spectrum of sputtered atoms can be narrowed with a collimator (a plate with holes of definite depth-to-diameter ratio) that is placed between the target and substrate [1]. A disadvantage of this method is that the collimator decreases the deposition rate, which, in addition, varies with time because of the shrinking of the holes due to the metal deposition on their walls. Moreover, this technique fails to provide a high-quality metal coating for structures with opening diameters less than 0.25 μm and aspect ratios larger than 3.

This problem can be resolved by ionizing the sputtered metal atoms because the motion of the produced ions can be controlled by the external magnetic field or the electric field in the sheath near the substrate.

One of the possible methods for ionizing metal atoms is to combine a magnetron source with an inductively coupled discharge source.

One- to three-turn RF antenna is placed between the magnetron and substrate. The antenna is powered at 13.56 MHz to produce an inductively coupled plasma. The atoms of the sputtered metal are ionized during their motion from the magnetron target to the substrate. The degree of ionization of the sputtered metal attains 30%, and the fraction of metal ions (whose velocities are much higher than the atom velocity) in the total flux ranges from 20% at a pressure of 5 mtorr to 80% at a pressure of 50 mtorr [2–5]. There is an optimum ratio between the powers of the magnetron discharge and the inductively coupled discharge. At high magnetron powers such that the density of the metal atoms is higher than the argon density, the quality of the metal coating decreases. Since the ionization energies of copper and aluminum are lower than that of argon, the presence of a large amount of metal atoms reduces the plasma temperature and, consequently, the ionization rate.

Another method is based on the use of a microwave electron-cyclotron resonance (ECR) discharge, in which the plasma is produced in a magnetic field due to the strong absorption of microwave radiation under the ECR conditions. In such a discharge, a plasma with a density higher than 10^{11} cm^{-3} and degree of ionization of metal atoms from 30 to 90% can be created at pressures of several mtorr [6–8].

In this paper, the spatial distributions of the xenon plasma parameters behind an aluminum target and the influence of sputtered metal atoms on these parameters are studied using probe and spectroscopy techniques. We note that metal plasma is difficult to investigate because the probe measurements are hampered by coating the probe insulator with metal, whereas the optical methods for measuring the electron temperature and atom density do not provide good accuracy.

2. EXPERIMENTAL SETUP AND DIAGNOSTIC TECHNIQUES

We carried out experiments on the sputtering of an aluminum target in a plasma source based on a microwave ECR discharge in a hybrid magnetic field. A schematic of the experimental facility is shown in Fig. 1. A detailed description of it is given in [9]. The vacuum chamber consists of a plasma source (15 cm in diameter and 25 cm long) and a reactor (35 cm diameter and 60 cm long). The working gas is xenon. The magnetic field is produced by three electromagnets and twelve

1063-780X/01/2707-0625$21.00

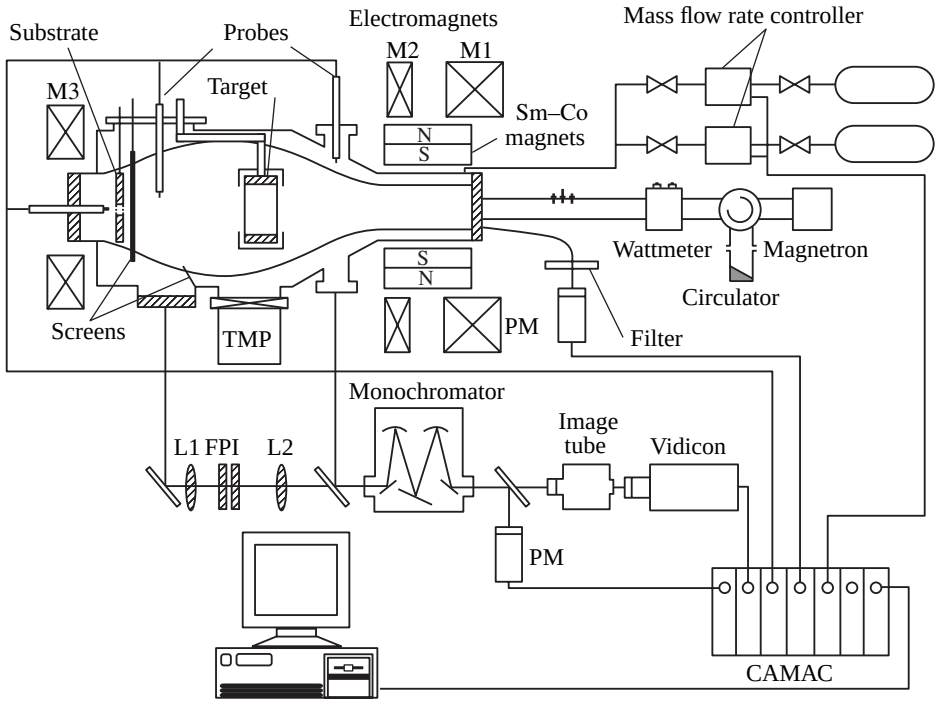

Fig. 1. Schematic of the experimental apparatus.

permanent Sm–Co magnets. The axial profile of the magnetic field at a current of 210 A is shown in Fig. 2. This profile allowed us to produce a plasma with a density higher than 10^{11} cm^{-3} at a distance of 40 cm from the source. A hollow 5-cm-long aluminum cylinder with an inner diameter of 8 cm served as a target. The cylinder was enclosed by an insulated stainless steel shield and was placed at a distance of 15 cm from the source (40 cm from the quartz window through which the microwave power was supplied). The incident, absorbed, and reflected powers were measured using a wattmeter. Coating the entrance window with a sputtered metal over ten hours of device operation only slightly affected the reflected power. The power supplied to the target was varied within the 200–400 W range. A 120-mm-diameter quartz substrate with a 7-mm-hole for fixing a probe was placed at a distance of 20 cm from the target. The third electromagnet was set in such a way that its magnetic field lines were normal to the substrate.

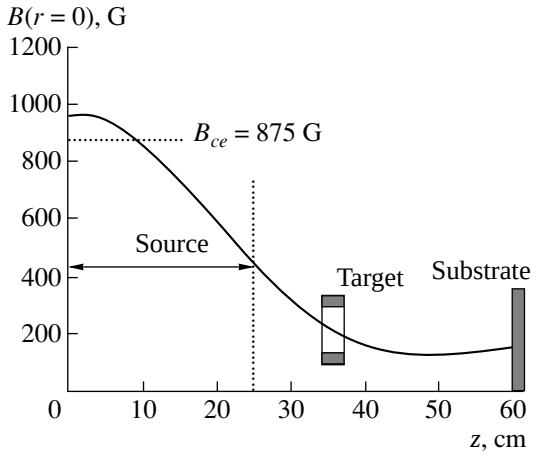

Fig. 2. Magnetic field produced by the electromagnets at I_{magn} = 210 A and r = 0 cm.

The efficiency of ionization of metal atoms depends on the atom and electron densities, electron energy, and the presence of metastable atoms of the plasma-forming gas. The electron temperature, electron energy distribution function, ion density, floating probe potential, and plasma potential were determined from probe measurements. Most of the measurements were taken with cylindrical probes because they are less sensitive to metal dusting. The probe tip was made of a tungsten wire 0.35 mm in diameter and 6 mm long. To reduce the influence of the magnetic field, the probe tip was set normal to the magnetic field lines. The probe tip was encased in ceramic (0.6 mm i.d.) and quartz (5 mm i.d.) tubes to prevent an electric short circuit. Before measuring the current–voltage (I–V) characteristic, a voltage of –80 V was applied to the probe in order to clean it by ion bombardment. A 3-mm-diameter disc-shaped plane probe was used to measure the ion density at the

discharge axis. The magnetic field in the measurement region behind the target was less than 150 G.

The *I–V* characteristics were recorded with the help of CAMAC modules and a special computer code. The recording system consisted of a digital-to-analog converter, a voltage amplifier (with an output voltage range from –80 to +80 V at an output current of up to 500 mA and a voltage rise time of up to 10 V/μs), a measurement unit, an analog multiplexer, and an analog-to-digital converter (f = 1 MHz). The probe *I–V* data included up to 640 points (voltage–current pairs, each of them being an average over ten measurements) and was recorded in a time less than 5 s. A built-in graphic program permitted us to monitor and select the data obtained.

The *I–V* data obtained were smoothed with cubic splines; then, the first and second derivatives of the probe current were calculated to determine the plasma potential V_s and the electron energy distribution function (EEDF) $f(E)$, respectively. The electron temperature T_e was determined from the slope of the logarithm of the probe electron current versus voltage to the left of the plasma potential.

Without sputtering, the plasma density was determined from the ion saturation current using the technique proposed in [10]. However, the ion saturation current of a cylindrical probe changes due to formation of a sheath. In this case, the ion current was determined by the formula $I_{Xe^+} = en_{Xe^+}S(kT_e/2\pi M_{Xe})^{1/2}i_i$, where M_{Xe} is the xenon ion mass, S is the probe area, e is the electron charge, k is the Boltzmann constant, and T_e is the electron temperature. The values of the correction coefficient i_i, which depends on the r/λ_D ratio (where λ_D is the Debye radius), and the dimensionless potential $X = e(V_s - V_p)/kT_e$ (where V_s and V_p are the plasma and probe potentials, respectively) were taken from [10]. The obtained density values agree within a 30% accuracy with those derived from the ion saturation current of a plane probe by the formula $I_{Xe^+} = 0.61en_{Xe^+}S(kT_{e1}/M_{Xe})^{1/2}$.

With sputtering, the probe also collects metal ions. Hence, taking into account the Bohm formula for the ion velocity, the ion current to a plane probe is

$$I_{Xe^+ + Al^+} = 0.61eS\left(\frac{n_{Al^+}}{\sqrt{M_{Al}}} + \frac{n_{Xe^+}}{\sqrt{M_{Xe}}}\right)\sqrt{kT_{e2}},$$

where n_{Al^+} is the density of Al ions. This formula was used to estimate the value of n_{Al^+} from the difference between the ion currents with and without target sputtering. The measurements show that the electron temperature T_{e2} and the intensity of the Xe ion emission decrease by several percent on applying the voltage to the target. Assuming that the Xe ion density does not change, the difference between the ion currents in the discharge with and without applying the voltage to the target is equal to the Al ion current. The density of Al ions was calculated by the formula

$$n_{Al^+} = n_{Xe^+}\sqrt{\frac{M_{Al}T_{e1}}{M_{Xe}T_{e2}}}\left(\frac{I_{Xe^+ + Al^+} - I_{Xe^+}}{I_{Xe^+}} + 1 - \sqrt{\frac{T_{e2}}{T_{e1}}}\right).$$

Due to the influence of the magnetic field, the electron density n_e determined from the electron current at the probe under the plasma potential is lower by a factor of 2.5–3. On the other hand, the value of n_{Al^+} can also be estimated from the ratio between the electron densities measured with and without applying voltage to the target.

The plasma emission spectra were studied with the help of a monochromator. The emission could be observed from the regions located at a distance of 10 cm in front of the target and 10–20 cm behind the target and also through the source entrance window using an optical fiber (Fig. 1). The atom and electron temperatures were determined using a Fabry–Perot interferometer (FPI), which was placed in front of the monochromator. A vidicon with an electron-optical converter was used as a detector.

3. RESULTS AND DISCUSSION

Measurements were carried out in xenon plasma at electromagnet currents of 210 A, which corresponded to a magnetic field induction of B_w = 960 G near the quartz window. It was shown in [11] that, within an 8-cm-diameter region where the target was situated, the discharge plasma in such a field was rather dense, but spatial variations in the plasma density attained 40%.

Figure 3 presents the ion current (squares) measured by a probe located at a distance of 12 cm from the target in the center of the discharge and the target current (circles) as functions of the microwave power. The ion current increases proportionally to the microwave power and does not saturate at high powers. The target current I_{targ} and the intensity J of the Al 396.1-nm spectral line versus the target voltage U_{targ} are shown in Fig. 4. The rapid increase in the target current is followed by its saturation at $U_{targ} > 200$ V. The intensity of Al line emission increases linearly until U_{targ} = 500 V; then, the growth rate decreases. Such a dependence is explained by the fact that the metal sputtering yield increases within the 100–500 V voltage range.

The current–voltage characteristics measured with a plane probe located at the chamber axis behind the Al target, at a distance of 15 cm from it, with and without target sputtering are shown in Fig. 5. The characteristics are easily reproducible. The ion (see the inset in Fig. 5) and electron currents are seen to increase on applying the voltage to the target. Note that the average density of the target ion current is approximately half of

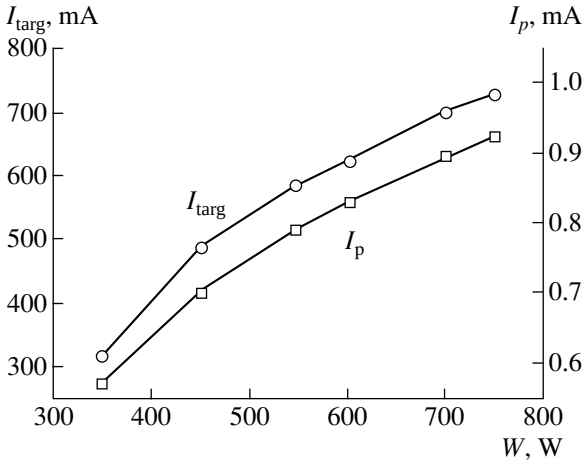

Fig. 3. Target current and saturation ion current of a plane probe vs. absorbed microwave power for p = 2.4 mtorr, 30-sccm flow rate, and U_{targ} = 500 V.

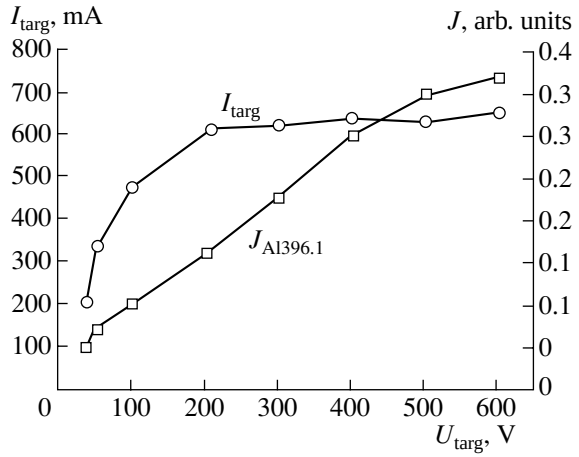

Fig. 4. Target current and the intensity of the Al 396.1-nm spectral line vs. target voltage for p = 2.4 mtorr, 30-sccm flow rate, and W_{abs} = 600 W.

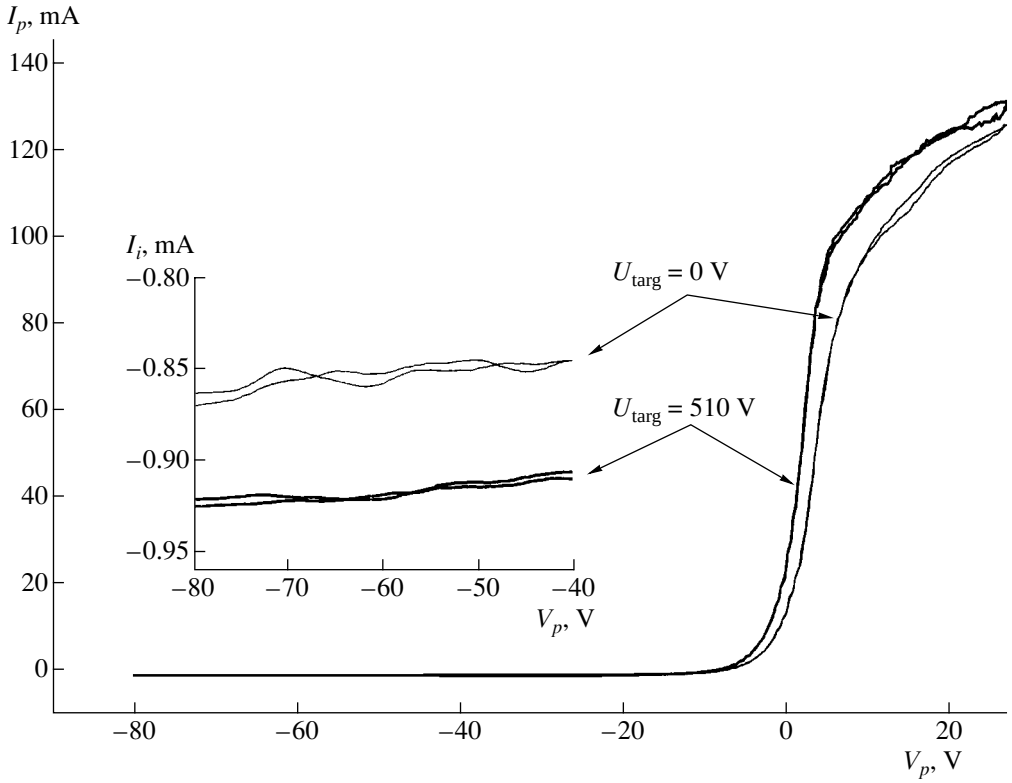

Fig. 5. Current–voltage characteristics of a probe placed at a distance of 15 cm from the Al target with (heavy curves) and without (light curves) sputtering for p = 2.4 mtorr, 30-sccm flow rate, W_{abs} = 750 W, U_{targ} = 510 V, I_{targ} = 725 mA, $n_{Xe^+} = 6.3 \times 10^{11}$ cm^{-3}, and $n_{Al^+} = 3 \times 10^{10}$ cm^{-3}.

the probe ion current. The erosion of the target indicates that the current is distributed nonuniformly over the target, being higher at its forepart. In addition, the plasma density at the chamber axis is higher than at r = 4 cm, where the target is located. The density n_{Xe^+} derived from the ion current without applying the voltage to the target is 6.3×10^{11} cm^{-3}. The density of aluminum ions n_{Al^+} derived from the difference between the ion currents using the procedure described

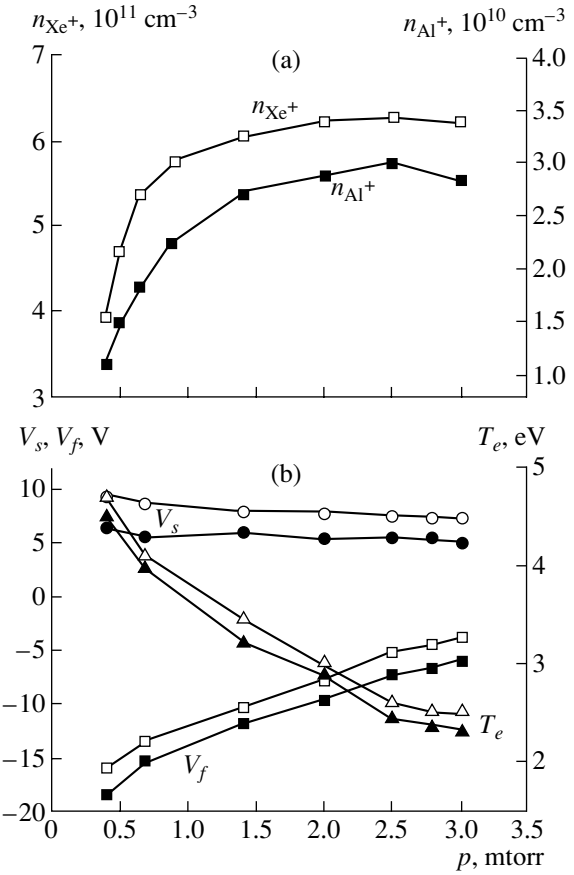

Fig. 6. Pressure dependences of (a) xenon and aluminum ion densities and (b) the plasma potential V_s, floating potential V_f, and electron temperature T_e 15 cm behind the target for W_{abs} = 700 W and W_{targ} = (open symbols) 0 and (closed symbols) 360 W.

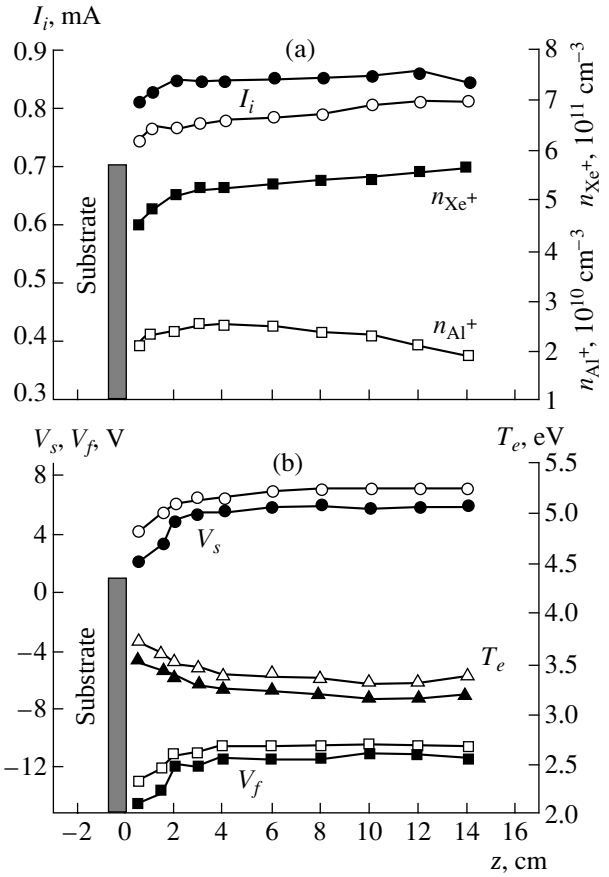

Fig. 7. Axial profiles (behind the target) of (a) the ion current I_i and xenon and aluminum ion densities and (b) the plasma potential V_s, floating potential V_f, and electron temperature T_e for p = 1.6 mtorr, 20-sccm flow rate, W_{abs} = 650 W, and W_{targ} = (open symbols) 0 and (closed symbols) 330 W.

above is 3×10^{10} cm^{-3}. On applying the voltage, the electron temperature changes only slightly (from 2.6 to 2.5 eV).

The pressure dependences of the discharge parameters behind the target, at a distance of 15 cm from it, are shown in Fig. 6. It is seen that the xenon ion density reaches its maximum at a pressure of 2.5 mtorr and then decreases. Note that the xenon ion density in this region is determined mainly by the plasma flow from the source, rather than local ionization. The ionization rate in the source is proportional to the pressure and the ionization rate constant, which depends on the ionization cross section and electron energy distribution function. At low pressures, the plasma density decreases due to the low density of neutral atoms; at high pressures, it decreases due to the decrease in the electron temperature. Downstream from the source, the plasma density profile is affected by ion–neutral collisions. As a result, the maximum plasma densities in the source and reactor are attained at different pressures [11]. In contrast, the Al ion density is determined by local ionization. The mean free path for the ionization of aluminum ions is equal to $\lambda_i = u_{Al}/\langle\sigma_i v_e\rangle n_e$, where u_{Al} is the velocity of sputtered aluminum atoms, $n_e\langle\sigma_i v_e\rangle = \int_{E_i}^{\infty} v\sigma_i f(E)dE$, σ_i is the ionization cross section, and E_i is the ionization energy. As the pressure increases, the velocity of sputtered Al atoms decreases due to collisions with Xe atoms (thermalization effect), which compensates for the decrease in the electron temperature. Furthermore, the increase in the pressure increases the probability of Al ionization due to nonresonant charge transfer.

Both the plasma potential and the absolute value of the floating potential (Fig. 6b) decrease with pressure because of a decrease in the number of high-energy electrons. When the voltage is applied to the target, the electron temperature decreases by only several percent because the metal ion density is no higher than 10% of the xenon ion at the given sputtering powers.

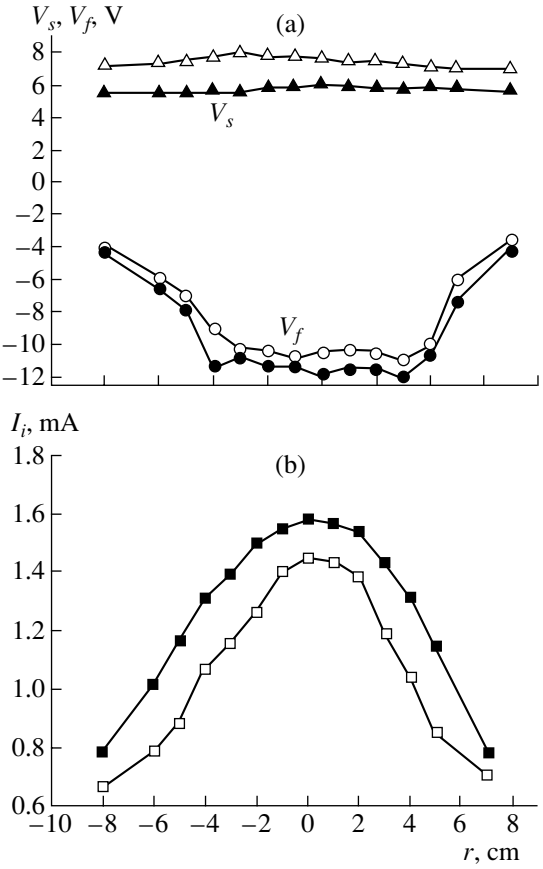

Fig. 8. Radial profiles of (a) the plasma and floating potentials and (b) the ion current I_i behind the target (at a distance of 15 cm from it) with (closed symbols) and without (open symbols) sputtering (cylindrical probe, p = 1.6 mtorr, 20-sccm flow rate, W_{abs} = 650 W, and W_{targ} = 330 W).

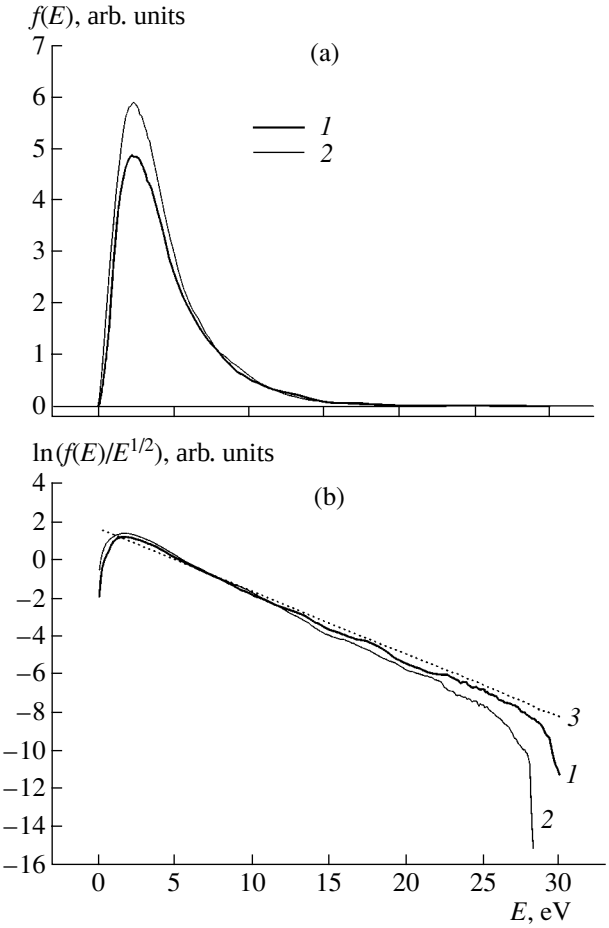

Fig. 9. (a) EEDF and (b) EEPF 15 cm behind the target at p = 2.4 mtorr, 30-sccm flow rate, W_{abs} = 730 W, and W_{targ} = 360 W for (*1*) U_{targ} = 0 V and E_{mean} = 4.5 eV and (*2*) U_{targ} = 510 V and E_{mean} = 4.3 eV. Curve *3* shows the EEPF for a Maxwellian distribution and E_{mean} = 4.5 eV.

Figure 7a shows the ion currents versus the distance from the substrate with (closed circles) and without (open circles) sputtering. The target is at a distance of 20 cm from the substrate. It can be seen that the difference between these currents and the Al ion density both increase with distance. This is obvious because ionization probability increases with the path length. The xenon density slightly decreases with distance from the target. Figure 7b shows the plasma potential V_s, floating potential V_f, and electron temperature versus the distance from the substrate. On applying the voltage to the target, the plasma potential V_s decreases by 1–2 V, the floating potential V_f becomes more negative, and both the difference $V_s - V_f$ and T_e slightly decrease. It is known that, when the electron energy distribution is Maxwellian, the difference $V_s - V_f$ and T_e are related by the formula $V_s - V_f = (T_e/2)\ln(I_{es}/I_{is})$, where I_{es} and I_{is} are the electron and ion saturation currents. Under the given conditions, the electron temperature T_e derived from this formula is lower than that determined from the *V–I* characteristic, because the magnetic field suppresses the electron current. Note that the low value of the plasma potential is explained by the fact that the plasma is confined in the transverse direction by the magnetic field and in the longitudinal direction by the electric field of the substrate, which is at the floating potential. The plasma potential, which depends slightly on the radius, decreases from 8.5 to 6 V on applying the voltage to the target (Fig. 8a). The floating potential V_f is negative and depends on the radius. The difference $V_s - V_f$ reaches its maximum (19 V) inside the target ($|r| < 4$ cm), where the high-energy electrons are located. At the periphery, the difference $V_s - V_f$ falls to 11–12 V. Figure 8b shows the radial profiles of the ion current at a distance of 15 cm from the target. Within the 8-cm-diameter region, the radial drop in the ion current changes from 40 to 20% when the sputtering voltage is turned on.

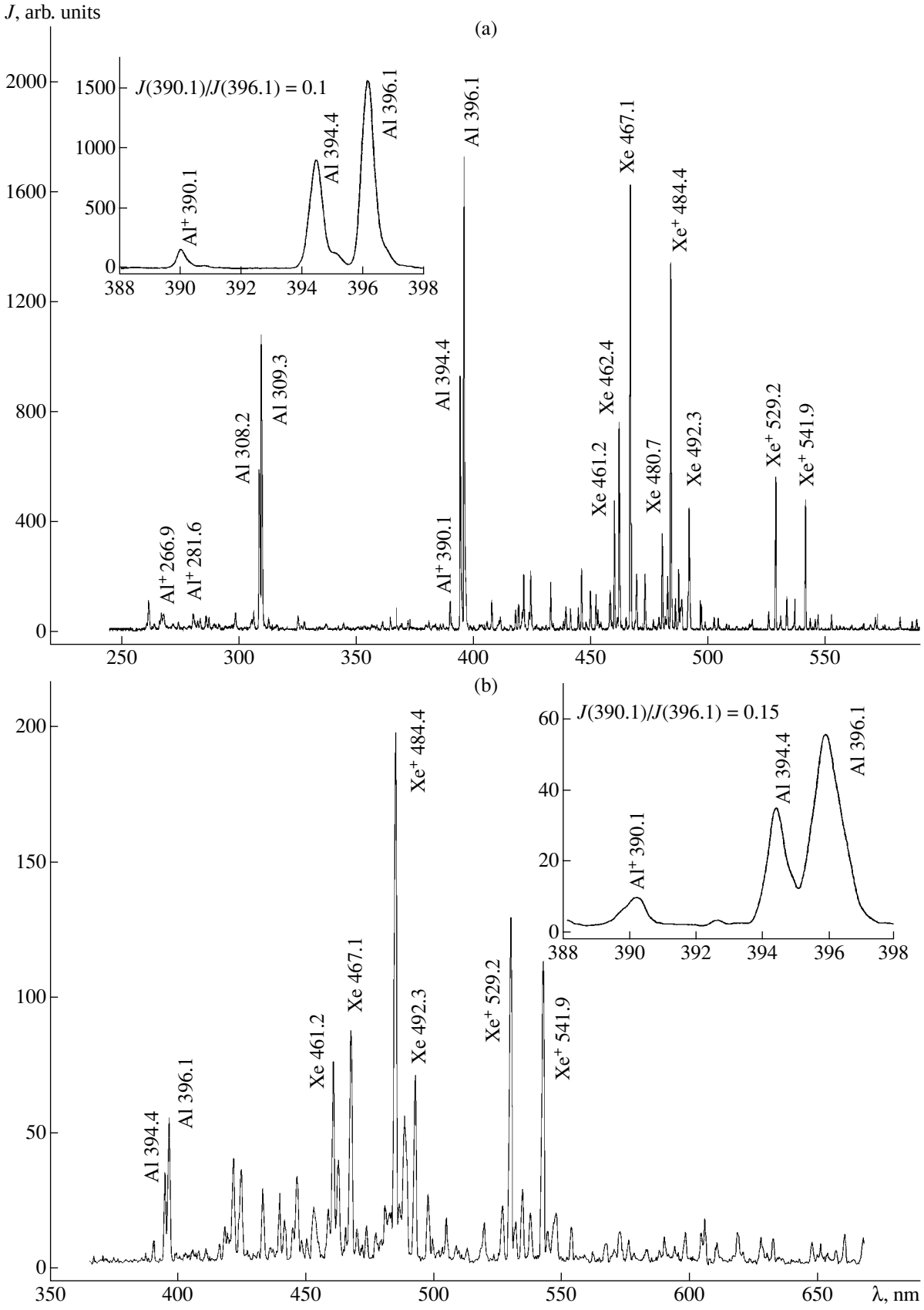

Fig. 10. Emission spectrum of the plasma (a) 15 cm behind the target and (b) in the source for p = 1.6 mtorr, 20-sccm flow rate, W_{abs} = 750 W, and W_{targ} = 360 W.

Figure 9a presents the nonnormalized EEDF $f(E)$. The area below the curve is proportional to the electron density. When the voltage U_{targ} is applied to the target, this area increases by 10%. The distribution function increases mainly in the low-energy region, and the mean electron energy $E_{\text{mean}} = \frac{1}{n_e} \int_0^\infty f(E) E dE$ changes only slightly (from 4.5 eV at $U_{\text{targ}} = 0$ to 4.3 eV at $U_{\text{targ}} = 510$ V). The electron energy probability functions (EEPF) obtained by dividing $f(E)$ from Fig. 9a by $\sqrt{E}$ [12] are shown in Fig. 9b on the logarithmic scale. For comparison, the figure also shows an analogous probability function for a Maxwellian electron energy distribution. This function is convenient because, for a Maxwellian distribution, its logarithm depends linearly on the electron energy. Due to inelastic collisions with atoms and ions, the number of electrons with energies higher than 10 eV is depleted as compared to a Maxwellian distribution. Moreover, with the sputtering power turned on, the high-energy tail of the EEDF decreases more rapidly. This is related to the presence of metal atoms in the discharge. The excitation and ionization energies of Al (~3 and 5.98 eV, respectively) are lower than those of Xe (~10 and 12.13 eV, respectively), whereas the cross sections for electron-impact excitation and ionization of Al are higher than those of Xe. As a result, the number of high-energy electrons and the line emission intensities of Xe atoms and ions decrease. Furthermore, the difference between the plasma potential V_s and the substrate floating potential V_f can be regarded as a potential barrier through which only electrons with sufficiently high energies can pass. Due to plasma quasineutrality, the value of this barrier is established at such a level that the electron and ion fluxes toward the substrate balance each other. When the number of high-energy electrons that are able to overcome this barrier decreases, the balance between the electron and ion fluxes is violated. In order for the electron flux to increase, the difference $V_s - V_f$ should decrease, as is observed in the experiment.

The plasma emission spectrum behind the target is shown in Fig. 10a. As the distance from the target increases from 5 to 17 cm, the ratio between the intensities of the Al^+ 390.1-nm and Al 396.1-nm lines increases from 0.02 to 0.1. For reference, Fig. 10b shows the plasma emission spectrum in the source. It is seen that the ion lines are dominating, which indicates a high degree of Xe ionization. The relative intensities of the Al lines decrease as the distance from the target increases. However, the ratio between the intensities of the Al^+ 390.1-nm and Al 396.1-nm lines increases. Thus, the degree of ionization increases with distance both upstream and downstream from the target.

Now, we make some estimates that cannot be considered completely accurate because of the large scatter in the data available in the literature. Nevertheless, they provide a good idea of the order of magnitude of the estimated values. According to measurements [13], the most probable energy of sputtered Al atoms is $E_{\text{prob}} = 3$ eV, which corresponds to the velocity $u_{\text{Al}} = 4.6 \times 10^5$ cm/s. Taking the value of σ_i from [4] and the values $n_e = 6.3 \times 10^{11}$ cm^{-3} and $T_e = 2.5$ eV measured at $p = 2.5$ mtorr, we obtain that the mean free path with respect to ionization is $\lambda_i \approx 105$ cm. Then, according to the formula $n_{\text{Al}^+}/n_{\text{Al}} = 1 - \exp(-z/\lambda_i)$, about 13% of Al atoms will be ionized over the path length $z = 15$ cm. Using the above value $n_{\text{Al}^+} = 3 \times 10^{10}$ cm^{-3}, we obtain that the Al atom density is $n_{\text{Al}} = 2 \times 10^{11}$ cm^{-3}.

The rate of metal film deposition depends on the atom and ion fluxes. The flux of Al ions is $\Gamma_{\text{Al}^+} = 0.61 n_{\text{Al}^+} u_{\text{Al}^+}$. The velocity of ions arriving at the substrate is determined by the Bohm formula $u_{\text{Al}^+} = (kT_e/M_{\text{Al}})^{1/2} = 2.95 \times 10^5$ cm/s; hence, $\Gamma_{\text{Al}^+} = 5.5 \times 10^{15}$ cm^{-2} s^{-1}. The flux of Al atoms is $\Gamma_{\text{Al}} = 0.25 n_{\text{Al}} u_{\text{Al}}$. The atom and ion temperatures were determined using an FPI and a vidicon as a detector (Fig. 1). The measured temperatures of Xe atoms and ions were 0.05 and 0.4 eV, respectively. The temperature of Al atoms was not measured. At the given pressure, the mean free path of Al atoms between collisions with Xe atoms is equal to 3.5 cm. At a distance of 15 cm from the target, the most probable energy of Al atoms after four collisions is $(1 - q)^4 E_{\text{prob}} = 0.11$ eV, where $q = 4M_{\text{Al}}M_{\text{Xe}}/(M_{\text{Al}} + M_{\text{Xe}})^2$ is the energy fraction lost by an Al atom per collision. Then, we have $u_{\text{Al}} = 0.9 \times 10^5$ cm/s; the flux $\Gamma_{\text{Al}} \approx 4.5 \times 10^{15}$ cm^{-2} s^{-1}; and the relative contribution of ions to the total flux, $\Gamma_{\text{Al}^+}/(\Gamma_{\text{Al}^+} + \Gamma_{\text{Al}})$, is 55%.

4. CONCLUSION

The spatial distribution of the degree of ionization of metal sputtered with a microwave ECR discharge has been studied using the probe and optical emission spectroscopy techniques. The study is aimed at developing a system for the metallization of submicron ULSI structures.

ACKNOWLEDGMENTS

This study was supported by the Ministry of Education of the Russian Federation (under the program "Critical Technologies").

REFERENCES

1. S. M. Rossnagel, Thin Solid Films **263**, 1 (1995).
2. J. Hopwood and F. Qian, J. Appl. Phys. **78**, 758 (1995).
3. C. A. Nickols, S. M. Rossnagel, and S. Hamaguchi, J. Vac. Sci. Technol. B **14**, 3270 (1996).

4. M. Dickson and J. Hopwood, J. Vac. Sci. Technol. A **15**, 2307 (1997).
5. S. Shibuki, H. Kanao, and T. Akahori, J. Vac. Sci. Technol. B **15**, 60 (1997).
6. S. Takehiro, N. Yamanaka, H. Shindo, *et al.*, Jpn. J. Appl. Phys. **30**, 3657 (1991).
7. W. M. Holberg, J. S. Logan, H. J. Grabarz, *et al.*, J. Vac. Sci. Technol. A **11**, 2903 (1993).
8. S. M. Gorbatkin, D. B. Poker, C. Doughty, *et al.*, J. Vac. Sci. Technol. B **14**, 1853 (1996).
9. N. P. Poluektov and Yu. P. Tsar'gorodtsev, Prib. Tekh. Éksp., No. 4, 150 (1996) [Instrum. Exper. Techniques **39**, 611 (1996)].
10. C. Steinbruchel, J. Vac. Sci. Technol. A **8**, 1663 (1990).
11. N. P. Poluektov, Yu. P. Tsar'gorodtsev, and I. G. Usatov, Fiz. Plazmy **25**, 981 (1999) [Plasma Phys. Rep. **25**, 905 (1999)].
12. M. A. Lieberman and A. J. Lichtenberg, in *Principles of Plasma Discharges and Materials Processing* (Wiley, New York, 1994), p. 177.
13. R. V. Stuart, G. K. Wenher, and G. S. Anderson, J. Appl. Phys. **40**, 803 (1969).

Translated by N. N. Ustinovskiĭ